TAIGA-HiSCORE: a new wide-angle air Cherenkov detector for multi-TeV gamma-astronomy and cosmic ray physics

DISSERTATION

zur Erlangung des akademischen Grades
doctor rerum naturalium
(Dr. rer. nat.)
im Fach: Physik
Spezialisierung: Experimentalphysik

eingereicht an der
Mathematisch-Naturwissenschaftlichen Fakultät
der Humboldt-Universität zu Berlin

von

M.Sc. Andrea Porelli

Präsident der Humboldt-Universität zu Berlin:
Prof. Dr.-Ing. Dr. Sabine Kunst

Dekan der Mathematisch-Naturwissenschaftlichen Fakultät:
Prof. Dr. Elmar Kulke

Gutachter: 1. Dr. Gernot Meier, Deutsches Elektronen-Synchrotron, Zeuthen
2. Prof. Dr. Elisa Bernardini, Humboldt-Universitä zu Berlin
3. Prof. Dr. Jörg Hörandel, Radboud University Nijmegen

Tag der mündlichen Prüfung: 05/08/2019

To my parents

Declaration of Independent work for inclusion in the thesis

I declare that I have completed the thesis independently using only the aids and tools specified. I have not applied for a doctor's degree in the doctoral subject elsewhere and do not hold a corresponding doctor's degree. I have taken due note of the Faculty of Mathematics and Natural Sciences PhD Regulations, published in the Official Gazette of Humboldt-Universität zu Berlin no. 42 on July 11 2018.

Abstract

The TAIGA (Tunka Advanced Instrument for cosmic ray physics and Gamma Astronomy) experiment aims to establish a new technology for ground-based gamma-astronomy by combining both Cherenkov imaging and non-imaging timing techniques. By detecting cosmic rays (CR) above 100 TeV and gamma-rays in the energy range from 10 TeV up to several PeV, TAIGA will address CR composition and spectral measurements in the Galactic/extragalactic transition region, and the origin of CRs by searching for galactic PeVatrons.

The main topic of this work is TAIGA-HiSCORE, the wide-aperture air Cherenkov timing array. The focus is on precision shower arrival direction reconstruction, that is achieved by (1) sub-nsec time-synchronization between all array stations based on a dedicated hardware timing system, and (2) a newly developed time calibration procedure that minimizes mispointing. The performance is verified using events originating from extensive air shower (EAS) and from a LIDAR laser beam from the International Space Station (ISS).

First, we analyse HiSCORE 9 data collected with a data acquisition system based on the White Rabbit (WR) timing system. The station time offset calibration is obtained using a LED light source signal and allows a precise arrival direction reconstruction of the detected EAS data. The analysis of both EAS and LED data allows to verify the sub-nsec time synchronization of the WR system.

In the analysis of the HiSCORE 28 data, taken from 2015-2018, we address the problem of achieving an easy-to-perform array time calibration for large area ground-based Cherenkov detectors. The intrinsic limits of the "self-time calibration method", which uses EAS to estimate the time offsets, are discussed. A new "hybrid" calibration method is developed, which makes use of EAS data, and requires direct LED calibration of only a few array stations. The efficiency and stability of the hybrid method has been tested using MC simulations. As for HiS9, the analysis of both EAS and LED data allow to verify the sub-nsec time synchronization of the timing system. Finally, the "chessboard" method is applied on the reconstructed data to obtain a MC-independent estimation of the detector angular resolution. It is found to be 0.4° at threshold (~ 50 TeV) and $\leq 0.2^\circ$ above 100 TeV.

A serendipitous discovery was made in this work: events that originate from the CATS-LIDAR on-board the ISS were found in the HiSCORE 28 data sample. After understanding their main characteristics, these "ISS-events", which make up a quasi-point-source, are used to verify the array time synchronization, the correctness of the array time calibration and event reconstruction, and the detector absolute angular pointing ($\leq 0.1^\circ$). This absolute pointing calibration is particularly important since a strong gamma point source has not yet been detected by the TAIGA-HiSCORE 28 detector.

The final part of the work presents a first approach to a wide aperture point source analysis, developed for the TAIGA-HiSCORE detector in stand-alone operation. The analysis is tested on the three years HiS28 data sample, with a focus on the region around the Crab Nebula. After showing the preliminary results, the limits of the current implementation and improvements to increase the detection potential are discussed.

Zusammenfassung

Das TAIGA Experiment (Hochentwickeltes Tunka Instrument zur Untersuchung der geladenen kosmischen Strahlung und fuer Gamma Astronomie) zielt auf die Etablierung einer neuen Technologie fuer bodengebundene Gamma Astronomie, durch die Kombination sowohl abbildender als auch nicht-abbildender Techniken. Die Messung geladener kosmischer Strahlung mit Energien oberhalb $100\,\mathrm{TeV}$ und von Gamma-Strahlung von $10\,\mathrm{TeV}$ bis zu einigen PeV mit TAIGA wird beitragen zur Untersuchung von Energiespektrum und Zusammensetzung der geladenen kosmischen Strahlung im Bereich des Uebergangs von galaktischer zu extragalaktischen Quellen und wird auch beitragen zur Suche nach dem Ursprung der kosmischen Strahlung ueber die Suche nach galaktischen PeVatronen.

Im Zentrum dieser Arbeit steht TAIGA-HiSCORE - ein Luftschauer-Detektorfeld mit grosser Apertur. Dabei steht die hochgenaue Rekonstruktion der Schauerrichtung im Mittelpunkt, die erreicht wird mittels (1) sub-nanosekunden genauer Synchronisation zwischen allen Stationen im Detektorfeld, die auf einen dezidierten hardware-basierten Zeitsystem basiert, und (2) eine neuentwickelte Kalibrationsmethode, die eine fehlerhafte Ausrichtung minimiert. Die Methode wird verifiziert unter Benutzung von atmosphaerischen Luftschauerereignissen (EAS), und Ereignissen die durch einen LIDAR Laserstrahl von der Internationalen Raumstation (ISS) erzeugt werden.

Zuerst analysieren wir Daten von HiSCORE 9, die erhalten wurden mit einem Datennahmesystem das auf dem White Rabbit Zeitsystem (WR) basiert. Die Kalibration der Zeitverschiebungen erfolgt ueber Signale einer LED Lichtquelle, und ermoeglicht die genaue Richtungsbestimmung der aufgezeichneten Daten von EAS Schauern. Die EAS und LED Daten erlauben eine Bestaetigung der Zeitsynchronisationsgenauigkeit des WR-Systems im Sub-Nanosekundenbereich.

Im Zusammenhang mit der Analyse der HiSCORE 28 Daten von 2015-2018 wenden wir uns der Frage nach einer einfach zu handhabenden Zeit-Kalibration fuer grossflaechige bodengebundene Cherenkov Detektoren zu. Dargelegt werden die intrinsischen Grenzen der "Zeit-Selbst-Kalibrationsmethode", die die EAS Daten zur Bestimmung der Zeitverschiebungen benutzt. Eine neue "hybride" Kalbrationsmethode wurde entwickelt, die EAS Daten benutzt und fuer lediglich einige wenige Stationen eine direkte LED Kalibration erfordert. Effizienz und Stabilitaet der hybriden Methode wird in MC Simulationen getestet. Wie fuer HiS9, ergibt die Untersuchung von EAS und LED Daten eine Genauigkeit des Zeitsystems unterhalb einer Nanosekunde. Die Anwendung der "Schachbrett Methode" auf rekonstruierte Daten erlaubt eine MC-unabhaengige Abschaetzung der Winkelaufloesung des Detektors. Diese wird bestimmt zu 0.4° an der Schwelle ($50\,\mathrm{TeV}$) und $\leq 0.2^\circ$ oberhalb von $100\,\mathrm{TeV}$.

Eine zufaellige Entdeckung wurde im Rahmen dieser Arbeit gemacht: Im HiSCORE-28 Datensatz wurden Ereignisse gefunden, die auf den CATS-LIDAR auf der ISS zurueckzufuehren sind. Nachdem ihre Eigenschaften verstanden wurden, werden diese "ISS Ereignisse", die eine Quasi-Punktquelle darstellen, benutzt um Zeitsynchronisation, Zeitkalibration, korrekte Ereignisrekonstruktion und ausserdem die absolute Richtungskalibration von $\leq 0.1^\circ$ zu verifizieren. Im Schlussteil der Arbeit wird eine erste Version einer Punktquellen-Suche fuer den HiSCORE Detektor im "Standalone-Mode" ueber einen grossen Himmelesbereich vorgestellt. Die Methode wird getestet mit dem HiS28 3-Jahres-Datensatz, angewandt auf den Bereich um den Krebsnebel. Zusammen mit den vorlaeufigen Ergebnissen werden Grenzen der gegenwaertigen Analyse und Verbesserungen mit dem Ziel eines vergroesserten Nachweispotentials diskutiert.

Contents

Chapter 1

Cosmic ray physics and gamma-ray astronomy

An introduction to the field of cosmic ray (CR) physics and gamma-ray astronomy is given in this chapter, presenting the scientific background and context of this work. Section 1.1 gives an overview on cosmic rays physics. The main CR measurements are summarized, detailing the all-particle spectrum features, the composition, and the observed anisotropies in the arrival direction distribution. Based on observations, possible sources of cosmic rays are discussed, together with possible acceleration mechanisms, and the transport through the interstellar medium. In section 1.2, an introduction to gamma-ray astronomy is presented, showing the most recent results in the very high energy domain (VHE, 30 GeV - 30 TeV). The detection of gamma-rays in the ultra high energy domain (UHE, > 30 TeV) is also discussed, pointing out the implications of such measurements on determining the origin and the acceleration processes of Galactic CRs. Finally, section 1.3 gives an overview of the experimental techniques used in CR physics and gamma-ray astronomy, with the main focus on the air Cherenkov technique, on which the TAIGA experiment is based. A more detailed description of the TAIGA experiment and the TAIGA-HiSCORE detector is given in chapter 2.

1.1 Cosmic rays

Cosmic rays are high energetic particles reaching the Earth from outside the Solar System. With the term cosmic ray one usually refers to ionized atomic nuclei, although electrons, positrons, antiprotons, gamma-rays and neutrinos also arrive.

Discovered by Hess in 1912 with balloon-borne experiments (Hess, 1912), CRs played a fundamental role in particle physics during the first half of last century as source of high energy particles, allowing the discovery of new particles such as the positron (Anderson, 1933), the muon (Neddermeyer and Anderson, 1937) and the pion (Lattes et al., 1947). In 1937 Pierre Auger concluded from ground-based measurements that CRs were able to generate extensive air showers of secondary particles (EAS) as a consequence of their interaction with at-

mospheric nuclei (Auger et al., 1939).

Although the sources, the acceleration and propagation mechanisms of CRs are still subject of intense research, significant progress has been made during the last decade, and a consistent picture from CR observations begins to emerge, as reported in the next sections.

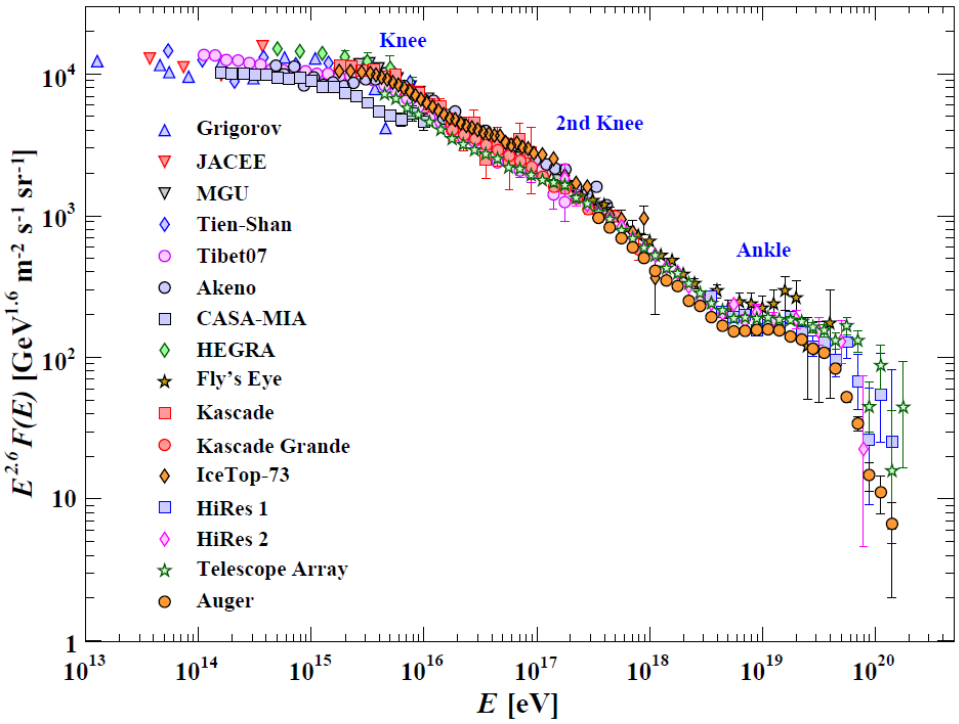

Figure 1.1: Measured all-particles differential CR flux (multiplied by $E^{2.6}$) as a function of energy ($E \geq 10^{13}$ eV). Figure from Patrignani,C., et al. (Particle Data Group) (2016).

1.1.1 Energy spectrum

The measured primary CR energy spectrum, presented in figure 1.1, extends from ~ 1 GeV to beyond 100 EeV, with the differential flux dropping by more than 30 orders of magnitude over this energy rage. It is determined by direct measurements for energies below few hundred TeV, and by indirect ground detection of EAS at higher energies. The flux measurements by different experiments sometimes differ significantly. This is mainly due to different energy calibrations performed by experiments using different detection techniques, or to differences in the energy resolutions.

The CR spectrum is well described by a power law, $dN/dE \propto E^{-\gamma}$, with the spectral index γ slightly changing depending on the energy range. The fact that the CR spectrum is ap-

proximately a power law clearly indicates that they get accelerated in non-thermal processes. Looking in detail, the following spectral features can be noticed:

- Up to few PeV, the overall spectrum has a spectral index $\gamma \approx 2.7$;
- At energies ~ 4 PeV, a steepening to $\gamma \approx 3$ of the total spectrum is observed (*knee*);
- A further steepening to $\gamma \approx 3.3$ is observed at about 0.1 EeV (2^{nd} *knee*);
- At about 5 EeV, the spectrum becomes harder again, with $\gamma \approx 2.6$ (*ankle*);
- At energies beyond ~ 40 EeV a strong suppression becomes apparent.

Besides these main features, a hardening is observed at about 20 PeV (*low-energy ankle*), with the spectrum being a bit steeper ($\gamma \approx 3.1$) from the *knee* up to this feature, and a bit harder ($\gamma \approx 2.9$) from this energy up to the 2^{nd} *knee* (IceCube collaboration, 2013; Prosin et al., 2014).

The shape of the spectrum between the *knee* and the *ankle* is explained with a rigidity dependent effect ($R = p/eZ$, with p the particle momentum, and eZ the total charge) leading to a steepening in the overall spectrum and an associated increase in the average CR mass (Peters, 1961; Hillas, 2006). Measurements by KASCADE and KASCADE-Grande (Apel et al., 2009, 2013b) show the spectrum of protons becoming steeper at ~ 4 PeV (*knee*), and the heavier elements suppression compatible with a rigidity dependent effect: $\sim 4 \times Z$ PeV. Thus, the 2^{nd} *knee* is interpreted as the steepening of the Fe flux, at an energy $\sim 26 \times 4$ PeV. In this scenario, the *low-energy ankle*, at about 20 PeV, could be interpreted as cross-over between the steeply falling He and CNO[1] fluxes and the harder Fe and Si fluxes.

The *ankle* is considered to be the natural place for the transition between the Galactic and extragalactic CR components, with the spectral hardening at ~ 5 EeV associated with the emergence of the extragalactic flux above the steeply falling Galactic flux. However, recent measurements of $< X_{max} >$[2] (figure 1.3) and CR anisotropies (P. Abreu, et al. (The Pierre Auger Collaboration), 2012, 2013) at EeV energies, suggest that the transition could be taking place somewhere between the 2^{nd} *knee* and the *ankle*.

Concerning the suppression observed at ~ 40 EeV, a similar effect was first proposed in 1966 by Greisen, Zatsepin and Kuzmin (GZK cut-off, Greisen (1966); Zatsepin and Kuzmin (1966)), shortly after the discovery of the cosmic microwave background (CMB). The cut-off is caused by the strong interaction between particles of energy above $5 \cdot 10^{19}$ eV originated more than 50 Mpc outside the galaxy and the CMB, leading to a significant energy loss and flux suppression above this energy. Except for early results from AGASA (Medina-Tanco, 1999), later measurements from the Auger (Abraham et al., 2008), HiRes (Abbasi et al., 2008), and the Telescope Array (Abbasi et al., 2014) appear consistent with the GZK cut-off.

[1] Carbon, Nitrogen, Oxygen.
[2] See section 1.3.1 for a definition of X_{max}.

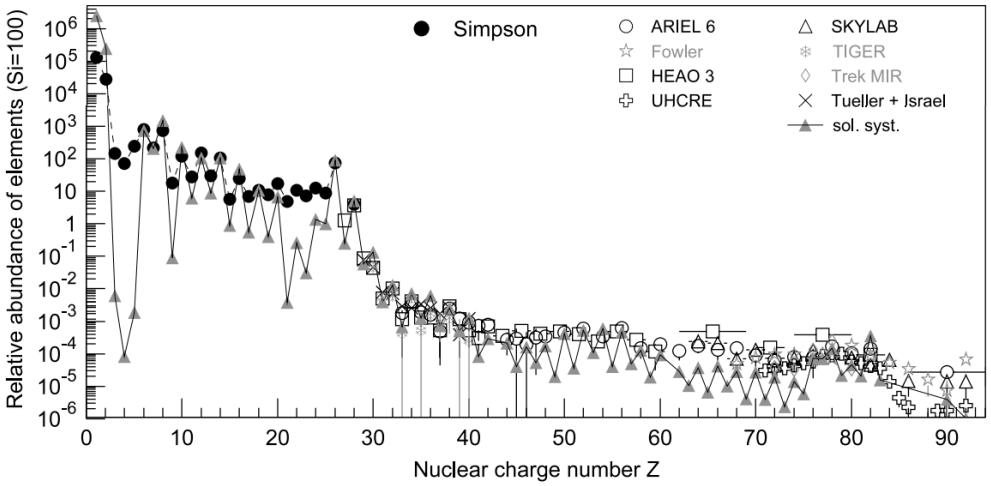

Figure 1.2: Abundance of elements in cosmic rays as a function of their nuclear charge number, Z, at energies $\sim$ 1 GeV/n, normalized to Si ($Z = 14$) (Hörandel, 2006). Abundance for nuclei with $Z \leq 28$ according to (Simpson, 1983). As reference, the grey triangles show the abundance of elements in the solar system. Figure from Blümer et al. (2009).

1.1.2 Composition

Figure 1.2 shows the abundance of elements in low energy CRs ($E \sim 1$ GeV). While it presents many similarities with the abundances in the solar system (grey triangles), some interesting differences are observed. The most common elements, H (87%) and He (12%) (Mewaldt, 1983), are less abundant in CRs, most likely reflecting the composition of the medium in the acceleration regions and also the relatively large ionization potential of these elements that may be an obstacle for their injection in the acceleration process (Mollerach and Roulet, 2017). On the other hand, several elements are more abundant in the CRs, as these are produced as secondaries in interactions between primary CRs and the interstellar medium (ISM). As an example, Li, Be and B are produced in the spallation of the more abundant CNO, in turn F is produced in the spallation of Ne, and elements from Sc to Mn in the spallation of Fe and Ni.

The determination of the CR mass composition at the highest energies ($\geq 10^{15}$ eV) is a more complicated task. Due to the low flux, only indirect measurements via EAS detection are possible. The sensitivity of shower parameters to the primary mass is low, with the main uncertainties coming from the simulation of hadronic interactions. The mass of the primary particles is usually derived using two methods: measuring the average air shower depth, X_{max} (Kampert and Unger, 2012), or the ratio of muons to electrons, N_e/N_μ(Apel et al., 2009, 2013a). Figure 1.3 shows measurements of $< X_{max} >$ as a function of energy. The average mass composition presents a transition from light to heavy nuclei between 10^{15} and 10^{17} eV, and back to light nuclei between 10^{17} and 10^{18} eV. Above 10^{18} eV the average mass appears to increase again

with the energy, although the low statistics and experimental systematics do not allow for a clear picture.

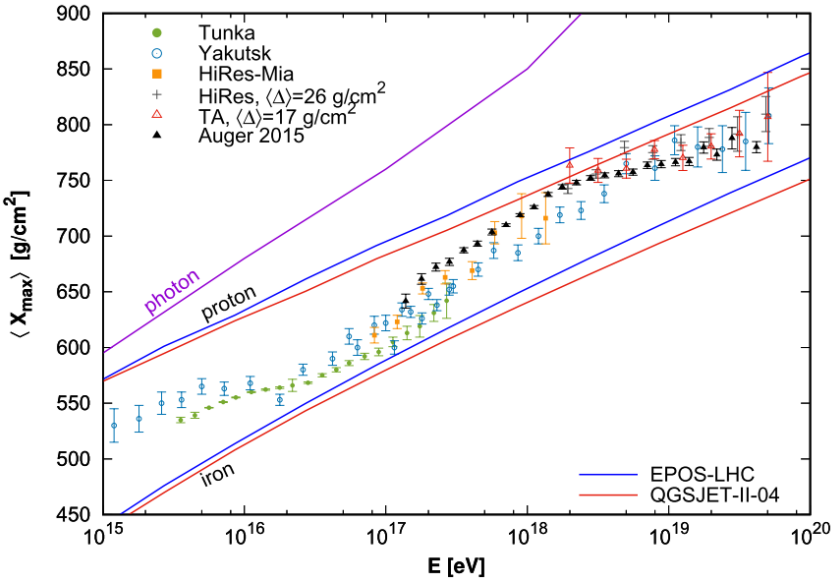

Figure 1.3: $< X_{max} >$ measurements as a function of primary energy. The solid lines show the predictions from photon, proton and iron initiated showers, using different recent hadronic models. Data from Kampert and Unger (2012) and Pierre Auger Collaboration (2014). HiRes and TA data have been corrected for detector effects (see Kampert and Unger (2012) for details). Figure adapted from Mollerach and Roulet (2017)

1.1.3 Arrival direction anisotropy

The CR arrival directions are in general uniformly distributed in the sky, as the charged particles are deflected by the presence of the galactic and extra-galactic magnetic fields. The effect of the magnetic fields on the CR trajectory can be estimated with the Larmor radius

$$r_L = \frac{E/c}{|q|B} = \frac{R}{B} \tag{1.1}$$

where R is the magnetic rigidity. For a magnetic field $B = 3-5\,\mu$G (Fletcher, 2011), a proton of 1 PeV has a gyro-radius of $0.36 - 0.2$ pc, much smaller than the Milky Way radius (~ 15 kpc). This means that it is not possible to correlate the CR arrival direction with the position of sources far from the solar system.

However, small-scale anisotropies at $10^{-3} - 10^{-4}$ level in the TeV-PeV energy range have been recently measured by various experiments (Tibet-ASγ (Amenomori et al., 2005), Super

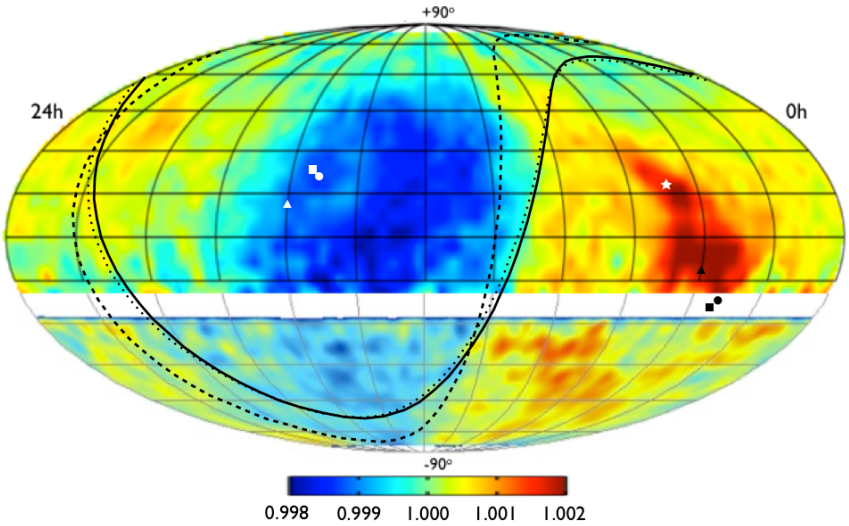

Figure 1.4: Map in equatorial coordinates of relative intensity distributions of cosmic ray counts measured by Tibet-ASγ ($< E >\sim 5$ TeV, Amenomori et al. (2011)) in the northern hemisphere and by IceCube ($< E >\sim 20$ TeV, Abbasi et al. (2010)) in the southern hemisphere. The color scale indicates relative excess (red) and deficit (blue) with respect to average intensity. See Desiati and Lazarian (2013) for details.

Kamiokande (Guillian et al., 2007), MILAGRO (Abdo et al., 2008), EAS-TOP (Aglietta et al., 2009), ARGO (Bartoli et al., 2013) and HAWC (BenZvi, 2015) in the northern hemisphere, IceCube (Abbasi et al., 2010) and its surface air shower array IceTop (Aartsen et al., 2013) in the southern hemisphere). Figure 1.4 shows a combined sky map of the CRs relative intensities measured by Tibet-ASγ and IceCube. While there are several theories regarding the origin of this anisotropy, including structures in the heliomagnetic field, non-diffusive propagation, and turbulence in Galactic magnetic fields (see Ahlers and Mertsch (2017) for a review), it is not possible to associate any specific CR sources using the available data.

A different scenario is expected for particles at energies above the GZK cut-off (UHECR). Due to the strong energy losses, particles with energies $> 10^{20}$ eV are expected to originate mainly from relatively nearby sources (< 100 Mpc), with the high rigidity limiting the deflection ($< 10°$) by the magnetic fields (see equation 1.1). As a consequence, the UHECR arrival directions distribution may show correlations with possible sources, depending on their composition, the propagation models, and the configuration and strength of the extra-galactic magnetic fields.

The Pierre Auger Collaboration reported in Abraham et al. (2007) a correlation of events with the AGNs in the Veron-Cetty & Veron (VCV) catalogue (Véron-Cetty and Véron, 2006), which had initially led to establish an anisotropy at the 99% confidence level, but which was not confirmed with subsequent data (Kampert and The Pierre Auger Collaboration, 2012). Similar

searches have been performed on the data collected by Telescope Array (Abbasi et al., 2014): despite the observation of a "hot-spot" centred at ($R.A. = 146.^{\circ}7$, $\delta = 43.^{\circ}2$), with a Li&Ma significance of $5.1\,\sigma$, no astrophysical counterpart has been found in that region of the sky. The results so far obtained still present a remarkable degree of isotropy, and more statistics is needed to establish the nature of the observed signals. A complete report on the current status for UHECR anisotropy searches can be found in Deligny et al. (2013, 2017)

1.1.4 Cosmic rays sources

As said at the beginning of this chapter, the shape of the energy spectrum and the high energies observed indicate that CRs are accelerated in non-thermal processes. Starting from Fermi's original idea (Fermi, 1949) that the acceleration could result from the encounter of CRs with moving magnetized regions, such as molecular clouds (MC), it was later realized that a much more advantageous situation could result in the neighbourhood of shock waves through magnetized media (Axford et al., 1977; Krymskii, 1977; Blandford and Ostriker, 1978; Bell, 1978). In this model the particles pass through a shock-front many times, gaining energy at each cycle. Since the energy gain is linear in the shock velocity, this mechanism is dubbed *first-order Fermi acceleration*, or *diffusive shock acceleration* (DSA).

Assuming a CR spectrum at the source $\sim R^{-\gamma_s}$ and a rigidity dependent Galactic escape time, $\tau_{esc} \propto R^{-\delta}$, it is expected that the final spectrum observed at Earth scales as

$$\frac{dN}{dE} \propto R^{-(\gamma_s+\delta)} \tag{1.2}$$

Recent measurements show a value of $\delta \simeq 1/3$ (Aguilar et al., 2016), that combined with the DSA expectations, $\gamma_s \simeq 2.1 - 2.3$, predict a spectral index $\gamma \simeq 2.4 - 2.6$, compatible with the one observed below the *knee*. Under the hypothesis that different sources accelerate CRs up to different maximum rigidities, their superposition can lead to an effective steepening in the overall source spectral index, resulting in an effective spectral index of $\sim 2.6 - 2.7$ at the Earth location (Ptuskin et al., 2010).

Supernova remnants (SNRs) are so far considered the most plausible source of Galactic CRs. The energy density for CRs can be sustained by 1-3 supernovae (SNe) per century, assuming that 10-30% of the explosion energy is converted into particle acceleration (e.g. see Bykov et al. (2018) for a recent review on CRs production in SNe). However, the simple combination of SNRs with the DSA model predicts a maximum particle acceleration up to energies of no more than $\leq Z \times (10 - 100)$ TeV (Lagage and Cesarsky, 1983), in disagreement with the idea that at least up to the knee ($4 \times Z$ PeV) CRs have Galactic origin. A solution to this problem is represented by the *non linear diffusive shock acceleration* model (NLDSA, see Malkov and Drury (2001) for a review). Taking into account the dynamical reaction of the accelerated particles on the shock wave, a large amplification of the magnetic fields can be achieved, allowing to accelerate CRs up to $Z \times 3 \cdot 10^{15}$ eV (Blasi, 2013). Important evidences for this mechanism are

given by the observation of narrow filaments of non-thermal X-ray radiation along the shock front in young SNRs (Katsuda et al., 2010), and of the characteristic π^0 signature in SNR (Ackermann et al., 2013). On the other hand, the super-massive black hole in the Galactic center seems to be accelerating CRs up to PeV energies (Abramowski et al., 2016).

Regarding the spectrum region above the 2^{nd} *knee*, if different sources accelerate CRs up to different maximum rigidities, their superposition can lead to an effective steepening in the overall source spectral index, with heavy nuclei (iron) accelerated up to 10^{18} eV (Ptuskin et al., 2010). Another hypothesis sees the CRs between the 2^{nd} *knee* and the *ankle* as the result of a second Galactic component, represented by either a re-acceleration of the primary component at a Galactic wind termination shock, or supernova explosions of Wolf-Rayet stars (Thoudam et al., 2016).

In summary, while SNe can be considered the main source of Galactic CRs, it is not clear yet through which mechanisms the particles are accelerated, escape from the acceleration regions, and are transported in the Galaxy, in order to explain the observed CR spectrum below 10^{18} eV.

Concerning the origin of Extragalactic CRs, the observations at energies above 10^{20} eV require the existence of cosmic accelerators capable of accelerating particles to at least these energies. Since the acceleration mechanisms require the particles to be confined magnetically inside the boundaries of the accelerating object, the product of its size and its magnetic field must be large. Given these requirements, the most promising candidates are represented by Active Galactic Nuclei (AGN, Murase et al. (2011); Caprioli (2015)), gamma-ray bursts (Vietri, 1995; Waxman, 1995), and newly-born millisecond pulsars (Vietri, 1995; Blasi et al., 2000).

The short review on CRs presented here shows how the study of CRs alone is not sufficient to identify their sources and to understand their generation in detail. However, two other messenger particles can be used to help solve this puzzle: high energy neutrinos and gamma-ray photons. Both are produced in the vicinity of cosmic ray accelerators and can be used to pinpoint these accelerators since they are not affected by magnetic or electric fields. While no astrophysical objects have been associated yet with the observed flux of high energy neutrinos (IceCube Collaboration et al., 2016), hundreds of sources of VHE gamma-ray emission have been detected so far, and some of these sources show evidence for cosmic ray acceleration. A more detailed description of gamma-ray astronomy and its potential contribution to solve the question of the CRs origin is presented in the next section.

1.2 Gamma-ray astronomy

For centuries astronomical observations have been limited within the visible region of the electromagnetic spectrum. Only in the last century, thanks to technological progress, it was possible to expand the observation window to radio, infrared, UV, X-ray and the wide range of gamma energies, as shown in figure 1.5. Due to the atmospheric absorption, direct observation of the electromagnetic radiation from ground are only possible in the visible and radio bands.

In the other frequencies (gamma, X-ray, UV and partly infrared), the observations are only possible using space-based experiments. However, at high photon energies ($\geq$ 30 GeV) it is possible again to detect radiation from the ground indirectly, by detecting the extensive air showers produced by the interaction of these highly energetic photons with the atmosphere, as explained in detail in section 1.3.2.

As shown in figure 1.5, the gamma-ray band is usually divided into four energy sub-regimes (Aharonian, 2004):

- Low energy (LE): up to 30 MeV
- High energy (HE): 30 MeV to 30 GeV
- Very high energy (VHE): 30 GeV to 30 TeV
- Ultra high energy (UHE): Above 30 TeV

The next sections will give an overview of the VHE gamma-ray astronomy field developed in the last two decades (section 1.2.1), and present the motivations for an extension to the yet poorly covered UHE regime (section 1.2.2).

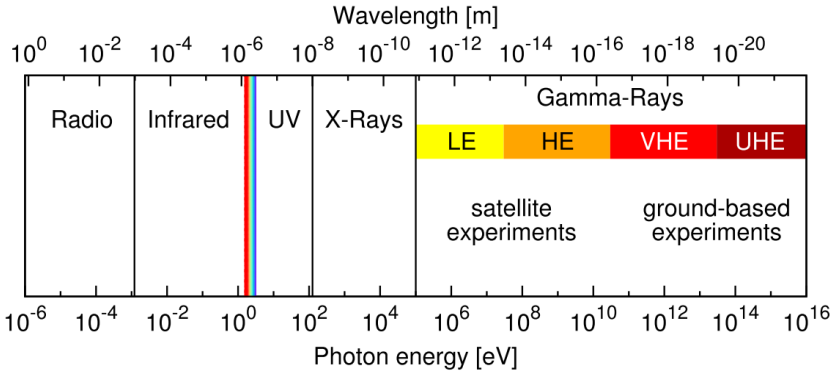

Figure 1.5: Photon energy bands in modern astronomy. The visible regime is indicated by the rainbow colours at about 1 eV. The energy bands of gamma-ray astronomy are: Low energy (LE), high energy (HE), very high energy (VHE) and ultra high energy (UHE).

1.2.1 Very high energy gamma-ray astronomy

In the last two decades, very high energy (VHE) gamma-ray astronomy has been established as a new field in astronomy, mainly using Imaging Air Cherenkov Telescopes (IACT, see section 2.4.5) covering the photon energy range from about 30 GeV to about 100 TeV. More than 200 sources of VHE gamma-ray emission have been observed so far (see figure 1.6), some with clear

counterparts (75%) in other wavelength regimes, some without ("dark sources"). The sources are almost equally distributed between Galactic (SNRs, PWN, X-ray binaries, stellar clusters, etc.) and extragalactic (mostly AGNs). The "dark sources" represent the 25% of the total, and understanding their origin remains an open challenge for the field (Aharonian et al., 2008; Tibolla et al., 2009). One hypothesis associates these "dark sources" as the emission ancient PWN (Tibolla et al., 2013).

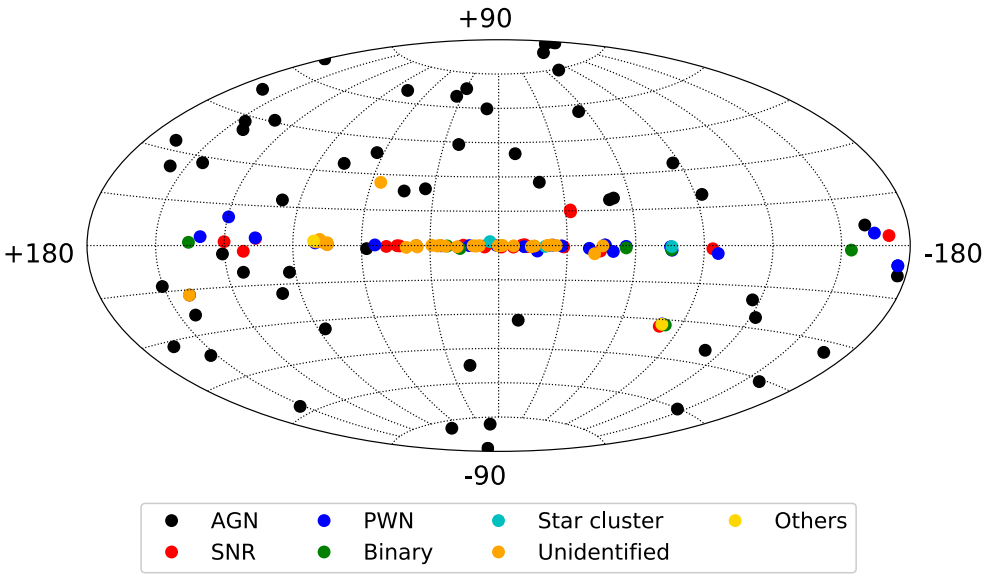

Figure 1.6: Map in galactic coordinate of currently known sources of VHE gamma-ray emission (January 2018). AGN, Active Galactic Nuclei, collects all the extragalactic sources. PWN, SNR and Binary represent all the sources of their type. The sources without counter part ("dark sources") are grouped under "Unidentified". Sources list from TeVCat (Wakely and Horan, 2008).

Thanks to the good angular resolution ($\leq 0.1°$) of Cherenkov telescope systems, spatial features of many extended Galactic sources and interesting regions of the Galactic center have been resolved and studied in detail. Among the most important discoveries are the shell-type SNR, where the bubble structure seen in other wavelength bands can also be seen in gamma-rays, like SN 1006 (Acero et al., 2010) or RX J13713.7-39486 (Aharonian et al., 2006), shown in figure 1.7.

One of the key science objectives of VHE gamma-ray astronomy is searching for CR sources (Drury et al., 1994). However, while a gamma-ray signal from an astrophysical object is a clear indication for particle acceleration at the site, it is not straightforward to uniquely identify this object as a source of hadronic cosmic rays, as gamma-rays can be efficiently produced also by leptonic particles. In the *hadronic scenario*, highly energetic hadrons collide with the

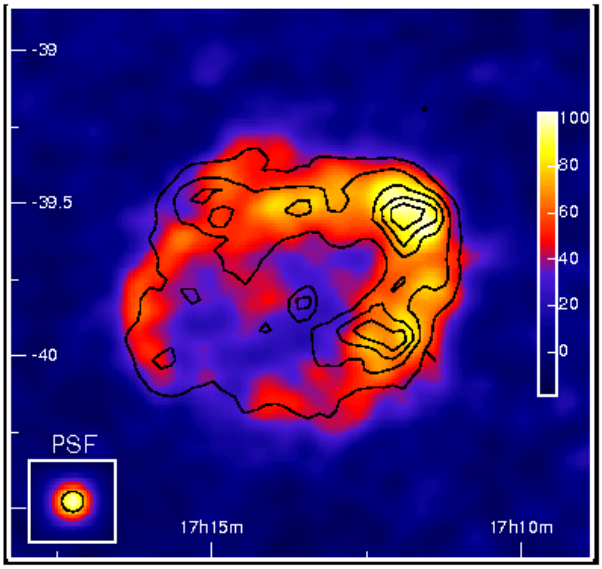

Figure 1.7: RX J1713.7-3946 as seen by H.E.S.S. (colors) and by ASCA in the $1 - 3\,\mathrm{keV}$ energy band (contours), showing an evident shell-like morphology at both TeV and X-ray energies. Figure from Aharonian et al. (2006).

ISM and neutral pions are produced, decaying almost immediately into gamma-rays. Such a process leaves a clear signature (*pion-decay bump*) at $\sim 0.4\,\mathrm{GeV}$ (Huang, 2003) in the source spectral energy distribution (SED). In the *leptonic scenario*, gamma-rays are produced by the inverse Compton effect (IC), in which the electrons transfer their energy to a low energy photon (e.g. CMB or nearby star thermal photon), or in a dense surrounding medium through non-thermal bremsstrahlung (Aharonian, 2004).

One way to overcome this ambiguity is to study the broad band SED of the source, from radio wavelengths to VHE gamma-rays, comparing it with different emission models. An example is represented by the two SNRs, IC443 and W44: the recent observation of the characteristic pion-decay bump spectral feature in the GeV energy range, combined with observation in the radio, provide a clear indication for proton cosmic rays acceleration (Ackermann et al., 2013). On the other hand, more complex is the case of the young shell-type SNR RX J1713.7-3946, identified as a good cosmic ray source candidate by VHE observations (Aharonian et al., 2007). In this case, observations in the X-ray as well as in the HE and VHE γ regime do not allow for a clear and unique scenario (H.E.S.S. Collaboration et al., 2018). In many other cases, however, the source of the VHE gamma-ray emission cannot be identified unambiguously, as the model-dependency in the interpretation of multi-wavelength data often introduces large uncertainties.

An important result was recently obtained with deep gamma-ray observations of the Galac-

tic Centre regions by H.E.S.S., indicating the presence of PeV particles in the central region of the Galaxy (Abramowski et al., 2016). The strong correlation between the VHE gamma-rays distribution and the massive gas-rich clouds location points to a hadronic origin of the diffuse gamma-ray emission, result of the interactions of relativistic protons with the ambient gas. The leptonic scenario is disfavoured by the radiative losses that multi-TeV electrons would suffer in the Galactic Centre region.

Although VHE gamma-ray astronomy has produced a wealth of new information and increased our knowledge on the non-thermal universe, some questions still remain open, like the nature of the "dark sources", and a conclusive picture about the origin of cosmic rays. In particular, current data cannot answer the question about what kind of sources are responsible for CRs acceleration up to PeV energies, and for many sources the emission scenario (leptonic or hadronic) is still uncertain. The next section will show how extending the range of gamma-ray observations to the UHE regime may help answer these questions.

1.2.2 Ultra high energy gamma-ray astronomy

As discussed in section 1.1.4, objects able to accelerate cosmic rays up to energies of above 10^{17} eV (*PeVatrons*) are expected to be hosted in our Galaxy. Due to the kinematics of cosmic ray acceleration in the hadronic scenario, these objects should also emit gamma-rays up to energies of several 100 TeV (Gabici and Aharonian, 2007), and gamma-ray observations at these energies should lead to the identification of these *PeVatrons*.

While no gamma-ray source has been observed at energies above 100 TeV, mainly because of the small effective areas of current gamma-ray observatories, there exists a large number of Galactic gamma-ray sources where no cut-off in the energy spectrum was found in the sensitivity range of current instruments, leaving open possible detections of gamma-ray emissions at higher energies. Among them are several SNRs, e.g. RX J0852.0-4622 (Aharonian et al., 2007) or the already mentioned RX J1713.7-3946, and pulsar wind nebulae, e.g. MSH 15-52 (Aharonian et al., 2005a) or Vela X (Aharonian et al., 2006).

Besides explaining the acceleration of Galactic CRs up to PeV energies, the detections of gamma-ray sources in the UHE regime and the analysis of their spectra could also be used to distinguish between leptonic and hadronic accelerators. In the first case, the Klein-Nishina effect, i.e. the decreasing cross-section for the IC scattering at UHE, and radiative synchrotron energy losses of primary electrons in magnetised post-shock environments should result in a clear drop in the observed gamma-ray spectrum in the UHE regime (Rowell et al., 2008).

Giant molecular cloud have also been proposed as possible sources of UHE gamma-rays, being tracers of nearby SNe. While the SNe can only accelerate particles to the highest possible energies only for a short interval after the explosion, the particles may produce a visible UHE signal as a result of the interaction with matter in a nearby molecular cloud for a longer period of time (Gabici and Aharonian, 2007). Other interesting candidates for UHE gamma-ray emission are the few known young SNe in the Galaxy or its vicinity, e.g. SN 1987A in the Large Magellanic Cloud, or the local supercluster (Kneiske et al., 2009).

The absorption via pair production of gamma-rays by the interstellar radiation field (ISRF) and the cosmic microwave background (CMB) becomes stronger at energies above few 10^{13} eV, resulting in a steeper energy spectrum of the measured emission. Depending on the source position in the Galaxy, this may limit the observations in the UHE regime. Figure 1.8 shows the transmittance for gamma-rays, $T = \exp(-\tau_{\gamma\gamma})$, i.e. the fraction of photons not absorbed, as a function of the energy, according to simulation by Moskalenko et al. (2006). Here, $\tau_{\gamma\gamma}$ represents the optical depth for pair production process. For a source near the Galactic Centre, the absorption is $\sim$ 23% at 100 TeV and reaches $\sim$ 65% at 1 PeV. It is significantly greater for sources further away, and can become as strong as 95% at 1 PeV for a source at the other end of the Galaxy. On the other hand, knowing the spectrum at the source with sufficient certainty, it could be possible to estimate the source distance from the analysis of the detected spectrum (Tluczykont et al., 2009).

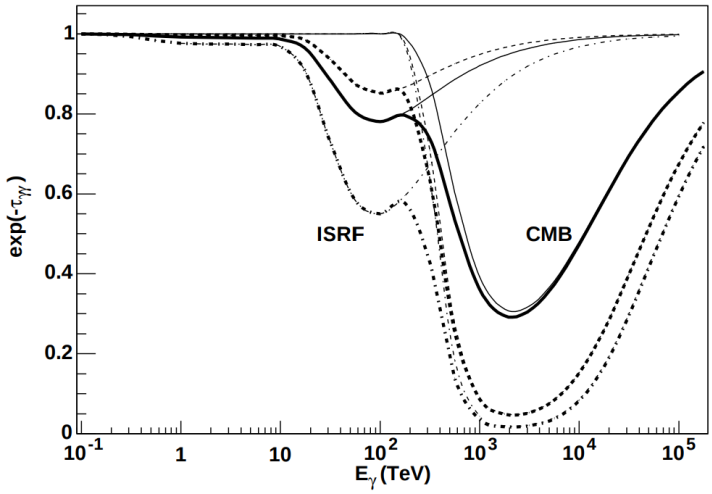

Figure 1.8: Transmittance for gamma-rays, $T = \exp(-\tau_{\gamma\gamma})$, as a function of gamma-ray energy, E_γ (Moskalenko et al., 2006). The thick lines show the total absorption, while the thin lines show the contributions by ISRF and CMB. The three different line styles refer to different positions of the source in the Galaxy: near the Galactic Centre (GC) (solid lines), at 20 kpc from the GC, perpendicular to the line from the Sun to the GC (dashed lines), and at 20 kpc behind the GC (dash-dotted).

The observation of a UHE gamma-ray signal from extragalactic sources is highly suppressed due to the long path the photons have to travel, that increases the probability to interact with the ISRF and the CMB (Hauser and Dwek, 2001; Kneiske and Dole, 2009; Raue and Mazin, 2010). However, current results from Cherenkov telescopes indicate that the gamma-ray absorption for distant sources may be weaker than commonly assumed (Horns and Meyer, 2012; Meyer et al., 2013). An eventual detection of UHE gamma-ray signals from extragalactic sources could raise interesting questions about the transparency models of the universe, or be a hint for new

physics, like the photon conversion to axion-like particle (ALP) (Mirizzi and Montanino, 2009; Vogel et al., 2017).

1.3 EAS ground based detection techniques

In general, similar techniques are used for the detection of both cosmic ray and gamma-ray particles. At lower energies, cosmic particles are detected directly by balloon-borne and/or satellites based detectors, while at higher energies indirect ground-based detection techniques are used. For CRs, direct measurements are possible up to 100 TeV (see figure 1.1), while for gamma-rays, because of the lower flux, direct detection reaches energies up to few hundred GeV. Since all gamma-ray detectors are also sensitive to charged cosmic rays, methods for primary particles discrimination are essential in order to extract gamma-ray signal against the much higher and isotropic flux of charged CRs.

This section gives a description of different ground-based detection techniques, with the focus on Cherenkov detectors for gamma-ray astronomy, as the work described in this thesis is set in this field. Section 1.3.1 presents an introduction to extensive air showers, that can be directly detected using air shower detector arrays (section 1.3.2). Section 1.3.3 describes the Cherenkov light emission induced by secondary superluminal charged particles in the EAS, that can be used by IACT telescopes (section 1.3.4) and timing arrays 1.3.5 to infer information about the primary particle.

Some other important EAS detection techniques will not be discussed here, as they are not closely related to the main topic of this thesis. Among these are the fluorescence detection, which is used especially for cosmic ray physics at the highest energies, e.g. by telescopes in the Pierre Auger Observatory (Abraham et al., 2004) or Telescope Array (Ogio et al., 2005), or the measurement of radio signals emitted by charged particles in the influence of the terrestrial magnetic field using arrays of radio antennas (Schröder, 2017).

A review on direct measurements and recent results on CR physics and γ-astronomy can be found (Maestro, 2015; Marrocchesi, 2017) and (Bühler, 2015) respectively.

1.3.1 Extensive air showers

The interaction with the air molecules of a highly energetic particle (either cosmic ray or gamma-ray photon) reaching the top of the atmosphere leads to the generation of a cascade of secondary particles, called extensive air shower, EAS.

EAS composition. As shown in figure 1.9, an EAS mostly consists of three main components: hadronic, electromagnetic, and muonic.

The hadronic component contains mostly neutral and charged pions, produced in strong interactions during hadronic particles collision with air molecules. Due to the short lifetime

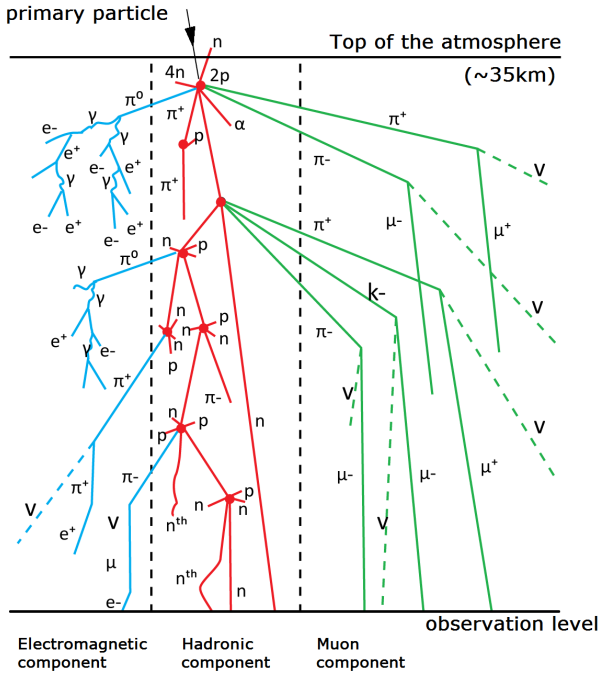

Figure 1.9: Sketch of EAS different components discussed in the text. Adapted from Gosse and Phillips (2001).

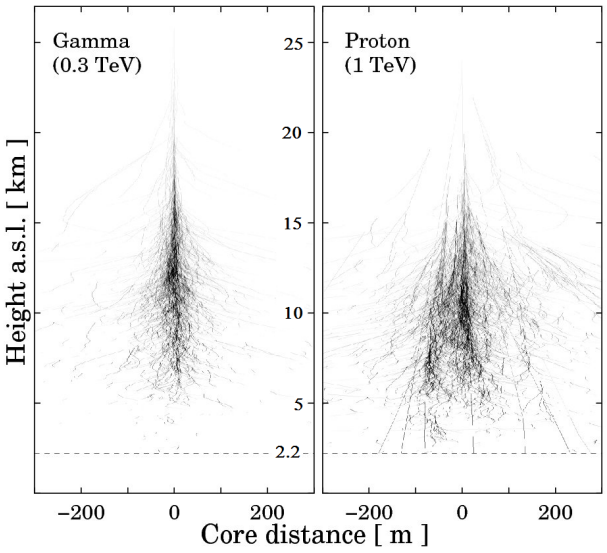

Figure 1.10: Comparison between gamma and proton induced air showers development in the atmosphere. Figure from Bernlöhr (2008).

($\sim 10^{-16}$ s, taking into account time dilation caused by their relativistic velocities) the neutral pions decay into two photons, feeding the electromagnetic component. The mean lifetime of the charged pions is considerably longer ($> 10^{-7}$ s), so that they can contribute to the hadronic cascade, before eventually decaying into muons and muon neutrinos (Grieder, 2001).

The electromagnetic component consists mainly of electrons (including also positrons) and photons. The secondary electrons produce highly energetic photons through bremsstrahlung, which in turn produce new electrons through pair production, thus sustaining the electromagnetic cascade. This process continues until the electrons reach the critical energy, $E_c \approx 84.2$ MeV (Berger and Seltzer, 1964), where the energy losses due to bremsstrahlung and ionisation processes are equal. At this point, no new particles are produced, and eventually the electromagnetic cascade dies out.

The muonic component consists mainly of the decay products of the hadronic cascade. Despite muons have a relatively short lifetime ($\sim 2.2 \times 10^{-6}$ s), the relativistic time dilation allows most of them to reach the ground, while only a small part decay into an electron, a neutrino and an anti-neutrino.

Difference between hadron and photon initiated showers. The nature of the primary incident particle determines how the three different components contribute to the particle cascade, and their evolution in the atmosphere. In the case of a primary γ or $e^{\pm}$ (*electromagnetic shower*), the first iteration consists of either bremsstrahlung generation ($e^{\pm}$ primary) or pair production (γ primary). Thus, the electromagnetic component is started immediately and is more abundant than the hadronic and muonic ones, started only later. In contrast, in a shower induced by a nucleus (*hadronic shower*), the primary particle interaction consists mostly of spallation processes, with the hadronic component (mostly π^0 and $\pi^{\pm}$) started immediately and much larger with respect to an *electromagnetic shower*. The electromagnetic component is produced by the decay of neutral pions into photons pair, absorbing roughly 1/3 of the energy of the primary particle. In a similar way, the muonic component is fed by the decay of charged pions into muons and muonic neutrinos.

The different composition and evolution in the atmosphere of *electromagnetic* and *hadronic showers* results in different lateral and longitudinal shower profiles. An electromagnetic cascade is usually concentrated close to the shower axis, while a hadronic cascade spreads out into sub-showers with large transversal momentum, as shown in figure 1.10. These differences in the shower morphology can be used to discriminate primary gammas from hadrons, if they can be detected by the experiment. The longitudinal evolution of the different components as a function of the altitude (and shower depth) is shown in figure 1.9, for three different primary particles (γ, p, Fe) with the same energy. In all cases the electromagnetic component dominates the particle cascade, with a total amount of particles several orders of magnitude larger than the hadronic and muonic components. The hadronic and muonic components are much larger in *hadronic showers*, with the total amount of particles increasing with the atomic number. At the same primary energy, primary protons produce slightly fewer electrons than

γs, and iron nuclei even fewer. This causes a particle-dependent shift of the reconstructed energy in experiments that are sensitive only to the electron component or the total number of charged particles, such as Cherenkov detectors. Because the electromagnetic component dominates the air shower, its maximum also defines the shower maximum, defined as the point (altitude or depth) at which the air shower contains the largest number of particles. As shown in figure 1.11, it is slightly higher for protons than for γs, and significantly higher for iron primaries, but is also proportional to the logarithm of the primary energy, as shown in the following.

A simple EAS model. A model proposed by Heitler (Heitler, 1954) helps to explain the showers features described so far. While the model is meant to describe the evolution of *electromagnetic showers* in the atmosphere, it is applicable, in first approximation, also for *hadronic showers*.

Here one assumes that after every characteristic length, λ, the number of particles in the shower doubles, with the energy equally shared among the newly generated particles. Under these assumptions, the number of particles and their energy at the depth X are then given by

$$N(X) = 2^{X/\lambda} \tag{1.3}$$

$$E(X) = E_0/N(X) \tag{1.4}$$

where E_0 is the energy of the primary particle. When the energy of the particles falls below E_c, no new particles are generated and the maximum number of particles is given by

$$N_{max} = E_0/Ec \tag{1.5}$$

Combining this result with equation 1.4, one obtains the depth of the shower maximum:

$$X_{max} = \frac{\lambda}{\ln 2} \ln\left(\frac{E_0}{E_c}\right) \tag{1.6}$$

Turning to the case in which the primary are nuclei, the main properties of the air showers can be understood on the basis of the superposition model, i.e. considering the shower produced by a primary nucleus with mass number A and energy E_0, equivalent to a superposition of A showers produced by protons of energy E_0/A. In this case, the depth of the maximum is at

$$X_{max} = \frac{\lambda}{\ln 2} \ln\left(\frac{E_0}{AE_c}\right) \tag{1.7}$$

The model correctly predicts the logarithmic dependence between the shower depth and the primary particle energy, as well as the smaller depth for heavier particles (figure 1.11). However, more complex simulations show that the difference in shower depth between hadrons

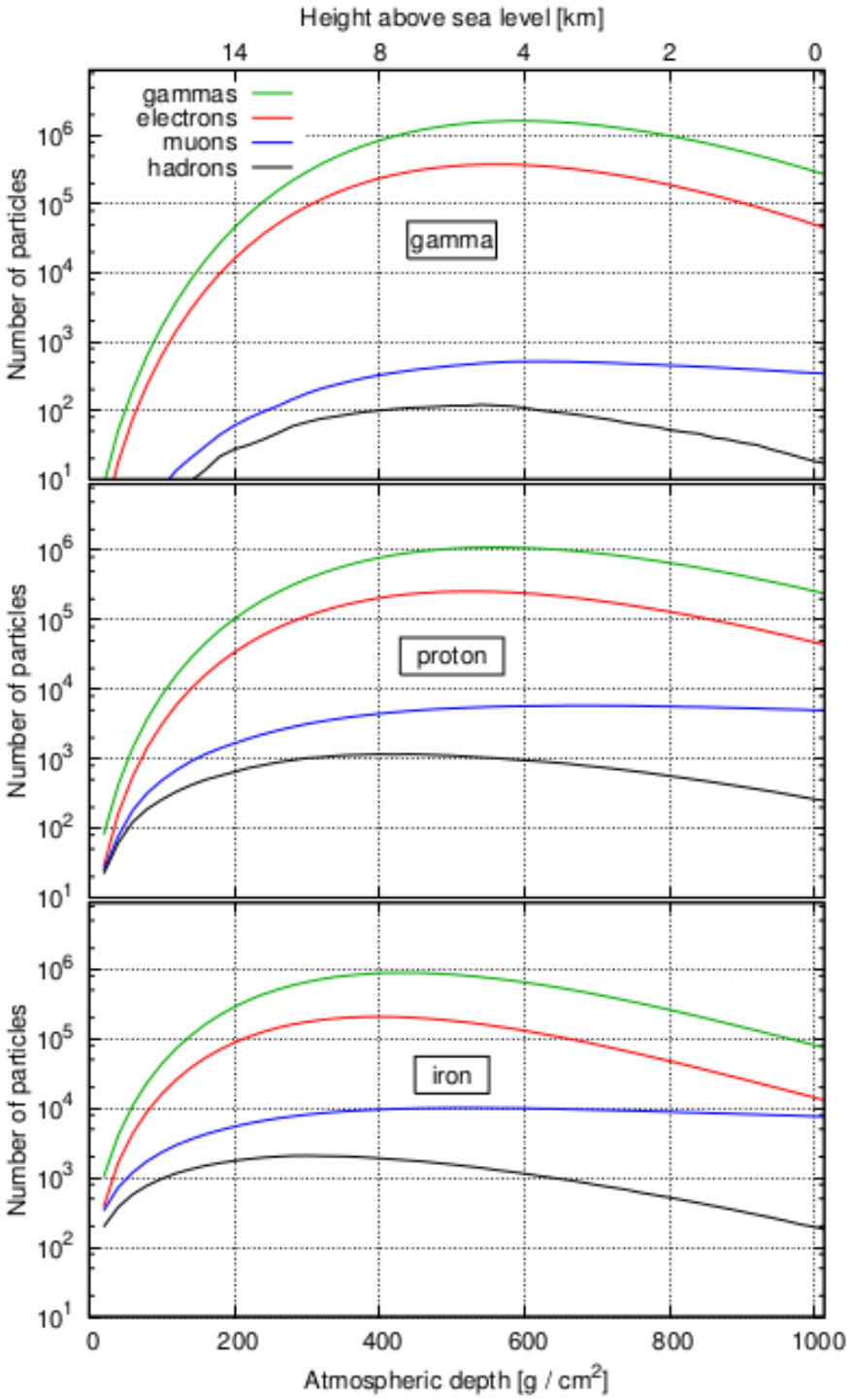

Figure 1.11: Number of particle species as a function of atmospheric depth (or altitude) for γ (top), proton (middle) and iron (bottom) initiated showers. Electrons are $e^{\pm}$, muons are $\mu\pm$. The longitudinal profiles are obtained averaging over 100 simulated (CORSIKA, Heck et al. (1998)) vertical showers with 500 TeV primary energy. Figure from Hampf (2012).

of different mass is overestimated by this model.

Equation 1.7 defines the correlation between the primary particle energy, E_0, the atomic number, A, and the shower maximum, X_{max}. If the energy of the particle is accurately estimated, the average shower depth can be used to estimate the mass of a detected particle (see figure 1.3). Another method to discriminate between the primary particles is the independent detection of the electronic and muonic components with respective detectors at the observation level. A high N_μ to N_e ratio implies a heavier primary particle, a very low ratio a γ primary.

1.3.2 EAS detectors

Present day EAS experiments measure the secondary particles cascade with scintillation or water Cherenkov detectors. In both cases the charged particles reaching the observation level produce light signals inside the detector eventually read out with photomultipliers. Additionally, some experiments make use of muon detectors in order to gain information about the nature of the primary particle, e.g. the HEGRA detector (Just et al., 1993) or KASCADE (Arteaga-Velazquez et al., 2013). AGASA, with its 111 surface detectors and 27 muon detectors distributed over an area of $100\,km^2$, was the largest experiment using scintillation detectors, allowing the detection of cosmic rays up to energies above 10^{20} eV (Agasa Collaboration, 2006). The Pierre Auger Observatory (PAO) in Argentina is the largest EAS detector build so far, with an effective area of about $3000\,\mathrm{km}^2$, and combining water Cherenkov detectors and fluorescence telescopes (Aab et al., 2015). The large area allows to study in detail the CRs energy spectrum and the arrival directions of particles above the GZK cut-off discussed in section 1.1.1 (Kampert, 2017).

Though all EAS detectors are in principle sensitive to gamma-rays, it was only recently that the first gamma-ray sources could be detected by the air shower experiments MILAGRO, Tibet-ASγ and ARGO-YBJ, thanks to their low energy threshold and good angular resolution.

MILAGRO was a water Cherenkov detector located at an altitude of $2630\,\mathrm{m}$ in New Mexico, USA (Atkins et al., 2000). With a large water pool ($60\,\mathrm{m}\times80\,\mathrm{m}\times8\,\mathrm{m}$) surrounded by a sparse $200\,\mathrm{m}\times200\,\mathrm{m}$ array of 175 smaller outrigger stations, it achieved a gamma-ray threshold of $\sim$ 1 TeV, allowing the observation of gamma-ray emission of several sources, including 14 sources also seen by the FERMI satellite in the high-energy band (Abdo et al., 2009), and from the Cygnus region (Abdo et al., 2007). The Tibet-AS array, located in Tibet (China) at an altitude of $4300\,\mathrm{m}$, currently has a surface array with 789 scintillator detectors covering an area of $36900\,\mathrm{m}^2$ and the $4500\,\mathrm{m}^2$ underground water Cherenkov pools used to select muons (Zhang et al., 2017). It observed the Crab Nebula at 6.9σ significance, Mrk-501 at 3.7σ and Mrk-421 with 5.1σ (Takita, 2016). The ARGO-YBJ detector, also in Tibet, uses resistive plate chambers (RPC) detectors, covering an area of about $10^4\,\mathrm{m}^2$ (Aielli et al., 2006). It observed several previously known sources of VHE gamma-ray emission, including the Crab Nebula (17σ), Mrk-421 (14σ), and Mrk-501 ($> 6\sigma$) (Di Sciascio and Collaboration, 2012).

Following the MILAGRO experience, the HAWC detector (Mexico, $4100\,\mathrm{m}$. a.s.l.) is currently

(a)

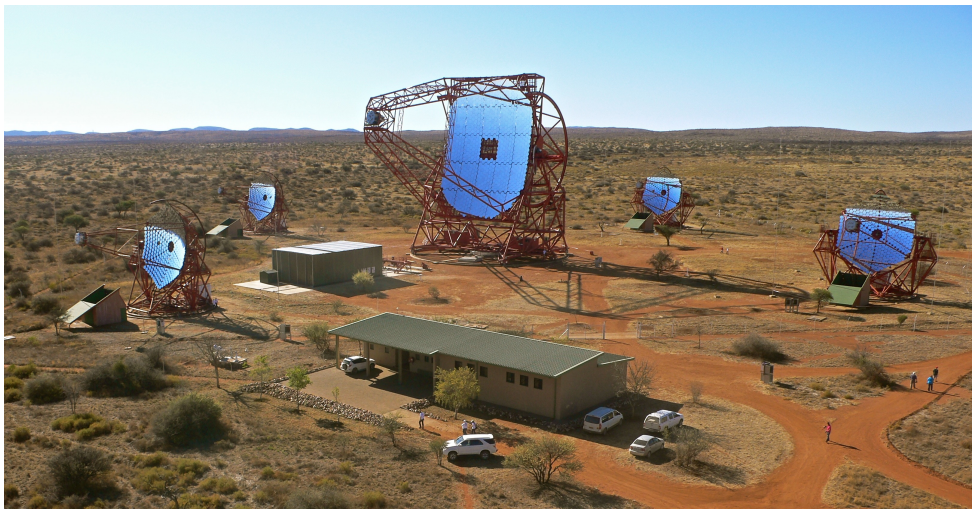

(b)

Figure 1.12: (a) HAWC detector array. (b) H.E.S.S. II telescope array.

the major EAS detector dedicated to the observation of gamma-rays between $0.1 - 100$ TeV (Tepe, 2012). The HAWC main array consists of big cylindrical water Cherenkov detectors (WCDs) of 7.3 m diameter and 4.5 m height, equipped with four photomultipliers, for a total instrumented area of 20.000 m^2 and a 2 sr FOV. An outrigger array of 350 smaller tanks (1.55 m diameter, 1.65 m height) of diameter with one photomultiplier has been recently deployed in order to improve the shower cores location. The higher altitude and the larger instrumented area make HAWC 10 to 15 times more sensitive to gamma-ray sources than MILAGRO. HAWC will address the main questions on CR physics, Galactic and Extragalactic γ-astronomy, as well as fundamental physics. A list of recent results can be found in (MAGIC Collaboration et al., 2017).

Looking at future experiments, the LHAASO detector is expected to be the most sensitive project in the energy range $10^{11} - 10^{17}$ eV (Di Sciascio, 2016). Located at 4410 m of altitude in the Sichuan province of China, and covering an area of ~ 1.3 km^2, it will combine 5242 electromagnetic particle detectors (scintillator detectors), 1146 underground water Cherenkov tanks, 3 surface water Cherenkov detectors, and 12 wide field-of-view air Cherenkov telescopes. This new generation multi-component experiment will be able to continuously survey the gamma-ray sky for steady and transient sources from about 100 GeV to PeV energies, opening the $10^2 - 10^3$ TeV range to the direct observations of the high energy cosmic ray sources. In addition, the different observables (electronic, muonic and Cherenkov components) will allow the study of the origin, acceleration and propagation of the CRs by measuring the energy spectrum, elemental composition and anisotropy with unprecedented resolution. The commissioning of 1/4 of the detector will be implemented in 2018, with the full installation completes by the end of 2021.

1.3.3 Air shower Cherenkov light emission

The emission of Cherenkov light occurs when charged particles move through a dielectric medium with a velocity v greater than the speed of light in the medium, i.e. if

$$v > \frac{c}{n} \Longleftrightarrow \beta = \frac{v}{c} = \frac{1}{n} \tag{1.8}$$

where n is the refractive index of the medium. The molecules of the medium are polarised for a brief moment by the travelling charged particles, forming small dipoles. Each dipole generates electromagnetic radiation that, if the condition in equation 1.8 is satisfied, produce a constructive interference (see figure 1.13) resulting in a conical wave front. The characteristic emission angle is given by

$$\cos\theta_C = \frac{c}{nv} = \frac{1}{n\beta} \tag{1.9}$$

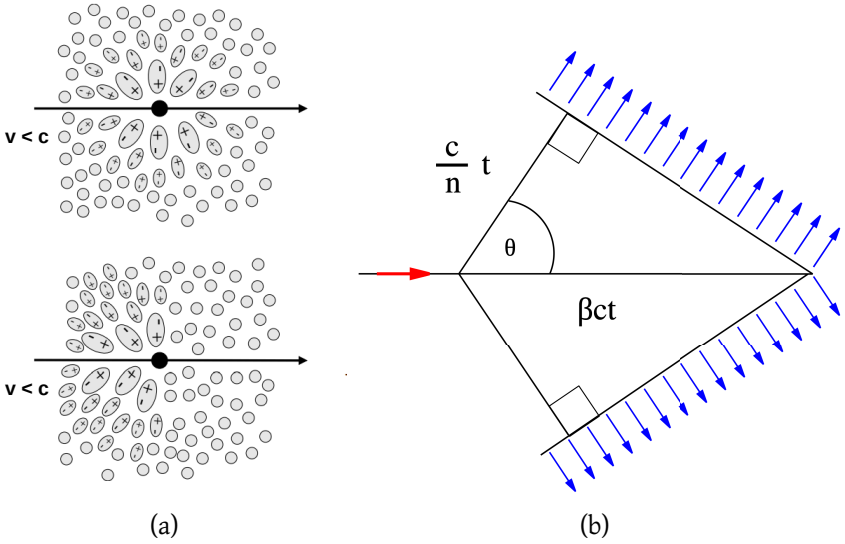

Figure 1.13: (a) Polarization of molecules in a medium caused by charged particles that move slower (top) and faster (bottom) than the speed of light in the medium. (b) Cherenkov light front produced by the constructive interference of individual waves emitted along the track of the charged particle.

The minimal energy that a relativistic particle of mass m must have for the emission of Cherenkov radiation (Patrignani,C., et al. (Particle Data Group), 2016) is given by

$$E_{th} = \frac{mc^2}{\sqrt{1-\beta^2}} = \frac{mc^2}{\sqrt{1-(1/n)^2}} \tag{1.10}$$

Ground-based EAS Cherenkov detectors use the fact that most of the secondary particles in the shower satisfy the Cherenkov conditions. As the air refractive index changes with pressure, E_{th} and $\cos\theta_C$ depend on the altitude and the atmospheric conditions. Typical values for an atmosphere refractive index $n = 1.00011$ (U.S. Standard Atmosphere, 1976), at a shower maximum height $\sim 8\,\mathrm{km}$, are $E_{th} = 67 m_0 c^2$ ($\sim 34\,\mathrm{MeV}$ for electrons and $7\,\mathrm{GeV}$ for muons), and $\theta = 0.85°$ (assuming $\beta = 1$).

The number of photons emitted per unit of length and wave length for a relativistic particle with charge eZ is given by

$$\frac{\partial^2 N}{\partial x \partial \lambda} = 2\pi\alpha Z^2 \left(1 - \frac{1}{\beta^2 n(\lambda)^2}\right) \frac{1}{\lambda^2} \tag{1.11}$$

where $\alpha \approx 1/137$ is the fine structure constant and $n(\lambda)$ the wavelength dependent refractive index of the medium. The Cherenkov light spectrum follows a λ^{-2} dependence in the visible

light window, where $n(\lambda) \sim$ constant. Due to the atmospheric absorption (Rayleigh scattering, aerosol and molecular absorption) Cherenkov light is attenuated in air and the spectrum will be slightly modified, as shown in figure 1.14.

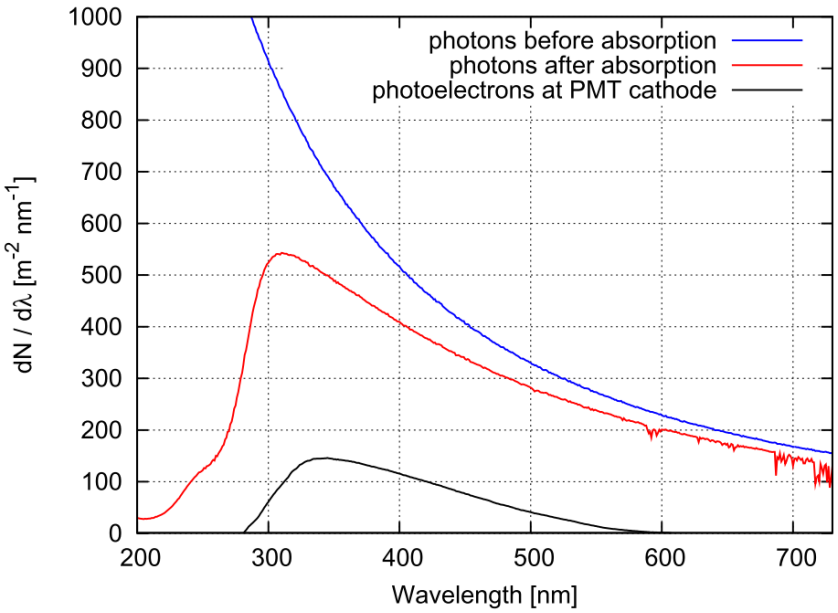

Figure 1.14: The spectrum of Cherenkov light from 750 TeV events before (blue) and after (red) atmospheric absorption, and after taking into account the detector quantum efficiency. The Cherenkov spectrum is taken from CORSIKA simulations, the atmospheric absorption is done using MODTRAN (Kneizys et al., 1996), and the quantum efficiency of the PMT is modelled using the the values given in the data sheet of the Electron Tubes PMT 9352KB. Figure from Hampf (2012).

The duration of a Cherenkov signal from air showers ranges between few nanoseconds near the shower core up to about 40 ns at few hundred metres away from the core. A primary particle of 1 TeV energy results in a Cherenkov photon density of about 100 photons per m^2 (Hinton, 2009), while the brightness of the night sky is at least $2 \cdot 1012$ photons/(s·sr·m^2) (Hampf, 2012). Thus, the main requirements for detectors of Cherenkov light are a large light collection areas to achieve a good signal to noise ratio, and fast photo-sensors and electronics with nanosecond resolution.

1.3.4 IACT detectors

Imaging Air Cherenkov Telescopes (IACTs) collect the Cherenkov light generated by extensive air showers using a large segmented mirror, and focus it on a camera consisting of an array of photomultipliers. The image produced in the camera contains important informations (e.g.

size and shape) regarding the EAS, which are used to determine the main features of the primary particle, like the arrival direction, the energy, the shower maximum, and the nature of the primary particle.

One of the most important features of the imaging technique, determining its success in gamma-ray astronomy, is the very good suppression of the hadronic cosmic ray background. As discussed in section 1.3.1, *hadroninc* showers differ from the *electromagnetic* ones. Here, a compact and elliptical shaped images characterize gamma-ray initiated showers, while broader images are produced by hadronic induced EASs due to their larger transversal momentum. A cut on the image width, first proposed in Hillas (1985), provided a mean for γ hadron separation.

The Whipple telescope was the first experiment that successfully made use of Cherenkov imaging. With a 10 m mirror and a 37 pixels camera, it detected the first source of VHE gamma-ray emission, the Crab Nebula (5σ significance) (Weekes et al., 1989), and discovered the first extra galactic source of TeV emission, the active galaxy Mrk-421 (Punch et al., 1992). Many improvements of the technique were developed in the following decade, and implemented in experiments like CANGAROO (Hara et al., 1993) and HEGRA (Daum et al., 1997). One of the main achievements was the development of the stereoscopic technique by H.E.S.S (Hinton, 2004). Using two or more telescopes placed at about hundred meters distance from each other, allowed to observe the same shower from different angles, improving the reconstruction of primary particle arrival direction and energy (Kohnle et al., 1996; Hofmann et al., 1999).

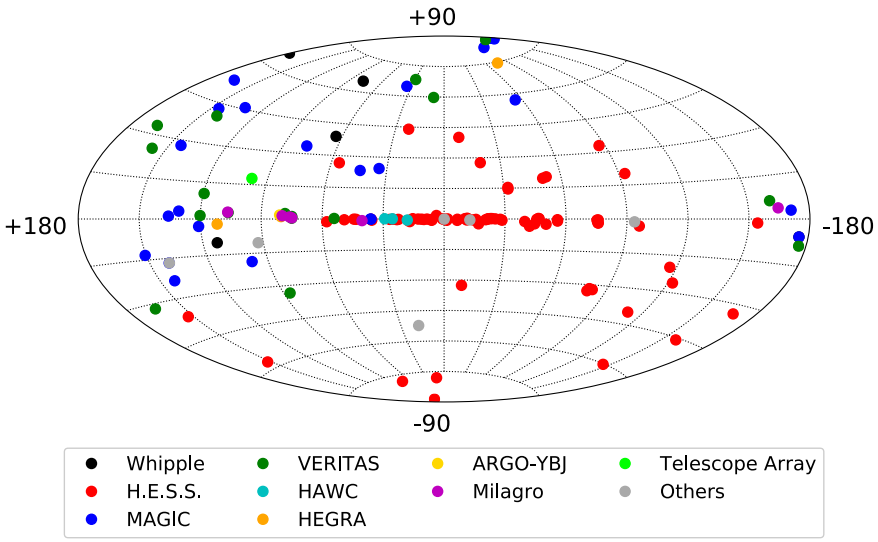

Figure 1.15: Map in galactic coordinate of currently known sources of VHE gamma-ray emission (January 2018). The color code shows the detector that discovered the source. Sources and detectors list from TeVCat (Wakely and Horan, 2008).

The last 2 decades have been characterized by the 3^{rd} generation of Cherenkov telescopes, consisting of three main experiments: H.E.S.S. (Hinton, 2004), MAGIC (Albert et al., 2008), and VERITAS (Holder et al., 2008).
H.E.S.S. is a stereoscopic system of 5 (4 during Phase I) imaging Cherenkov telescopes located in Namibia. Each of the Phase I telescopes has a $107\,\mathrm{m}^2$ mirror and a 960 pixels camera. With an energy threshold of about $100\,\mathrm{GeV}$, it can detect a source with flux of $1\,\mathrm{Crab}$ in only $30\,\mathrm{s}$. The location in the southern hemisphere favours the observation of the Galactic plane and in particular of the Galactic centre region. Recent deep gamma-ray observations of the Galactic Centre showed the expected tracer of the presence of PeV particles (Aharonian et al., 2006; Abramowski et al., 2016). In 2012, the fifth telescope was added (Phase II), lowering the detection threshold to $20\,\mathrm{GeV}$. With its $28\,\mathrm{m}$ of diameter, it is one of the biggest of its kind worldwide.
MAGIC is a system of two Cherenkov telescopes of $236\,\mathrm{m}^2$ mirror area, operating in La Palma, Spain. The first telescope started routine operation in 2004 (Phase I), the second in 2009 (Phase II). The very low threshold of $25\,\mathrm{GeV}$ achieved during Phase I, allowed the first ground-based detection of the Crab pulsar (Aliu et al., 2008), while recently (Phase II) the highest pulse emission ever detected from the Crab reaching up to $1.5\,\mathrm{TeV}$ has been reported (Ansoldi et al., 2016). The location in the northern hemisphere and the low energy threshold favour the extra-galactic observations, thanks to the longer γ photons mean free path at lower energies (Hauser and Dwek, 2001). This led to the recent detection of two of the furthest very high energy objects detected: the radio quasar PKS 1441+25 (MAGIC Collaboration et al., 2015), and the gravitationally lensed blazar QSO B0218+357 (MAGIC Collaboration et al., 2016).
VERITAS consists of an array of four $12\,\mathrm{m}$ optical reflectors, located in Arizona, USA. It is most sensitive between $85\,\mathrm{GeV}$ and $30\,\mathrm{TeV}$ and since 2007 it has been used to regularly observe the Northern sky. The scientific reach of VERITAS covers the study of both extragalactic and Galactic objects as well as the search for astrophysical dark matter (The VERITAS Collaboration, 2013; Smith et al., 2013). Most recent highlights have been presented in Staszak et al. (2015); Mukherjee (2016); Benbow (2017).

The Cherenkov Telescope Array (CTA) will be the major global observatory for VHE gamma-ray astronomy over the next decades. Covering an energy range from $20\,\mathrm{GeV}$ to $300\,\mathrm{TeV}$, and employing IACTs of three different sizes, CTA will improve on all aspects of performance with respect to current instruments. CTA will operate one array in each hemispheres (99 telescopes on the southern site, 19 telescopes on the northern site) to provide full sky coverage and will hence maximize the potential for the observation of the rarest phenomena such as very nearby supernovae, gamma-ray bursts or gravitational wave transients (The Cherenkov Telescope Array Consortium, 2011). The scientific potential of CTA is extremely broad: from understanding the role of relativistic cosmic particles to the search for dark matter (The Cherenkov Telescope Array Consortium, 2017).

Besides CTA, there are several initiatives for smaller, more specialised instruments. An example is given by FACT (First G-APD Cherenkov telescope) (Anderhub et al., 2011), that is the first telescope using silicon photon detectors (G-APD/SiPM). Built on the mount of the HEGRA

CT3 telescope, FACT is in operation since October 2011 at la Palma.

Figure 1.16 shows the 5σ sensitivity of the three major IACT detectors operating today, and the expected one for CTA.

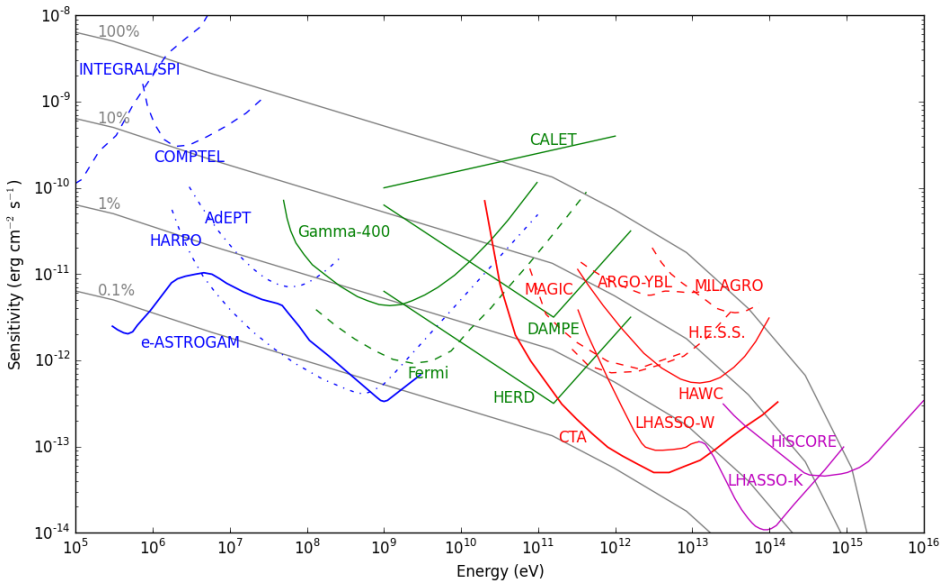

Figure 1.16: Differential 5σ sensitivity of gamma-ray telescope. Colours distinguish the energy domains (blue for low and medium energy, green for high energy, red for very high energy and magenta for ultra high energy. The grey lines show the Crab differential energy flux, as well as 10%, 1% and 0.1% of that flux for reference. For HiSCORE, the integral sensitivity is shown. For more details on the different detectors sensitivity see Knödlseder (2016).

1.3.5 Timing array detectors

A different technique for the detection of EASs Cherenkov light emission is represented by the wide-angle timing array detectors. These experiments consist of arrays of non-imaging light sensitive stations, with a typical light collecting areas ≤ 1 m^2. Each station is usually equipped with one or more large area photomultiplier, and in some cases a light concentrator in order to increase the light sensitive area. The shower detection is obtained sampling the Cherenkov light wavefront, with every detector inside the Cherenkov light pool recording the density and timing of the Cherenkov photons. The relative timing of the recorded signals, their amplitude and shape are used for the event reconstruction.

The non-imaging timing technique presents several advantages with respect to IACT: the wide field of view (FOV) allows a continuous survey of a large portion of the sky, favouring an unbiased search and a long exposure for every possible γ source. Also, the FOV is very well

suited for the study of extended emission regions, that may be too large larger for traditional IACT observations. Another advantage is the reduced cost of the detector, making it possible to instrument a large area at a reasonable effort, making them the ideal instruments for studying of the very weak fluxes in the ultra high energy domain. On the other hand, the detectors small collection area reduces the signal-to-noise ratio, increasing the energy threshold, and the potential for particle identification, affecting the gamma-hadron separation.

So far, wide-angle Cherenkov detectors have been developed and used mainly to study charged cosmic rays studies. Early examples are Yakutsk (Dyakonov et al., 1973), the Buckland park detector (Kuhlmann et al., 1977), while more recent example are the BLANCA (Fowler et al., 2001), TUNKA-133 (Prosin et al., 2016) (still operational).

First Themistocle (Baillon et al., 1993), and then the AIROBICC detector (as part of the HEGRA air shower array, (Karle et al., 1995)), tried to use the non-imaging Cherenkov technique for VHE gamma-ray astronomy. AIROBICC, with is dense station spacing ($30\,\mathrm{m}$), and the high altitude ($2200\,\mathrm{m}$ a.s.l), provided an angular resolution $\sim 0.1^\circ$ and an energy threshold below $30\,\mathrm{TeV}$. However, the small area of only $3 \cdot 10^4\,\mathrm{m}^2$ did not allow to achieve the necessary sensitivity, and no gamma-ray source could be detected (Aharonian et al., 2002).

1.3.6 Hybrid Cherenkov detectors

The IACT technology proved high efficiency on the primary particle identification and gamma-hadron separation in stereoscopic-mode, but suffering at higher energies due to the small effective area. On the other hand, timing arrays offer the opportunity to cover large instrumented areas ($10 - 100\,\mathrm{km}^2$) at reasonable effort and with good EAS reconstruction, but with low gamma-hadron efficiency due to the small sensitive area.

The new hybrid TAIGA experiment, that combines both IACT and timing detector technologies, represents a new concept for gamma-ray astronomy in the multi-TeV and UHE regime and CRs above 100 TeV (Budnev et al., 2017b). The TAIGA-HiSCORE timing array will provide an angular resolution comparable to AIROBICC (0.1°), with a much larger instrumented area (up to $100\,\mathrm{km}^2$) thanks to the large station spacing ($100 - 200\,\mathrm{m}$), and good energy resolution ($\leq$ 30%). The TAIGA-IACT array, characterized by a large telescope spacing (600-1000 m) and operating in monoscopic mode, will provide informations about the nature of the primary particles, allowing efficient CR background rejection.

The next chapter will introduce the TAIGA experiment, with a main focus on the TAIGA-HiSCORE timing array.

Chapter 2

The TAIGA experiment and the TAIGA-HiSCORE timing array

The TAIGA (**T**unka **A**dvanced **I**nstrument for cosmic ray physics and **G**amma **A**stronomy) experiment aims at the exploration of the accelerator sky, using indirect EAS observation of CRs from $100\,\text{TeV}$ to $1\,\text{EeV}$ and gamma-rays in the energy range from $10\,\text{TeV}$ up to several PeV (UHE regime). The main questions TAIGA will address are CR composition and spectral measurements in the Galactic/extragalactic transition region, and the origin of CRs by searching for gamma-ray emissions from Galactic *PeVatrons*.

By combining Cherenkov imaging and timing techniques (see sections 1.3.4, 1.3.5), TAIGA represents a new technology for EAS Cherenkov detection. It will consist of a net ($600-1000\,\text{m}$ spacing) of IACTs, TAIGA-IACT, and a wide-angle timing array, TAIGA-HiSCORE, composed of small detector with $100-200\,\text{m}$ spacing. The TAIGA-HiSCORE array will allow to achieve, with a reasonable effort, a large effective area of $10\,\text{km}^2$ up to $100\,\text{km}^2$, necessary to detect the low photon flux expected in the UHE regime, and to perform an accurate reconstruction of the EAS parameters. The TAIGA-IACT telescopes, operated in monoscopic mode, will provide the necessary CR background suppression, allowing the search of UHE gamma-ray sources.

Section 2.1 will present the TAIGA experiment under construction at the Tunka Astrophysical Center in the Tunka Valley ($50\,\text{km}$ West of Lake Baikal, Russia), the scientific goals and the detector concept. The second part of the chapter will focuses on the TAIGA-HiSCORE timing array. Section 2.2 will give a detailed description of the TAIGA-HiSCORE detector station, while sections 2.3 and 2.4 are dedicated to the detector simulation and event reconstruction, respectively.

2.1 The TAIGA experiment and the HiSCORE timing array

This section presents the TAIGA experiment, its scientific goals, and the detector concept. An overview of the TAIGA detector development during the last years is also given, with a focuses on the TAIGA-HiSCORE timing array.

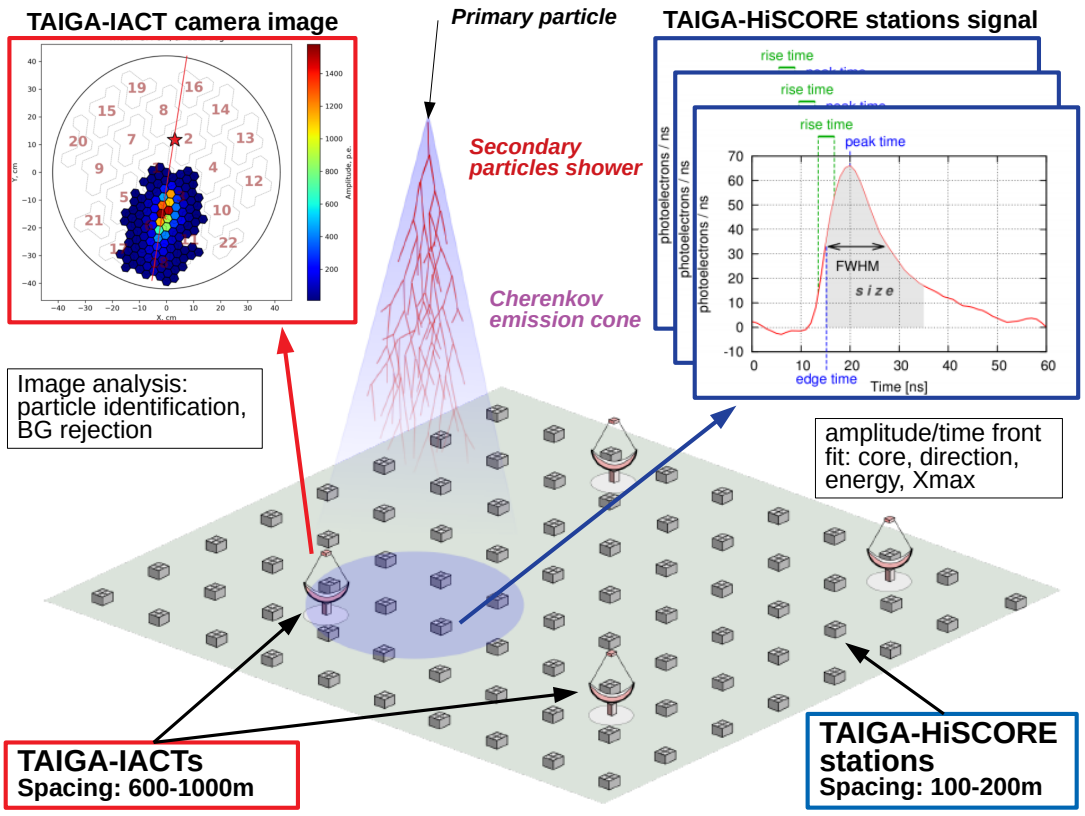

Figure 2.1: TAIGA hybrid Cherenkov detector concept, featuring both Cherenkov imaging (TAIGA-IACTs) and timing (TAIGA-HiSCORE) techniques. The EAS Cherenkov emission produces an image in the IACT camera (top-left), and a pulse in the HiSCORE stations (top-right). The analysis of the both signals (image and station pulses) allow to reconstruct the EAS parameters (HiSCORE: core, direction, energy, X_{max}), and to identify the nature of the primary particle and reject CRs background (IACT-mono: image shape analysis).

2.1.1 The TAIGA experiment: scientific goals and detector concept

The Tunka Astrophysical Center in the Tunka Valley (51°48'35" N, 103°4'2" E, 675 m a.s.l.) has been so far devoted to the study of charged CRs energy spectrum and composition, around and above the *knee*, with the three detector arrays Tunka-133 (Berezhnev et al., 2012), Tunka-Rex (Bezyazeekov et al., 2016) and Tunka-Grande (Monkhoev et al., 2017). The TAIGA experiment will extend the study of CR and gamma-ray in the energy range between 10^{13} and 10^{18} eV, aiming at answering to the main open questions about the origin of CRs, with a focus on the search for Galactic *PeVatrons* (see chapter 1).

Scientific goals. The primary goals of the TAIGA project is the search and study of gamma-

ray sources in the multi-TeV and UHE regime. As mentioned in section 1.2.2, the detection of Galactic sources of gamma-rays emission in this energy range would be a direct evidence of CR acceleration at the sources up to the *knee* in the all particle CR spectrum, identifying these sources as *PeVatrons*. The spectral analysis of the detected gamma-ray emission will also give clear indications on the mechanisms responsible for gamma-ray production (*leptonic* or *hadroninc*). TAIGA will also be able to detect hadronic CR above 100 TeV, adding new information to the existing CRs picture describe in chapter 1, measuring the spectrum, the arrival directions anisotropy and the composition in the interesting region around and above the *knee*.

Additionally, some particle physics questions can be addressed indirectly using the cosmic ray and gamma-ray measurements. As an example, the existence of hidden sector particles or axion-like particles can be probed as they would change the expected absorption of gamma photons in the UHE regime (Mirizzi and Montanino, 2009). A more detailed discussion about of the TAIGA scientific goals is presented in Tluczykont et al. (2011).

Detector concept. TAIGA experiment will consists of a new hybrid detector system, composed by a wide-angle timing Cherenkov array, TAIGA-HiSCORE, and a IACT telescopes array, TAIGA-IACT. While the HiSCORE detector can provide with good accuracy the main EAS parameters (core, arrival direction, energy and shower maximum), the less dense IACT telescopes array and the muon arrays will allow gamma-hadron separation below 100 TeV. An additional underground net of muon detectors, TAIGA-Muon, will allow gamma-hadron separation above 100 TeV. An illustration of the TAIGA Cherenkov (HiSCORE+IACT) hybrid detection concept is given in figure 2.1.

The immediate goal is to install by the end of 2019 the first stage of $1\,\mathrm{km}^2$ TAIGA array, shown in figure 2.2, which will consist of $100 - 120$ HiSCORE stations, distributed on an area about $1\,\mathrm{km}^2$, three TAIGA-IACTs and a $200\,\mathrm{m}^2$ surface of TAIGA-Muon detectors. Figure 2.3 shows the expected integral sensitivity for the described setup and 300 h of source observation. This first stage should allow to demonstrate the potential of the hybrid approach for high energy gamma-ray detection, and to start with systematic observational program. Future plans ($>$ 2020) aim at the construction of a $5 - 10\,\mathrm{km}^2$ TAIGA array.

TAIGA-IACT. The TAIGA-IACT array will consist of IACT telescopes distributed over an area up to $5\,\mathrm{km}^2$, with a spacing of up to $600 - 1000$ m (Budnev et al., 2017a). In December 2016 a first TAIGA-IACT (figure 2.2) was put into test operation. A second and a third TAIGA-IACT telescope are planned for 2018 and 2019 respectively.

The telescope reflector has a Davies-Cotton design with a focal length of 475 cm, consisting of 34 spherical mirrors with 60 cm diameter. The camera, consisting of a matrix of 547 PMTs of XP1911 type with 2 cm photo-cathode diameter, has a field of view of $\sim 6^\circ \times 6^\circ$, and an angular size of 0.36° per pixel Lubsandorzhiev et al. (2017). Each PMT is equipped with a hexagonal Winston cone with an opening angle of 35°. The camera array is divided into clusters of 28

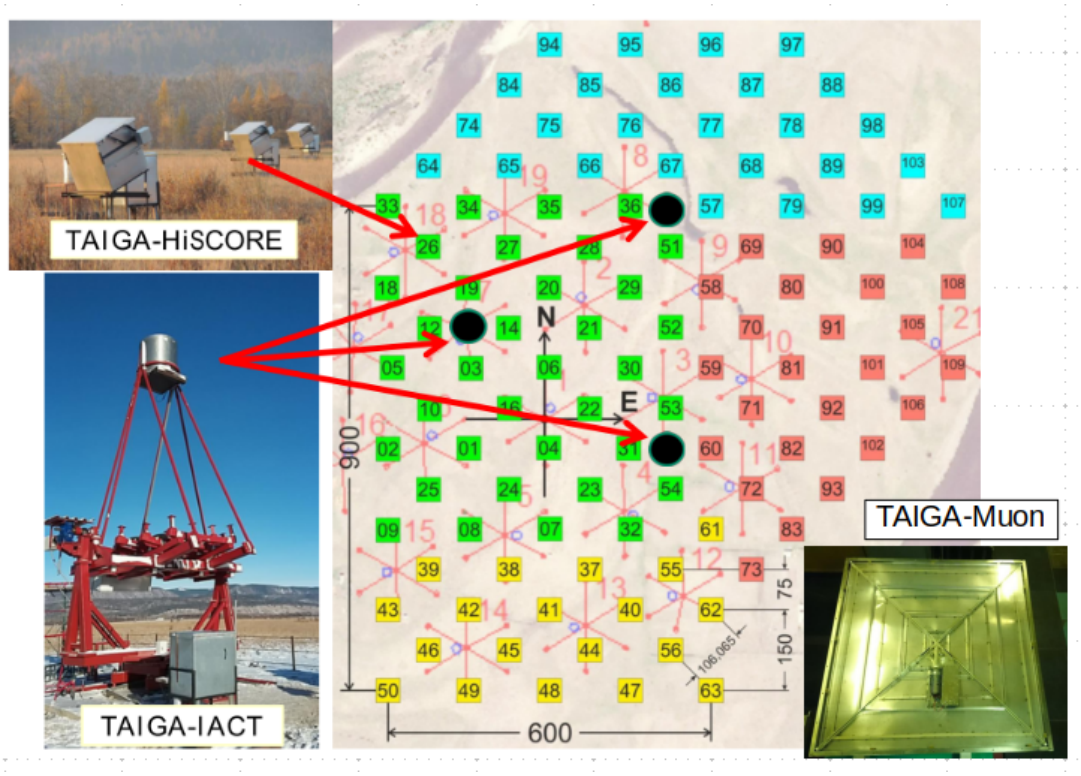

Figure 2.2: Planned configuration of 1 km^2 TAIGA prototype array. The green squares represent the TAIGA-HiSCORE array in operation since 2015 (cluster-1), the yellow ones represent the 2017/18 extension (cluster-2), while the red (cluster-3) and blue (cluster-4) squares represent the extensions planned for seasons 2018/19 and 2019/2020, respectively. The black dots represent the position of the Imaging Atmospheric Cherenkov Telescopes (TAIGA-IACT).

PMTs each. Each cluster is equipped with a 64-channel ASIC MAROC-3 electronic board (Budnev et al., 2017a).

TAIGA-Muon array. The TAIGA-Muon will consist of an array of efficient and low-cost muon counters capable to operate for a long time under the two-meter layer of the wet soil, in order to cover with reasonable efforts an area of $2000 - 3000\,\mathrm{m}^2$, i.e. about $0.2 - 0.3\%$ of the total area of TAIGA detector.

The single counter have 4 triangular scintillators arranged in a $1\,\mathrm{m}^2$ square detector. The scintillator plates have a cross-section of $\sim 10 \times 160\,\mathrm{mm}^2$, located between wavelength shifting bars ($5 \times 20\,\mathrm{mm}^2$), allowing to use small photo-cathode PMTs and reduce the scintillator total volume. The first TAIGA-Muon counters with $1\,\mathrm{m}^2$ area have been be deployed and tested at the Tunka site in July 2017, while a first cluster of 50 counters will be deployed in fall 2019 Astapov et al. (2019).

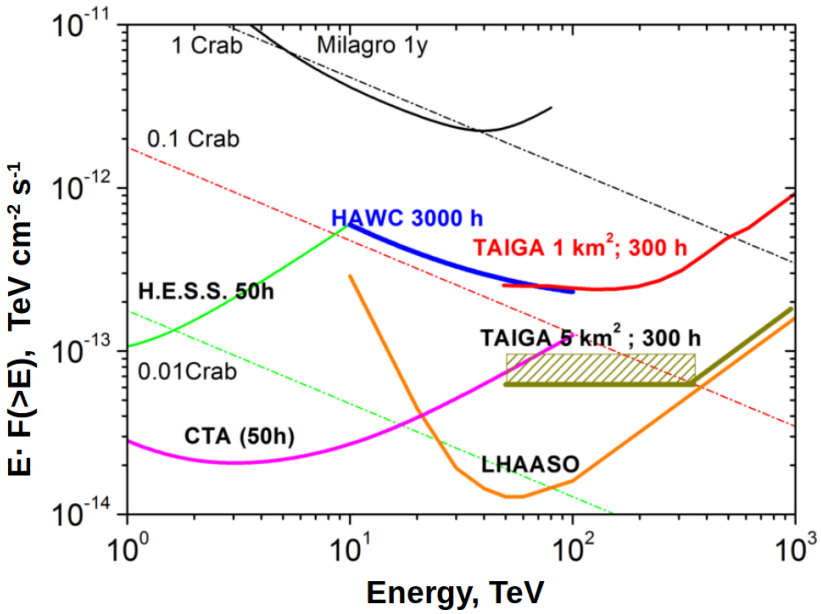

Figure 2.3: Expected integral flux sensitivity for the TAIGA $1\,\mathrm{km}^2$ (red line) and $5\,\mathrm{km}^2$ (green line) setup, for 300 hours point source observation.

An early phase of the TAIGA-Muon array saw the construction of the Tunka-Grande array, consisting of 19 scintillation stations, each of them with a surface and an underground parts. Each surface detector includes 12 scintillation counters with a size $80 \times 80\,\mathrm{cm}^2$, formerly operated as part of the EAS-TOP and the KASCADE-Grande arrays.

HiSORE-IACT hybrid detection. The energy range between $10\,\mathrm{TeV}$ up to $100\,\mathrm{TeV}$ represents the overlap region between the VHE and the UHE bands (figure 1.5), thus the eventual detection of gamma-ray emissions in this region will extend the current gamma-ray sources spectra measured with IACTs (section 1.3.4). Due to the low gamma-ray fluxes at these energies a large detector area ($\geq 1\,\mathrm{km}^2$) and an efficient gamma-hadron separation are needed.

TAIGA, with its HiSOCRE-IACT hybrid detection, aims to solve both these problems: the TAIGA-HiSCORE array will allow to cover the required large area at reasonable costs and provide the main shower parameters (core, arrival direction, energy and shower maximum), while the TAIGA-IACT telescopes, operated in monoscopic mode, will provide the required gamma-hadron separation.

Dedicated simulations of the hybrid HiSCORE-IACT detection technique are currently under investigation. Preliminary results show the potential to achieve a gamma-hadron separation Q-factor ≥ 4 (figure 2.4(a)) by combining the EAS reconstructed core by HiSCORE with the IACT image width (Maike Helena Kunnas, 2017), much better than HiSCORE-only reconstruc-

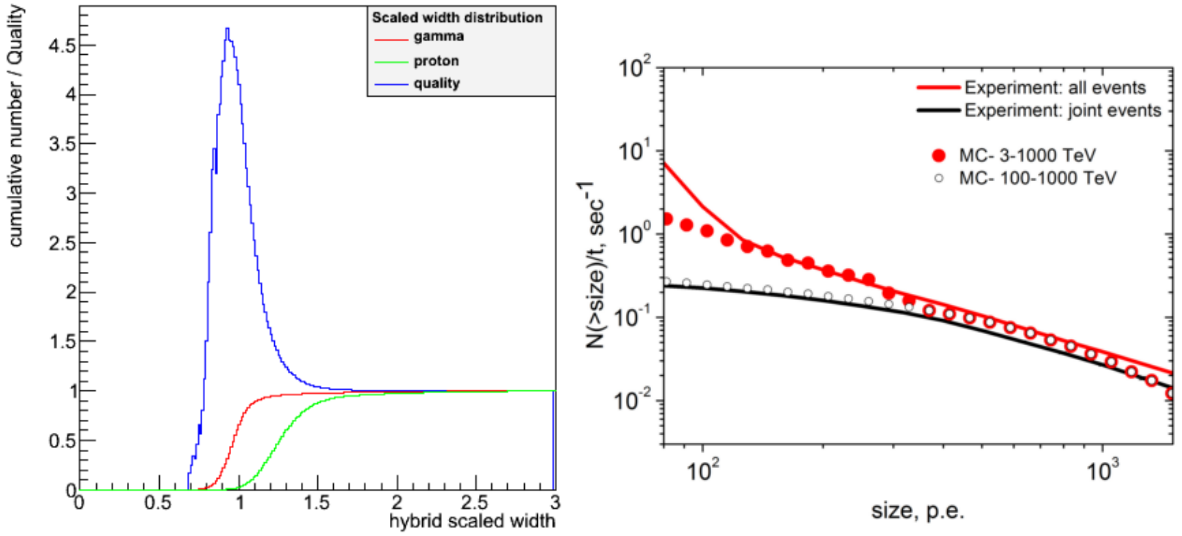

(a) (b)

Figure 2.4: TAIGA hybrid operations: (a) Cumulative distribution and Q factor for the scaled width cut. A maximum Q factor of ~ 4.5 is achieved for $E_\gamma < 50$ TeV (see Maike Helena Kunnas (2017) for detail on the analysis). (b) Image size integral spectra detected during one night by IACT only (red line), and by IACT+HiSCORE joint events (black line). The solid lines show the Monte Carlo predictions for different energy thresholds. More details in Postnikov et al. (2017).

tion: $Q \sim 1$ for $E_\gamma < 100$ TeV and $Q \sim 2$ for $E_\gamma \geq 100$ TeV (Hampf, 2012).

During season 2016/17 the first TAIGA-IACT was installed and tested. In the second half of the season the commissioning phase of operating the IACT in time coincidence with HiSOCRE started. The first results, described in details in (Postnikov et al., 2017), show good agreement with MC expectations.

More in general, the EAS hybrid Cherenkov detection opens to the possibility to develop a new hybrid shower reconstruction by combining informations from both the detectors. As an example, the shower arrival direction could be obtained by fitting together timing information from both IACT and HiSCORE. This would allow a reduction of the minimum HiSCORE events multiplicity, thus reducing the detector energy threshold.

2.1.2 The wide-angle TAIGA-HiSCORE timing array

The TAIGA-HiSCORE detector consists of a wide-angle EAS Cherenkov timing array, composed of small detector stations deployed at $100 - 200$ m from each other. Each detector contains 4 PMTs, each of them equipped with a Winston Cone light collector, for a total sensitive area of $\sim 0.5\,\mathrm{m}^2$ and a FOV of 0.6 sr. A more technical and detailed description of the TAIGA-HiSCORE

detector station is given in section 2.2.

The EAS reconstruction in HiSCORE is performed using the strength and the timing of the signal produce by the EAS Cherenkov photons collected at each detector. Using only these informations it is possible to reconstruct with good accuracy the main EAS parameters: core, arrival direction, energy and X_{max} (see section 2.4).

The main steps of the TAIGA-HiSCORE detector development at the Tunka site in the last years are given in the following.

First field tests. After a period of study and tests in laboratory, in April 2012 a first HiSCORE prototype station was deployed in the Tunka valley for the first field tests. Containing only two PMTs, the station was jointly operated with the Tunka-133 array, detecting events between 1 and 130 PeV (Nachtigall et al., 2013).

During fall 2012, three new HiSCORE prototype stations (two with 4 PMTs, one with 2 PMTs) were installed, arranged in a right angle triangle shape (short sides$= 150$ m). The main goal of the prototype stations was baseline functional tests, cross-verification with showers from Tunka-133, estimation of the shower energy threshold of the optical station, and to study possible ways of threshold reduction (Gress et al., 2013; Wischnewski et al., 2013). Two parallel data acquisition systems (DAQ-1 and DAQ-2) were deployed in this phase inside the stations (Epimakhov et al., 2013). In particular, DAQ-2 was dedicated to the first field tests of the White Rabbit timing system used for event time stamping and station synchronization (Brückner and Wischnewski, 2013; Brückner et al., 2013).

HiSCORE-9 (HiS9). A 9 (3×3) station array was installed during fall 2013, with a station spacing of 150 m, and a total instrumented area of $0.09\,\mathrm{km}^2$.

Again, each station was equipped with two different DAQ systems (same naming as before), with the same goals of the previous season tests. The larger number of stations allowed to check the accuracy of the EAS reconstruction methods developed for HiSCORE. Results of the DAQ-1 data analysis were presented in Berezhnev et al. (2015). A detailed description of the HiS9 array, its station configuration and the data analysis performed on the data collected with DAQ-2 system is presented in chapter 4.

HiSCORE-28 (HiS28). During fall 2014, the HiSCORE array was extended to 28 stations, with the full array starting to be fully operational since season 2015/16 (green squares in figure 2.2). The new stations present a hybrid DAQ system, featuring the main characteristics of the two HiS9 DAQs (see chapter 5 for more detail).

As HiS28 represents, together with the first TAIGA-IACT in 2016, the first phase of the $1\,\mathrm{km}^2$ TAIGA prototype array, one of the main goals of HiS28 was the detection of gamma-ray signal from the Crab Nebula test source, in conjunction with TAIGA-IACT in hybrid mode. In addition, a Crab signal search in HiSCORE stand-alone mode was tested (see chapter 7). To enhance the chance of Crab signal detection with the HiSCORE array, the station spacing was reduced

to $\sim$ 106 m, to reduce the detector threshold, and the station optical boxes were tilted 25° southward, to increase the exposure to the source. A detailed description of the HiS28 array setup and the analysis of the data collected during seasons 2015/16, 2016/17 and 2017/18 are presented in chapter 5.

1 km^2 TAIGA prototype array. During fall 2017 the TAIGA-HiSCORE array was extended to a total of 47 stations, while in fall 2018 an extension up to 60 stations is expected (plus a second TAIGA-IACT). The final extension is programmed for fall 2019, where a final TAIGA-HiSOCRE array of 100-120 (plus the third TAIGA-IACT) is planned, for a total instrumented area of 1 km^2, as shown in figure 2.2.

2.2 The HiSCORE detector station

This section will give a description of basic HiSCORE detector station, composed by an optical and an electronic box, with the main focus on the mechanical and optical components of the first one. The characteristics of the optical box components have been almost the same since the beginning of the HiSCORE station development.

On the other hand, major changes and improvements have been applied to the electronics box components, in particular to the DAQ(s). While the basic concept behind the HiSCORE DAQ will be presented here, a more detailed description of the employed DAQ(s) will be given in chapters 4 (HiSCORE-9) and 5 (HiSCORE-28), which represent two different phases of the HiSCORE detector development, during which different DAQ systems were tested.

2.2.1 Optical box

Mechanical setup. The key design goals of the HiSCORE detector station are (i) be inexpensive, (ii) provide long durability in harsh environments, (iii) reliability of the moving parts. The casing (of both optical and electronics boxes) is meant to protect the internal components and instrumentation, e.g. Winston Cones, PMTs, electronics and cables, from rain, snow, and diurnal light (to protect the PMTs), and to keep a tolerable internal temperature. The skeleton and the four sides, the bottom and the lid are made of aluminium, chosen to be the best construction material in terms of durability, weight and workability. The lid of the optical box is also equipped with a remotely controlled motor, that allows to open the upper side during night operational mode, or keep it close during daily off-mode. The top of the optical box is sealed with a 3 mm plexiglas lid (GS 2458), in order to keep off dust and to maintain the desired temperature inside of the box during operation. The choice of the material is based on its high transmittance at short wavelengths (figure 2.6), fundamental for the measurement of Cherenkov light. In order to prevent ice coverage of the plexiglas lid and Winston cone surfaces, the box is warmed by a heating wires. Figure 2.5(a) shows the HiSCORE detector station

(a)

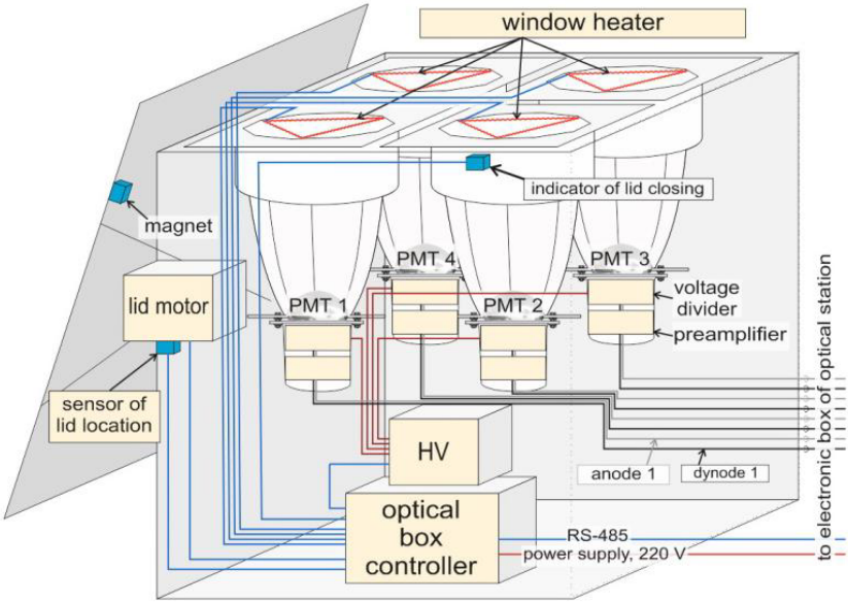

(b)

Figure 2.5: TAIGA-HiSCORE station detector. (a) Picture of the TAIGA-HiSCORE detector station. (b) Schematic view of the standard 4 PMTs HiSCORE optical box. Figure from Budnev et al. (2015).

in its standard configuration, with the PMTs pointing at the Zenith, used during test operation and HiSCORE-9 campaign (see chapter 4. Since observation season 2015/16 the optical box operates in a fixed, 25° southward tilted configuration. Future development include the possibility to control remotely the station tilting. A detailed scheme of the HiSCORE optical box is shown in figure 2.5(b).

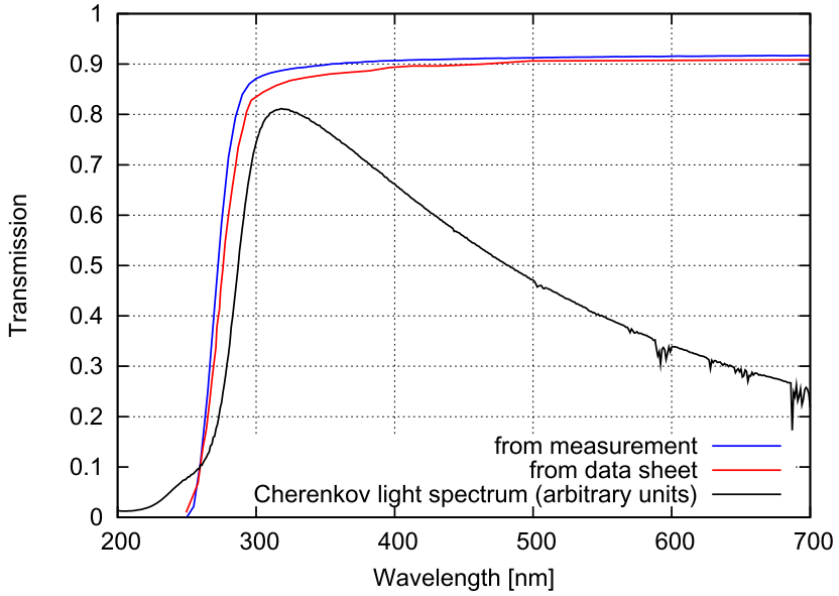

Figure 2.6: Transmission spectrum of Plexiglas GS 2458 from data sheet and from measurement (see Hampf (2012) for more details). For reference, a typical Cherenkov light spectrum after atmospheric absorption is shown. Figures from (Hampf, 2012).

Winston cone. One of the main components of the HiSCORE optical stations is the Winston cone light collector (WC). The WC has two functions: to maximize the PMT light collection area and to minimize the night sky background noise (NSB), reducing the station field of view. The shape is optimised in order to collect as much light as possible at angles below the cut-off angle Θ and present a steep cut-off in the angular transmission (Roland Winston, 1970). Equation 2.1 shows the relation between the desired increase of the light sensitive area and the cut-off angle, Θ:

$$sin\Theta = \frac{R_2}{R_1} \tag{2.1}$$

where R_1 and R_2 are the upper and lower WC opening. The height of the Winston cone is determined by the relation:

$$H = \frac{R_1 + R_2}{tan\Theta} \tag{2.2}$$

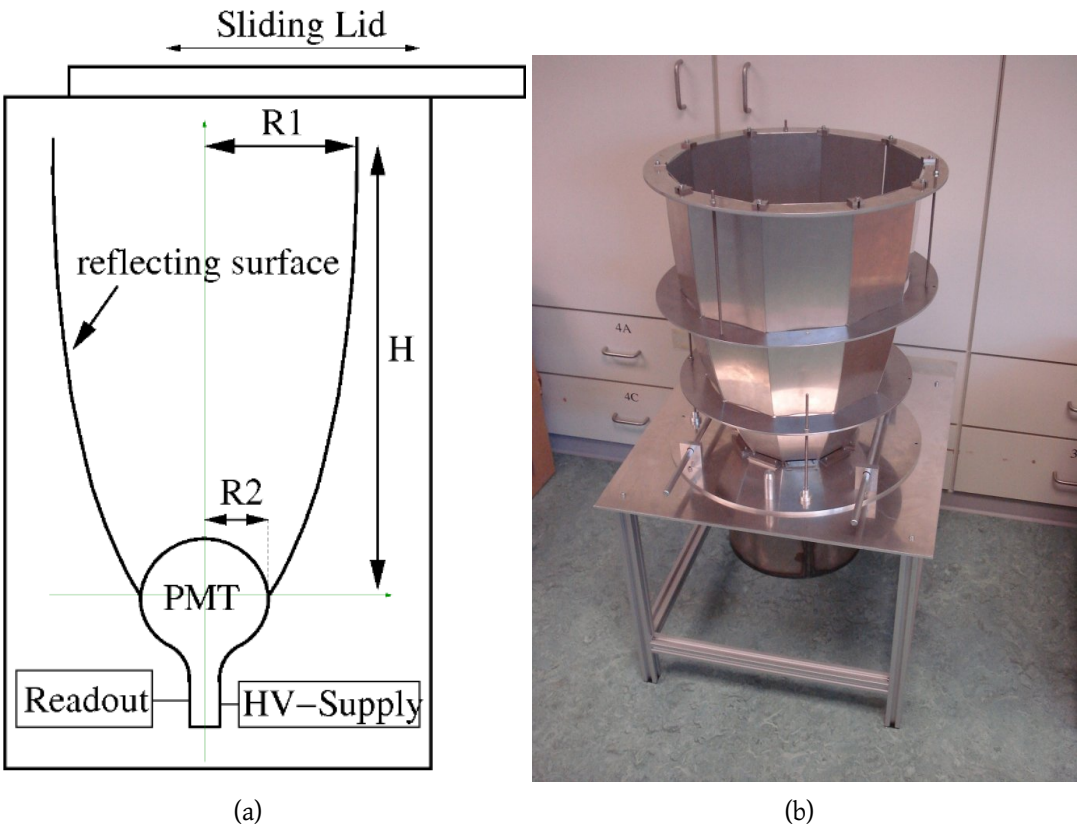

(a) (b)

Figure 2.7: Winston cone (WC) light collector. (a) Geometrical scheme. (b) Picture of a HiSCORE WC prototype, made of segmented aluminium foils. Figures from (Hampf, 2012).

The WC installed in the HiSCORE optical modules are build with $R_1 = 20\,\text{cm}$ and $R_2 = 10\,\text{cm}$, resulting in a factor 4 in the collection area increase, a cut-off angle $\Theta = 30°$ and a height $H = 52\,\text{cm}$.

Detailed ray-tracing simulations (Hampf, 2012; Epimakhov, 2015) have been carried out to study the reflectivity of the WC. The angular acceptance does not only depend on the geometry, but also on the PMT position at the bottom (see figure 2.8), the PMT photo-cathode uniformity and Fresnel losses (Epimakhov, 2015). The resulting observable solid angle can be calculated via:

$$\Omega = 2\pi \int_0^{\Theta} \epsilon(\theta) \sin\theta \cos\theta d\theta \tag{2.3}$$

where the $\cos\theta$ term takes into account the effective area seen by photons with incident angle θ. For the *middle* configuration, a solid angle of ~ 0.6 sr is obtained. The different station viewing angle results in change of time difference distribution between two stations, $\Delta t = t_i - t_j$.

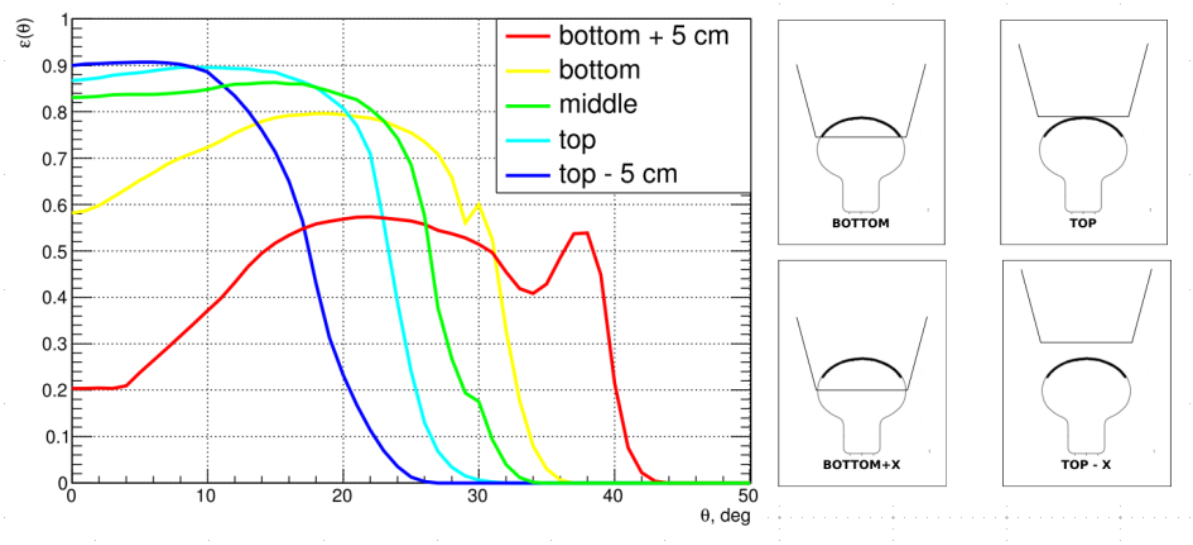

Figure 2.8: Simulated WC reflectivity (angular acceptance) for different PMT positions (Epimakhov, 2015). The *middle* configuration (green line) is the one that better reproduce the station configuration currently operating, resulting in a solid angle of ~ 0.6 sr.

The maximum value of Δt is sensitive to the cut-off angle, and can be used for verification.

The WC is realized using ten 0.5 mm aluminium foils (see figure 2.7(b)), obtaining a good approximation of the ideal WC shape. The internal surface is coated with the commercially available ALANOD3 4300UP, used to ensure a high reflectivity at short wavelengths and a high durability. A detailed study of the HiSOCRE WC properties is presented in Hampf (2012).

Manufacturer	Model	Diameter [cm/inch]	Dynodes	Gain
Hamamatsu	R5912	20.2 / 8	10	10^7
Hamamatsu	R7081	25.3 / 8	10	10^7
Electron Tubes	ET9352KB	20.6 / 10	6	10^4

Table 2.1: List of photomultiplier tested and used for the HiSCORE detector.

Photomultipliers. The main components of the HiSCORE detector station are the photomultiplier tubes (PMTs). In order to achieve a sufficient light sensitive area with only a four channels, large spherical PMTs are needed. Three PMT types have been tested and used in the field so far: Hamamatsu R5912 and R7081, and Electron Tubes ET9352KB. The main characteristics of these PMTs are summarized in table 2.1.

The 10^7 high gain of the ten-stages Hamamatsu PMTs leads to a night sky brightness (NSB)

induced dark current of ~ 50 mA, more than 2 order of magnitude higher than the maximum anode current given by the manufacturer of 0.1 mA. To overcome this, these PMTs are operated using only the first 6 dynodes, obtaining a gain of $\sim 10^4$. These condition (gain $\sim 10^4$) is already satisfied by the ET9352KB by Electron Tubes, originally developed for the AIROBICC experiment. A detailed study of these PMTs characteristics and their applicability in HiSCORE has been done in Nachtigall (2011).

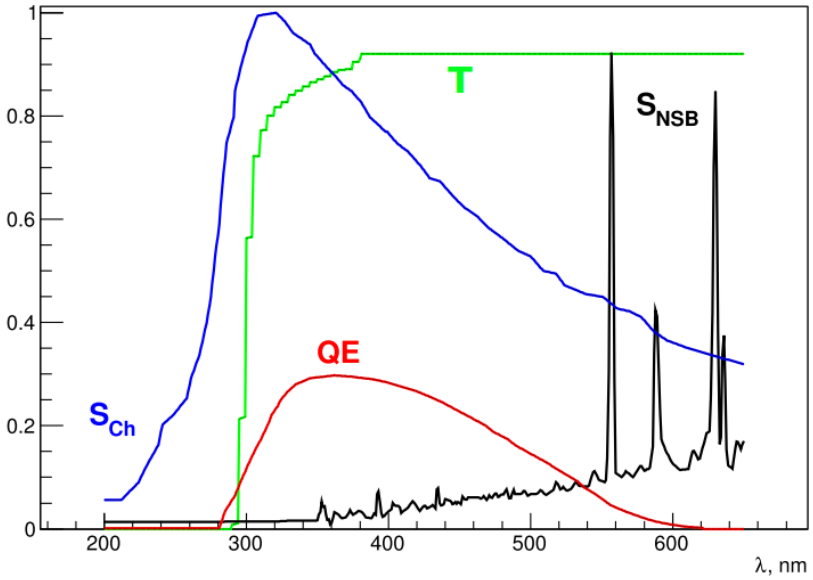

Figure 2.9: Quantum efficiency of the ET9352KB PMT as a function of the incident light wavelength. The plexiglas transmission, T, night sky brightness spectrum, S_{NSB}, and the attenuated Cherenkov spectrum, S_{Ch}, are shown for comparison. Figure from Epimakhov (2015).

The typical quantum efficiency (QE) for the PMTs operating inside the HiSCORE stations is shown in figure 2.9. It reaches a maximum at $\lambda = 340 - 400$ nm and smoothly decreases up to 600 nm, proportionally to the Cherenkov spectrum ($S_{Ch} \propto \lambda^{-2}$ for $\lambda > 300$ nm). At short wavelengths, the QE sharply drops due to the inefficient plexiglas transmission, limiting the energy threshold of the detector. A reduction of the detector energy threshold could obtained by using wavelength shifters, which absorb short wavelength photons ($200-300$ nm) and emit longer wavelength photons within the PMT sensitive range. The convolution of the quantum efficiency with the Cherenkov spectrum and the plexiglas transmission returns an average quantum efficiency, $< QE >^{Ham} \sim 0.14$ ph.e./photon for the Hamamatsu R5912, and $< QE >^{ET} \sim 0.19$ ph.e./ph for the ET9352KB (Epimakhov, 2015).

The collection efficiency (CE) represents another important parameter of PMTs. It's defined as the probability that a produced photo-electron reaches the active area of the first dynode, and has values around $0.8 - 0.9$ (Hamamatsu, 2006). In this work, a collection efficiency of 0.9

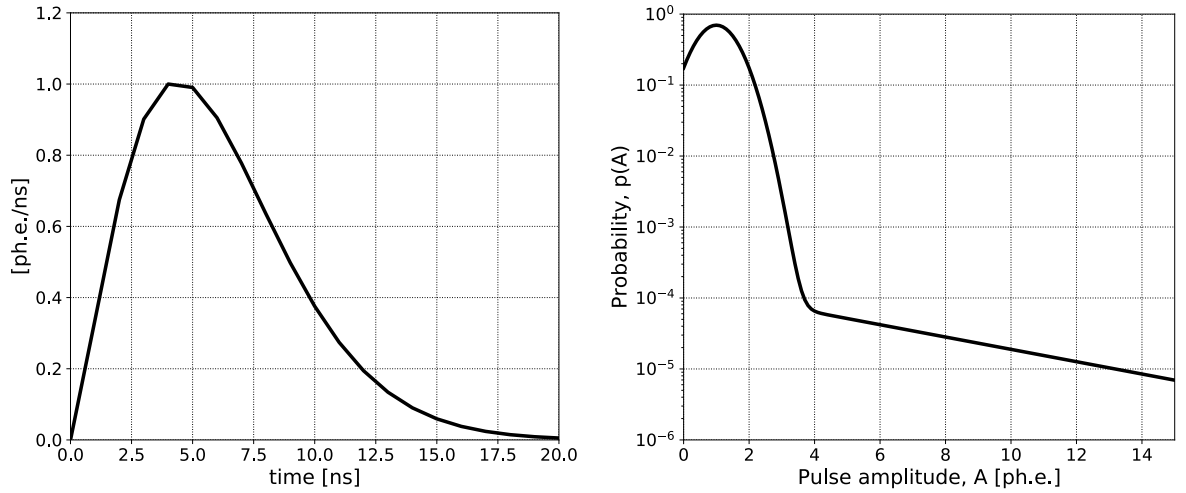

(a) (b)

Figure 2.10: PMT single ph.e. response function, characterised by the pulse shape (left, equation 2.4) and the amplitude distribution (right, equation 2.5). See Hampf (2012) for references.

is used to simulate the detector response (section 2.3).

Two other important features of the PMTs, that directly affect the detector response, are the pulse shape, which describes the signal produced by a single ph.e. and the amplitude spread of the single ph.e. response. Figure 2.10(a) shows the pulse shape from the AIROBICC simulations for the ET9352KB PMTs (Henke, 1994), described by the following equation:

$$R(t) = \frac{7}{4}\frac{c b^{\frac{a+1}{c}}}{\Gamma\left(\frac{a+1}{c}\right)} \cdot \left(\frac{7}{4}t\right)^{a} \cdot \exp\left(-b\left(\frac{7}{4}t\right)^{c}\right) \tag{2.4}$$

where $a = 1.25$, $b = 0.0414$, $c = 1.48$ and the time t is given in nanoseconds. The function peaks at 0.1259 ph.e./ns, and its width (FWHM) is about 7.4 ns. The amplitude spread, i.e. the probability that a single photon causes an amplitude A, is described by the sum of a Gaussian function and an exponential tail to include the effect of rare but large after-pulses (Bernlöhr, 2008):

$$p(A) = \frac{1}{1.433}\left(\exp\left(-\frac{1}{2}\left(\frac{A-\mu}{\sigma}\right)^{2}\right) + 2 \cdot 10^{-4} \cdot \exp\left(\frac{-A}{5}\right)\right) \tag{2.5}$$

with $\mu = 1$ ph.e. and $\sigma = 0.6$ ph.e.. The normalisation factor is calculated by integrating the function from 0 to 40 ph.e. The single ph.e. pulse shape and the amplitude spread functions shown in figure 2.10 are used to simulate the HiSCORE detector response, described in section 2.3.

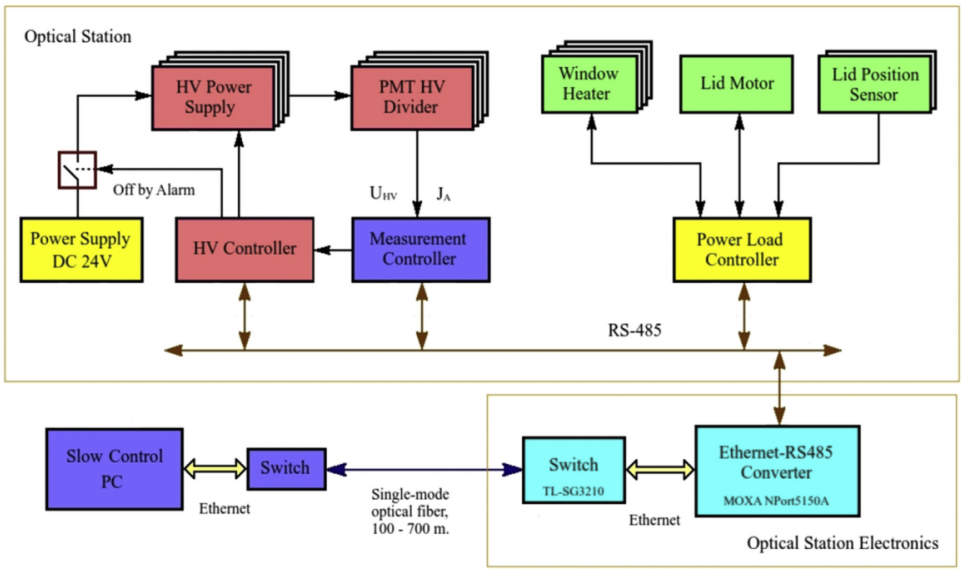

Figure 2.11: Block diagram of the HiSCORE slow control system currently operating in the Tunka valley. Figure from Gress et al. (2017).

Slow control system. The slow control (figure 2.11) consists of three controllers (HV Controller, Measurement Controller and Power Load Controller), based on the 16-Bit Flash Microcontroller PIC24FJ64GA004I-PT, all connected in single board. The controllers board, located inside the optical box, is connected to the MOXA NPort5150A converter via RS-485 bus. An 8-Port Gigabit L2 Managed Switch TL-SG3210 with 2 SFP Slots and the Moxa NPort5150A Serial Ethernet Converter are placed in the electronics box, with special temperature control (Gress et al., 2017). The main tasks of the slow control system are controlling the station lid position and the plexiglas windows heating, monitoring load currents of the lid motor and heating, controlling HV power supply of PMTs, monitoring HV and PMT anode currents, and auto turn-off by over-current or at the end of the run. The slow control system provides data communication via fibre cables between the optical station controllers and main control PC in the central DAQ building. The software for the slow control system was written in the development environment LabVIEW (LabVIEW, 2018).

2.2.2 Electronics box

This section will describe the main components of the electronics box: the data acquisition system and the monitoring system.

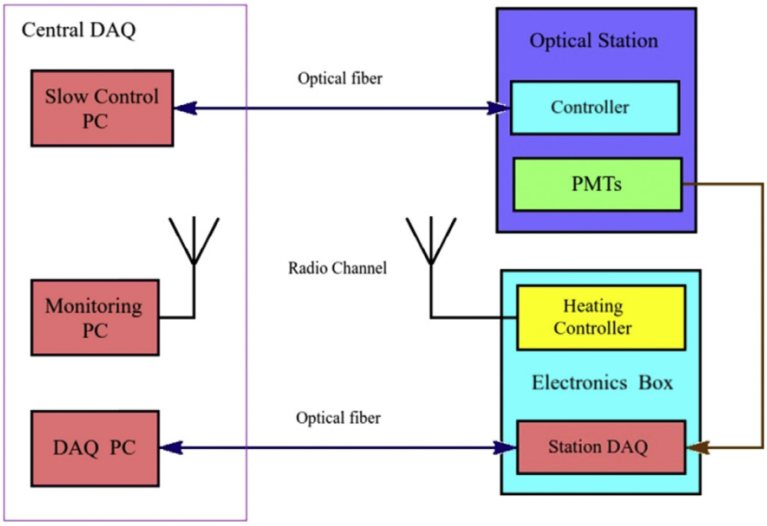

Figure 2.12: Diagram of the basic HiSCORE electronics units currently operating in the Tunka valley. Figure from Gress et al. (2017).

Data acquisition system The main component of the electronics box is the data acquisition system. The station DAQ consists of two main elements: the analogue summator (Kunnas, 2012) and the signal digitalization and read-out board.

The summator takes as input the four PMT anodes signals, and returns their analogue sum (AS) as output. The AS signal is used as trigger signal, allowing to reduce the trigger rate due to the NSB by a factor 2, and to lower the signal trigger threshold (and the detector energy threshold as a consequence). The signal digitalization and read-out board is based on the DRS4 (Domino Ring Sampler) chip developed by the Paul Scherrer Institute (DRS, 2018), allowing a fast signal sampling up to 5 GSamples/s with 1024 sampling points. It receives in input the 8 signals from the PMTs (4 anodes, 4 dynodes), the AS trigger signal, and the synchronization signal.

A local trigger is issued if the AS signal is above a certain threshold (Thr) for a time larger than a certain fixed time over threshold (TOT), i.e. $t_{AS>Thr} \geq TOT$. The choice of the TOT value is usually based on the FWHM of the detector response (see figure 2.10), while the trigger threshold is set in order to have a minimum AS integrate charge of ~ 200 ph.e.. For each triggered AS signal, a time-stamp is produced using the synchronization signal as reference, and the traces of the 8 PMT channels plus the synchronization signal are read-out and sent to the central DAQ for storage and further processing.

A detailed description of the specific DAQs tested during the different phases of the HiSCORE detector development are presented in chapters 4 and 5.

Monitoring system. The main functions of the monitoring system are remote monitoring of

the temperature and current consumption of the different electronics box components during operations. It also allows to set (i) the temperature at which the controller turns on power to the station DAQ, (ii) the temperature of the switch on/off heater and fan of cooling, (iii) switching on/off the power supply of the station DAQ by the operator. The monitoring system includes a Heating Controller with connected XBee-PRO ZB RF Module router located at each station, and a computer in the central DAQ connected to the XBee-PRO ZB RF Module coordinator via USB-connector. Heating Controller is designed on the 16-Bit Flash Microcontroller PIC24FJ64GA004I-PT to control the power load (on/off power, heating and cooling). The XBee-PRO ZB RF Modules (DIGI, 2018) operate within the ISM 2.4 GHz frequency band with a low data rate (250 Kbps). Each station in the array is connected via fibre cables and radio antennas to the central DAQ building as illustrated in figure 2.12.

2.3 Detector response simulation

2.3.1 EAS simulation

The EAS generation is performed with the CORSIKA v6.99 program (Heck et al., 1998). The QGSJET01c and GHEISHA models are used to simulate hadronic interactions at high and low energy, respectively. The IACT package (Bernlöhr, 2000, 2008) is used to simulate the superluminal secondary particles Cherenkov photons generation and their propagation down to the detector level. Only Cherenkov photons found inside a 1.5 m diameter sphere around each detector station are stored into an output binary *.iact* file.

Proton and gamma-ray initiated EASs are generated in the energy range from 10 to 5000 TeV, with an energy spectrum $dN/dE \propto E^{-1}$, in order to have more statistic at higher energies. The arrival direction of the primary particles is set to be uniform in ϕ (Azimuth) and $cos(\theta)$ (Zenith), with $\phi \in [0°, 360°)$, and $\theta \in [0\,°, 60°]$. The EAS cores are uniformly distributed inside the generation area, a rectangular region extended up to 400 m from the detector edges, in both x and y directions, with the geometry of the detector array defined in the CORSIKA input file.

2.3.2 Station response

The HiSCORE station response is simulated using the *sim_score* software (Tluczykont et al., 2011; Hampf et al., 2011). Based on *sim_skeleton* (Bernlöhr, 2008), *sim_score* reads in *.iact* files and computes the signals seen by each station. The final station signal is given by the sum of the NSB and Cherenkov light induced signals.

NSB signal simulation. The NSB induced noise signal is obtained by uniformly distributing ~ 18.3 ph.e./ns $\cdot T$ photoelectrons within the time interval T, following the example in Hampf (2012). The photoelectron rate is obtained multiplying the NSB photon flux ($2.7 \cdot$

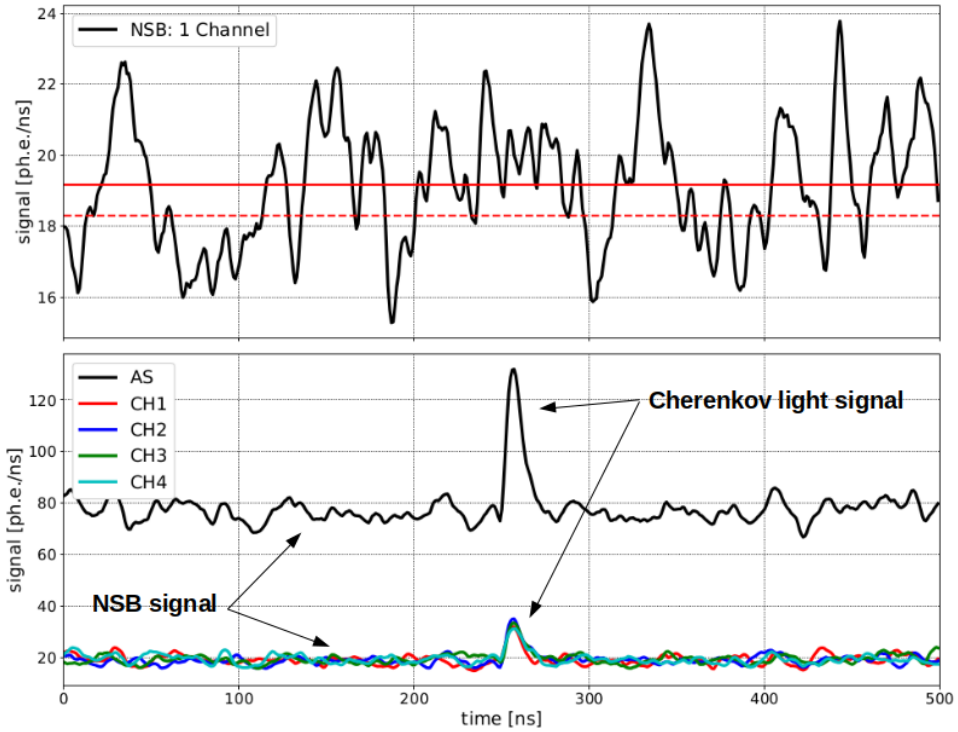

Figure 2.13: Example of simulated HiSCORE station signal. Top: simulated NSB signal for one channel (1 PMT). The solid (dashed) line indicates the initial (final) ph.e. rate. Bottom: combined NSB + Cherenkov light signal for the 4 PMTs (CH#, coloured lines) and their analogue sum (AS, black line). The AS line clearly show the reduction by a factor 2 of the S/N ratio. While the simulation of the station trigger is performed using only the signal generated by the Cherenkov light, the event reconstruction is performed using the full station signal (NSB + Cherenkov), as described in section 2.4.

10^{12} ph. m^{-2} s^{-1}) for the average plexiglas transmission (0.9), the WC acceptance area ($0,126\,\mathrm{m}^2$) and solid angle (0.6 sr), and the average PMT QE (0.1) and QC (0.9). The photoelectrons time distribution is then folded with the detector response, in the same way as done for the Cherenkov photons. This increase the average photoelectron rate from 18.3 to 19.3 ph.e./ns, as shown in the 500 ns NSB sample shown in the upper panel of figure 2.13.

Cherenkov signal simulation. For each Cherenkov photon stored in the *.iact* file, its position $(x, y, z)_{Ch}$, arrival direction $(\theta, \phi)_{Ch}$ are known. The number of photoelectrons generated by the collected Cherenkov photons is calculated taking into account atmospheric (MODTRAN, Kneizys et al. (1996)) and plexiglas absorptions (figure 2.6), the WC geometrical acceptance (figure 2.8), PMTs QE (figure 2.9), and average QC (0.9). The signal produced by each PMT anode channel is obtained folding the resulting photoelectrons time distribution with the pulse shape and the amplitude spread functions shown in figure 2.10. An arrays of 4000 bins, each

one representing 1 ns, is used to sample the PMT signals. The array time frame is centred around the zero point of the CORSIKA time frame, defined as the time at which the primary particle would have reached the observation level without interacting in the atmosphere.

The final PMT output signals are obtained summing up the NSB and the Cherenkov photons induced signals. The lower panel of figure 2.13 shows an example of simulated HiSCORE station response: the coloured signals represent the signal from the 4 PMTs, while the black line gives their analogue sum (AS). This example clearly shows the S/N improvement by a factor 2 in the AS signal w.r.t. the single PMT signal.

Signal trigger simulation. A station trigger is issued if the AS signal is above a certain threshold, L_{Thr} for more than 7 ns. The number of photoelectrons needed to produce a trigger is given by:

$$N_{ph.e.}^{trigger} = \frac{L_{Thr} - < NSB >}{0.1259 \cdot 0.552} \tag{2.6}$$

where $< NSB >$ is the average noise level, 0.1259 is pulse shape peak value, and 0.552 is the level at which the pulse shape width is ~ 7 ns. L_{Thr} is set in order to get $N_{ph.e.}^{trigger} \sim 180$ ph.e. In real experiment, the actual number of photoelectrons needed to generate a trigger will be a little higher than $N_{ph.e.}^{trigger}$, since not all photons will arrive at exactly the same time. However, the signal trigger simulations use L_{Thr} and the AS signal without NSB (only Cherenkov photons induced signal).

2.4 Event reconstruction

The EAS reconstruction in TAIGA-HiSCORE is performed with *reco_score* software, developed in Hampf (2012). The software consists of a collection of Python scripts, that allow to perform EAS parameters reconstruction (core, direction, energy and X_{max}), reconstruction calibration (correct energy and X_{max} estimation), and gamma-hadron separation analysis. The following sections will describe the main steps of the TAIGA-HiSCORE EAS reconstruction, showing the accuracy for the main parameters, and the gamma-hadron separation performances. The results hereafter shown are obtained using the *standard* TAIGA-HiSCORE layout, a squared array of 484 stations (22×22), with 150 m station spacing, for a total instrumented area of $\sim$10 km^2 (Hampf, 2012).

For this work, the reconstruction has been adapted to be used on the real experiment data (see chapters 4, 5 and 6), and integrated with different reconstruction methods derived from the Tunka-133 shower reconstruction (equations 2.9 and 2.14, Prosin et al. (2009, 2014)). Several routines have also been developed and integrated in the software, in order to perform real detector time calibration, and angular resolution evaluation (sections 4.2.1, 5.3.2, 5.3.1, 5.3.3 and 5.4.3), and ISS CATS/LIDAR signal analysis (see chapter 6 for detail on this last topic).

2.4.1 Station signal processing

As mentioned in section 2.3, the TAIGA-HiSCORE reconstruction is performed by using the sum of the 4 channel signals, AS (analogue sum). The first step of the reconstruction consists of the parametrization of the AS signal with the following quantities:

- intensity, S [ph.e.]: Integrated area below the signal inside a readout window between -15 ns to 25 ns relative to the trigger time (determined in *sim_score*);
- peak amplitude, A [ph.e./ns]: maximum amplitude reached by the signal;
- peak time, t_{peak} [ns]: time at which the signal reaches its maximum (no interpolation);
- edge time, t_{edge} [ns]: time at which the signal reaches 50% of the peak amplitude (linear interpolation between adjacent time bins);
- rise time, t_{rise} [ns]: time duration in which the signal rises from 20% to 80% of the peak amplitude (interpolated);
- width, w [ns]: signal full width half maximum, FWHM.

Figure 2.14 give an illustration of the AS signal parametrization.

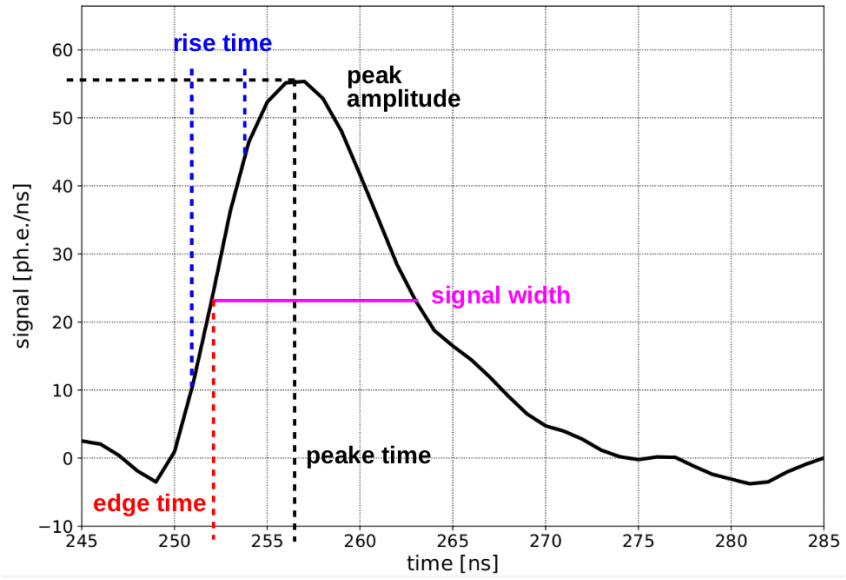

Figure 2.14: Signal parametrization in *reco_score*. The pulse intensity, S, is given by the signal integral over the shown time window.

2.4.2 EAS preliminary reconstruction

The preliminary event reconstruction consists in the determination of the EAS core and arrival direction with two simple models: a signal centre of gravity (COG) for the core, and a plane wave (PW) approximation of the EAS light front. A minimum of 4 triggered stations (possible extension down to 3) are required. The preliminary core and direction (shower axis) allows to perform a more precise reconstruction by sitting on the EAS system of reference.

Signal centre of gravity (COG). The COG method consists of a weighted average of the triggered stations positions, $\overrightarrow{X}_i = (x_i, y_i, z_i)$, using the station signal strength, S_i or A_i, as weights:

$$\overrightarrow{X}_{COG} = \frac{\sum \overrightarrow{X}_i A_i}{\sum A_i} \tag{2.7}$$

By definition, the method can precisely reconstruct only EAS with cores inside the array. A resolution of $\sim 20-30$ m is obtained at low energy, while a good resolution of 10 m is achieved at energies above few 100 TeV.

Plane wave (PW). A plane wave approximation of the EAS light front is used for a preliminary estimation of the EAS arrival direction. The arrival time at the *i*-th station, t_i is defined as follow

$$ti^{PW} = \frac{1}{c}(x_i \sin(\theta)\cos(\phi) + y_i \sin(\theta)\sin(\phi) - z_i \cos(\theta)\cos(\phi)) + t_0 \tag{2.8}$$

where θ and ϕ are zenith and azimuth angles that define the arrival direction, and c the speed of light. The fit parameter t_0 is used only to adjust the function to the absolute time frame and carries no physical information. The PW model well approximates the EAS front close to the core, giving a good estimation of the arrival direction for low multiplicity events, with core inside the array. The PW reconstruction accuracy ($\sim 1°$) is enough for a more precise estimation of the EAS parameters, as shown in the next sections.

2.4.3 Core reconstruction

If an event successfully passes the preliminary reconstruction, a more precise estimation of the EAS core is performed using more realistic models for the EAS description. Two parametrizations are used in this work: the lateral light density function (LDF, Hampf (2012)), and the amplitude distance function (ADF). Both models are derived from the LDF/ADF models developed for the Tunka-133 experiment (Prosin et al., 2009, 2014).

ADF. The ADF model performs the EAS core reconstruction by fitting the amplitude distribution function as a function of the distance from the EAS axis, R. The model parametrization

is given by $ADF(R) = ADF(200m)f(R)$, with $f(R)$ describe as follow:

$$f(R) = \begin{cases} exp\left(\frac{(R_{kn}-R)}{R_0}\left(1+\frac{3}{R+2}\right)\right) & \text{for } R \leq R_{kn} \\ (R/200)^{-b2} & \text{for } R_{kn} < R \leq 200\,\text{m} \\ \left(\frac{R/400+a}{1+a}\right)^{b_A}\left(\frac{1+a}{0.5+a}\right) & \text{for } 200 < R \leq 400\,\text{m} \\ \left(\frac{R/400+1}{2}\right)^{b_A}\left(\frac{1+a}{0.5+a}\right) & \text{for } R > 400\,\text{m} \end{cases} \tag{2.9}$$

where

$$d = b_A - 5 \tag{2.10a}$$
$$R_0 = 275/d \tag{2.10b}$$
$$R_{kn} = 145 - 115\log_{10} d \tag{2.10c}$$
$$a = 0.89 - 0.29\log_{10} d \tag{2.10d}$$
$$b_2 = \begin{cases} 2.4 + 2(\log_{10} d - 0.15) & \text{for } b_A \geq 6.41 \\ 2.4 & \text{for } b_A < 6.41 \end{cases} \tag{2.10e}$$

The free parameters are the normalization factor $ADF(200m)$, the slope b_A, and the core coordinates (x_C, y_C). A minimum of 5 triggered stations are required, and the parametrization is optimized for being used only with the pulse amplitudes.

LDF. The LDF model is meant for EAS core reconstruction by fitting the lateral distribution of the Cherenkov photons density (i.e. the pulse intensity, S). However, given the simple model parametrization, it can also be applied to fit the distribution of the pulse amplitudes, A. The model (equation 2.11) is described by an exponential in the range $0 < R < R_{LDF}$, and a power law for $R > R_{LDF}$, with R the distance from the EAS axis, and $R_{LDF} \approx 120\,\text{m}$ (as suggested in (Fowler et al., 2001)). besides the two core coordinates (x_C, y_C), the free parameters are the normalization factor P, the inverse decay-length of the exponential function d, the power law index k. A minimum of 6 stations are required. If at least 7 stations are available, R_{LDF} can be let free, with a slight improvement of the core determination.

$$LDF(R) = \begin{cases} Pexp(dR) & \text{for } R \leq R_{LDF} \\ QR^k & \text{for } R_{LDF} > R \end{cases} \tag{2.11}$$

where

$$R = \sqrt{x^2 + y^2} \tag{2.12}$$

$$Q = \frac{Pexp(dR_{LDF})}{R_{LDF}} \tag{2.13}$$

The core resolution obtained with the LDF method (using the pulse intensity) is presented in figure 2.15.

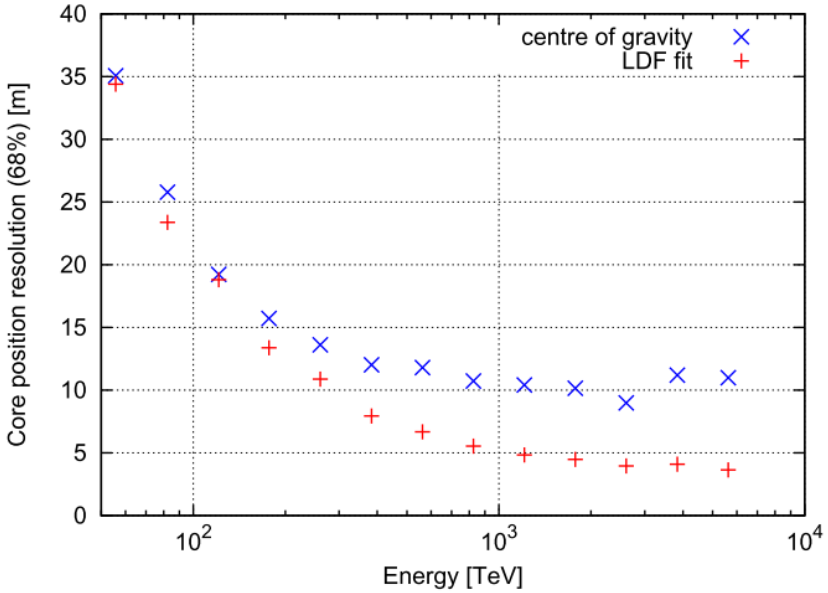

Figure 2.15: Core resolution (68% of containment) as a function of the true primary energy, obtained for the COG and LDF fit models. Figure from Hampf (2012).

2.4.4 Arrival direction reconstruction

Like for the EAS core position, two methods are used for the reconstitution of the EAS arrival direction: a parabolic front approximation (PARAB) derived from the Tunka-133 reconstruction, and an analytical model (VIC) of the Cherenkov photons arrival time developed in Hampf (2012).

Curved EAS front model (PARAB). An accurate reconstruction of the EAS arrival direction is achieved by taking into account the EAS front curvature. Following the reconstruction procedure used in Tunka-133, the arrival time at the given station, t_i, is defined by the superposition of a plane wave (equation 2.8) and a one-dimensional curved function, $Dt(R_i)$:

$$ti = t_i^{PW}(\theta, \phi, t_0) + Dt(R_i) \tag{2.14}$$

with

$$Dt(R_i) = \frac{(R_i + R_c)^2}{cR_s^2} \tag{2.15}$$

where R_i is the station distance from the EAS axis, $R_c = 250\,\mathrm{m}$, and $R_s = 200\,\mathrm{m}^{1/2}$. The PARAB model requires signal from at least 4 stations.

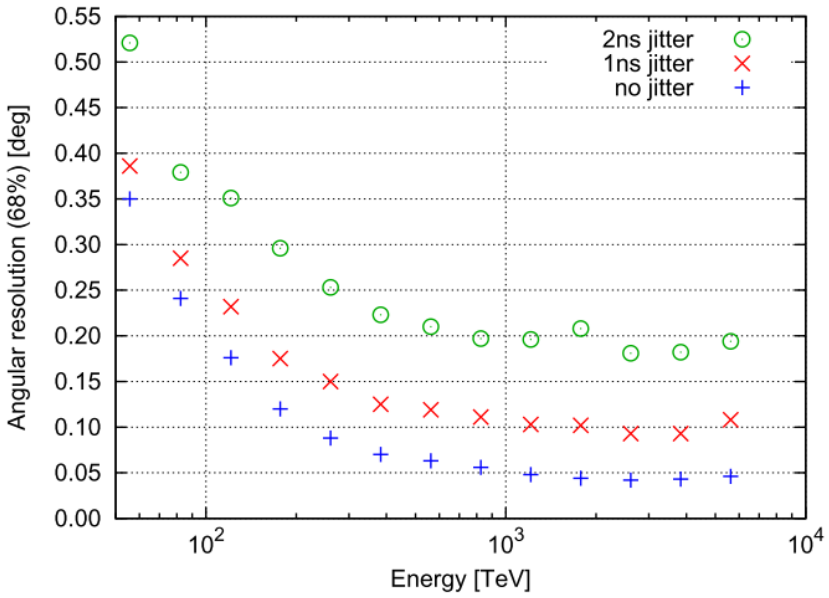

Figure 2.16: Angular resolution (68% of containment) as a function of the true primary energy, obtained for the arrival time model (VIC), using different values for the time jitter between individual signals. Figure from Hampf (2012).

Arrival time model (VIC). If signals from at least 5 stations are available, it is possible to use the model for the light arrival time developed by (Stamatescu et al., 2011) for timing stereoscopy with IACT detectors, and adapted in (Hampf, 2012) for timing array detector. The expected arrival time at a given station, t_i, is parametrised as a function of the detector position, (x_i, y_i, z_i), the vertical height of the EAS maximum, Z, and the primary particle arrival direction, θ and ϕ:

$$t_i = \frac{1}{c}\sqrt{k}\left(1 + \frac{\eta_0 h_0(\exp(-z_i/h_0) - \exp(-Z/h_0)}{Z - z_i}\right) + t_0 \tag{2.16}$$

with

$$k = r_i^2 + \frac{Z^2}{\cos^2(\theta)} - 2z(z_i - r_i \tan(\theta)\cos(\phi')) + z_i^2 \tag{2.17}$$

where $\phi' = \phi_i - \phi$ (see Hampf (2012) for details on the derivation). besides the determination of the arrival direction, the VIC model allows the estimation of the EAS maximum height, that can help in the primary particle identification and gamma-hadron separation analysis.

Figure 2.16 shows the angular resolution obtained for the VIC model, for different station time resolutions (time jitter). A crucial role is then played by the detector timing system, from which a sub-nsec inter-stations *time synchronization* is required (see results presented in chapters 4 and 5) to achieve an reasonable detector angular resolution ($\sim 0.1^{\circ}$). Another crucial role in the EAS direction reconstruction is played by the detector *time calibration*, i.e. the correct estimation (and correction) of eventual systematic time offsets in the stations time measurements. The presence of such offsets has two main effects: 1) a general worsening of the detector angular resolution, 2) the introduction of a systematic angular offset in the EAS arrival direction reconstruction. A detailed discussion on the *time calibration* for ground-based EAS detector (with particular focus on HiSCORE) is given in chapter 3, while different *time calibration* methods are tested and compared in chapter 5 (see also section 6.3.1).

2.4.5 Energy reconstruction

As discussed in section 1.3.1, the number of particles in a EAS is proportional to the primary particle energy, while the amount of Cherenkov light emitted by each secondary is independent from its energy. This turns the atmosphere in a giant calorimeter for high energy particle, read out by a Cherenkov detector.

Due to the small HiSCORE sensitive area (1 m^2 per station), the LDF function obtained in the core fitting (section 2.4.3) is used for energy reconstruction. The LDF weakly depends on the EAS depth at core distances between 200 and 300 m, and the value at 220 m, LDF(220) is chosen as energy estimator. Figure 2.17(a) shows the energy resolution, $\Delta E/E$, for gamma-ray, proton and iron. For gamma-ray a resolution of 35% is obtained below 100 TeV, while it improves below 10% at higher energies. The resolution for hadrons is in general higher with respect to gamma-rays, direct consequence of the lower electromagnetic component generated and the larger fluctuations during the EAS development.

2.4.6 X_{max} reconstruction

The vertical position of the EAS maximum, representing the point where the number of secondary particles reaches its maximum, is an important parameter for the event reconstruction, that allows to separate gamma-rays from hadrons, and estimate the primary nuclei mass. The EAS maximum, X_{max}, is usually defined as the air column the EAS traversed before reaching its maximum, in units of g/cm^2:

$$X_{max} = \frac{1}{\cos\theta} \int_{z_{max}}^{\infty} \rho(z) dt \tag{2.18}$$

with θ the EAS inclination, $\rho(z)$ the air density profile of the atmosphere, and z_{max} the height of the EAS maximum.

Three different methods are implemented in *reco_score* for the reconstruction of X_{max}: the *timing* method, the *LDF* method and the *width* method.

Timing method. As mentioned in section 2.4.4, the arrival time model for the arrival direction reconstruction also estimates the height of the EAS maximum, Z. Since the *edge time* is used in the arrival direction reconstruction, the fit returns a higher estimation of the EAS height. A better results is obtained by using the pulse *peak time*.

LDF method. Like for the energy, the LDF function can be used also to estimate the EAS depth. In HiSCORE the ratio LDF(50 m)/LDF(220 m) is used as estimator for the EAS depth.

Width method. Another way to reconstruct the EAS depth is using the correlation between the EAS maximum and the recorded Cherenkov pulses width in the stations at large distance from the core ($\gtrsim$ 200 m) (Patterson and Hillas, 1983). The pulse width distribution as a function of the core distance is fitted with a linear function, $W(r) = a + br$, using signals only from stations between 150 and 400 m from the core. The fitted width at 300 m from the core, W(300 m), is chosen as estimator.

Figure 2.17(b) shows the X_{max} resolution as a function of the true primary particle energy. All the methods achieve the same accuracy, and improve with the energy thanks to the better estimation of the signal parameters. The black dots give the resolution for the combined X_{max}, obtained by averaging the available depth estimations for the single event. The combined method results in a better resolution compared to the single methods alone.

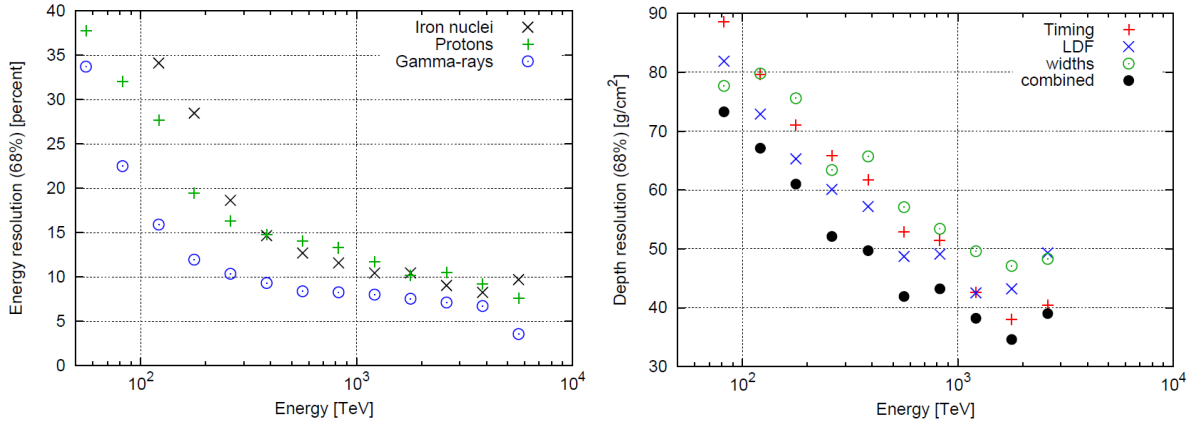

(a) (b)

Figure 2.17: Energy (a) and X_{max} (b) resolution (68% containment) for gamma-ray, proton and iron nuclei as a function of the true primary particles energy (Hampf, 2012). Figures from Hampf (2012).

2.4.7 Particle identification and gamma-hadron separation

Particle identification. The particle identification analysis implemented so far for HiSCORE (Hampf, 2012) is obtained using three parameters, P_1, P_2 and P_3, defined as follow:

$$\begin{aligned} P_1 &= X_{max}^{width} - X_{max}^{timing} \\ P_2 &= X_{max}^{exp} - X_{max}^{timing} \\ P_3 &= t_{rise} \end{aligned} \tag{2.19}$$

where X_{max}^{width} and X_{max}^{timing} are the EAS depths obtained respectively with the *width* and the *timing* methods, and t_{rise} is the pulse rise time of the event central station. X_{max}^{exp} is obtained by fitting the correlation between X_{max}^{timing} and the reconstructed energy for gamma-rays with the following function:

$$\frac{X_{max}^{exp}(E)}{[g/cm^2]} = a + b \log_{10}\left(\frac{E}{[TeV]}\right) \tag{2.20}$$

gamma-hadron separation. Combining the three parameters defined above allows to distinguish between EAS induced by primary gamma-rays or hadrons. The gamma-hadron quality factor, $Q_{\gamma/h}$, is defined as the ration between the fraction of surviving gamma-rays, ϵ_γ, and the square root of the fraction of surviving background events, ϵ_{bg}:

$$Q_{\gamma/h} = \frac{\epsilon_\gamma}{\sqrt{\epsilon_{bg}}} \tag{2.21}$$

Two different parameters combinations have been proposed in Hampf (2012):

- Comb-1: Individual cut values are determined for the three parameters by requiring an $\epsilon_\gamma = 80\%$. Only events surviving all the three cuts are selected as gamma-ray.
- Comb-2: The distributions of the three parameters are mapped between 0 to 1, with hadron particles characterised by higher values, and gamma-rays by lower values. A fourth parameter, P_4, is obtained by multiplying the three normalized parameters (figure 2.18(a)). The optimal cut value for P_4 is found by maximising $Q_{\gamma/h}$.

Figure 2.18 shows the efficiencies ϵ_γ and ϵ_{bg}, and the resulting $Q_{\gamma/h}$, obtained with Comb-2. Below 100 TeV, no separation can be achieved. The main reason is the bad quality of the depth reconstruction, needed for parameters $P1$ and $P2$, in turn due to the low light intensities at large core distances. However, parameter $P3$ (t_{rise}) alone can achieve a moderate quality factor of 1.2 to 1.3 between 50 TeV and 100 TeV. At higher energies (> 100 TeV) the quality factor gradually increases, reaching ~ 2 above 1 PeV.

The results so far achieved are not very satisfactory, in particular at threshold energies (≤ 100 TeV). However, the analysis is still in a preliminary phase, using only few parameters, and performed with simple selection cuts. A more robust analysis, using a larger number of

parameters and modern machine learning analysis tools (e.g. boosted decision trees and/or artificial neural networks), will surely improve the potential for HiSCORE stand-alone particle identification and gamma-hadron separation.

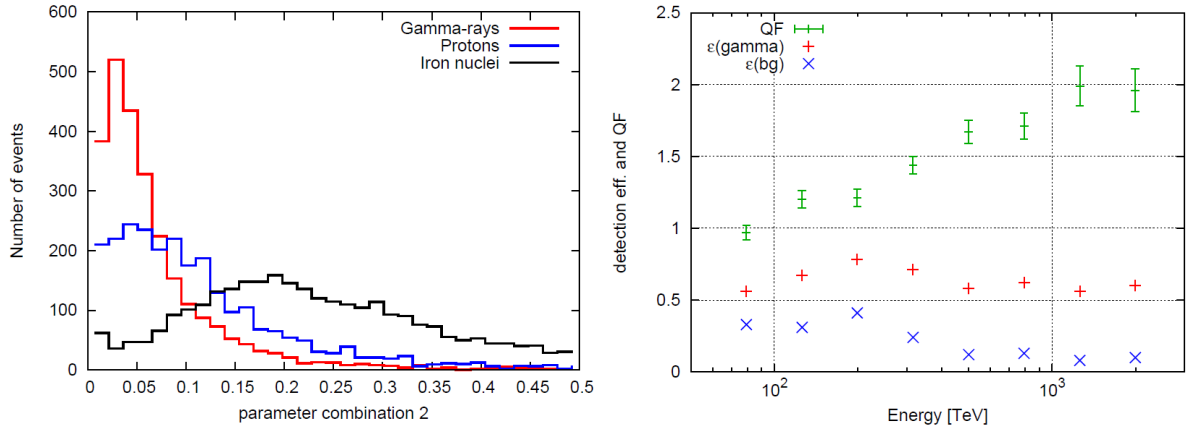

(a) (b)

Figure 2.18: TAIGA-HiSCORE stand-alone particle identification and gamma-hadron separation (Hampf, 2012). (a) Distribution of parameter P_4 (product of normalized $P1$, $P2$ and $P3$) for gamma-ray, proton and iron nuclei in the energy range from 100 TeV to 1 PeV. (b) Gamma-ray and cosmic ray (background) survival probabilities, ϵ_γ and ϵ_{bg}, and resulting quality factor, $Q_{\gamma/h}$, after the application of cut Comb-2, versus the reconstructed energy. Figures from Hampf (2012).

2.4.8 Effective area and point source sensitivity

Effective area. The detector effective area as a function of the energy, $A_{eff}(E)$, is defined as:

$$A_{eff}(E) = \frac{A_{sel}}{A_{gen}} \cdot \epsilon(E) \tag{2.22}$$

where A_{gen} and A_{sel} are respectively the core generation and selection areas, and $\epsilon(E)$ is the detection efficiency as a function of the simulated energy. Figure 2.19 shows the HiSCORE effective area obtained with the *standard* simulated layout. In the left panel the effective is given after acceptance cut (triggered stations ≥ 3, reconstructed core inside the array perimeter, reconstructed $\theta \leq 25°$), while the right panel shows the effective area after gamma-hadron cut (Comb-1).

Sensitivity. An important performance figure for gamma-ray detectors is the point source sensitivity, i.e. the potential to see a weak gamma-ray source over a large CR background. The sensitivity is defined as the minimal integral flux, $\Phi_\gamma(E \geq E_0)$, above a given energy E_0 that

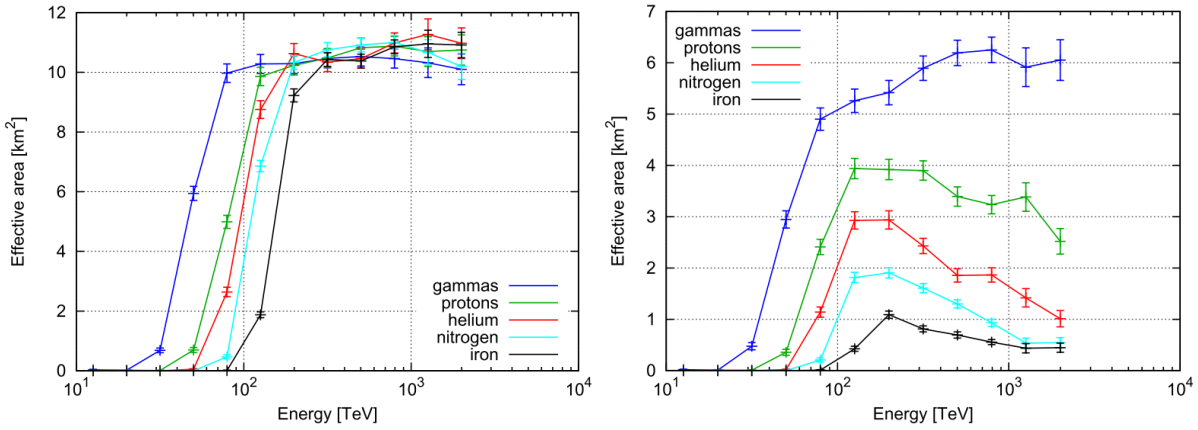

Figure 2.19: TAIGA-HiSCORE effective areas for the simulated *standard* detector layout ($\sim$ 10 km^2, 150 m station spacing) as a function of true primary energy, for five simulated primary particle species. (a) Effective area after acceptance cuts: triggered stations ≥ 3, reconstructed core inside the array perimeter, reconstructed $\theta \leq 25°$. (b) Effective area after gamma-hadron cuts: Comb-1. Figure from Hampf (2012).

must arrive from a source in order to be detected by the instrument. A source is classified as detected if the signal in the source region exceeds the homogeneous CR background by at least five standard deviations. This way, the probability of a false detection caused by a background fluctuation are below 10^{-6}. Additionally, a minimum of 50 gamma-ray events are required.

The detection significance is defined as (Li and Ma (1983), equation 9):

$$S = \frac{N_{on} - N_{off}}{\sqrt{\alpha(N_{on} + N_{off})}} \tag{2.23}$$

where N_{on} and N_{off} are respectively the number of detected events in the source and background regions of equal area. Assuming $N_{on} = N_\gamma + N_{bg}$, and $N_{off} = N_{bg}$, with $\alpha = 1$, the minimum number of gammas required is given by:

$$N_\gamma(E \geq E_0) = 12.5 + \sqrt{156.25 + 50 N_{bg}(E \geq E0)} \tag{2.24}$$

Here the background, $N_{bg}(E_0)$, is calculated multiplying the CR rate by the observation time, T, and reduced to the solid angle of the source region, defined as a small circle of radius equal to the angular resolution shown in figure 2.16 (assuming 1 ns jitter). This way, about 68% of the gamma photons are included at all energies, while the background level is kept relatively small. A detailed description of the CR background is given in Hampf (2012), obtained by folding the

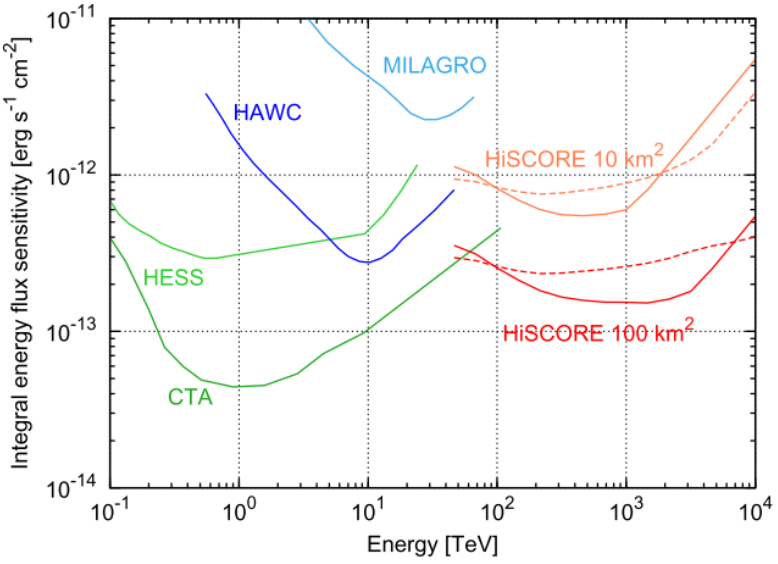

Figure 2.20: TAIGA-HiSCORE stand-alone point source sensitivity for the simulated *standard* detector layout ($10\,\mathrm{km}^2$) and $100\,\mathrm{km}^2$ detector, assuming 1000 h (5 years) of observation time. The dashed lines indicate the sensitivity without gamma-hadron separation. For comparison, the sensitivities of other experiments are plotted for comparison. Figure from Hampf (2012).

effective areas shown in figure 2.19(b) with the different nuclei rates determined using the polygonato model (Hörandel, 2003).

The gamma-ray flux needed to detect N_γ photons is calculated using a source spectrum with $dN/dE \propto E^{-\Gamma}$ (no cut-off), the effective area for gamma-rays, and the observation time, T:

$$\Phi(E \geq E_0) = \frac{N_\gamma(E \geq E_0)}{T} \cdot \frac{\int_{E_0} E^{-\Gamma}}{\int_{E_0} E^{-\Gamma} A_{eff}(E)} \tag{2.25}$$

Figure 2.20 shows the calculated point source sensitivity for a $10\,\mathrm{km}^2$ HiSCORE detector array (as simulated) and for a $100\,\mathrm{km}^2$ array. The latter is obtained by scaling effective areas by a factor 10, and using the same performance figures (angular resolution, gamma-hadron separation, etc.) used for the $10\,\mathrm{km}^2$ array, resulting in a conservative estimation. An observation time of 1000 h (5 years) is assumed.

As the the point source sensitivity linearly depends on the angular resolution, which in turn depends on the accuracy of the array time synchronisation between the stations, a sub-nsec time resolution will improve the shown sensitivity of up to a factor of 1.5 to 2.

In conclusion, the $100\,\mathrm{km}^2$ HiSCORE detector can achieve a better sensitivity in the UHE gamma-ray regime with respect to the sensitivity in the VHE regime achieved by current Cherenkov telescope systems. This will allows HiSCORE to extend the range of current gamma-

ray observations to higher energies.

2.5 Summary and conclusions

This chapter introduced the TAIGA experiment, new a ground-based wide-angle EAS detector, featuring both Cherenkov imaging and timing techniques, aiming at the study of CR physics above 100 TeV, and gamma-ray astronomy in the multi-TeV and UHE regimes. A description of the TAIGA scientific goals and detection concept are given, together with a description of the detector development at the Tunka site in the last years and future plans.

The second part of the chapter focused on the TAIGA-HiSCORE timing array. The main station components and the detector response simulation software (*sim_score*) have been described in details. The station simple setup and the low construction cost will allow to cover an area of $10\,\mathrm{km}^2$ up to $100\,\mathrm{km}^2$.

A detailed description of the methods used to reconstruct the main EAS parameters (core, arrival direction, energy and EAS maximum) has also been presented. The main results consists on the good angular resolution ($\sim\ 0.1^\circ$) achieved at higher energies (100 TeV). However, this results strongly depends on the sub-nsec relative *time resolution* between the stations achieved by the timing system, and the full array *time calibration*. These two topics are the main subjects of investigation in this work, addressed in details in the next chapters. The main limit of the HiSCORE detector consists in the gamma-hadron separation: while the $Q_{\gamma/h}$ reaches values between 1.5 and 2 above 100 TeV (Hampf et al., 2013), the bad reconstruction quality at low energy (≤ 100 TeV) returns a $Q_{\gamma/h} \sim 1$. Such limitation should be overcome by the TAIGA hybrid HiSCORE-IACT joint operations, combining the accurate EAS reconstruction of TAIGA-HiSCORE, with the efficient gamma-hadron separation provided by the TAIGA-IACT in monoscope operation.

More detailed analysis of the TAIGA-HiSCORE in stand-alone operations are presented in the next chapters. Chapter 4 will present the setup of the TAIGA-HiSCORE 9 array, and the analysis of the data collected with the data acquisition system DAQ-2. Chapter 5 will present the setup of the TAIGA-HiSCORE 28 array, and the analysis of the data collected during 3 years of operations, i.e. from season 2015/16 to season 2017/18. In particular, the data analysis focuses on the full array *time calibration*, with *Hybrid* calibration method presented in chapter 3 tested and proposed as standard time calibration method for TAIGA-HiSCORE. Chapter 6 will present the detection of the first TAIGA-HiSCORE "point source": the CATS/LIDAR on board of the ISS. Finally, chapter 7 will present a first systematic point source analysis performed on the 3 years data collected with TAIGA-HiSCORE 28 in stand-alone operation.

Chapter 3

Time calibration in a EAS Cherenkov timing array

In a EAS Cherenkov timing array, the arrival direction of the primary particle is determined using the Cherenkov photons arrival time at the different detector stations. To reconstruct the arrival direction with the desired accuracy, a sub-nsec *time synchronization* is required between the array stations, as discussed in section 2.4.4 (figure 2.16).

Another effect that affects the accuracy of the reconstructed primary particle direction is the presence of systematic time offsets inside the station time measurements. These time offsets worsen the detector angular resolution, and even more seriously introduce a systematic angular offset in the detector absolute pointing. The result is a distortion of the reconstructed Azimuth and Zenith distributions, as shown in Elo and Arvela (1999a,b,c). Thus, a precise *time calibration* is essential to remove such systematic offsets, in particular if the detector is dedicated to gamma-ray astronomy, where an optimal angular resolution is required to discern the signal form the background, and a precise pointing is needed to associate the signal with astrophysical sources. This chapter will address the problem of obtaining a precise time calibration in a EAS Cherenkov timing array, and more in general in EAS ground-based array.

Typical time calibration procedure of EAS Cherenkov arrays uses a central light source (e.g. LED, see chapter 4), directly illuminating all (or many) detector stations. This becomes difficult when the size of the array (and the number of stations) increases up to several km^2, together with the need of periodical checks due to the variation of the detector conditions in time. Another time calibration concept adopted in EAS array time calibration is the "self-calibration" method (Calabrese Melcarne, 2006; He et al., 2007), allowing a full detector calibration by using the collected EAS data. As shown in section 3.1, it is based on two steps: 1) a minimization of the reconstruction fit residuals, *Residual correction*, and 2) a correction based on the Characteristic Plane (CP) concept (*CP correction*), introduced in (He et al., 2007). The *CP correction* plays a fundamental role, and is needed to fully correct the average mispointing introduced by the non-zero station time offsets. However, the method assumes a precise knowledge a priori of the detected EAS true arrival directions distribution (i.e. the detector acceptance), not always possible with the required accuracy.

The *Hybrid* time calibration method is introduced in section 3.2. Based on a different approach to the *CP correction*, it represents an alternative to the mentioned "self-calibration" method. The name *Hybrid* comes from the combined usage of the detected EAS data, with precise external measurement of the time offsets for a small subset of the array stations. The method is here tested by means of MC simulation, and a study of the method systematics is performed.

3.1 Array time self-calibration

In a ground-based EAS array, the time self-calibration allows to determine the detectors time offsets using the data collected during normal operations. A mathematical description of how the station time offsets affect the EAS direction reconstruction and the method used to correct them are presented in this section.

For an event i, the arrival time t_j is measured at each detector unit j of coordinate (x_j, y_j), and the arrival direction angles (θ_i, ϕ_i) are usually determined with a least squares fit. If Δt_j is the typical station time offset of the j-th station, the EAS front equation goes like:

$$c(t_{ij} - \Delta t_j - t_{0i}) = x_j l_i + y_j m_i + \omega(R_{ij}) \tag{3.1}$$

where c is the speed of light, $[l_i = \sin(\theta_i)\cos(\phi_i), m_i = \sin(\theta_i)\sin(\phi_i)]$ are the direction vector cosines, and t_{0i} is another fit parameter. The term $\omega(R_{ij})$ describes the EAS front deviation form the planar solution (front curvature), as a function of the station distance from the EAS axis, $R_{ij} = R_{ij}(\theta_i, \phi_i)$.

The goal of the time calibration is to determine the unknown values of the station time offsets, Δt_j.

3.1.1 Residual correction

A common way to correct the detector time offsets is reducing the residuals, δt_{ij}^{res}, with respect to the fitted EAS front. However, this does not guarantee the full correction of the initial time offsets.

To prove the last statement, and better understand the limits of the *Residual correction*, a simple test is performed to check the correlation between the initial offsets distribution (that we want estimate and correct) and the fit residual distribution (that represents the correction). The test consists of generating different set of initial station time offsets, fit them with a plane function, and compare the fit residual distribution with the initial time offsets. For the array, the HiS28 layout is used (see figure 5.1(a)). The initial time offsets are extracted from a uniform distributions of $r.m.s.$ up to 20 ns. For each value of the $r.m.s.$, 10^4 distributions are generated.

As shown in figure 3.1(a), a linear correlation with slope < 1 is obtained, meaning that the offset calibration obtained with the *Residual correction* only reduce the initial time offsets.

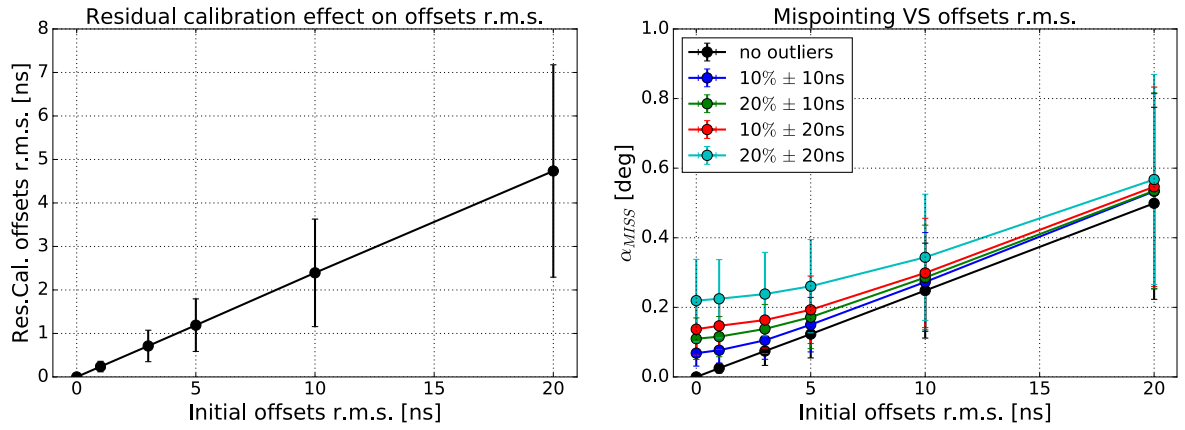

(a) (b)

Figure 3.1: *Residual correction* test. (a) Correlation between the initial offsets $r.m.s.$ and the plane fit residual $r.m.s.$ (median), representing the *Residual correction*. (b) Average mispointing angle, α_{MIS}, as a function of the initial offsets $r.m.s.$. Few outliers can lead to a large systematic mispointing, even for a good initial guess for most of the time offsets (i.e. small initial offsets r.m.s). In this example, $\pm 10(20)$ ns are added to the 10%(20%) of the array stations, resulting in a large pointing error, α_{MIS}, even for small initial time offsets $r.m.s.$.

Figure 3.1(b) shows the median of the mispointing angle distribution, α_{MIS} (i.e. the angle between the fitted plane normal vector and the vertical axis), as a function of the initial offsets $r.m.s.$. Another linear correlation is observed, with reasonably small α_{MIS} ($< 0.1°$) obtained for small values of the initial offsets $r.m.s.$ (< 5 ns). For this reason, the *Residual correction* has been used in different experiment (AIROBICC (Karle et al., 1995), HiS28 section 5.3.1) together with precise pre-calibrated time offsets, in order to reduce the initial error in the fit procedure. However, also this kind of procedure is not fully safe, as shown in figure 3.1(b): the presence of few outliers, with large difference with respect to the initial guess, can lead to a large uncorrected mispointing.

The real effect of the *Residual correction* is finally shown in figure 3.2: subtracting the residual offset calibration from the initial offsets leads to the alignment of the station offsets on a plane, as clearly visible in figure 3.1(b). As will be shown in section 3.2.1, this effect contributes to improve the detector angular resolution, in particular at low multiplicity. However, the average mispointing introduced by the time offsets, α_{MIS}, remains uncorrected.

Given these observations, it is correct to assume that the time offsets Δt_j are the sum of two terms, the residual term, δt_j^{res}, and another unknown term, consisting in a planar correction that fully remove the detector mispointing, α_{MIS}. The determination of the unknown planar correction is described in the next sections.

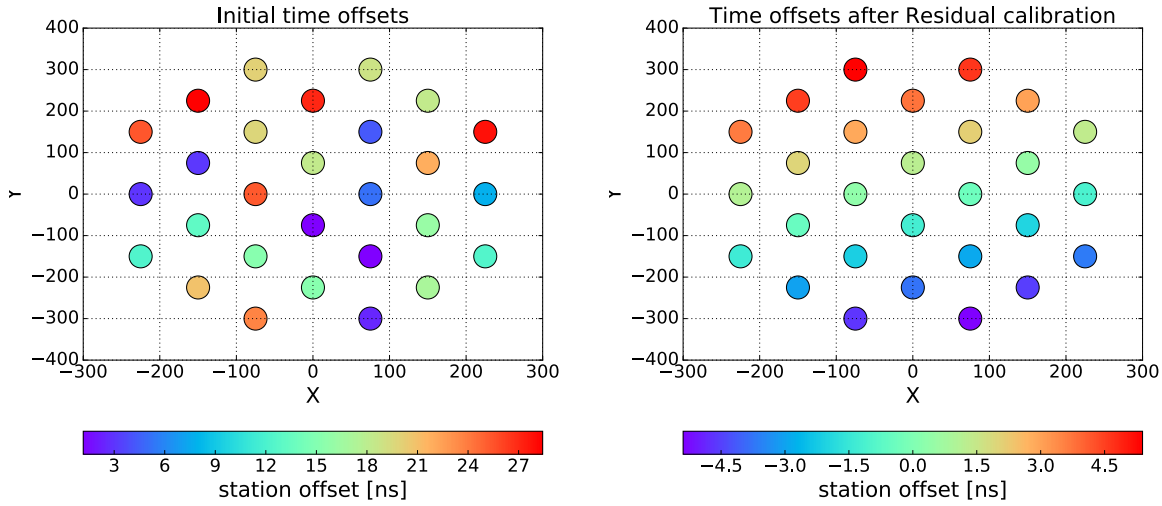

(a) (b)

Figure 3.2: Effect of the *Residual correction*. (a) Initial time offsets with uniform distribution between [0 ns, 30 ns]. (b) Station time offsets after *Residual correction*. The station time offsets are aligned on a plane (see section 3.1.2).

3.1.2 Characteristic Plane (CP)

Characteristic Plane definition. After applying the *Residual correction*, the EAS front fit equation becomes:

$$c(t_{ij} - \delta t_{ij}^{res} - t'_{0i}) = x_j l'_i + y_j m'_i + \omega(R'_{ij}) \tag{3.2}$$

resulting in the inaccurate direction cosines [$l'_i = \sin(\theta'_i)\cos(\phi'_i)$, $m'_i = \sin(\theta'_i)\sin(\phi'_i)$]. Combining (3.1) and (3.2), we obtain:

$$\Delta_j = A_i \frac{x_j}{c} + B_i \frac{y_j}{c} + \delta_{ij}^{res} + \delta t_{0i} + \delta\omega_{ij} \tag{3.3}$$

where $A_i = l'_i - l_i$ and $B_i = m'_i - m_i$. The constant $\delta t_{0i} = t'_{0i} - t_{0i}$ is equal for all the stations. The term $\delta\omega_{ij} = \omega(R'_{ij}) - \omega(R_{ij})$ is a small radial deviation from the planar solution. The quantities A_i and B_i determine the Characteristic Plane (CP), representing the difference between the reconstructed fake plane (FP) and the real plane (RP). The CP of a detector array is defined as the average difference between FPs and RPs of all the reconstructed events, i.e. the systematic deviation between FP and RP (pointing accuracy). The array CP is fully determined

by the equation:

$$\Delta t_j = A\frac{x_j}{c} + B\frac{y_j}{c} + < \delta t_j^{res} > + < \delta_0 > \tag{3.4}$$

with the plane cosines defined as follow:

$$A = < l' > - < l > = \sin(\theta_0)\cos(\phi_0) \tag{3.5a}$$
$$B = < m' > - < m > = \sin(\theta_0)\sin(\phi_0) \tag{3.5b}$$

where (θ_0, ϕ_0) is the direction defining the normal vector to the array CP. From equation (3.4) one sees that, knowing the CP cosines, (A, B), and of the residual correction $< \delta t_j^{res} >$, the time offset of the j-th station, Δt_j, is univocally determined by its coordinate (x_j, y_j).

CP correction. To determine the array CP cosines, (A, B), one needs to know the mean value of the distorted directions cosines ($< l' >, < m' >$), and of the true directions cosines ($< l >$, $< m >$). While the first are directly obtained when reconstructing the EAS directions to determine the *Residual correction*, to estimate the seconds one needs to know the true distribution of the arrival directions of the detected events, i.e. the detector acceptance in θ and ϕ.

An easy solution is obtained for a detector with a symmetrical acceptance along the Azimuth, ϕ (He et al., 2007). In this case, $< l > = < m > = 0$, leading to a simple estimation of the array CP cosines and the CP correction. However, also in this simple case, the true arrival directions distribution can be distorted due to the effect of the geomagnetic field (Ivanov et al., 1999; He et al., 2005), requiring a more complicate solution for the true directions cosines (Bartoli et al., 2014). The situation becomes even more complicated if the acceptance symmetry is lost, like in the case of the HiS28 (chapter 5). More in general, inhomogeneous detector acceptances make difficult the correct and precise estimation of the *CP correction*, affecting the absolute pointing calibration of the array significantly, limiting the precision of the instrument.

Radial deviation from the CP. The term $< \delta\omega_j > = < \omega(R'_{ij}) - \omega(R_{ij}) >$ has been neglected in the formulation of array CP (equation 3.4). As can be seen from its mathematical description, two components contribute to this term: 1) the presence of the station time offsets (introducing the term $\omega(R'_{ij})$ through R'_{ij}), and 2) the intrinsic error introduced when approximating the EAS fronts curvature with $\omega(R_{ij})$. When averaging over the sample of reconstructed EAS events, a small radial trend is observed in the distribution of the station time offset (i.e. the CP plane is actually slightly curved) as shown in figure 3.4(b). A similar effect is observed in (Calabrese Melcarne, 2006; Bernardini et al., 2005), but with a different radial trend, due to the different (conical) EAS front approximation. As will be shown in the sections 3.2.2, $< \delta\omega_j >$ can be reduced selecting events with large multiplicity for the *Residual correction* estimation.

3.2 Hybrid time calibration

The previous section showed how to correctly estimate the station time offsets in a ground based EAS array using the self-calibration method. Two steps are needed: the *Residual correction* and the *CP correction*. While the *Residual correction* is easy to obtain, the *CP correction* requires the precise knowledge of the detector acceptance, in order to correctly estimate the CP orientation (ϕ_0, θ_0), an finally solve equation 3.4. However, it is not always possible to know the detector acceptance with the required precision, and correctly estimate the *CP correction*.

A new method for precise time offset calibration is here presented, based on a different approach for solving equation 3.4. The CP equation can be rewritten as follows:

$$\delta t_j^{CP} = \Delta t_j - < \delta t_j^{res} > = A\frac{x_j}{c} + B\frac{y_j}{c} + < \delta t_0 > \tag{3.6}$$

Since the system of equations 3.6 has only 3 free parameters (A, B, $< \delta t_0 >$), it can be easily solved knowing, for at least 3 stations, the values of Δt_j, i.e. the true values of the station offsets. These values can be obtained in several ways (e.g. manual calibration, external LED light source, etc.). Obtained the CP parameters, it is possible to derive a precise estimation of time offsets for all the other stations in the array.

The method is dubbed *Hybrid* since it combines informations from the EAS to estimate the *Residual correction*, $< \delta t_j^{res} >$, and from external time calibration for the *CP correction* (only few stations needed, ≥ 3).

3.2.1 MC verification

The *Hybrid* calibration method is tested here by means of MC simulations. First, a simple and fast simulation is used to check the method concept. Then, a more accurate test is performed using the full HiSCORE simulation chain: EASs (CORSIKA), detector response, and EAS event reconstruction. In both tests, the same set of initial station time offsets is used, extracted from a uniform distribution between 0 and 30 ns (see figures 3.2(a) and 3.3(a)). As a detector, the HiS28 layout is used (see figure 3.2).

Fast simulation. The first test on the *Hybrid* method is performed using a simple and fast simulation (toy-MC), where 10^4 fake EASs are generated with azimuth and cos(zenith) uniformly distributed in $[0°, 360°)$ and $[1, \cos(30°)]$ respectively. The arrival time at each station is simulated using a simple plane model, plus a small time jitter of 1 ns $r.m.s.$. The event multiplicity is finally obtained randomly choosing *n* stations, with $n \in [4, 28]$.

The events arrival direction is reconstructed with a least square fit, collecting the residuals for each station. The residual distributions are then fitted with a Gaussian function, and the mean value is used to define the *Residual correction*, $< \delta t_j^{res} >$. As shown in figure 3.2(b), applying the *Residual correction*, all the station time offsets are aligned on a plane: the array CP.

The *CP correction* is obtained as follows. First, one assumes the k stations (in this case the 4 central ones) as pre-calibrated, and calculates δt_k^{CP} for each of them. Second, the space-time vectors of the k stations, (x_k, y_k, δt_k^{CP}), are fitted with a plane, obtaining the 3 CP parameters: A^{fit}, B^{fit} and $< dt_0 >^{fit}$. The final step consists of the estimation of the station time offset for all the array stations, Δt_j^{HYB}:

$$\Delta t_j^{HYB} =< \delta_j^{res} > +\delta t_j^{CP}(x_j, y_j | A^{fit}, B^{fit}, < \delta t_0 >^{fit}) \tag{3.7}$$

Figure 3.3 shows the results of the test: the distribution of the initial time offsets is shown on the left (figure 3.3(a)), while on the distribution of the station offsets after this full *Hybrid* calibration procedure is shown on the right (figure 3.3(b)). The method reduces almost to zero the time offsets ($r.m.s. \leq 0.1$ ns), fully removing the reconstruction mispointing as a consequence.

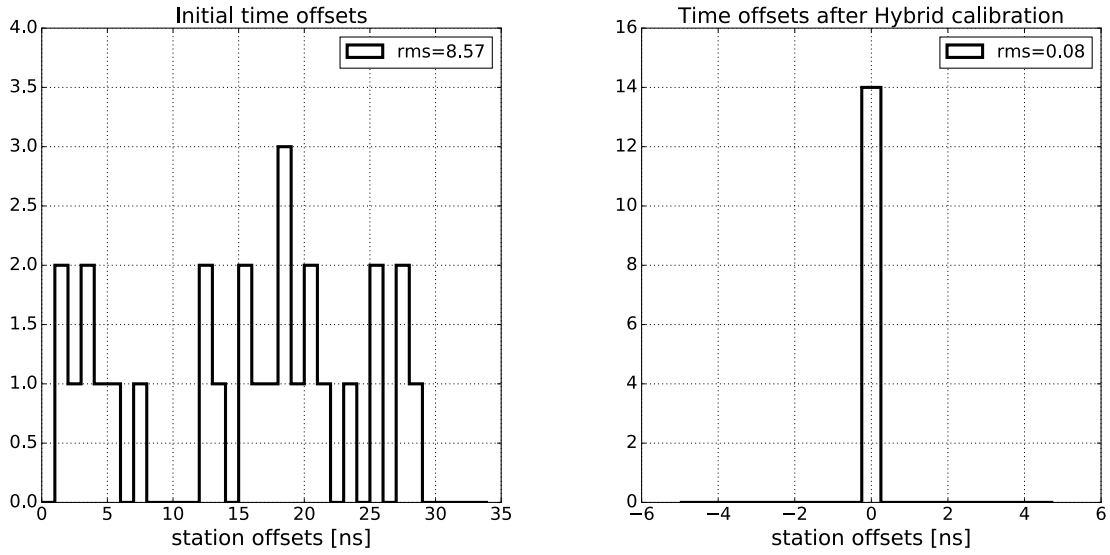

(a) (b)

Figure 3.3: Hybrid calibration test with the fast simulation. (a) Initial time offset distribution (uniform in [0 ns, 30 ns]). (b) Time offset distribution after the Hybrid calibration: final offsets are ~ 0.1 ns (compare with figures 3.1(a) and 3.2(b)).

Full EAS simulation. The second test consists on applying the *Hybrid* calibration method on a more realistic MC simulation, i.e. the standard HiS28 MC simulation described in section 5.4.1. The estimation of the station time offsets is performed following the same procedure used with the fast simulation. In particular, the *Residual correction* is obtained selecting only

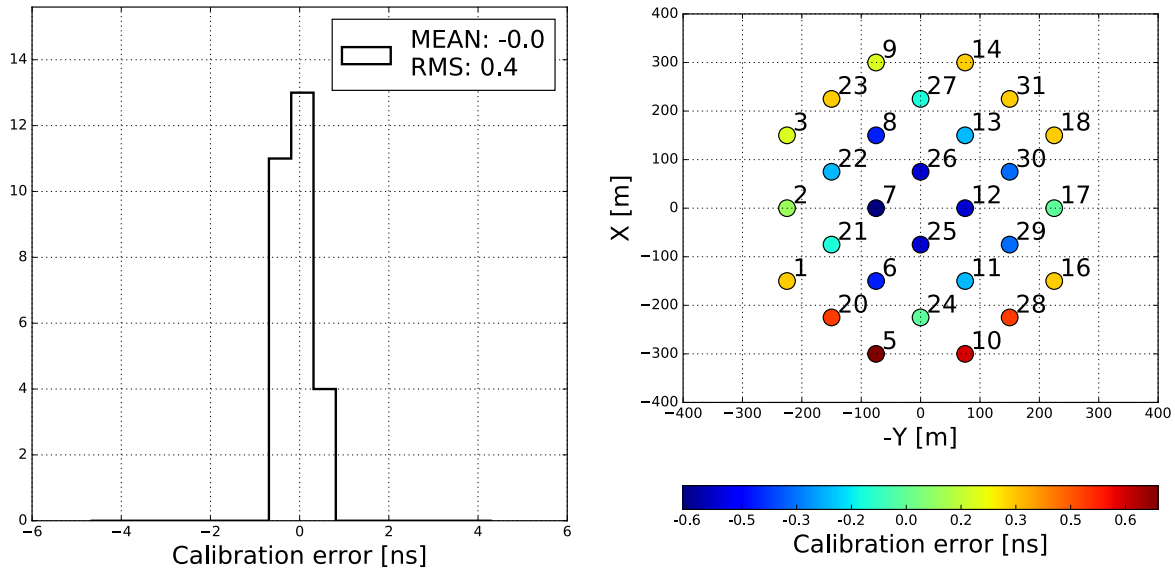

(a) (b)

Figure 3.4: Hybrid calibration with full EAS simulation. (a) Final time offsets distribution after Hybrid calibration. (b) Final time offsets distribution in the array. To be noted the radial trend discussed in section 3.1.2.

events with multiplicity ≥ 18.

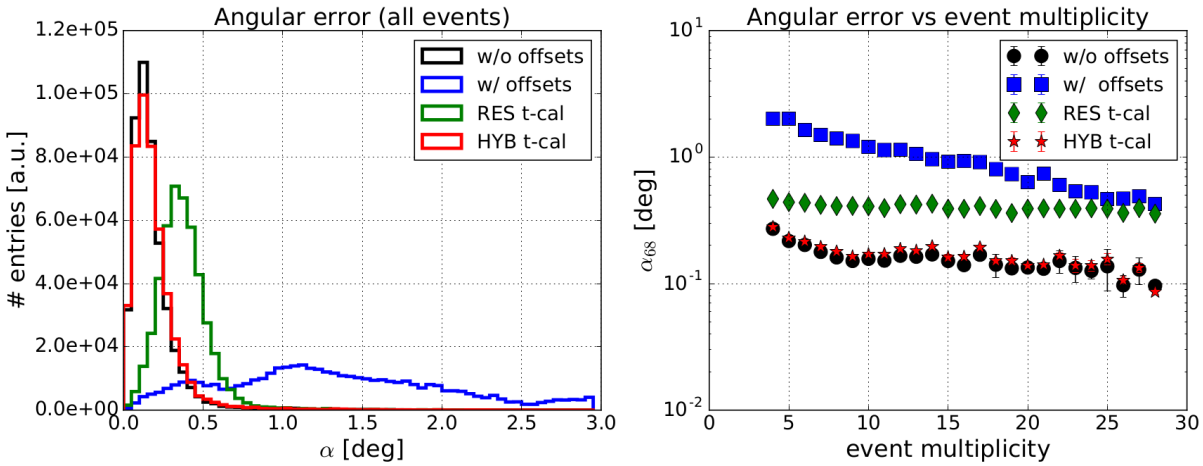

Figure 3.5: Effect of the different calibration steps on the angular error distributions (full EAS simulation). All events angular error distributions (left) and angular resolution, α_{68}, as a function of the event multiplicity (right), after applying different offsets corrections. Blue: uncorrected station time offsets. Green: after *Residual correction* - it only reduces the angular error at low multiplicity, but leaves a systematic mispointing uncorrected ($0.4°$ in this example). Red: Hybrid calibration - fully corrects the mispointing, reproducing the ideal case with no station offsets (black).

The results of this second test on the *Hybrid* calibration method are shown in figure 3.4. As for the Toy-MC, the station time offsets are almost reduced to 0 ($r.m.s. \sim 0.4$ ns, figure 3.4(a)), proving the high potential of the *Hybrid* method for EAS detectors time calibration. Figure 3.4(b) shows the final station time offsets distribution in the array: a radical improvement is achieved compared to the *Residual correction* (figure 3.2(b)), with the CP inclination almost fully removed. A small radial trend is visible, due to the presence of the neglected term $< \delta\omega_j >$. A systematic study on how $< \delta\omega_j >$ influences the time offsets correction is presented in section 3.2.2.

The effects of the different calibration steps on the arrival direction reconstruction are shown in figure3.5. The plot on the left shows the distribution of the angular error α for all reconstructed events, while the plot on the right shows the angular resolution, α_{68}, as a function of the event multiplicity. In blue are shown the distributions one obtains without correcting the station time offsets. The *Residual correction* (green) only reduces the angular error at low multiplicity, leaving uncorrected the systematic mispointing ($0.4°$ in this example) introduced by the initial time offsets, and represented by the inclination of the array CP. Only the Hybrid calibration (red) fully corrects the station offsets, removing the detector mispointing, and obtaining a reconstruction accuracy like for perfect detector timing calibration, i.e. for $\Delta t_j = 0$ (black).

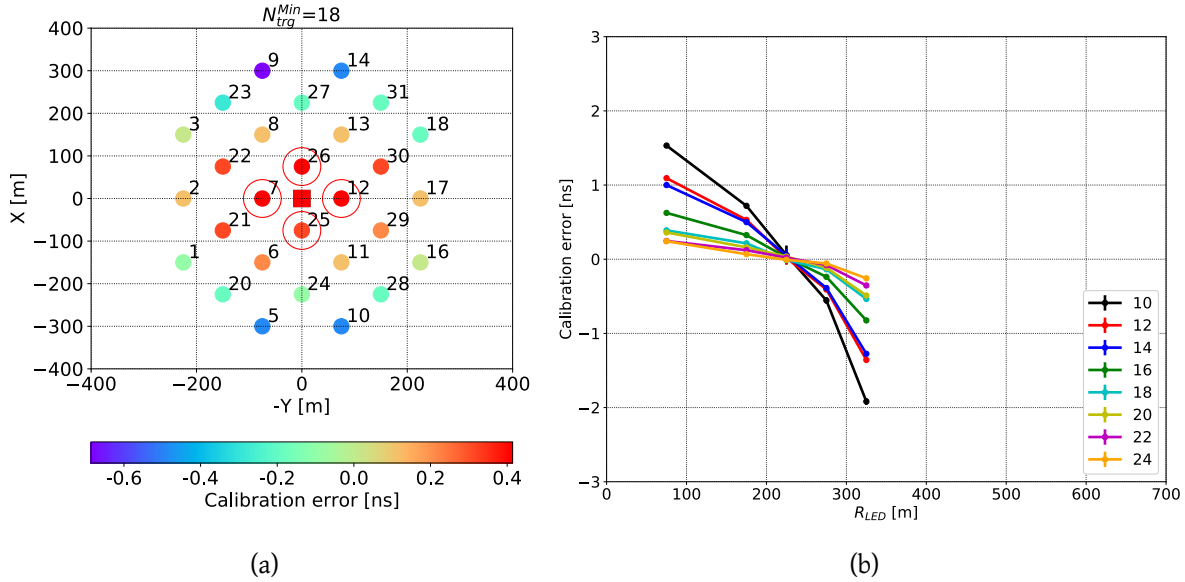

(a) (b)

Figure 3.6: Hybrid radial calibration error $< \delta\omega >= \Delta t^{true} - \Delta t^{HYB}$, as a function of the distance from centre of the pre-calibrated stations (red circles), located at the center of the array. (a) 2D distribution for $N_{trg}^{MIN} = 18$. (b) Radial distribution as a function of the distance from the pre-calibrated stations position (red square), for different values of N_{trg}^{MIN}.

3.2.2 Study of the HYB method systematics

The expression of the hybrid correction for station offsets, Δt_j^{HYB} is given by:

$$\Delta t_j^{HYB} =< \delta t_j^{res} > +\delta t_j^{CP}(x_j, y_j | A^{fit}, B^{fit}, < \delta t_0^{fit} >) > \tag{3.8}$$

Assuming precise external calibration Δt_k, and precise detector coordinates measurement x_j and y_j, the only source of error is represented by the *Residual correction* $< \delta t_j^{res} >$, that introduces a radial systematic error in the offsets estimation, $< \delta\omega_j >= \Delta t_j - \Delta t_j^{HYB}$, as shown using the full MC simulation in section 3.1.1. As the front curvature approximation is fixed (equation 2.15), the only variable parameter in the *Residual correction* is the minimum event multiplicity, N_{trg}^{MIN}, used for the event selection. In this small section, the systematic *Hybrid* calibration error, $< \delta\omega_j >$, is studied as a function of N_{trg}^{MIN}.

Figure 3.6 shows the results of a first test, using the 4 stations at the centre of the array as pre-calibrated. The plot on the left (figure 3.6(a)) gives the distribution of $< \delta\omega_j >$ over the array, for $N_{trg}^{MIN} = 18$, showing the same radial trend observed in 3.4(b). Figure 3.6(b) shows the average distribution of $< \delta\omega >$ as a function of the distance from the pre-calibrated stations, for different values of N_{trg}^{MIN}. It is clearly visible that the larger is N_{trg}^{MIN} the smaller is the error radial gradient, i.e. the difference between close and far stations errors.

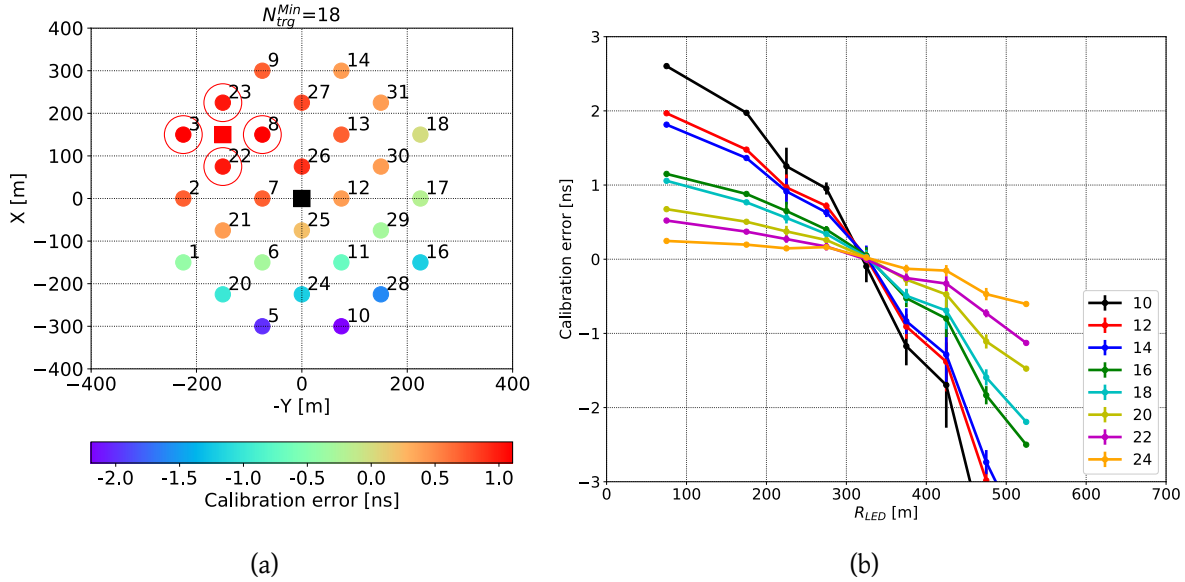

(a) (b)

Figure 3.7: Hybrid radial calibration error $< \delta\omega >= \Delta t^{true} - \Delta t^{HYB}$, as a function of the distance from centre of the pre-calibrated stations (red circles), located at the edge of the array. (a) 2D distribution for $N_{trg}^{MIN} = 18$. (b) Radial distribution as a function of the distance from the pre-calibrated stations position (red square), for different values of N_{trg}^{MIN}.

A second test is performed using 4 stations located in a peripheral position of the array as pre-calibrated. The results, presented in figure 3.7, show that the center of the radial trend corresponds to the average position of the pre-calibrated stations (red square), and not with the array centre (black square). As a consequence, for the same value of N_{trg}^{MIN}, the radial gradient is now larger compared to the previous test due to the larger distance in the array from the pre-calibrated stations. Nevertheless, the correlation large N_{trg}^{MIN} small gradient is confirmed, as shown in figure 3.7(b).

Figure 3.8 shows the $r.m.s.$ of the offset calibration error (left) and the residual mispointing (right) as a function of N_{trg}^{MIN}, obtained using central (black) and peripheral (red) pre-calibrated stations. The solid lines in figure 3.8(a) simply resume in terms of $r.m.s.$, the radial gradient observed in figures 3.6(b) and 3.7(b). A more interesting result is shown in figure 3.8(b). For the first case (central pre-calibrated stations, black), a constant α_{MIS} is observed, result of the symmetry w.r.t. the array centre. In the second case (red), a clear dependence is observe, with α_{MIS} getting smaller for large values of N_{trg}^{MIN}. The two tests converge to $\alpha_{MIS} < 0.05°$ for $N_{trg}^{MIN} \geq 20$.

The dashed lines show the results for the ideal case, without station time offsets (OFF $= 0$). As shown in figure 3.8(b), the calibration method introduces a small systematic mispointing when peripheral pre-calibrated stations are used. This effect is explained with the fact that, due to the EAS front approximation used, the *Residual correction* aligns the detector offsets on

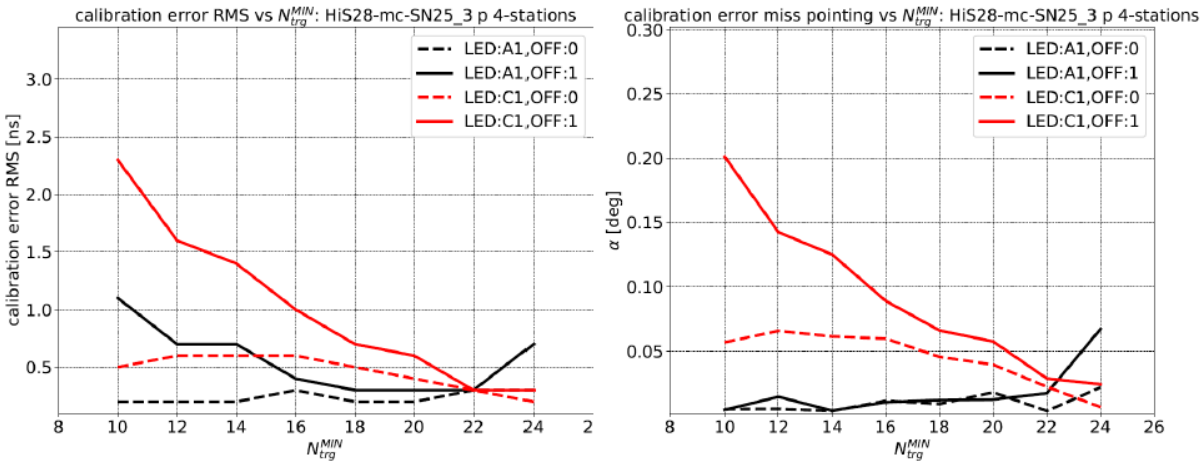

Figure 3.8: Hybrid calibration error distribution r.m.s (left) and residual mispointing α_{MIS} (right), as a function of N_{trg}^{MIN}. Black: central pre-calibrated stations location. Red: peripheral pre-calibrated stations location. The solid lines in both plots show the similar trends, confirming the direct correlation between the two different parameters. The dashed lines show the effect of the *Hybrid* calibration in the ideal case with no station time offsets (OFF $= 0$).

equation 3.8 and not on the plane defined by equation 3.6. Thus, when fitting the array CP using peripheral pre-calibrated stations, ones obtain an effect similar to the one obtained when fitting with a plane the EAS front of a EAS with the core outside the array.

In conclusion, the systematic tests performed on the *Hybrid* calibration method suggest to use a large number of N_{trg}^{MIN}, whether one is using central or peripheral pre-calibrated stations, with a preference for the first case, in order to minimize the error on the offset estimation and the residual detector mispointing.

3.3 Summary and conclusions

The precise estimation and correction of the station time offsets is a fundamental task in a ground based EAS Cherenkov arrays, in order to achieve optimal angular resolution and directional pointing precision. However, it is very difficult to perform a direct time calibration of the full detector at once (e.g. by using external light sources like LED) when dealing with large area arrays, making the task unpractical if frequent checks are required to monitor the detector conditions over time.

One solution is given by the self-calibration method, as developed and applied for ARGO-YBJ (Bernardini et al., 2005; Aielli et al., 2009). It allows precise calibration of all the array stations using EAS events detected during normal observation time, correctly removing the directional systematic mispointing. The method, based on the concept of array Characteristic Plane (CP)

(He et al., 2007), has the disadvantage of requiring an a priory knowledge of the distribution of the true arrival direction of the detected events, which is not always possible with the needed accuracy.

To overcome all these problems, the *Hybrid* calibration method was presented here, based on a different approach to the array CP solution for the *CP correction* estimation. Formally following the same mathematical procedure as the self-calibration, the *Hybrid* method combines information from EASs and external time calibration: the EASs are used for the *Residual correction*, while the *CP correction* is obtained using known pre-calibrated time offsets for only few array stations (≥ 3). A fast simulation was used to prove the method, obtaining a full reduction of the station time offsets. A more realistic EAS MC simulation was used to test the method on the HiS28 detector (including tilted stations), obtaining a reduction of the station time offsets below 1 ns.

Finally, one can concludes that the *Hybrid* time calibration presented here has a few advantages: (a) it does not rely on the a priori (and precise) knowledge of the detector acceptance, (b) it requires an external calibration only for a few array stations (≥ 4), and (c) it can be performed frequently and without too much effort. All this makes of the *Hybrid* method a good choice for calibration of upcoming large ground-based EAS Cherenkov arrays.

Chapter 4

TAIGA-HiSCORE 9

Following the first test in the field with three HiSCORE prototype stations during season 2012/13 (see section 2.1.2), the engineering phase of the HiSCORE detector development continued with the TAIGA-HiSCORE 9 array (HiS9), deployed and commissioned in October 2013.

As anticipated in section 2.2.2, HiS9 presents two different and independent data acquisition systems, DAQ-1 and DAQ-2, aiming to test different approaches in field to select technologies for the $1\,\mathrm{km}^2$ TAIGA array (section 2.1). Due to the short R&D period, a direct field evaluation was preferred to laboratory tests, since it also allowed to verify different essential components: station PMTs (including snow/ice proven conditions), slow control, long term timing stability under real Siberian field conditions ($-40 \ldots +30^\circ$ ambient temperature). Both DAQs are based on a DRS4 chip to digitize PMT signals, and use a custom-made time synchronization system (DAQ-1) and a standard Ethernet-based system (White Rabbit, DAQ-2). For both systems, HiS9 represented the first real on-field test.

This chapter focuses on the analysis of the data collected with DAQ-2. Section 4.1 introduces the HiS9 array, the DAQ-2 system, and the raw data processing. Section 4.2.1 presents the analysis of the data collected during calibration runs, performed using an external LED light source. The full EAS reconstruction, performed on the data collected during standard operations, is finally presented in section 4.2.2. The analysis allows to test the LED calibration and study the detector acceptance. Both LED and EAS analysis show a sub-ns time resolution achieved with the White Rabbit timing system.

4.1 HiS9 detector setup

The HiS9 consists of 9 HiSCORE prototype stations arranged in a 3×3 regular grid, with $150\,\mathrm{m}$ station spacing, for a total instrumented area of $0.09\,\mathrm{km}^2$. Figure 4.1(a) shows the HiS9 array inside the Tunka-133 installation, while a picture of the single detector station is given in figure 4.1(b), showing both the optical (left) and electronic (right) boxes. Each optical box is equipped with 4 PMTs of $20\,\mathrm{cm}$ diameter (Hamamatsu R5912), and presents the mechanical and electronical components as described in Chapter 2.

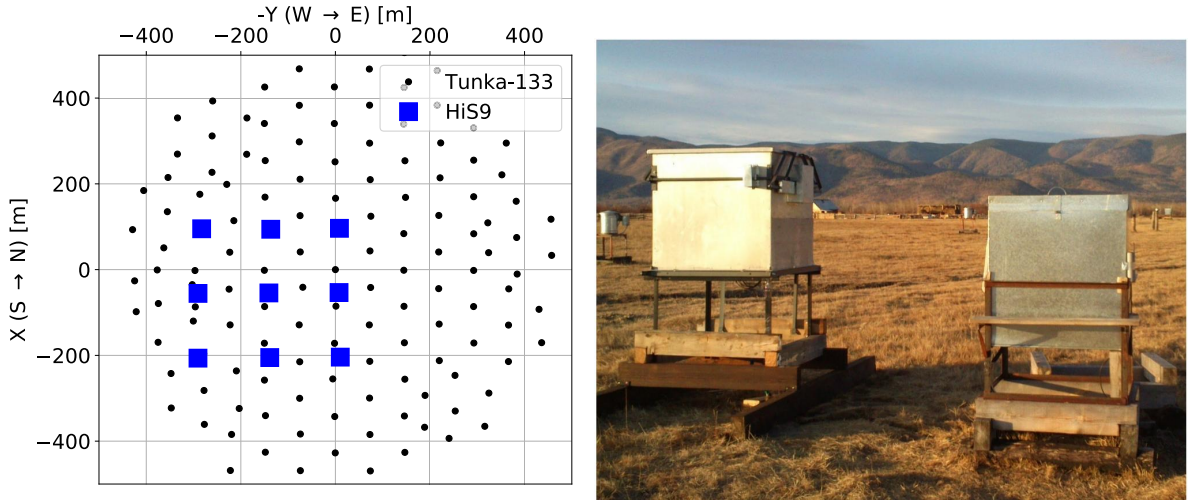

(a) (b)

Figure 4.1: (a) TAIGA-HiSCORE 9 (HiS9) array layout during observation season 2013/2014. (b) Picture of a HiS9 detector station showing the electronic box (right) and the taller optical box (left). The latter presents a double-lid mechanism, replaced by a more functional and stable single-lid mechanism in 2014/15 (see figure 5.1(b)).

The White Rabbit timing system (section 4.1.1) is at the base of the DAQ-2 system, described in details in section 4.1.2. One of the DAQ-2 goals is to prove the sub-ns station relative time resolution and synchronization needed to achieve the required angular resolution (figure 2.16).

4.1.1 The White Rabbit timing system

The White Rabbit system (WR) (Moreira et al., 2009; Serrano et al., 2013) is a fully deterministic Ethernet-based network for time synchronization, frequency and general purpose data transfer. Figure 4.2(a) gives a typical WR network setup, where up to 1000 nodes can be synchronized with sub-ns accuracy over fibre lengths of up to 10 km. The same fibre is used for synchronization and for standard Gigabit Ethernet (1000base-BX10) packet transportation. WR uses the SyncE standard for clock distribution, and the Precision Time Protocol to exchange information between the master and nodes. Thanks to the permanent phase shift correction, WR can easily compensate environmental (temperature induced) fluctuations.

An advantage of the WR system is that the core components, commercially available from several companies, are ready to use and ready to adapt to specific WR node functionalities. It is an open source project with access to all information necessary, and the big and active WR community has made the WR system a well debugged and calibrated system. The extensive usage and debugging of the WR-key components make it very reliable, in contrast to any

custom made synchronization/timing system, for which the amount of additional long-term verification is a huge time and cost factor.

All this gives to WR the potential to become a standard tool for modern large-scale astroparticle physics experiments, where time synchronization to nanosecond precision is required between up to thousands of data-acquisition (DAQ) stations.

WR system components The key component of the WR system is the WR Switch, which differs from standard Ethernet switches for its possibility to distribute the WR master clock (or its own clock if the switch is the master clock) over the network. The WRS-3/18 version used for HiS9 setup has 18 SFP connectors, see figure 4.2(b).

The WR SPEC (Simple PCIe FMC carrier) card is the commonly used WR node (figure 4.2(c)). Besides the FPGA (a Spartan-6), it features an SFP connector for the WR fibre link communication, and a USB terminal for timing and status information. The SPEC has a low pin count FMC (FPGA Mezzanine Connector). For the design discussed here, a 5 Channel Digital Input/Output FMC card (DIO5CH) is used and connected to this FMC port. The 5 channels are freely programmable as input or output, with an adjustable comparator threshold for incoming signals, and are used as PPS (Pulse Per Second) output(s), as trigger input or output, and as analog signal input in the setup developed for TAIGA-HiSCORE.

White Rabbit setup for TAIGA-HiSCORE 9. A detailed description of the WR setup developed at DESY for the TAIGA-HiSCORE detector is presented in (Brückner and Wischnewski, 2013). Here we present the main extension applied to the system in order to use WR for trigger time-stamping in HiSCORE. The SPEC FPGA-design was modified and allows now to

1. time stamp external digital trigger signals with ns-precision, and transfer the time-stamps and counter information via WR-fibre to the WR-master.

2. form the trigger decision on the WR-node by ns-sampling of an analog input signal, discriminated against a comparator threshold; generate a trigger after $\geq$ N consecutive ns-samples being above threshold (typically set to 9 ns); trigger signal time-stamping and transport, like for (1); additional DAQ-I/O signals (WR1/WR2, see section 4.1.2) are generated.

The clock performance (precision, resolution) of the modified WR setup were first tested in the laboratory. With a "table-top" setup, including climate chamber temperature tests (fibre: $-20... + 40°$C; SPEC: $0... + 30°$C) the basic timing precision (clock jitter) was measured to be better than $\sigma(WR) \sim 0.2$ ns, as well as an excellent stability of the nsec-trigger-stamping.

With the HiSCORE-3 prototype array (winter season 2012/13, see section 2.1.2) several WR-nodes were deployed in each station. The tests allowed to verify the clock phase stability and trigger stamping performance between different stations, and for independent (redundant) WR-nodes located inside a single station (Brückner et al., 2013). In particular, a "2 km-fibre

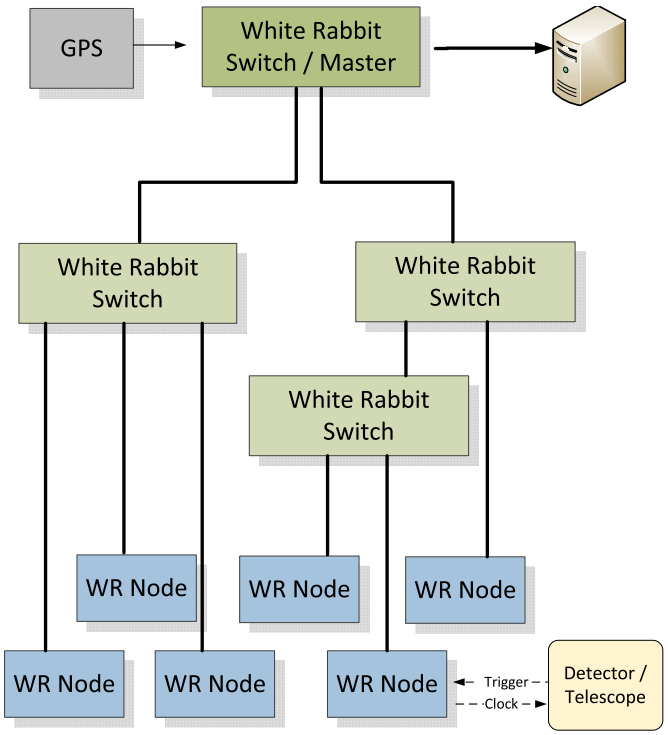

(a)

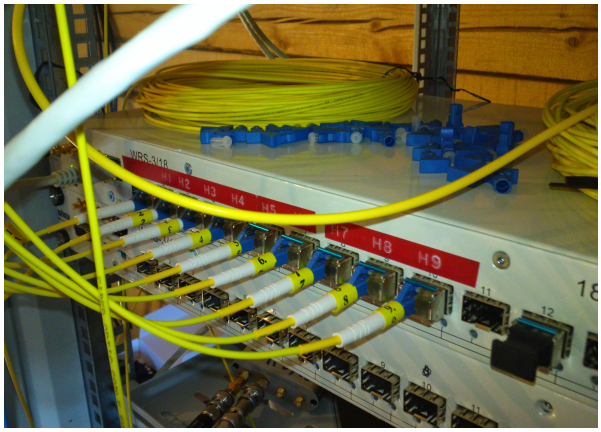

(b)

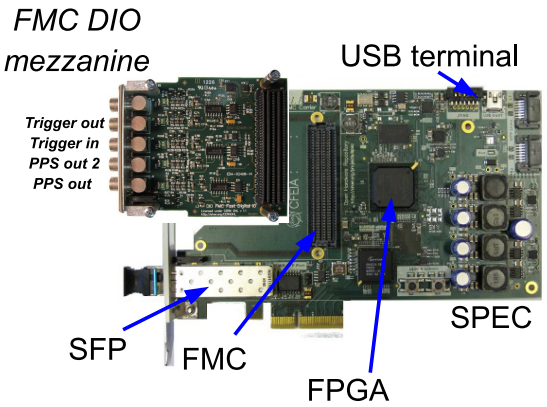

(c)

Figure 4.2: The White Rabbit system (WR). (a) Typical WR network made up of WR-switches (Grand Master and normal WRS) and of WR-nodes. The WR-nodes can deliver clock-signals to, and/or extract trigger time-stamps from the associated detectors, as symbolized for the lower-right WR-node. (b) WR switch and (c) WR SPEC card used for HiS9 (see also figure 4.4(b)). The precision time is kept on the FPGA, and synchronized through the fibre cable (SFP connector) to the master clock.

loopback setup" allows to study environmental and long-term effects. Here, the master WR-switch and a WR-node in the DAQ-centre are connected through a 2×1 km fibre to the far-away Tunka-23 station. Figure 4.3 shows the time difference between PPS pulses from the clock-master (WR-switch) and the WR-node, $\Delta T = T_{WRS} - T_{SPEC}$, for a typical run of 14 h, as measured by a DRS4-EB with 5 GHz sampling rate. The histogram (insert) shows the distribution of ΔT, with an extremely good (and close to the precision of the measurement) $r.m.s. < 0.2$ ns. A summary of all the experience with TAIGA-HiSCORE and the White Rabbit since 2012 is presented in Wischnewski et al. (2015).

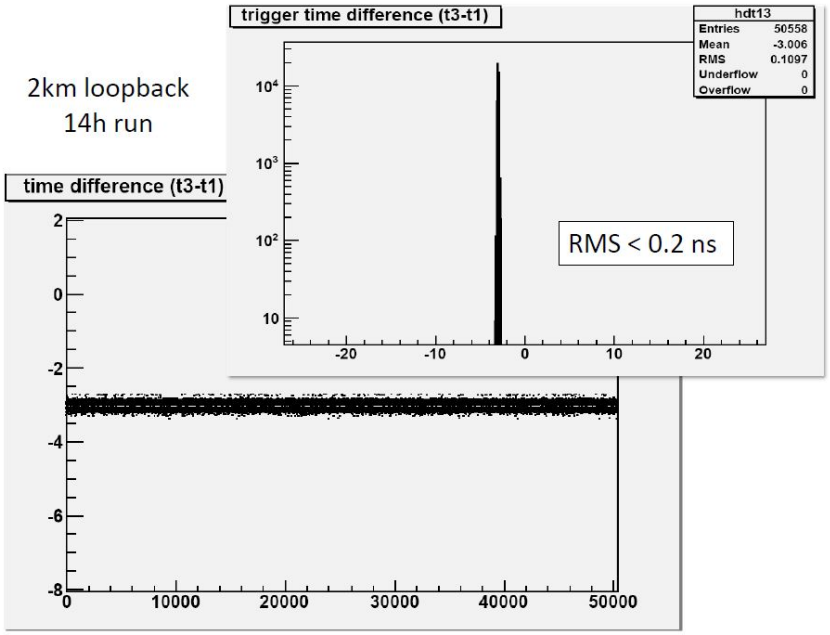

Figure 4.3: Time difference between PPS pulses from clock-master (WR-switch) and WR-node (SPEC), $\Delta T = T_{WRS} - T_{SPEC}$ (y-axis, in ns) for the 2 km fibre length, as a function of time (x-axis, in sec), for a 14 h run. The histogram gives the distribution with $r.m.s. < 0.2$ ns.

4.1.2 HiS9 DAQ-2 system

A scheme of HiS9 DAQ systems is shown in figures 4.4(a), with DAQ-2 represented by coloured boxes and DAQ-1 shown in grey at the bottom of the image, while a close picture of DAQ-2 setup inside the HiS9 electronic box is shown in figure 4.4(b). A description of the different DAQ-2 components and their function in the data acquisition logic is given in the following.

Pulse sampling. Two DRS4 evaluation boards (DRS (2018), blue boxes) are used for signal digitalization, allowing the sampling of a total of 8 input signals (4 channels each). One channel

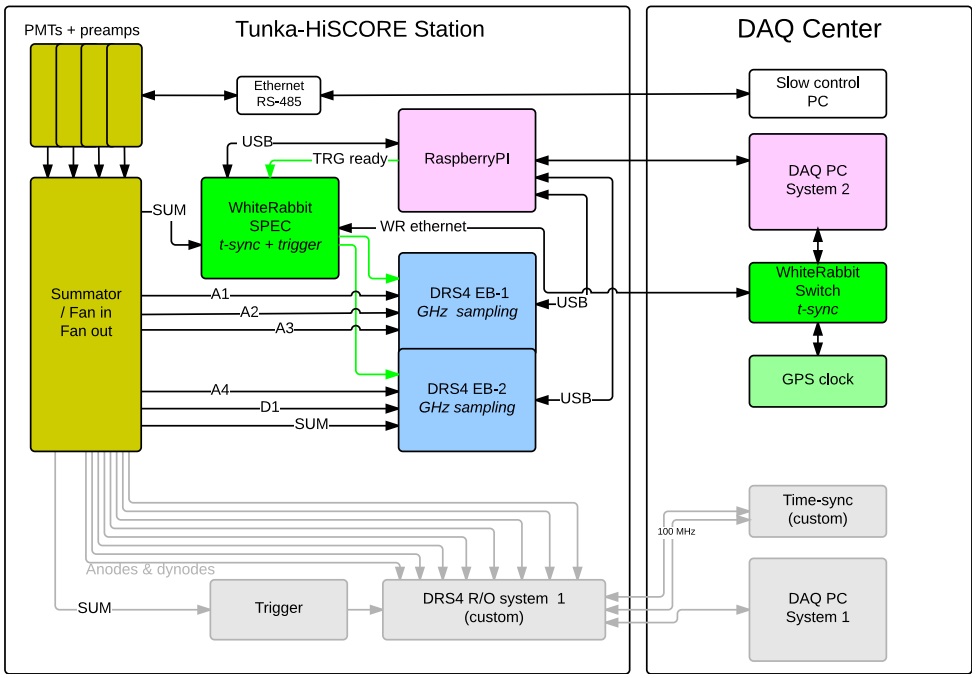

(a)

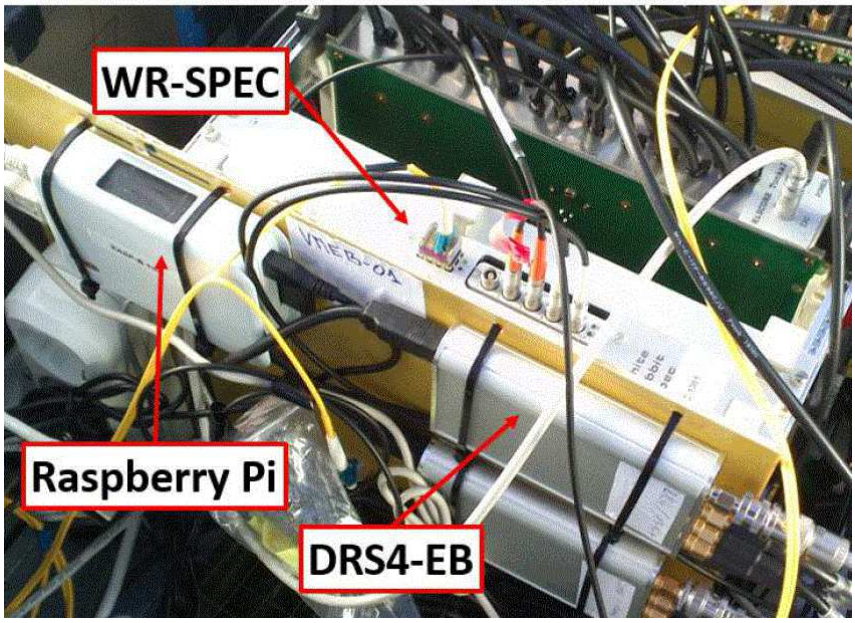

(b)

Figure 4.4: HiS9 DAQs. (a) Scheme of HiSCORE-9 data acquisition systems, DAQ-1 (grey) and DAQ-2 (colors). DAQ-2 is based on WR time distribution, a dedicated firmware DAQ on the WR-SPEC, and the commercial DARS4-EB board for digitization. The number of connections (arrows) is redundant, and does not reflect the real connections (3 cables) between stations and DAQ center. (b) Picture of DAQ-2 setup inside the electronic box.

per board is dedicated to WR trigger signal, while the remaining six channels are used to sample the PMT signals as follow: 4 PMT anodes, ($A1$, $A2$, $A3$, $A4$), the anode signals sum (SUM) and a PMT dynode ($D1$). All the input signals are digitized with a step of 1 ns in a 1024 bins buffer ($\sim 1\,\mu$s trace length). The DRS4 operates in unipolar mode from 0 V to +1 V. An example of a station event recorded with the two DRS boards is shown in figure 4.5.

Pulse triggering. The SUM signal produced by the summator (yellow box) is used as trigger signal. The SUM is sent to the WR SPEC (green box), where it is analysed by the DIO5CH comparator to check the trigger condition (SUM time over threshold ≥ 9 ns) with 1 GHz resolution. If the trigger condition is satisfied, a time stamp is produced and two output signals ($WR1/WR2$, figure 4.5) are sent to the two DRS4 boards. The WR SPEC-card carries the UTC clock, which is synchronized to the central WR-clock.

Data read-out. Once a trigger signal is issued, the signals read-out is managed by a RaspberryPI mini PC (RaspberryPI (2018), pink box), directly connected to DRS board and the WR SPEC. At the end of the read-out process, a signal (*TRG ready*) is sent to the WR SPEC to communicate that the system is ready for triggering and reading-out the next event. Besides this, the RaspberryPI is also used for remote system control, monitoring, and firmware update.

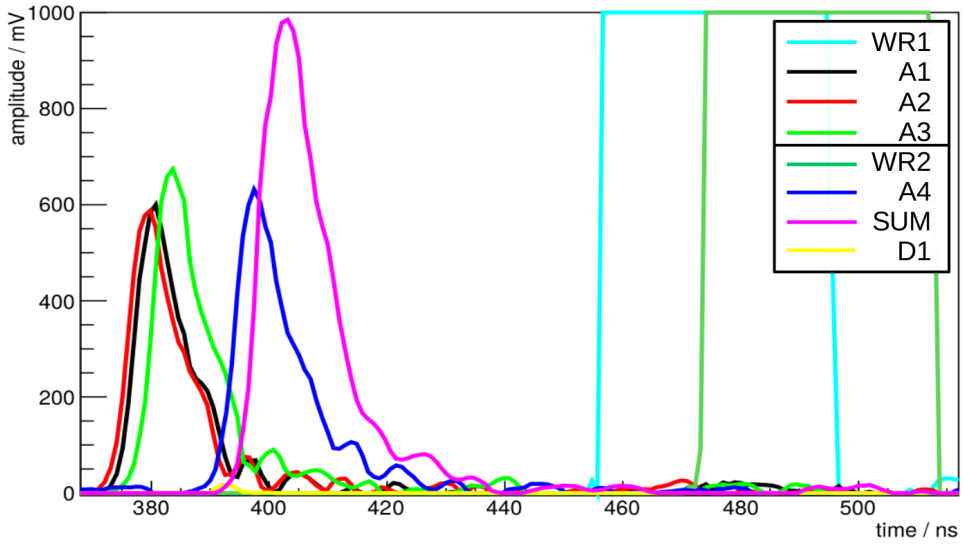

Figure 4.5: Example of HiS9 DAQ-2 station event traces recorded with the two DRS4 boards (legend boxes): 4 anodes channels ($A1$, $A2$, $A3$, $A4$), one anodes sum (SUM), one dynode ($D1$), and the two WR synchronization signals ($WR1/2$). The legend shows the two DRS boards setup. The time shift between the two WR pulses clearly shows the time misalignment between the two DRS4 boards (also visible between the Anode pulses from different boards). The 3 Anode pulses in board 1 (black/red/green lines) show the misalignment due to the time shift introduced by the single PMT.

4.1.3 Raw data processing

For each run, two different types of data files are produced by DAQ-2 during data taking operations. Nine binary files (one per station) containing all the traces recorded with the DRS4 boards, are stored in the DAQ center. The WR system produces one single ASCII file, containing the timestamps of the triggered events in all the array stations. A detailed description of the data processing and analysis of the 10 (9+1) data files is given in the following.

DRS data analysis. In this step all the 9 DRS output files are analysed. Each of the 8 signal traces recorded with the two DRS boards (6 PMT + 2 WR, figure 4.5) is analysed in order to extract the main pulse parameters (figure 4.6(a)) needed for the station event building, and the EAS reconstruction.

- **WR signal analysis:** Two parameters are extracted from the WR pulses: (a) the signal rise time, t_{WR}^{rise}, defined as the signal rise time at 500 mV, and (b) the pulse width, $FWHM_{WR}$. The rise time is needed to align the time of the two DRS boards, while $FWHM_{WR}$, equal to the time over threshold of the SUM signal, is needed to apply the pulse correction, δt^{pulse} (see later in the text).

- **PMT signal analysis:** The 6 PMT signals are analysed to extract the pulse amplitude, A_i, the edge time, t_i^{edge}, defined as the pulse rise time at $A_i/2$, and the trigger time, t_{SUM}^{trg}. Both t_i^{edge} and t_{SUM}^{trg} are obtained via interpolation.

Station event building. The station event is characterized by A_{SUM} and t_{SUM}, respectively the amplitude and time of the SUM signal. While A_{SUM} is directly obtained in the DRS data analysis, t_{SUM} is obtained by adding to the WR timestamp the pulse correction, defined as $\delta t^{pulse} = t_{SUM}^{edge} - t_{SUM}^{trg}$. The pulse correction introduces a fluctuation in the SUM pulse time measurement. An estimation of such fluctuation is obtained looking at the distribution of $t_{WR}^{rise} - t_{SUM}^{trg}$ (figure 4.6(b)). A Gaussian fit returns a time resolution of $\sigma_{DRS} \sim 0.34ns$.

It must be noted that, being SUM the output of the summator, it contains fluctuations coming from the misalignment of the 4 PMT pulses (see figure 4.5). Building a new anode signals sum pulse after correcting such misalignment, i.e. aligning the 4 PMT peaks at the same time, would reduce the fluctuation introduced by the pulse correction in the pulse time measurement.

Array event building. In this step, single station events are merged together into array events, in order to reconstruct and analyse the detected EASs. The photons arrival time difference between two stations is given by $\delta t = d\sin(\theta)/c$, with d the stations distance, θ the EAS inclination and c the speed of light. A time window $\delta t_{max} = 1.5\mu$ is used for building up the HiS9 array events, obtained for $d_{max} \sim 425$ m (HiS9 diagonal), and $\theta_{max} = 90°$ (horizontal EAS).

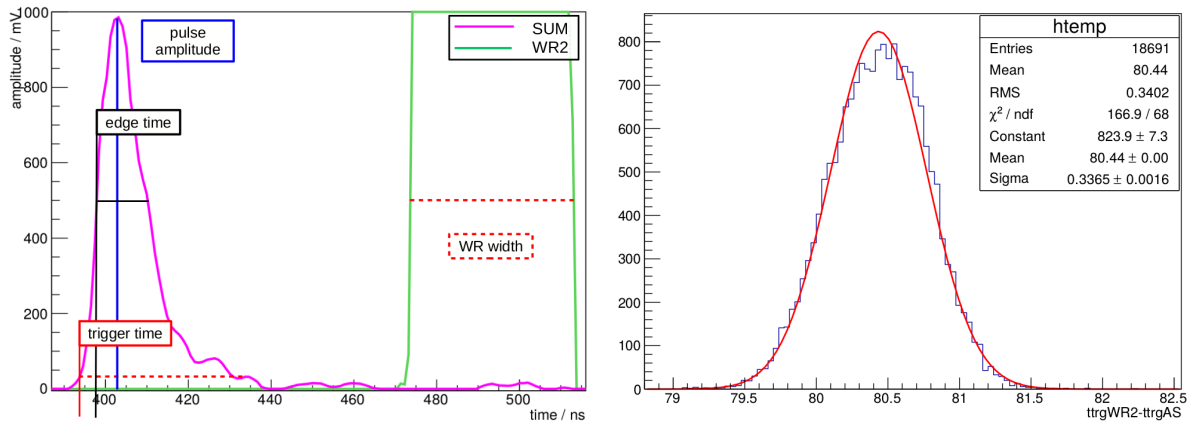

(a) (b)

Figure 4.6: (a) Pulse analysis. The WR width, $FWHM_{WR}$, equal to the time over threshold of the trigger signal (SUM), is used to determine the pulse trigger time, t^{trg}_{SUM}, and apply the pulse correction, $\delta t^{pulse} = t^{edge}_{SUM} - t^{trg}_{SUM}$. (b) single station $t^{trg}_{WR2} - t^{trg}_{SUM}$ distribution. The fitted width gives an estimation of the time fluctuation introduced by the pulse correction, $\sigma_{DRS} \sim 0.34$ ns.

Thanks to the precise and stable WR Master-Nodes synchronization, the merging is performed using only the WR time stamps, without taking into account additional time corrections, such as fibres transmission delays, etc. Figure 4.7 shows the array trigger for different event multiplicity (left), and event multiplicity distribution (right).

At the end of the event building step, an output ASCII file containing all the pulse informations extracted during the DRS data analysis is produced.

Run quality check. The array event rates is a simple and immediate way to check the stability of the detector performance during a run. Besides the mechanical and electronic station components, the main source of trigger rate instability comes from the environmental conditions in which the detector operates, e.g. clouds in the medium-low atmosphere above the detector. To reduce the impact of the weather conditions on the analysis of the detector performance, only runs with stable rates ($N_{trg} \geq 4$) are selected for the EAS reconstruction and analysis presented in section 4.2.2.

4.2 HiS9 data analysis

This section is dedicated to the analysis of the high level data obtained with the procedure described in the section 4.1.3. Two types of data are presented and analysed here: calibration run data (LED, section 4.2.1) and standard operation data (EAS, section 4.2.2). Both analysis are

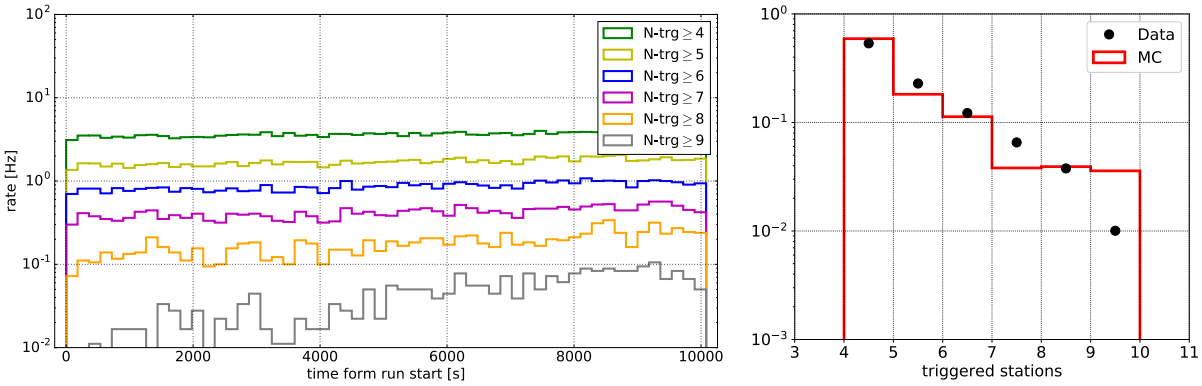

(a) (b)

Figure 4.7: (a) Array trigger rate for different event multiplicity. The rising rates for $N_{trg} \geq 8-9$ highlight the unstable behaviour of station 9 in this specific run. (b) Array events multiplicity distribution for data (black dots) and MC simulation (red line). The disagreement at large multiplicity ($N_{trg} \geq 7$) is mainly due to the non uniform array setup in the real experiment (number of PMTs per stations, HV, trigger threshold, etc.)

also used to estimate the single station time resolution, σ_t, described by the following relation:

$$\sigma_t = \sqrt{\sigma_{WR}^2 + \sigma_{DRS}^2 + \sigma_X^2} \tag{4.1}$$

where σ_{WR} is the time jitter due to the WR timing system, σ_{DRS} is the time fluctuation introduced by the DRS pulse correction (section 4.1.3), and σ_X is the contribution from all the other components that affect to the pulse time measurement.

4.2.1 LED time calibration

A series of calibration runs are performed using an external pulsed LED as light source. Thanks to the small size of HiS9 ($300\,\text{m} \times 300\,\text{m}$), all the stations are illuminated at once, allowing a full array calibration. The goal of the calibration is to determine the relative station time offsets, Δt_i, and check the single station time resolution, σ_t, on which the detector angular resolution depends (figure 2.16).

LED run setup and event selection. The LED calibration setup is given in figure 4.8(a). A bright wide-angle LED light source is positioned $\sim 100\,\text{m}$ outside the array perimeter, emitting light pulses with $\sim 6\,\text{Hz}$ frequency towards all the stations. Each station is equipped with a $45°$ inclined reflecting screen, to redirect the LED light into the optical box, as shown in the small insert in figure 4.8(a).

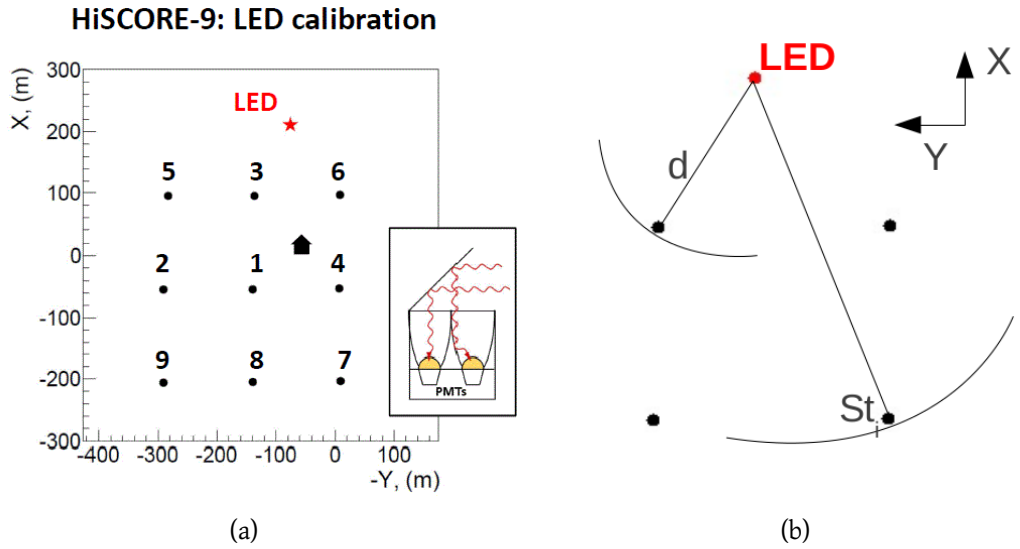

Figure 4.8: LED calibration: (a) HiS9 (black dots) LED calibration setup. Red star: LED source position. Black house: DAQ centre. In the insert, a sketch of the station setup for LED light collection, obtained with a 45° opaque mirror installed on top of the of the optical box. (b) Spherical model for LED light pulse propagation.

A total of 3 LED runs (see table 4.1) are selected for the analysis. The collected data is processed using the procedure described in sections 4.1.3. Figure 4.9(a) shows the typical station amplitude distribution: the Gaussian peak represents the LED light pulses ($\sim 80\%$), while the falling distribution comes from the EAS Cherenkov light pulses ($\sim 20\%$). Figure 4.9(b) present the typical array event multiplicity distribution obtained after the event building step ($1.5\,\mu$s time window). Selecting only events with $N_{trg} = 9$, one obtains a $\sim 100\%$ pure sample of events with only LED pulses (red lines in both figures 4.9).

Calibration procedure. Knowing the LED source position, $(x_{LED}, y_{LED}, z_{LED})$, and assuming a simple spherical model for the LED light propagation described in figure 4.8(b), the photon arrival time at the *i*-th station of coordinates (x_i, y_i, z_i), is given by:

$$t_i = \frac{1}{c}\sqrt{(x_i - x_{LED})^2 + (y_i - y_{LED})^2 + (z_i - z_{LED})^2} + t_0 = \frac{R_i}{c} + t_0 \qquad (4.2)$$

where t_0 is the emission time at the source, and c is the speed of light. The travelling time is then defined as $\Delta T_i = t_i - t_0$. Thus, a simple estimation of the *i*-th station time offset is obtained from the difference between the measured, ΔT_i^{EXP}, and the expected, ΔT_i^{CALC},

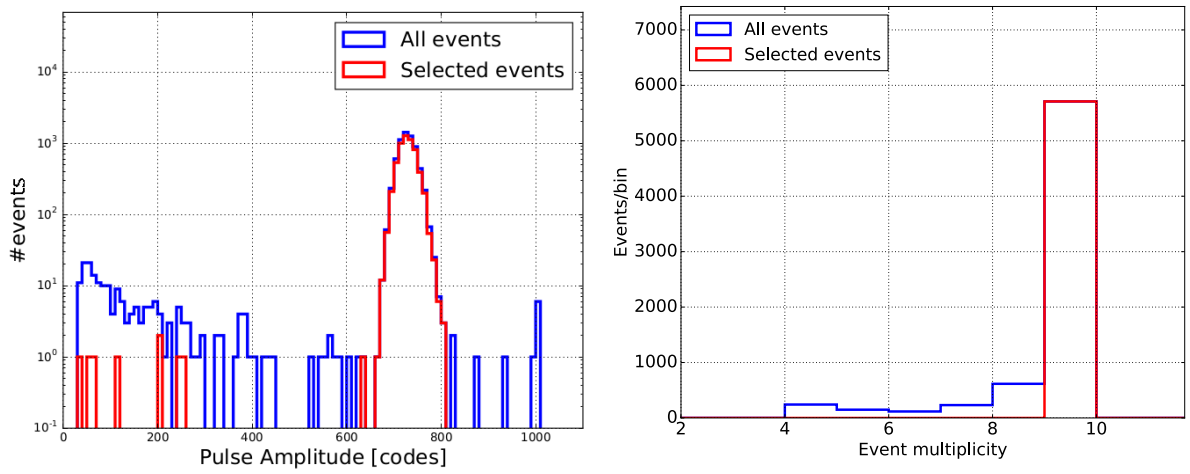

Figure 4.9: LED calibration: (a) Example of station amplitude distribution. In red the selected pulses after applying the multiplicity cut, $N_{trg} = 9$. (b) Array event multiplicity distribution for the LED calibration runs. Around 80% of the events have $N_{trg} = 9$.

travelling times:

$$\Delta t_i^{LED} = \Delta T_i^{EXP} - \Delta T_i^{CALC} = t_i^{EXP} - t_0 - R_i/c \tag{4.3}$$

Since t_0 is not known for any of the emitted LED pulses, all the station times need to be scaled with respect to a reference station, redefining the station time offsets as follow:

$$\Delta t_i^{LED} = t_i^{EXP} - t_{ref}^{EXP} - (R_i - R_{ref})/c \tag{4.4}$$

Using station 3 as reference station, the Δt_i^{LED} distributions are built for each array station. The result is shown in figure 5.9(a). A Gaussian fit of the distributions is performed, and the fitted means, $\mu_i(\Delta t^{LED})$, are used as an estimation of the station time offsets, Δt_i. The results of the HiS9 LED calibration are given in table 4.1.

The widths $\sigma_i(\Delta t^{LED})$ can be used to estimate the station time resolution, σ_t. Assuming the same time resolution in every station, and for an average value of $< \sigma(\Delta t^{LED}) >= 0.55$ ns, one obtains:

$$\sigma(t) \sim \sigma(\Delta t^{LED})/\sqrt{2} = 0.55/\sqrt{2} = 0.39\, ns \tag{4.5}$$

Using the expression given in equation 4.1, the estimated values for σ_t (0.39 ns, equation 4.5) and σ_{DRS} (0.34 ns, section 4.1.3), an upper limit for the WR system time resolution $\sigma_{WR} \leq 0.2$ ns is obtained.

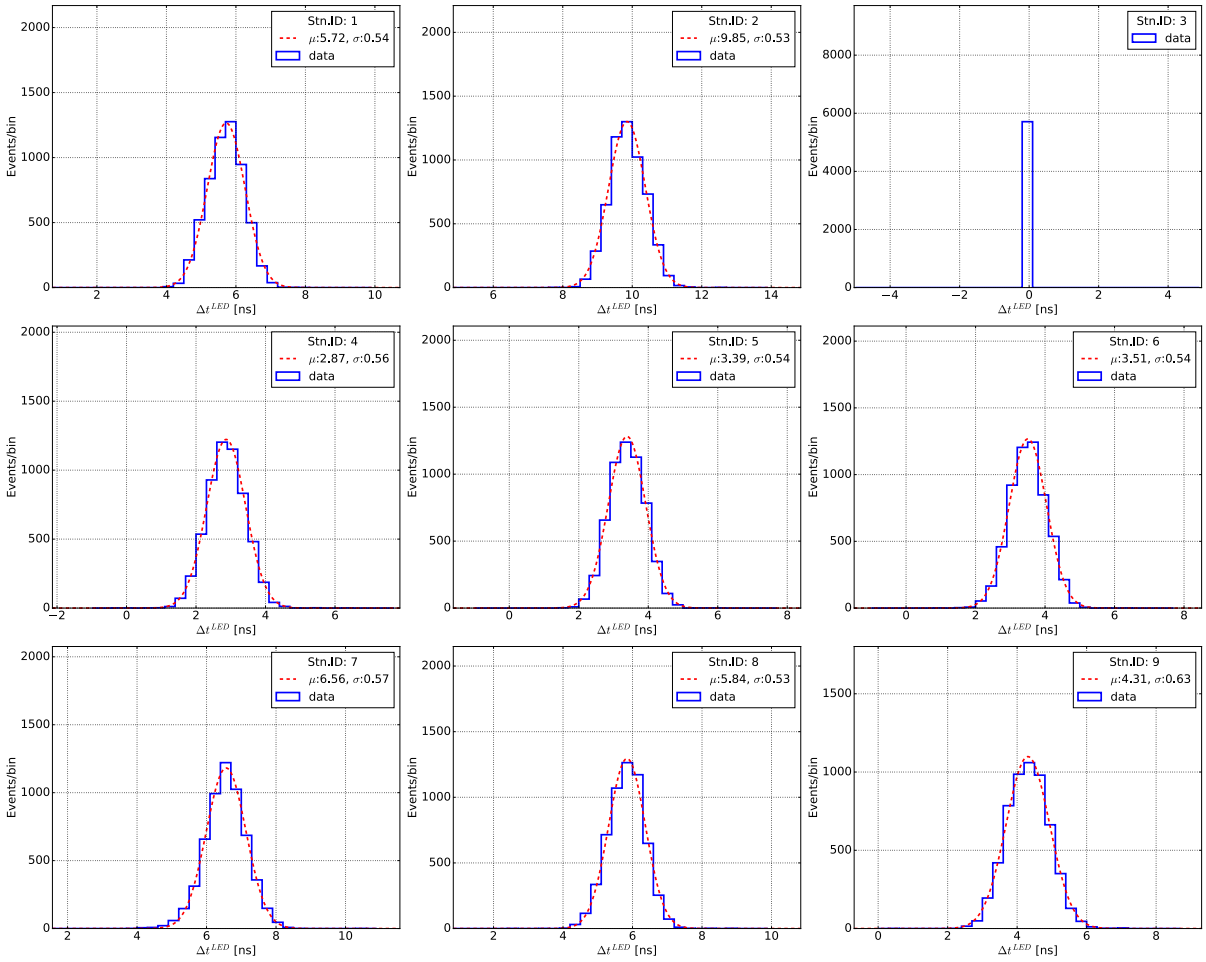

Figure 4.10: Δt^{LED} distributions. Station 3 is used as reference stations. Red line: Gaussian fit. The mean values are used as time calibration constants.

Run date	Station ID								
	1	2	3	4	5	6	7	8	9
25/02/2014-a	5.9	10.1	0.0	3.0	3.8	3.5	6.7	5.9	4.6
25/02/2014-b	5.8	10.1	0.0	2.9	3.8	3.4	6.7	5.9	4.5
07/03/2014	5.7	9.9	0.0	2.9	3.4	3.5	6.6	5.8	4.3
average	5.8	10.0	0.0	2.9	3.6	3.5	6.6	5.8	4.4

Table 4.1: HiS9 LED calibration constants Δt^{LED}. The last line shows the average values, used in the EAS event reconstruction presented in section 4.2.2.

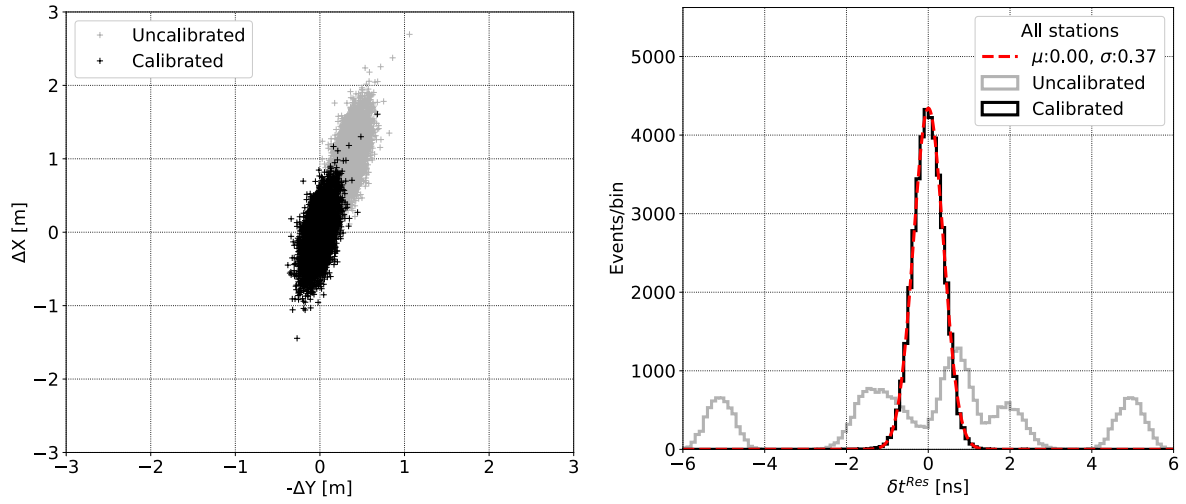

(a) (b)

Figure 4.11: HiS9 LED source reconstruction. (a) 2D distribution of the error on the reconstructed LED coordinates. (b) Residual fit distribution. In both figures, the calibrated data (black) is nicely distributed around 0, while the uncalibrated data (grey) presents systematic shifts, as expected.

LED position reconstruction. In order to test the correctness and the consistency of the calibration results, the LED source position is reconstructed. The calibrated station times are fitted with the spherical model described in eq. 4.2, using a least squares method. For simplicity and also to stabilize the fit procedure, only 3 (out of 4) parameters are let free in the fit procedure: X_{LED}, Y_{LED} and t_0.

Figure 4.11 shows the results of the reconstruction. The black crosses in figure 4.11(a) represent the 2D distribution of the errors on the reconstructed LED coordinates, ΔX_{LED} and ΔY_{LED}. The distribution is well centred around zero, proving that the calibration method works in the correct way. Also the fit residuals in figure 4.11(b) (black line) nicely reproduce a Gaussian distribution well centred around 0. The width of the residual distribution also gives an estimation of the station time resolution, $\sigma(t) = 0.37$ ns, in agreement with that obtained in the calibration procedure.

For comparison, the results obtained without applying the time calibration constants are also shown in grey. The systematic shift observed in the source position is the analogue of the systematic mispointing one obtains in the EAS arrival direction reconstruction due to the presence of the station time offset (as discussed in chapter 3). The residual distribution looks distorted, with the different peaks belonging to different stations.

It must be pointed out that a simple *Residual correction* (section 3.1.1), i.e. estimating the station time offsets from the residual distributions, would only reproduce the correct (black) residual distribution in figure 4.11(b), leaving the grey distribution in figure 4.11(a) the same,

thus without any effect on the wrongly reconstructed LED position.

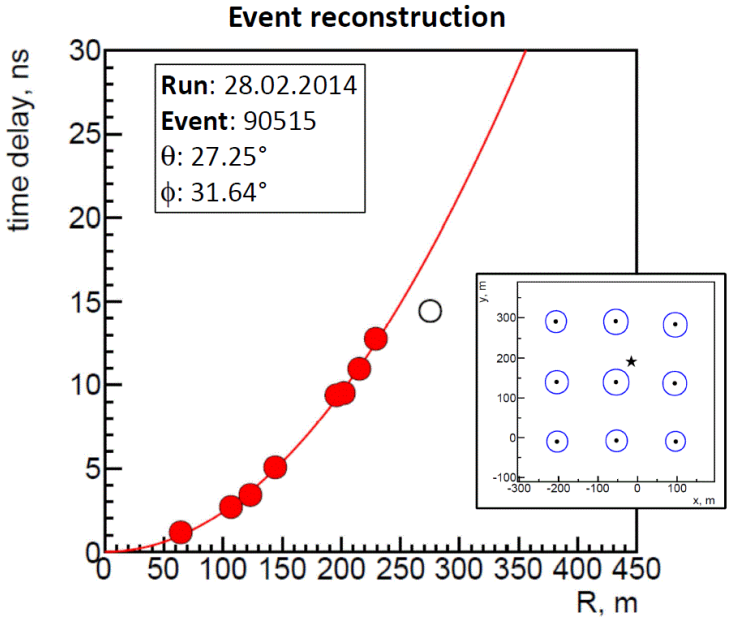

Figure 4.12: Example of reconstructed HiS9 EAS event. Main plot: shower front arrival arrival time profile fit for shower direction reconstruction. The full (empty) circles are the station times used (rejected) in the reconstruction procedure, as a function of the distance from the EAS axis. Red line: fitted EAS front curvature using the VIC model (equation 2.16). Small insert: reconstructed shower core location by using the LDF model (black star); the blue circles radius are proportional to the pulse amplitude.

4.2.2 EAS reconstruction

This section is dedicated to the reconstruction and analysis of the EASs detected with the HiS9 array. The main goal of the analysis is the overall proof of the quality of the data set and consistency with expected EAS properties. The WR timing system performance are also checked by means of EAS reconstruction, similarly to what has been done with the LED runs. The EAS reconstruction is performed using the methods introduced in section 2.4. The selected data sample consists of 13 clear night sky runs, for a total of ~ 40 h of observation, taken between the end of February and the beginning of March (same period of the LED runs).

An example of a HiS9 reconstructed event is given in figure 4.12. After the preliminary reconstruction (section 2.4.2), the accurate EAS core reconstruction is performed fitting the station amplitudes with the LDF model (equation 2.11), limiting the event multiplicity to a minimum of 6 triggered stations. No array amplitude calibration was yet available at the moment of this analysis, affecting the accuracy of the core reconstruction. The arrival direction is obtained fitting the pulse times with the VIC model (equation 2.16). Before reconstruction,

the station times are corrected using the LED calibration obtained in section 4.2.1. A dedicated simulation for HiS9 is performed for a data-MC comparison of the reconstructed parameters distributions (section 2.3).

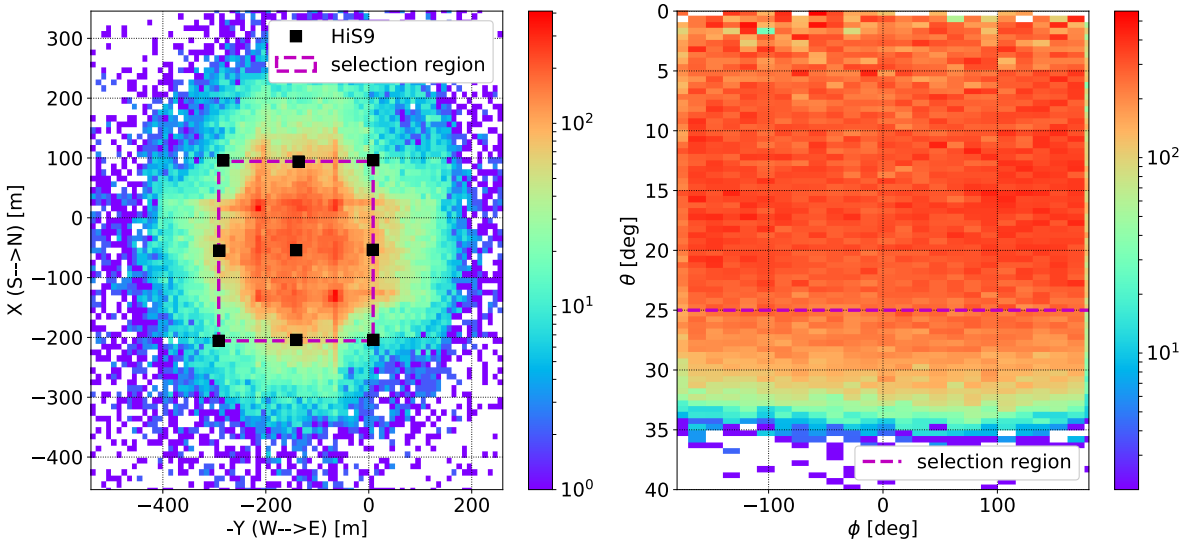

Figure 4.13: HiS9 detector acceptance. Left: 2D distributions for the reconstructed EAS cores. The non uniform core distribution (e.g. in the South-West corner of the array) reflects the non uniform setup of the HiS9 array (see text for more details). Right: 2D distribution of the reconstructed arrival direction angles. Each event is weighted with $w = 1/(\sin\theta\cos\theta)$. The purple dashed lines define the acceptance cuts for the reconstructed cores (inside the array perimeter) and arrival directions ($\theta \leq 25°$).

Detector acceptance. Figure 4.13 shows the detector acceptance for the reconstructed EAS cores (left) and arrival directions (right).

The non uniform distribution of the EAS cores (low density in the South-West corner of the array) reflects the non uniform array setup: different number of active PMTs in the stations, different trigger thresholds, missing amplitude calibration. To reduce the error in the arrival direction reconstruction, only events with core inside the array perimeter are selected.

A flat and uniform distribution up to $\theta \sim 30°$ is obtained for the distribution of the reconstructed EAS arrival directions, with the events weighted $1/(\sin\theta\cos\theta)$. The differential detector acceptance along θ and ϕ are shown in figure 4.14, showing a very good agreement between data and MC expectation. In particular, a direct correlation is observed between the reconstructed θ distribution and the WC acceptance (figure 4.14(a)), with a cut-off observed at $\theta \geq 25°$. This directly affects the reconstruction precision (Hampf, 2012), requiring a cut at $\theta = 25°$. A small modulations in ϕ is observed (figure 4.14(b)), probably due to the non uniform detector setup.

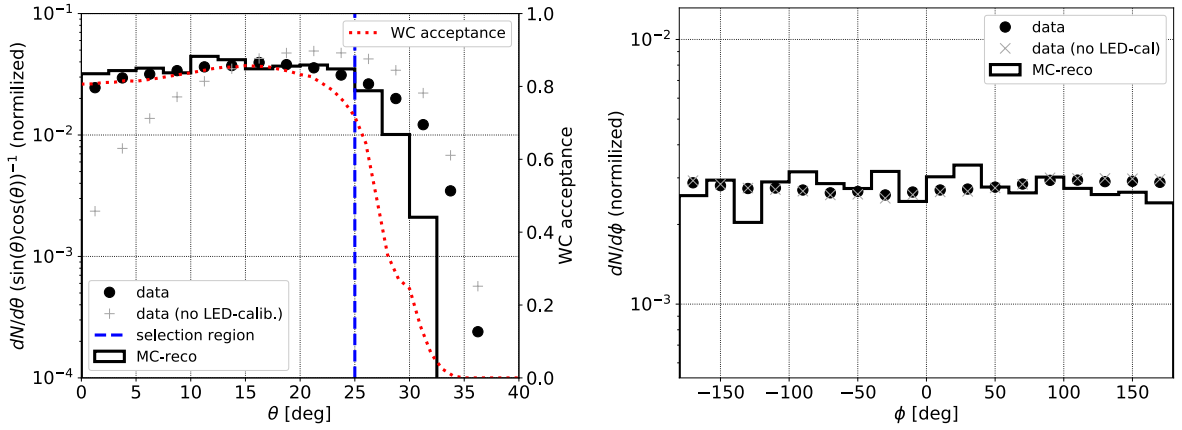

(a) (b)

Figure 4.14: HiS9 detector acceptance: reconstructed EAS θ (a) and ϕ (b) arrival angles, showing a good agreement between data (black dots) and MC expectations (black line). The selection cut at $\theta = 25°$ (blue dashed line) is based on the low Winston Cone (WC) acceptance (red dotted line) at $\theta \geq 25°$. Grey crosses: reconstruction performed without calibrated station times (no LED calibration). The θ distribution is peaked at large values as expected (Elo and Arvela, 1999a,b,c).

Station time resolution. The direction fit residuals distribution for all the reconstructed events is shown in figure 4.15. Again, a good agreement is observed between data and MC, with the Gaussian fit of the data returning a sub-ns station time resolution, $\sigma_t = 0.57$ ns. According to equation 4.1, this gives an upper limit for WR time resolution, $\sigma_{WR} \leq 0.45$ ns. While this result is larger than the one obtained with the LED run analysis ($\sigma_{WR} \leq 0.2$ ns.), it must be noted that the EAS analysis contains additional source of errors like the core reconstruction resolution (made even larger by the missing amplitude calibration) and the EAS front approximation used for the direction reconstructions (equation 2.16).

LED calibration check. Figures 4.14 and 4.15 show a good agreement between data and MC. For comparison, the distributions obtained with uncalibrated data (no LED time calibration) are also given in grey, proving the correctness, and most important, the need for a correct array time calibration.

The uncalibrated data distributions show the typical effects due to the presence of uncorrected station time offsets, such as the the expected reconstructed θ angle distribution peaked at large values (figure 4.14(a)), and the broad multi-peaks residuals distribution (figure 4.15). While a modulation in ϕ is also expected, both calibrated and uncalibrated data show almost the same modulation (figure 4.14(b)), leading to the conclusion that the observed modulation

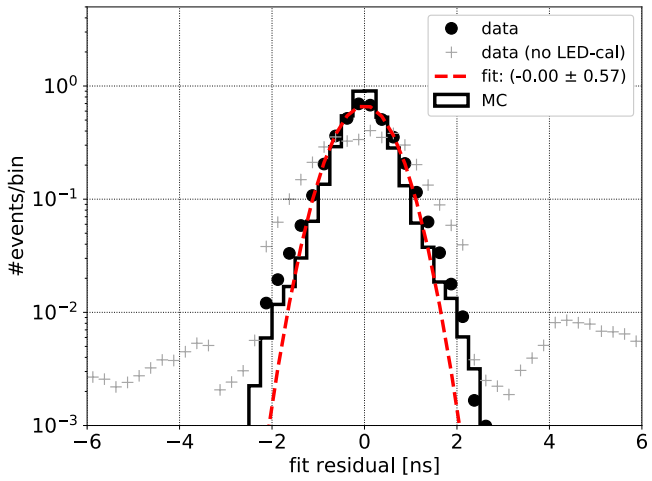

Figure 4.15: Arrival direction fit residuals distribution (all stations, VIC model), showing a good agreement between data (black dots) and MC expectation (black line). A Gaussian fit of the data (red dashed line) returns a station time resolution $\sigma_t = 0.57$ ns, resulting in an upper limit for WR time resolution, $\sigma_{WR} \leq 0.45$ ns. Grey crosses: distribution obtained using uncalibrated times in the EAS direction reconstruction.

is mainly due to the non uniform detector acceptance, direct consequence of the non uniform array setup.

4.3 Summary and conclusions

This chapter presented the TAIGA-HiSCORE 9 detector array, successfully operating during winter season 2013/14, and representing the engineering phase of the TAIGA-HiSCORE detector development. The analysis focused on one of the two DRS4-based data acquisition system deployed, DAQ-2, devoted to test the White Rabbit timing system. DAQ-2 consisted on the first field setup for astroparticle physics based on the White Rabbit timing system, used for station event time stamping and inter-station time synchronization.

The full raw data processing and analysis is described, showing a contribution to the station time resolution of ~ 0.34 ns coming from the DRS pulse analysis.

A detailed analysis of the calibration runs, obtained using an external LED light source, was performed. A calibration method for the determination of the station time offsets was tested, and proved to correctly work by reconstructing the LED source position (also afterwards by reconstructing the EAS directions). The analysis also allowed to check the single stations subnsec time resolution, $\sigma_t^{LED} \sim 0.4$ ns, from which an upper limit for the White Rabbit timing system time resolution of $\sigma_{WR}^{LED} \leq 0.2$ ns is obtained.

The last part of the chapter reported the results of the EAS reconstruction, performed on the data collected during standard operations. Despite the limited precision of the EAS core reconstruction due to the small array size, a very good agreement is observed when comparing the detector acceptance for the reconstructed directions with MC expectation. In particular, the direct correlation between the Winston Cone acceptance and the reconstructed θ angle distribution is confirmed, including the cut-off at $\theta \geq 25^{\circ}$. The analysis of the direction fit residuals confirmed the overall sub-ns station time resolution, $\sigma_t^{EAS} = 0.57$ ns ($\sigma_{WR}^{EAS} \leq 0.45$ ns). From MC simulations an angular resolution of 0.1° is expected at the highest energies for this station time resolution (figure 2.16).

The results and the experience with the HiSCORE stations obtained with the successful TAIGA-HiSCORE 9 campaign opened the way for the TAIGA-HISCORE 28 array (chapter 5), first step of the $1\,\mathrm{km}^2$ TAIGA array, aiming at hybrid IACT + HiSCORE operations.

Chapter 5

TAIGA-HiSCORE 28

After the successful HiSCORE 9 campaign in 2013/14, the TAIGA-HiSCORE array was extended up to 28 stations (HiS28) in autumn 2014, first phase of the $1\,\mathrm{km}\,2$ TAIGA array introduced in section 2.1. Figure 5.1(a) shows the HiS28 detector geometry, with $\sim$106 m stations spacing, and a total instrumented area of $\sim 0.25\,\mathrm{km}^2$. The reduced station spacing (150 m in HiS9 and original MC setup) is meant to lower the detector energy threshold below 100 TeV. Each station optical box (figure 5.1(b)) is equipped with 4 large-area PMTs of 20 cm (Hamamatsu R5912 and EMI ET9352KB) or 25 cm (Hamamatsu R7081) diameter, and is tilted by 25° southward to increase the detector exposure to the gamma-ray flux from the Crab nebula. Since 2015, the HiS28 detector is working in stable operation.

This chapter will presents the results of the analysis performed on the data collected with HiS28 during three observation seasons, form fall 2015 to spring 2017/18. An introduction to the hybrid HiS28 DAQ system is given in section 5.1, while the description of the data processing chain is given in section 5.2. Section 5.3 is dedicated to the array time calibration: a preliminary calibration method used for HiS28 is here discussed and compare with LED calibration (also used to check single station performance). The hybrid time calibration method described in chapter 3 is also applied here, compared to a preliminary and LED calibrations, and proposed as standard calibration procedure for HiS28 and future (larger) TAIGA-HiSCORE arrays. The last section (5.4) is dedicated to the EAS reconstruction (core and arrival direction), comparing the main results with MC predictions. The chessboard method is finally used to verify HiS28 detector angular resolution.

5.1 HiS28 DAQ system

This section shows the basic features of the HiS28 DAQ system, with a focus on the main upgrades with respect to the HiS9. As shown in figure 5.2, the HiS28 DAQ system is composed of two main parts: the *Central DAQ*, located in the data centre, and the *Station DAQ* in the electronics box. These two parts are interconnected by single mode optical fibre of different length, depending on the station distance from the main building. Each HiS28 station is operating

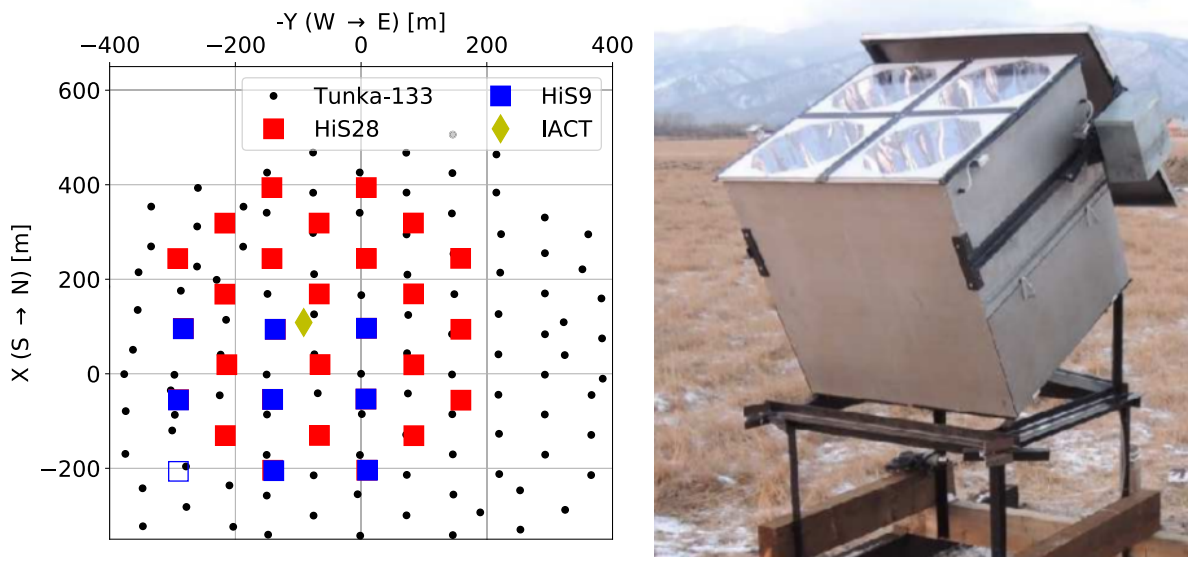

(a) (b)

Figure 5.1: (a) TAIGA-HiSCORE 28 (HiS28) array geometry, with $\sim$ 106 m station spacing, for a total instrumented area of 0.25 km^2. Red squares: new 20 HiSCORE stations (fall 2014/15). Blue filled squared: old HiS9 stations. Green diamond: first TAIGA-IACT (2017). (b) Picture of a HiS28 station optical box presenting the new single-lid mechanism, and tilted by 25° southward to increase the Crab exposure.

independent from all other stations.

The most relevant upgrade with respect to HiS9 is the new DRS4-based DAQ unit inside the *station DAQ*, integrating in one solution the main features of the two HiS9 DAQs, as shown in figure 5.3(a). Due to key importance of precision station timing, it was decided to build a hybrid station timing system, made of the two timing systems tested with HiS9: the custom timing system in DAQ-1 (TimeSyst-1), and the White Rabbit timing system in DAQ-2 (TimeSyst-2). As shown in figure 5.2, both systems are driven by independent central GPS clocks.

5.1.1 DRS4 board

The main component of the Station DAQ unit is the DRS4 board (blue box in figure 5.2), used for signal sampling, trigger, and digitization.

Signal sampling. The DRS4 board is equipped with 9 input channels. Two signals from each PMT (anode and 5^th dynode) are sampled at 2 GHz, for a total of 8 channels. The anode and dynode channels are amplified with a factor of 30 and 4 respectively. The 9^{th} channel of the DRS4-based readout board is used for sampling the 100 MHz clock signal distributed over optical fibre from the central DAQ to each array station, and used for time synchronization. The

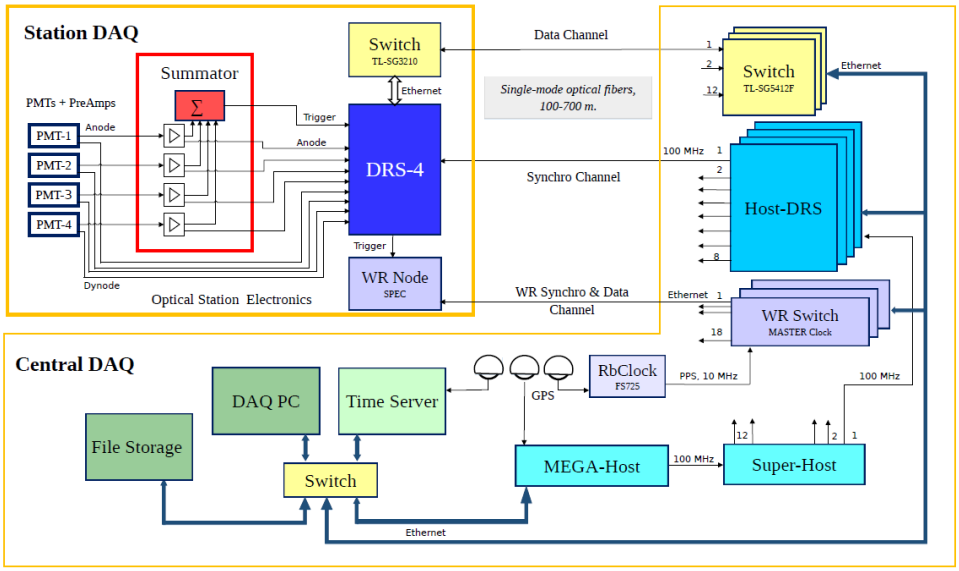

Figure 5.2: Scheme of the HiS28 DAQ system, composed by the *Central DAQ*, connected via optical fibres to the *Station DAQ* inside all array stations. The hybrid DAQ combines (see also in picture 5.3(a)) in the *Station DAQ* two timing systems: the custom DRS4-based (blue box) timing system (TimeSyst-1, light blue boxes), and the White Rabbit timing system (TimeSyst-2, grey boxes).

DRS-4 board has a 14 bit amplitude resolution and an input signal range of ± 2 V by each channel. Data are read out using an Ethernet interface to the DRS-4 board and sent via optical fibre link to a Central DAQ PC.

Signal trigger. An external analogue summator board (red box in figure 5.2) sums up the 4 anode signals, used for station trigger. A station trigger is issued if the analogue sum stays above a programmable threshold value for about $3 - 5$ ns (depending on the station configuration), starting the read out of all DRS4 channels. The analogue sum of the 4 PMT anodes allows a reduction of the NSB induced trigger rate, compared to single PMT triggering. This allows to work at lower energy threshold.

5.1.2 Time synchronization

TimeSyst-1 (Custom-DRS). A custom timing system (light blue boxes in figure 5.2) distributes a 100 MHz clock signal (Synch) to every station in the array. The Synch signal is sampled in the 9th DRS4 channel, and read out together with the 8 PMT signals. The Host-DRS is synchronization unit for all optical stations, providing a stable over run time station synchronization of ≤ 1 ns. MEGA-Host is the unit that keeps the GPS time and distributes the 100 MHz clock frequency to all Host-DRS via Super-Host. A description of an early version of the time syn-

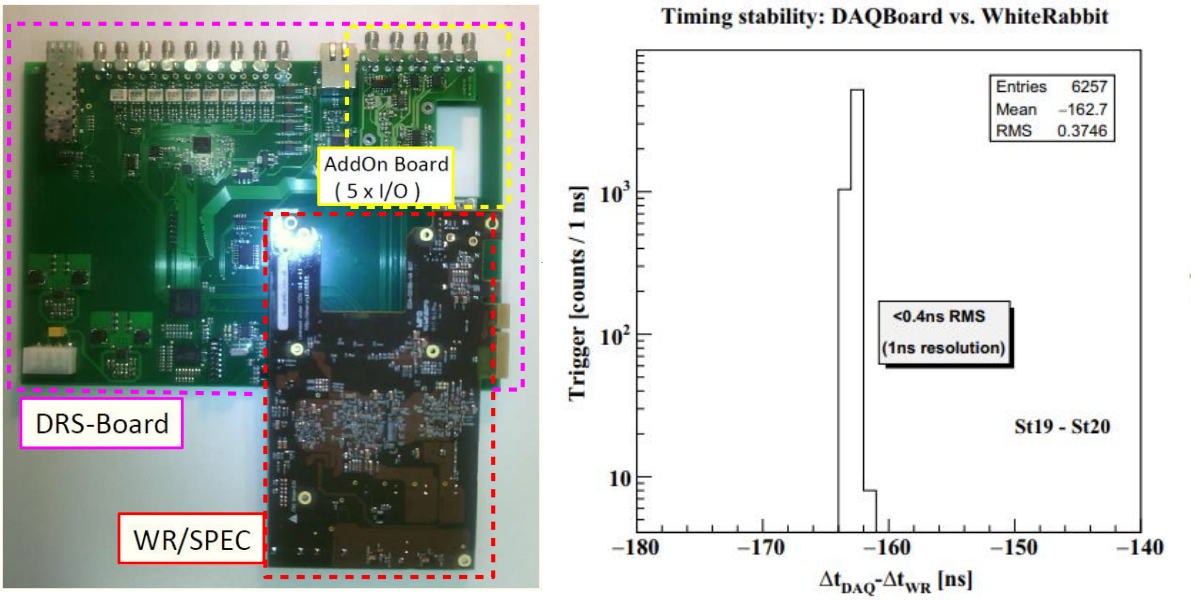

(a) (b)

Figure 5.3: (a) Hybrid HiS28 DAQ unit. Purple box: 9 channels (8 PMT channels, 1 synch channel) DRS4 board. Red box: WR-SPEC for independent event time stamping and station time synchronization. (b) Time stability between the two HiS28 timing systems: distribution of difference between two stations (S19 and S20) trigger time difference measured with TimeSystem-1 (Δt_{DRS}) and TimeSystem-2 (Δt_{WR}), showing an $r.m.s. \leq 0.4$ ns.

chronization is given in (Tunka-HiSCORE Collaboration, 2012). This custom system is not correcting clock drifts due to environmental effects (temperature), and does give absolute clock for each station only after off-line corrections by station-dependent clock transfer time.

TimeSyst-2 (WR). The WR timing system operating in HiS28 (grey boxes in figure 5.2) follows a similar concept described in section 4.1.1. In each station DAQ, a WR-SPEC card is combined with the DRS4 board as show in picture 5.3(a), and connected via fibre to the WR-Switches in the DAQ center. A WR-Switch (Master) distributes the GPS-disciplined Rubidium clock to all the WR nodes (Slave-Switches and station SPECs).

Figure 5.3(b) shows the relative stability between the two timing systems. Shown is the distribution of $\Delta t_{DRS} - \Delta t_{WR}$, where Δ_{DRS} and Δ_{WR} are the measured time differences between two stations (S19, S20) obtained for TimeSyst-1 and TimeSyst-2 respectively, for the same EAS events (Wischnewski et al., 2015). The distribution is characterized by an $r.m.s. \leq 0.4$ ns, and gives an estimation of the stability between the two timing systems, and an upper limit for the relative (inter-stations) time resolution for both systems. Since the two timing systems

are driven by different GPS clocks, no direct comparison is possible using the measurements from the same station, i.e. measuring the distribution of $t_{DRS} - t_{WR}$. Such variable would be dominated by the absolute difference between the two reference GPS clocks, at the moment under investigation.

Central GPS clock distribution. Special attention was on a stable central clock for the WR system. This is sketched in figure 5.4, showing the GPS-disciplined RbClock (Stanford FS725) that generates the PPS and 10 MHz signals for the WR-Grand Master Switch. Additionally, a Stratum-1 NTP server (Linux PS) control the Unix-Date. Multi-channel WR-nodes are monitoring at nsec resolution all relevant PPS-phases in TAIGA, e.g. from WR1, WR2, TimeSyst-1, and Ublox-GPS.

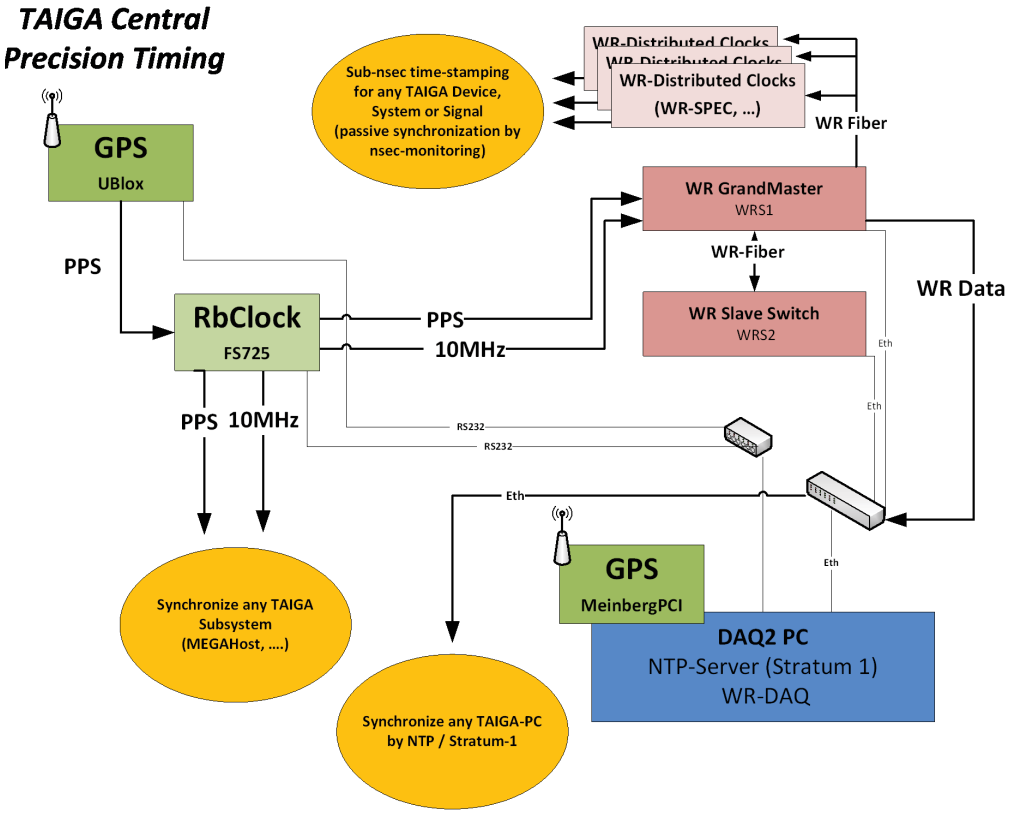

Figure 5.4: Overview of the TAIGA central timing system and the WR-setup, as used for HiS28. A GPS-disciplined RbClock synchronizes the WR-GrandMaster. WR-nodes in the DAQ-centre monitor all central PPS-signals (GPS-UBlox, WRS1,...,TimeSystem-1) for off-line phase correction at nsec-level.

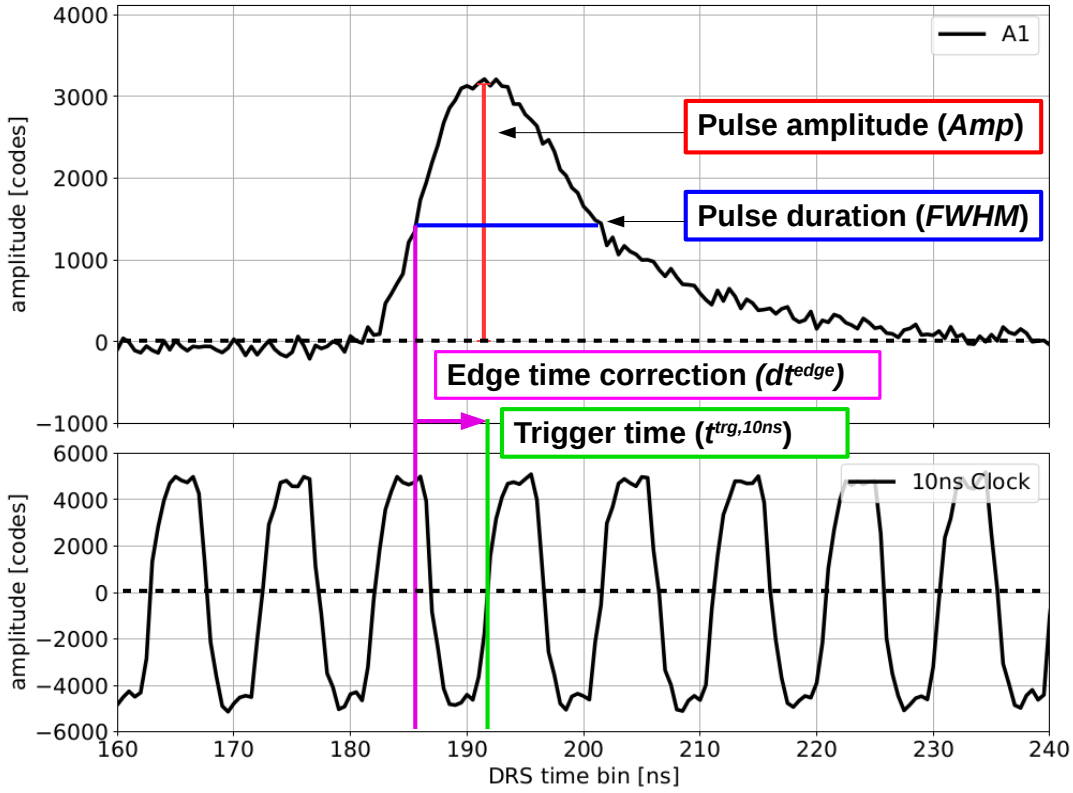

Figure 5.5: Top: PMT anode 1 signal trace; Bottom: 100 MHz clock signal. The trigger time $\delta t^{trg,10ns}$ is obtained at point 1 of section 5.2. The pulse amplitude Amp, and the edge time correction δt^{edge} are extracted during the pulse analysis performed at the end of point 1 (single PMT signal) and 3 (anodes/-dynodes sum).

5.2 Data processing

The HiS28 data processing chain is presented here. The analysis, applied to every data run, starts with the analysis of the single station event traces, and ends with the array event building. A description of the procedure and goals of each step is given in the following:

1 **DRS traces analysis:** For each active station operating during a run, all the event traces read out with the DRS4 board are analysed, in order to extract the main pulse parameters: trigger time $t^{trg,10ns}$ (the same for all the PMT traces), peak amplitude A, pulse area S, and edge time correction δt^{edge} (figure 5.5). The analysis of the single station data also allows to have an overview of detector operation quality, checking which stations/channels are actively participating to the run.

2 **PMT pulses calibration:** For each station, the distributions of the pulse parameters ex-

tracted in the previous point are analysed. The main goal of this step is to estimate (a) the relative PMT time delays (inside the same station), and (b) the time delay between anode and dynode channels, $\delta t^{A/D}$, due to the different signals amplification.

3 **Signal sum and analysis:** After applying the time corrections determined in the previous step, the anode and dynode traces are summed up, building the anode and dynode sum signals. The pulse analysis described at point 1 is repeated on these two signals. For each array station, an output file (*.prm) is produced, containing the extracted anode sum pulse parameters ($t^{trg,10ns}$, A, S, and δt^{edge}) of all the triggered and processed events. In case of anodes signals saturation, the dynode sum pulse is used.

4 **Array event building:** The single station events processed and stored at point 3 are merged together into array events. The procedure put together pulses from different stations, triggered within a $2\,\mu$s time window. The merging is based on the event time stamps $t_i^{trg,10ns}$ and the station transfer time delays. All the array events with ≥ 4 (≥ 2 since 2017) stations are stored into an output file containing the pulse parameters determined at point 3 for all the stations participating to the array event (.tim file, illustrated in figure 5.6).

Data calibration. The data processing ends with the .tim file production, one for each run. However, the data is not yet ready for EAS reconstruction, since a calibration of station amplitude and time is required. The amplitude calibration for the *i*-th station, obtained analysing the relative *.prm output file, consists of the determination of two main parameters per station:

$$\begin{aligned} R_i^{A/D} &=< A_i^{anodes}/A_i^{dynodes} > \\ C_i^{amp} &=< A > / < A_i > \end{aligned} \tag{5.1}$$

The first parameter, $R^{A/D}$, is the average ratio between anode and dynode sum amplitude, needed to correctly scale the dynode amplitude, used in case of anode saturation. The second parameter, C^{amp}, is needed to scale all the station amplitudes among each other. The array time calibration is described in detail in section 5.3. For each run, amplitude and time calibration constants are stored into output files: *cal<run-date>.dat* (amplitude) and *t_new<run-date>_<cal-mode>.nrm* (time).

With the .tim file and the amplitude/time calibration files it is possible to perform the shower reconstruction described in detail in section 5.4. The EAS reconstruction is performed using two parameters for each triggered station:

$$\begin{aligned} Amp_i &= A_i \cdot C_i^{amp} \cdot R_i^{A/D} \\ t_i &= t_i^{fibre} + t_i^{A/D} + t_i^{trg,10ns} + \delta t_i^{edge} + \Delta_i^{tCal} \end{aligned} \tag{5.2}$$

with $R_i^{A/D} = 1$ and $t^{A/D} = 0$ in case of anode pulse, t_i^{fibre} is the fibre delay (it depends on the station distance from the DAQ Centre), and Δ_i^{tCal} is the time offset correction.

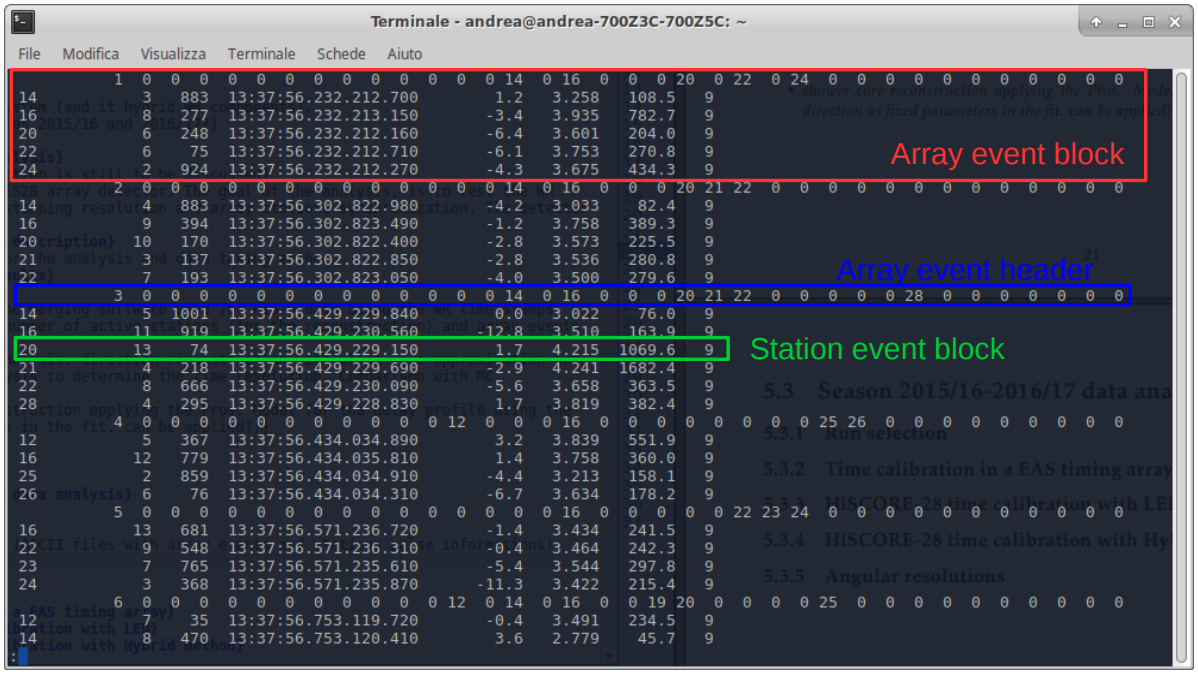

Figure 5.6: HiS28 array events .tim file format. It contains all the array events with $\geq$ 4 triggered stations ($\geq$ 2 from season 2017/18). The array event block (red box) contains an event header (blue box) and a station event block (green box) for each triggered station in the event. The event header consists of the array event index (or ID), plus 28 variables (one for each array station), equal to the station ID value if the station is triggered, 0 otherwise. Each station event block consists of 8 variables: station ID, station event index, station event trigger time $t^{trg,10ns}$, reference to synch pulse, pulse edge correction (δt^{edge}), pulse integrated charge ($\log_{10}(Q)$), pulse amplitude (Amp), channel type (Anode $= 9$, Dynode $= 10$). The last column is the sum pulse tag, indicating if the sum pulse is obtained from the anodes (9) or dynodes (10) signals sum. No pulse duration ($FWHM$) is at the moment available in the data.

5.3 Array time calibration

In this section the array time calibration of the HiS28 array is discussed. The *preliminary* time calibration for HiS28 is described in section 5.3.1, while section 5.3.2 describes the analysis performed on several LED calibration runs. Due to the limited array coverage ($\leq$ 50% of the stations), the LED runs are used only to check the correctness of the preliminary time calibration, and the single station time resolution. In section 5.3.3 the *hybrid* calibration method discussed in chapter 3 is applied to the HiS28 data, and shown to be superior to the preliminary calibration.

5.3.1 Preliminary time calibration

The large area of the HiS28 array does not allow to perform LED calibration runs that cover the full array at once, as done for HiS9. For this reason, a preliminary time calibration was defined and used for part of the analysis.

Essentially, it assumes a good a priori knowledge of the station time offsets, and uses the residual distributions from the EAS reconstruction to improve them (*Residual correction*, see chapter 3). A first approach assumed no initial guess for the station offsets, showing large disagreement with LED calibration results, and thus modified. besides the fibre delay, estimated independently and corrected during the data processing (see previous section), the PMT transit time is the main component of the station time offsets. As the transit time depends on the PMT high voltage, the preliminary calibration is hereafter also referred to as "HV" calibration. The preliminary time calibration procedure and some of its results are discussed in the following.

calibration procedure. The HV time calibration consists of a iterative procedure, based on the direction reconstruction of the EASs detected (and selected, see later in the text) in a given run. A starting time offset, $\Delta t^{j}_{0,i} = [0, +10, -15]$ ns, is associated to the *i*-th station, according to its PMT type j = [R5912, R7081, ET9352] (dashed lines in figure 5.7, top panel). At each iteration, the EAS directions are reconstructed, obtaining the fit residuals distribution for each station in the array. A Gaussian fit of the residual distribution is performed, and the mean values are used as new offsets in the next iteration. The procedure stops when the fitted mean values for all the stations are smaller than 0.5 ns. Only EAS with multiplicity $N_{trg} \geq 18$ are used, while no acceptance cut is applied to the EAS cores.

Figure 5.7 shows in the top panel the HV calibration for season 2016/17, where the set of calibration offsets obtained for each run, Δt^{HV}_{i}, is given a s function of the run date. A stable time offset distribution is observed along the season, indicating an overall stable performance. However, most of the stations present final offset corrections distant several nanoseconds (up to 5 ns) from the starting values, Δt^{i}_{0}. As discussed in section 3.1.1, this result indicates that the array average mispointing introduced by the station time offsets is reduced, but not fully corrected.

5.3.2 LED calibration

LED calibration runs were performed during each HiS28 observation season to check the correctness of the preliminary time calibration and the single station performance. LED runs 10.09.16, 29.09.16 and 18.10.2018 were performed with the same detector setup used during observation seasons 2015/16, 2016/17 and 2017/18 respectively, and thus used as reference. The LED source for these three runs is positioned in the same location, covering almost the same group of stations. Five additional runs have been performed during season 2016/17 (28.02.17-A/B, 01.03.17, 03.03.17-A/B), using three different locations for the LED source, with the aim

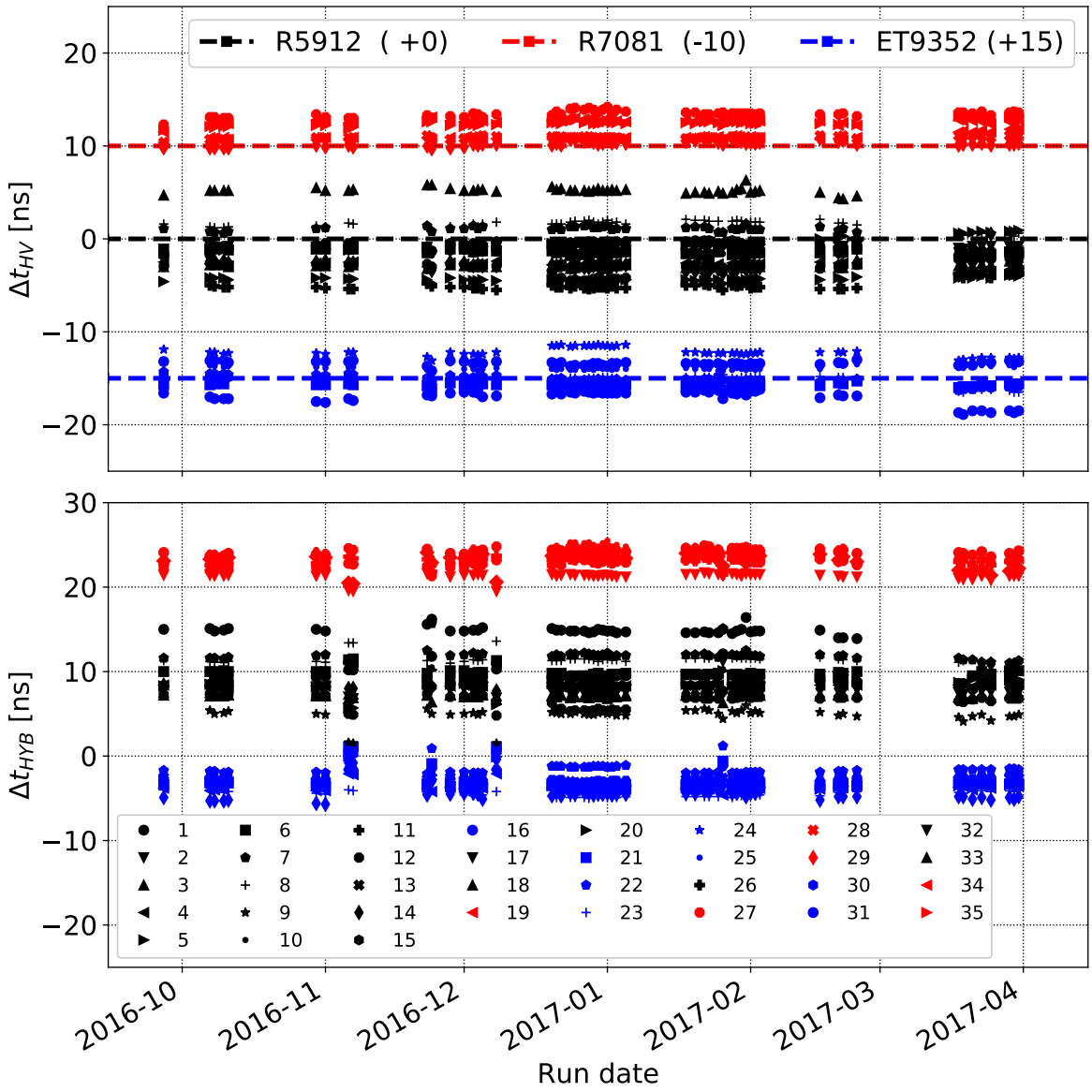

Figure 5.7: HiS28 time calibration for season 2016/17. For each processed run, the calibration offsets are displayed for preliminary (HV, top panel) and hybrid (HYB, bottom panel) calibration methods as a function of run date. The color code indicates the PMT type inside each station. Dashed lines: station staring values, $\Delta t^{j}_{0,i}$, used for the HV calibration.

to cover as many station as possible in a single LED calibration session.

Station offset calibration. The calibration procedure applied here is the same used to analyse HiS9 LED runs (see section 4.2.1), with station 16 used as reference station. The results of the HiS28 LED calibration are summarized in table 5.1. Figure 5.8 presents the measured station offset, Δt_{LED}, as a function of the station ID, showing the same three offset groups observed in figure 5.7.

An interesting result is observed in figure 5.8(b): for the same station (e.g. station 20, 23, 27), the difference between measured offsets in different runs can reach up to $3 - 4$ ns. This effect may be due to different factors, like (a) precise measurements of stations/LED coordinates, (b) the detector setup (i.e. the station PMTs HV), (c) the angle under which the LED source is seen by the specific stations. A detailed study of these systematics is needed in order to understand the effect on the recorded LED-signal in the station and the relative time offset measurement.

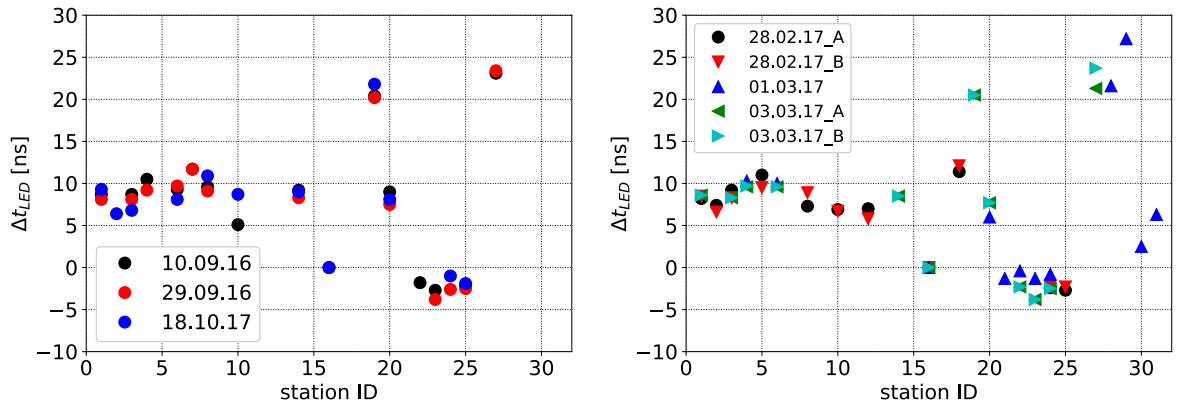

(a) (b)

Figure 5.8: HiS28 LED calibration runs. Estimated station offsets as a function of station ID for: (a) the three (one per season) reference LED runs, (b) the LED calibration session performed in February/March 2017. The analysis of the LED runs confirms the three time offset groups, related to the station PMT types, as shown in figure 5.7. 5.7

Station time resolution. The LED calibration can also be used to estimate the single station time resolution. Figure 5.9 shows the distributions of (a) the relative (to the reference station) time offset distribution, and (b) the residuals of the LED source position reconstruction (see also section 4.2.1). In the first case, the Gaussian fit gives a $\sigma_{\Delta t} = 0.35$ ns, corresponding to a single station $\sigma_t = 0.35/\sqrt{2} = 0.25$ ns, same result obtained from the LED position reconstruction fit residual distribution, $\sigma_t = 0.25$ ns.

	Run date # of calibrated stations							
Stn.ID	10.09.16 (15)	29.09.16 (14)	18.10.17 (12)	28.02.17-A (11)	28.02.17-B (11)	01.03.17 (12)	03.03.17-A (12)	03.03.17-B (12)
1	8.7	8.1	9.3	8.2	8.5	-	8.6	8.6
2	-	-	6.4	7.4	6.6	-	-	-
3	8.7	8.1	6.8	9.2	8.3	-	8.3	8.3
4	10.5	9.2	-	-	-	10.3	9.6	9.7
5	-	-	-	11.0	9.5	-	-	-
6	9.3	9.7	8.1	-	-	10.0	9.6	9.6
7	11.7	11.7	-	-	-	-	-	-
8	9.6	9.1	10.9	7.3	8.9	-	-	-
10	5.1	-	8.7	6.9	6.7	-	-	-
12	-	-	-	7.0	5.8	-	-	-
14	9.2	8.3	9.0	-	-	-	8.5	8.5
15	-	-	-	-	-	-	-	-
16	0.0	0.0	0.0	0.0	0.0	0.0	0.0	0.0
18	-	-	-	11.4	12.1	-	-	-
19	20.4	20.2	21.8	-	-	-	20.5	20.5
20	9.0	7.5	8.1	-	-	6.0	7.7	7.7
21	-	-	-	-	-	-1.3	-	-
22	-1.8	-	-	-	-	-0.4	-2.3	-2.3
23	-2.7	-3.8	-	-	-	-1.3	-3.8	-3.8
24	-	-2.6	-1.0	-2.4	-2.2	-0.8	-2.5	-2.5
25	-2.2	-2.5	-1.9	-2.7	-2.3	-	-	-
27	23.1	23.4	-	-	-	-	21.3	23.7
28	-	-	-	-	-	21.6	-	-
29	-	-	-	-	-	27.2	-	-
30	-	-	-	-	-	2.5	-	-
31	-	-	-	-	-	6.3	-	-
34	-	-	-	-	-	-	-	-
35	-	-	-	-	-	-	-	-

Table 5.1: Summary table for HiS28 LED calibration. For each LED run (columns), the calibration constants, Δt^{LED}, are listed. The first block (columns 1 to 3) reports the reference LED calibration for season 2015/16, 2016/17, and 2017/18 respectively, covering almost the same group of stations. The second block (columns 4 to 8) shows the results for a dedicated LED session in Feb/March 2017, where different groups of stations were covered by changing the position of the LED source. Station 16 is the common station to all LED runs, and is used as reference station. Stations 34 and 35 are not covered in any of the LED calibration runs.

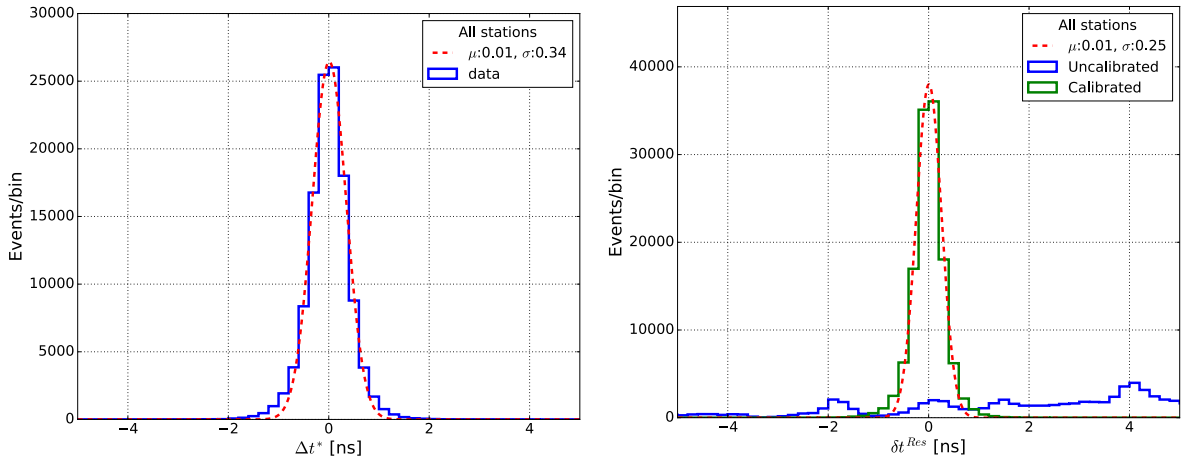

(a) (b)

Figure 5.9: Time resolution from LED runs. (a) All stations relative (to the reference station) time offsets distribution $\Delta t^* = \Delta t_i - < \Delta t_i >$. The Gaussian fit returns a $\sigma_{\Delta t^*} = 0.35$ ns, corresponding to a single station absolute time resolution $\sigma_t = 0.35/\sqrt{2} = 0.25$ ns. (b) LED source position reconstruction fit residual distributions for calibrated (green) and uncalibrated (blue) times. The Gaussian fit confirms the single station absolute time resolution $\sigma_t = 0.25$ ns.

5.3.3 Hybrid time calibration

The hybrid time calibration method (HYB) is here tested on the HiS28 data set, and shown to be superior to the preliminary (HV) time calibration. As describe in detail in chapter 3, the HYB method allows to easily perform both *Residual* and *CP corrections*. In particular, the *Residual correction* does not need a precise a priori knowledge of the station time offsets for all the array stations (like for the HV calibration). Instead, the precise a priori knowledge of the offset is required for the *CP corrections*, but only for a small number of array stations. Such a precise offset measurements can be obtained using an external calibration procedure, e.g. using LED calibration runs.

Calibration procedure. The *Residual correction*, $< \delta t_i^{res} >$, is obtained with the same iterative procedure used for the HV calibration (section 5.3.1), but without need of pre-calibrated initial values (i.e. $\Delta t_{0,i}^j = 0$). The *CP correction*, δt_i^{CP}, is than obtained in two steps. First, the CP parameters (A, B, $< \delta t_0 >$) are estimated by fitting $\{\delta t_k^{CP}, xk, yk\}$ with the plane function defined in equation 3.6, where $\delta t_k^{CP} = \Delta t_k^{LED} - < \delta t_k^{res} >$ and k is the number of LED calibrated stations (LED-stations hereafter). Once the CP parameters are obtained, the *CP correction* for the i-th station is obtained calculating the value of the CP plane (equation 3.6) at the station position, (x_i, y_i): $\delta t_i^{CP} = CP(x_i, y_i | A, B, < \delta t_0 >)$. Finally, the HYB calibration

constants, Δt_i^{HYB}, are obtained from the sum of the *Residual* and *CP corrections*:

$$\Delta t_i^{HYB} =< \delta t_i^{res} > +\delta t_i^{CP} \tag{5.3}$$

LED runs 10.09.16, 29.09.16 and 18.10.18 are used to estimate the *CP correction* for season 2015/16, 2016/17 and 2017/18 respectively.

Systematics check. In a similar way as done in chapter 3, two tests are performed to study some of the HYB method systematics:

1. **T1: LED-stations position:** the HYB calibration is performed using groups of 4 LED-stations, with different location within the array.

2. **T2: number of LED stations:** the HYB calibration is performed using a different number of LED-stations, k.

T1. The first test checks how the calibration result depends on the position of the LED-stations within the array. Five LED-stations groups are defined (*iG*), each of them with 4 stations and the same geometry, as shown in figure 5.10(a). For each group, the HYB calibration offsets (Δt_{HYB}^{iG}) are calculated for the full array, and compared to the LED calibration, Δt_{LED}.

The top panel of figure 5.10(c) shows the HYB offset errors, $\Delta t_{HYB}^{iG} - \Delta t_{LED}$, as a function of the station ID. The error distribution for the different groups have similar fluctuation (∼1-2 ns), resulting in large fluctuation of the *CP correction*, $\sigma(\alpha_{MIS}^{CP}) = 0.12°$, as shown in figure 5.10(b)). The bottom panel of figure 5.10(c) gives the *r.m.s.* of the HYB correction for the *j*-th station, $\sigma(\Delta t_{HYB}^{iG,j})$, as a function of the station ID, showing fluctuations up to 2.5 ns. The plot in figure 5.10(d) shows the offset errors as a function of the distance from the LED-stations (center). A small radial trend is observed, similar to what obtained in the HYB systematics check with MC simulation (chapter 3, figures 3.6 and 3.7).

To conclude, T1 results show no strong dependency from the LED-stations location. However, the fluctuations of the CP correction indicate that $k = 4$ is not enough to obtain a precise and stable calibration.

T2. The second test is meant to check how the HYB offsets depend on the number LED-stations, k. The different LED-stations groups are located at the centre of the array, with $k \in [4, 6, 8, 14]$ (see figure 5.11(a)). Like done for T1, the HYB calibration offsets are determined for different LED-stations groups, and compared to the LED calibration, Δt_{LED}.

Figure 5.11(c) shows the HYB offset errors, $\Delta t_{HYB}^{k} - \Delta t_{LED}$, as a function of station ID. From $k = 6$ up to 14, similar distributions are observed, with $r.m.s. \leq 1$ ns. This offsets stability results in a stable CP correction: figure 5.11(b) gives the distribution of the fitted direction of the CP corrections for the different groups, showing fluctuation $\sigma(\alpha_{MIS}^{CP}) = 0.02°$ (excluded $k = 4$). The plot in figure 5.11(d) shows the offset errors as a function of the distance from the array center. The same radial trend obtained in T1 is observed, with the error fluctuation at

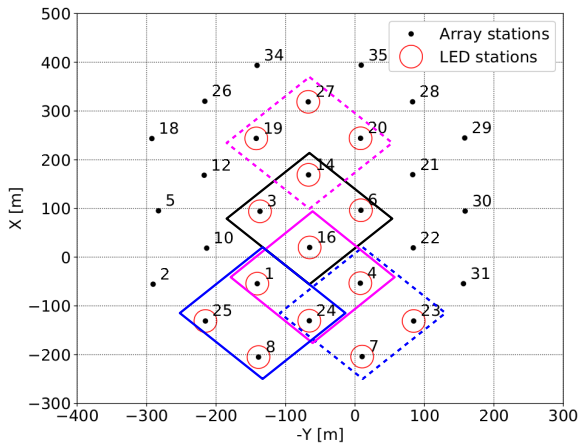

(a) LED-stations groups.

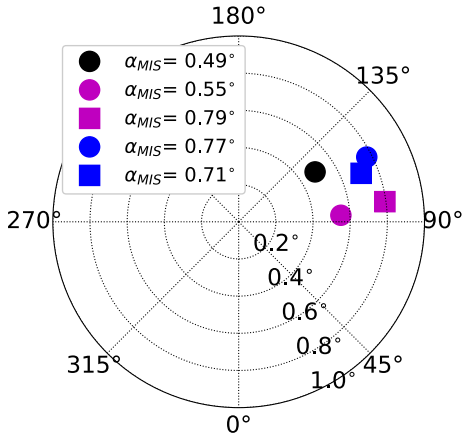

(b) Fitted CP direction for different LED-stations groups: $\sigma(\alpha^{CP}_{MIS}) = 0.12°$.

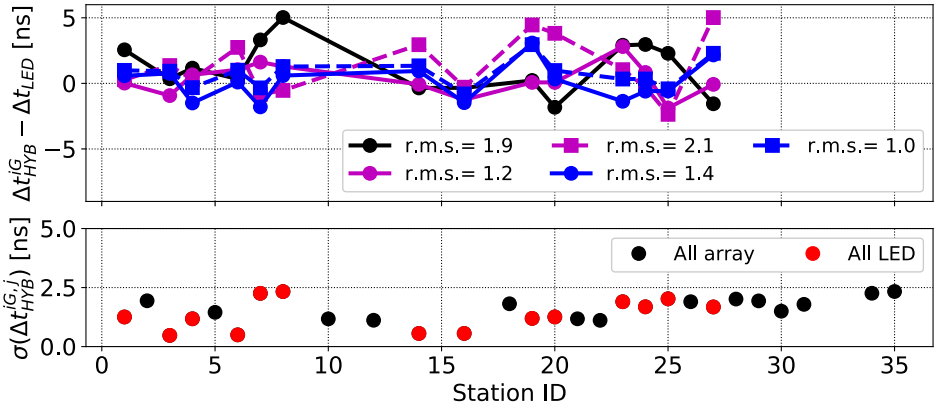

(c) Top: difference between HYB and LED offset vs station ID. The different groups have close (but large) error fluctuation ($\sim 1 - 2$ ns), resulting in large fluctuation of the CP correction (see figure (b)). Bottom: HYB correction $r.m.s.$ for the j-th station, $\sigma(\Delta t^{iG,j}_{HYB})$, vs station ID for all array stations (black dots) and station with LED calibration (red dots).

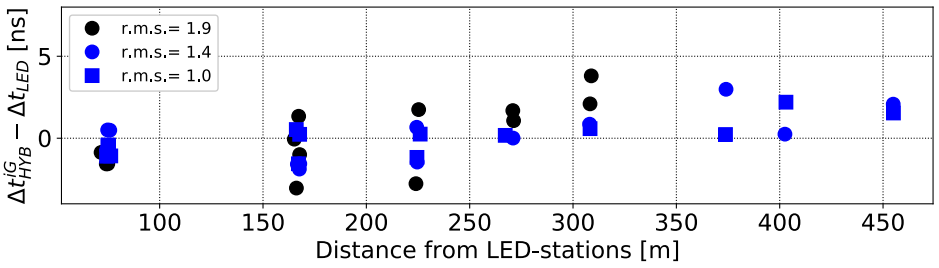

(d) Difference between HYB and LED offsets vs distance from LED-stations (array center). A radial trend is observed for different LED-stations positions, similar to the results in figures 3.6 and 3.7.

Figure 5.10: HYB calibration systematics check T1.

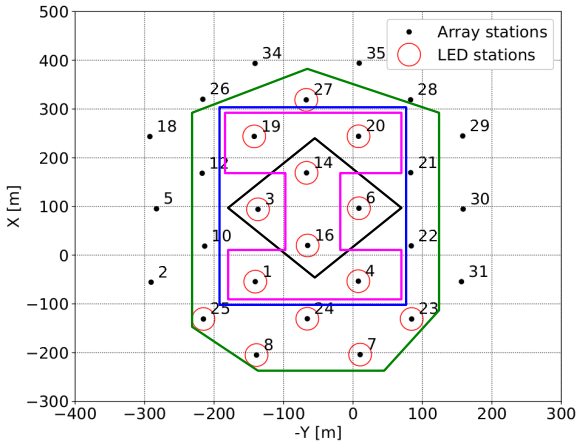

(a) LED-stations groups.

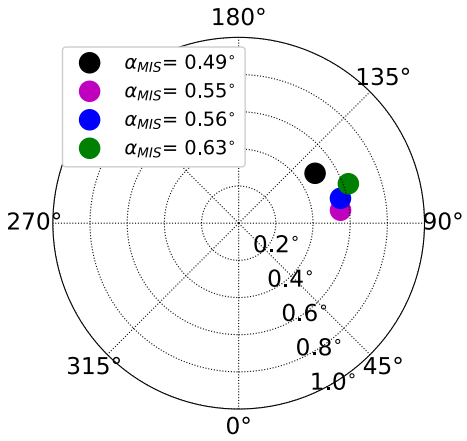

(b) Fitted CP direction for different LED-stations groups: $\sigma(\alpha^{CP}_{MIS}) = 0.03°$ (excluded $k = 4$).

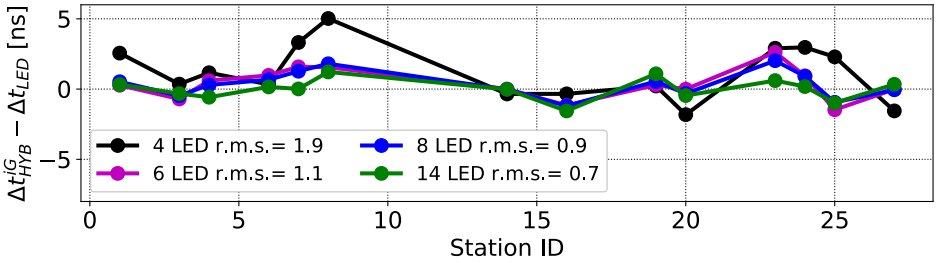

(c) Difference between HYB and LED offsets vs station ID. From 6 up to 14 LED-stations, the error fluctuations are stable, with $\sigma(\Delta t^{iG}_{HYB} - \Delta t_{LED}) \leq 1$ ns, resulting in a stable CP correction (see figure (b)).

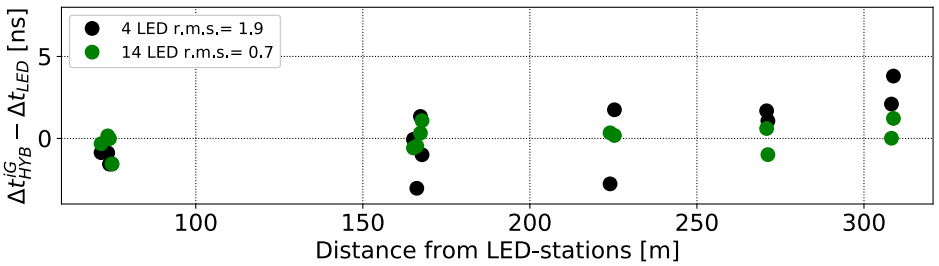

(d) Difference between HYB and LED offsets vs station distance from the array center. The radial trend of the offset error get smaller as the LED-stations increase.

Figure 5.11: HYB calibration systematics check T2.

large distance getting smaller as the number of LED-stations increases.

The results of T2 show that already at $k = 6$ is it possible to obtain a stable CP correction. This support the HYB method concept, i.e. obtaining a full array calibration starting from a precise external calibration of a small portion of the array.

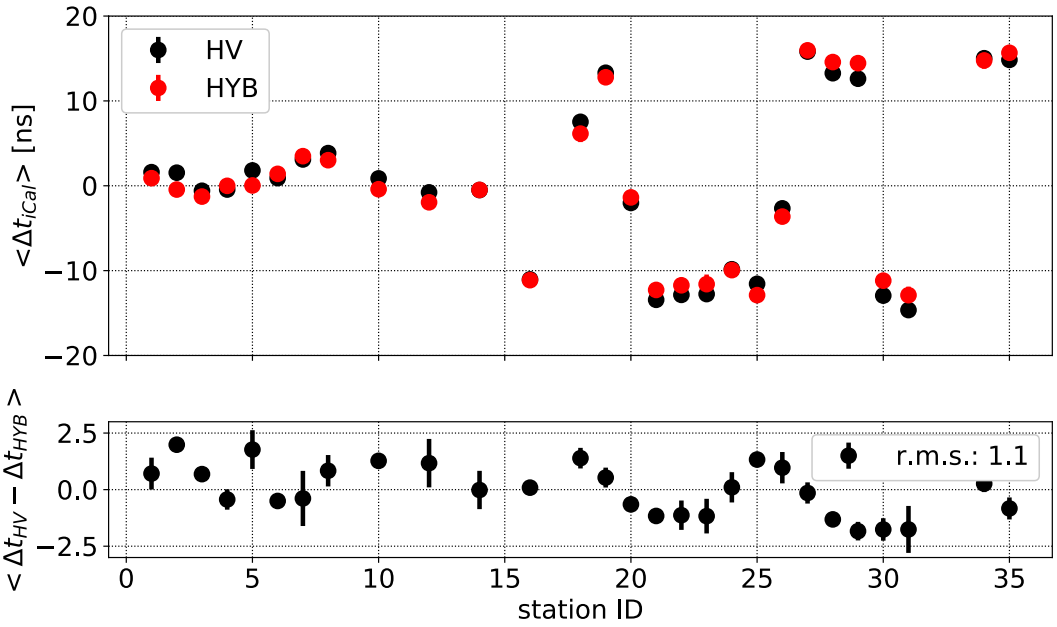

Figure 5.12: Comparison between HV and HYB calibrations for 2016/17 season. Top: average (over the full season) calibration offset as a function of the station ID, for HV (black) and HYB (red) methods. A very good agreement is observed, with the HYB method reproducing the three groups shown in figure 5.7. Bottom: average difference between HV and HYB methods, $< \Delta t_{HV} - \Delta t_{HYB} >$, as a function of station ID. Large differences up to 2 ns are observed for several stations, and an $r.m.s. = 1.1$ ns.

5.3.4 Comparison of time calibration methods

The results of the HV, LED and HYB calibration methods applied to 2016/17 data are here compared. The calibration offsets obtained from LED run analysis, Δt^{LED}, are here assumed to be the closest and more reliable measurement of the true station time offsets, Δt.

Figure 5.12 shows the first comparison between HYB and HV calibrations. The upper panel shows the average of the calibration offsets for the *i*-th station, $< \Delta t_i^{iCal} >$, as a function of the station ID, with a good agreement observed between the two methods. In particular, the HYB calibration (red dots) reproduces the three offsets groups assumed in section 5.3.1, and confirmed in 5.3.2, proving the correct application of the method. The average difference between the two methods for the *j*-th station, $< \Delta t_i^{HV} - \Delta t_i^{HYB} >$, is given in lower panel of

the figure. Large systematic differences are observed for several stations up to 2 ns, and an average $r.m.s. = 1.1$ ns. A fit of the $< \Delta t^{HV} - \Delta t^{HYB} >$ distribution with a plane function returns an angle $< \alpha_{HV-HYB} > \sim 0.13°$. Such angle gives an estimation of the average mispointing (over the season) between the reconstructed directions for the same EAS event, obtained applying the two different time calibration methods.

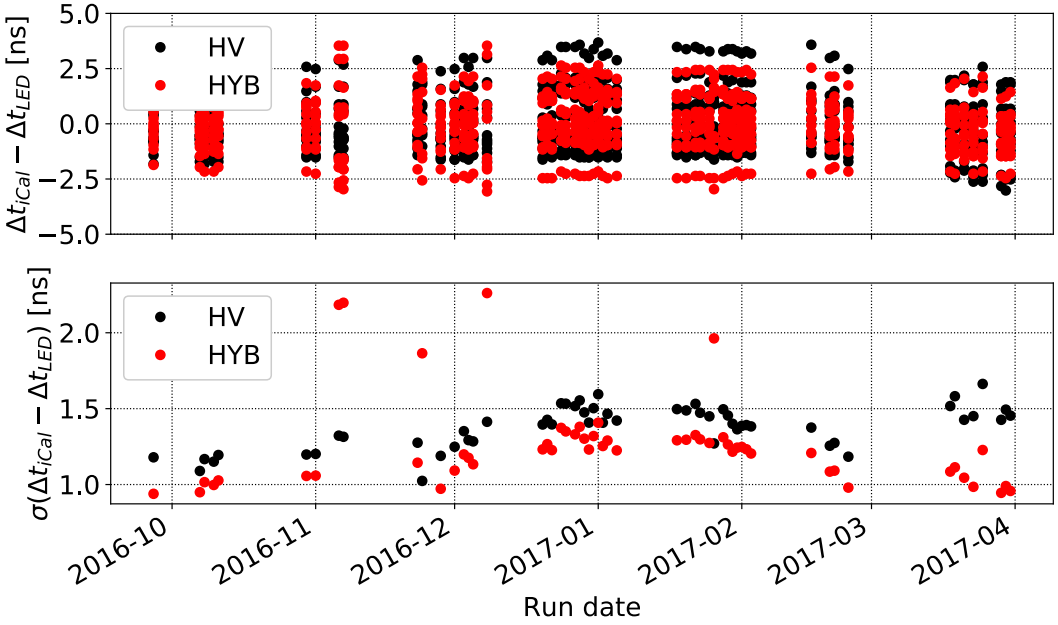

Figure 5.13: HV and HYB comparison with LED. Top: $\Delta t_{iCal} - \Delta t_{LED}$ distribution as a function of run date. Bottom: $\sigma(\Delta t_{iCal} - \Delta t_{LED})$ as a function of run date. The HYB calibration shows a better agreement with LED calibration over the season. Few (5) runs show large deviation between HYB and LED calibrations (see also figure 5.14).

Figure 5.13 shows the comparison of the two time calibration methods with the LED calibration. For each calibration method, the top panel shows the distribution of $\Delta t_{iCal} - \Delta t_{LED}$, while the lower panel gives the distribution *r.m.s.*, $\sigma(\Delta t_{iCal} - \Delta t_{LED})$, as a function of run date. On average, the HYB method shows a better agreement with the LED calibration (smaller *r.m.s.*) over the whole season.

Using the HV and HYB calibration offsets as a good approximation of the true station time offsets, and fitting their distribution with a plane, it is possible to estimate the order of magnitude of the corrected average mispointing. Figure 5.14(a) shows the distribution of the average mispointing directions for each run, while figure 5.14(b) shows the average absolute mispointing as a function of the run date. On average, the HYB calibration results in a mispointing angle $0.05°$ smaller than the HV calibration. The larger HV mispointing is likely due to the non precise initial guess adopted at the beginning of the HV calibration procedure (see section 5.3.1).

Looking more in detail at both figures 5.13 and 5.14, few (5) runs present HYB offsets with large fluctuations w.r.t. the LED calibration (figure 5.13), and very different mispointing w.r.t. the HV method (figure 5.14). The reason for such effect is not investigated here, and a further systematic study is required.

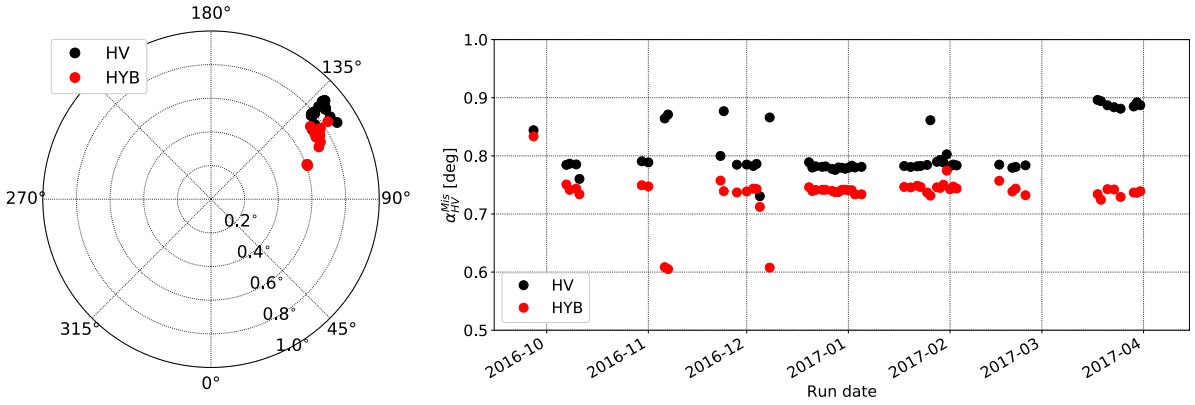

(a) (b)

Figure 5.14: HV and HYB mispointing comparison. (a) Distribution of the CP mispointing directions over 2016/17 season, for HYB and HV calibration methods. (b) Absolute mispointing angle as a function of the run date, for the two calibration methods.

5.3.5 Conclusions on time calibration

The station time offsets obtained with the HV method differ up to 5 ns from the pre-calibrated initial guess (figure 5.7), resulting in a partial correction of the absolute detector mispointing (see discussion in chapter 3).

The HYB calibration method presented in chapter 3 is tested here on the HiS28 data set, and found to be stable when using a number of LED-calibrated stations ≥ 6 ($\sigma(\alpha_{Mis}) \approx 0.03°$). Comparing the HYB and HV calibration with the LED calibration, a better agreement (smaller *r.m.s.* in the offset difference) is found for the HYB method, as shown in figure 5.13. This, together with a $\sim 0.05°$ smaller, and more stable corrected mispointing (figure 5.14), indicates a better precision of the HYB method for station offset estimation, ans mispointing correction.

The analysis of the reconstructed shower presented in the next section is for events calibrated using the HYB method.

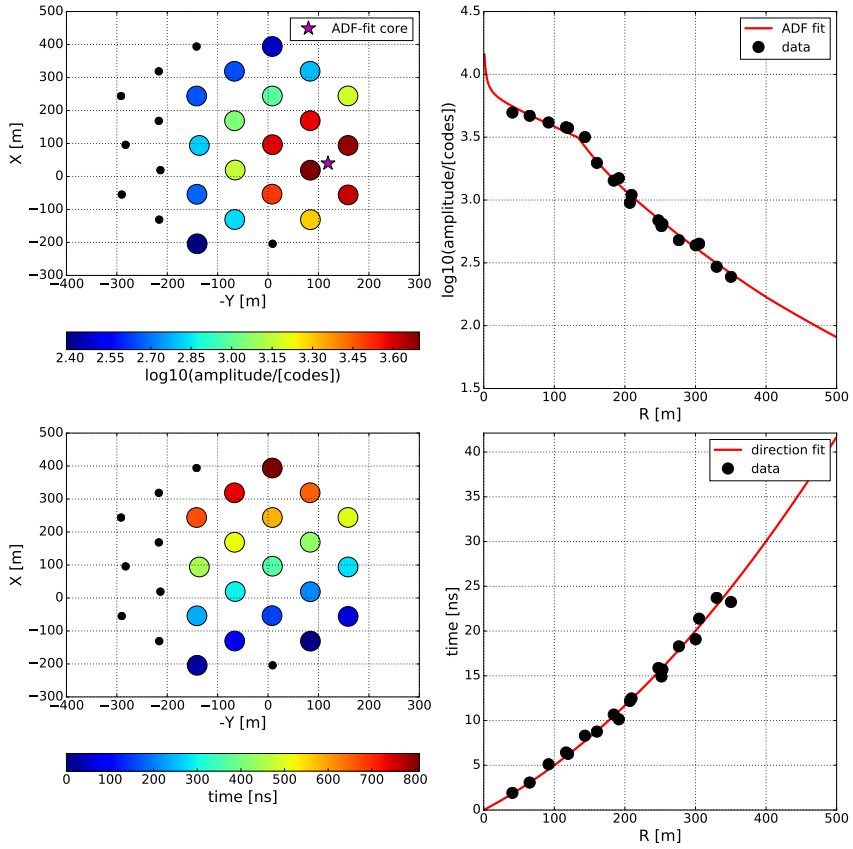

Figure 5.15: Example of a HiS28 reconstructed event. Top-left: station pulse amplitudes distribution. Purple star: reconstructed EAS core position by ADF amplitude fit (top-right). Bottom-left: station pulse arrival times (relative to first triggered station). Bottom-right: front time delays as a function of the distance from EAS core. Red lines: ADF and PARAB fit results.

5.4 Event reconstruction

After calibrating the station amplitudes and times (see equation 5.2), each array event processed is reconstructed following the reconstruction steps described in section 2.4. In particular, after the preliminary reconstruction 2.4.2, the EAS core location (X_C, Y_C) is obtained by fitting the recorded pulse amplitudes with the ADF model (equation 2.9), while the arrival direction (θ, ϕ) is obtained by fitting the measured pulse times with the PARAB model (equation 2.14). Another important parameter (used for event selection) is the angle ψ, defined as the space angle between the reconstructed direction and the detector pointing ($\phi_{det} = 0°$, $\theta_{det} = 25°$). An example of a reconstructed event is given in figure 5.15.

A dedicated MC simulation of the HiS28 detector is performed in order to evaluate the ex-

pected reconstruction accuracy (section 5.4.1). At the same time, it is used to compare the reconstructed data with the expectations (section 5.4.2). The chessboard method is finally used to verify the HiS28 detector angular resolution (section 5.4.3).

5.4.1 MC simulation

A dedicated simulation of the HiS28 detector is performed in order to estimate the expected core and direction reconstruction accuracy, and for a comparison with the results of the data reconstruction. The EAS generation setup for the primary particles (protons and gammas) is described in section 2.3.1, while the detector response is obtained using *sim_score*, with the tilting option set to 25° southward. After reconstruction, the simulated EAS statistics is normalized and re-weighted, in order to have a power-law spectral index $\gamma = -2.7$. The data-MC comparison is performed using protons.

Core resolution. The expected core resolution for gamma-ray induced EASs using the ADF model is given in figure 5.16(a). A resolution $\delta R_{68} \sim 40\,\text{m}$ is obtained at 5 triggered stations, improving below $10\,\text{m}$ at ≥ 15 triggered stations. The core resolution for proton initiated EASs is also given, showing a better resolution for triggered stations $\leq 10\,\text{m}$. This is due to the ADF method parametrization optimized for hadrons induced EASs reconstruction (Prosin et al., 2014). The same resolution ($\delta R_{68} \leq 10\,\text{m}$) is obtained at event multiplicity larger that 12.

Arrival direction resolution. The expected angular resolution for gamma-ray and proton initiated EASs using the PARAB model is shown in figure 5.16(b). The angular error, $\delta\alpha_{68} \sim 0.5^\circ$ at 4 triggered stations, improves below 0.15° at multiplicity ≥ 10, reaching $\sim 0.1^\circ$ for multiplicity ≥ 12. Similar to the ADF model, a slightly better resolution is obtained for protons.

5.4.2 Data-MC comparison

Detector acceptance. The results of the EASs reconstruction are summarized in figures 5.17 and 5.18. The first figure shows the detector acceptance for successfully reconstructed cores (figures 5.17(a)) and arrival directions (figures 5.17(b)), with data from run 25.03.2017 on the left, and the MC expectation on the right. The dashed lines indicate the selection regions for core and direction, in which the reconstruction accuracy showed in figure 5.16 are expected.

Figure 5.17(a) shows a non uniform core distribution in the data sample, direct consequence of the non uniform detector setup. In the real experiment, stations have different number of PMTs (3 or 4) of different types (3), and operating at different high voltage, resulting in different station detection threshold and trigger rate. Looking at the arrival direction distributions in figure 5.17(b), an extended detector acceptance up to $\theta = 60^\circ$ is observed in the data. This effect is better visible in the distributions of the single reconstructed parameters, θ, ϕ, and ψ, shown in figure 5.18. The larger detector acceptance in ψ in the data can be explained

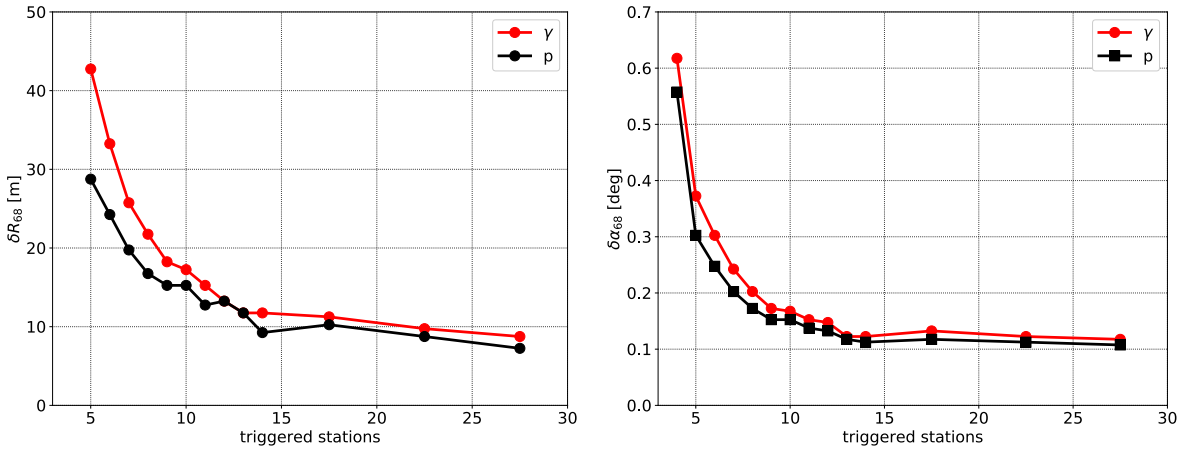

(a) (b)

Figure 5.16: Reconstructed core (a) and arrival direction (b) resolution (68% of containment) as a function of the number of triggered stations, for gamma-ray and protons induced EASs.

with a non correct simulation of the WC acceptance at large angle (a very good agreement is observed up to $\psi = 25°$). The disagreement observed in the θ distributions, with the maximum shifted at larger θ in the data, points to a higher energy threshold in the real experiment.

Array energy threshold. As shown in figures 5.17(b) and 5.18 (left panel), a clear disagreement is observed comparing the θ angle distribution for data and MC, with the data showing a peak at higher θ ($\sim 30°$) compared to the MC ($\sim 20°$). The order of magnitude of the discrepancy between the data and simulation ($\sim 10°$) excludes angular mis-reconstruction (e.g. by wrong time calibration, max mispointing estimated $\sim 0.1°$). The *sim_score* tilting option, introduced ad hoc for HiS28 simulation, has also been tested and proved to work correctly, as well as the simulated event normalization and weighting.

The observed shift of the θ distribution peak in the data can be explained by a higher energy threshold in the real experiment, compared to MC simulation. To test this hypothesis, the θ distribution from the data is compared with the MC θ distributions obtained for different energy cut-off, $E^{cut-off}$. For each value of $E^{cut-off}$, the two θ distributions (data and MC) are normalized and subtracted from each other. The *r.m.s.* of the distributions so obtained, $\sigma(DATA - MC_{E^{cut-off}})$, is used to estimate the distributions agreement. The test is performed scanning $E^{cut-off}$ in the energy range $40 - 100$ TeV, with steps of 5 TeV. Figure 5.19(a) shows the comparison between data (black dots) and the MC distributions obtained without cut-off (black line), and for $E^{cut-off} = 75$ TeV (red line). The result of the scan is given in figure 5.19(b), showing the minimum of $\sigma(DATA - MC)$ reached at $E^{cut-off} = 75$ TeV. The same analysis applied to simulated gamma initiated EASs gives a $E^{cut-off} = 50 - 55$ TeV.

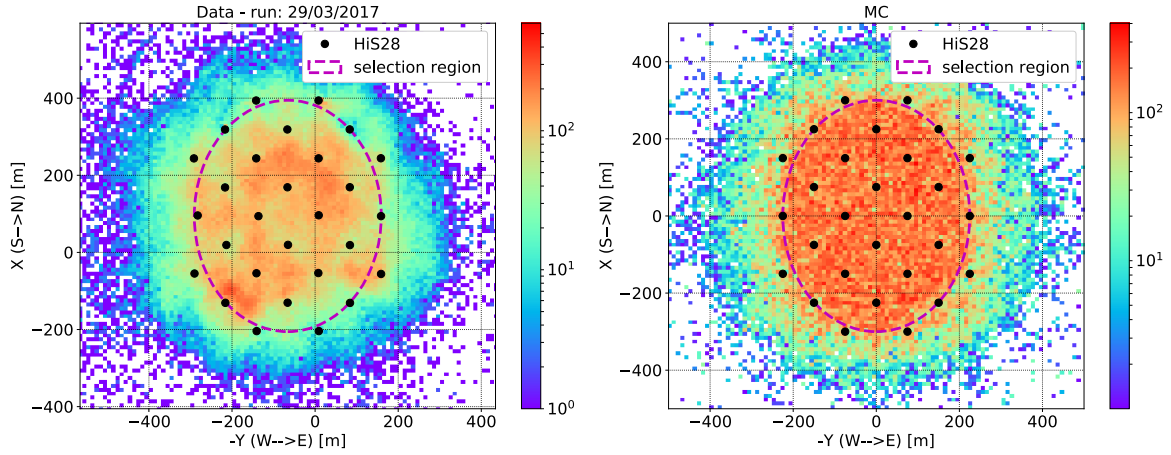

(a)

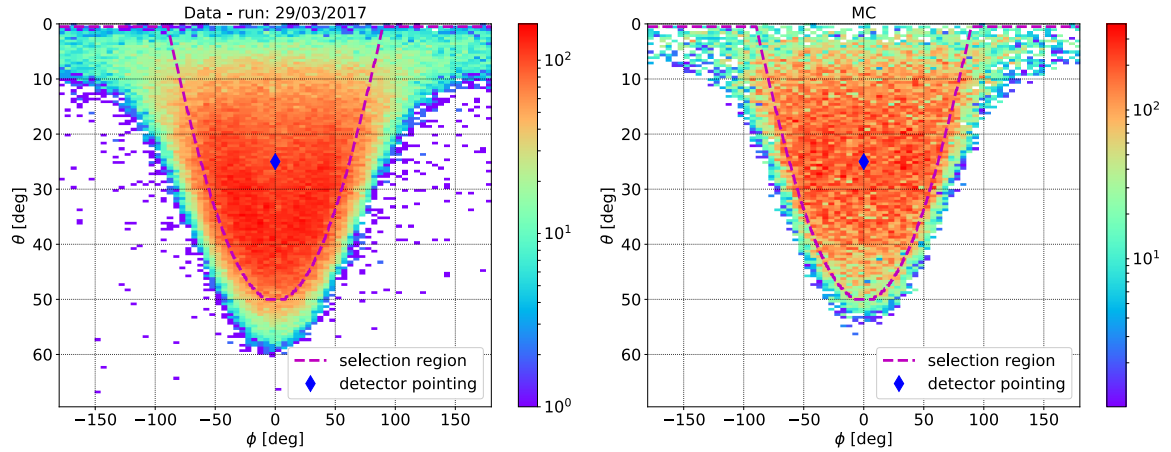

(b)

Figure 5.17: HiS28 EAS reconstruction: data (run 25/03/2017) vs. MC. (a) EAS core location (X_C, Y_C), using the ADF method, for data (left) and MC (right). (b) Arrival direction angles (ϕ, θ), using the PARAB method, for data (left) and MC (right). The dashed ellipse indicates the quality selection regions. Blue diamond: detector pointing direction ($\phi = 0°, \theta = 25°$).

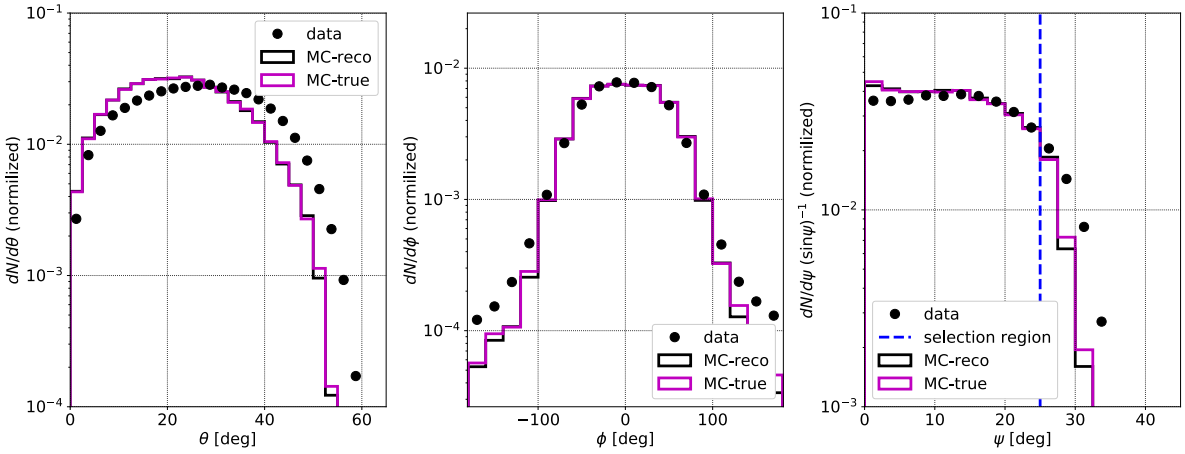

Figure 5.18: HiS28 arrival direction angles. (a) θ, (b) ϕ, and (c) ψ (angular distance between EAS direction (ϕ, θ) and detector pointing ($\phi = 0°$, $\theta = 25°$)) for data (black dots) and MC (black line). The true MC distributions are shown in purple.

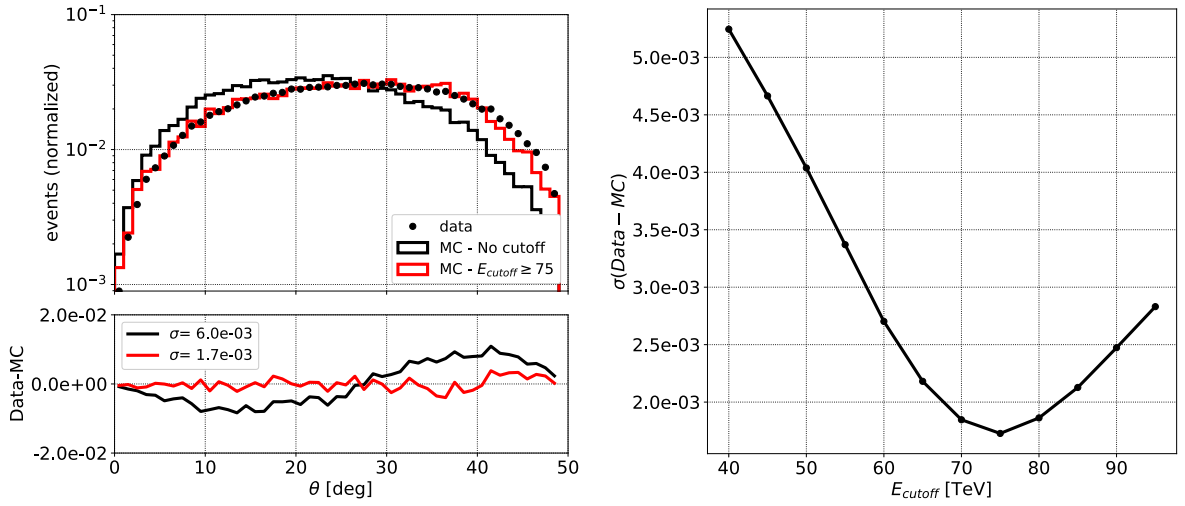

(a) (b)

Figure 5.19: HiS28 energy threshold estimation. (a) Reconstructed θ distribution for data (black dots), and MC without cut-off (black line) and for $E^{cut-off} = 75\,\text{TeV}$ (red line). (b) $\sigma(DATA - MC)$ as a function of $E^{cut-off}$, with minimum reached at $E^{cut-off} = 75\,\text{TeV}$ (protons).

5.4.3 Angular resolutions: Chessboard method

An estimation of the angular resolution can be inferred from MC simulation, as done in section 5.4.1, but this implies a correct simulation of all experimental details. An alternative method, largely independent of MC assumptions, is used here to infer the HiS28 angular resolution directly from experimental data: the *Chessboard* method. This method, successfully used in several EAS ground-based experiments (HEGRA/AIROBICC (Karle, 1991; Merck et al., 1996), ARGO-YBJ (Sciascio and Rossi, 2007)), represents a valid alternative to the Moon shadow analysis (Clark, 1957), which is not applicable to Cherenkov timing array like TAIGA-HiSCORE.

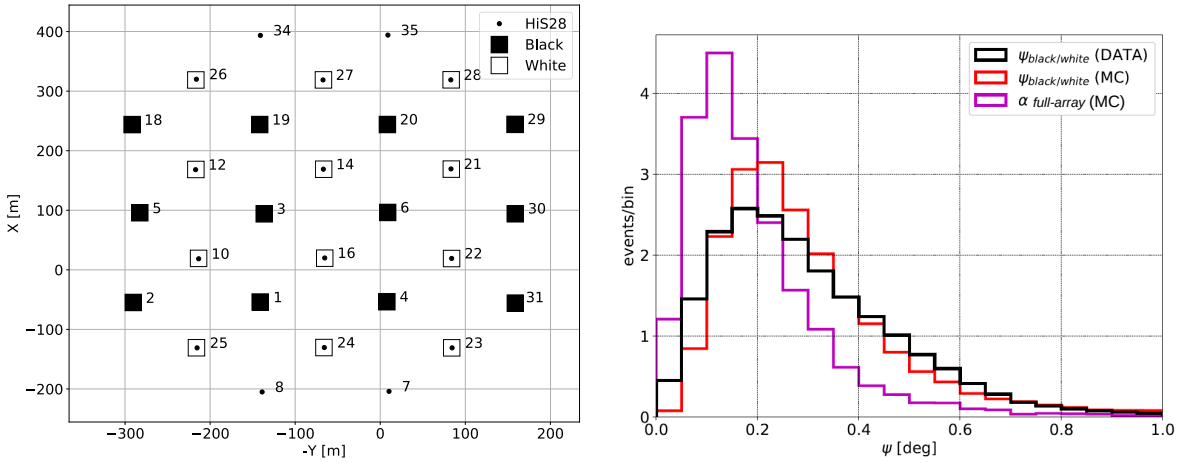

(a) (b)

Figure 5.20: Chessboard method. (a) HiS28 array chessboard splitting scheme. Stations [7, 8, 34, 35] are excluded in order to have two identical sub arrays, "Black" and "White". (b) $\psi_{Black/White}$ angle distribution for data (black, run 25.03.2017) and MC simulation (red). Purple line: full array angular error distribution, $\alpha^{MC}_{FullArray}$.

The method. The method consists in splitting the array in two independent sub arrays ("Black" and "White") as shown in figure 5.20(a), and reconstructing the arrival directions of the detected EASs (full-array events), as seen by the two sub arrays (sub-array events). The angular distance between the two reconstructed directions, $\psi_{Black/White}$, is used to estimate the full-array angular error, $\alpha_{FullArray}$. To reduce the systematic error due to the EAS core precision, the full array reconstructed core is used, thus the two sub arrays reconstruction are not fully independent from each other. Further, in order to guarantee that the reconstructed directions have similar statistical and systematic errors, it is required that the difference in multiplicity between the sub-events is ≤ 1. The MC simulation is used here to determine the correlation between $\psi_{Black/White}$ and $\alpha_{FullArray}$ to be used on the data, and to compare the results with

the expectations. Stations [7, 8, 34, 35] are excluded from the analysis, in order to have two identical sub arrays.

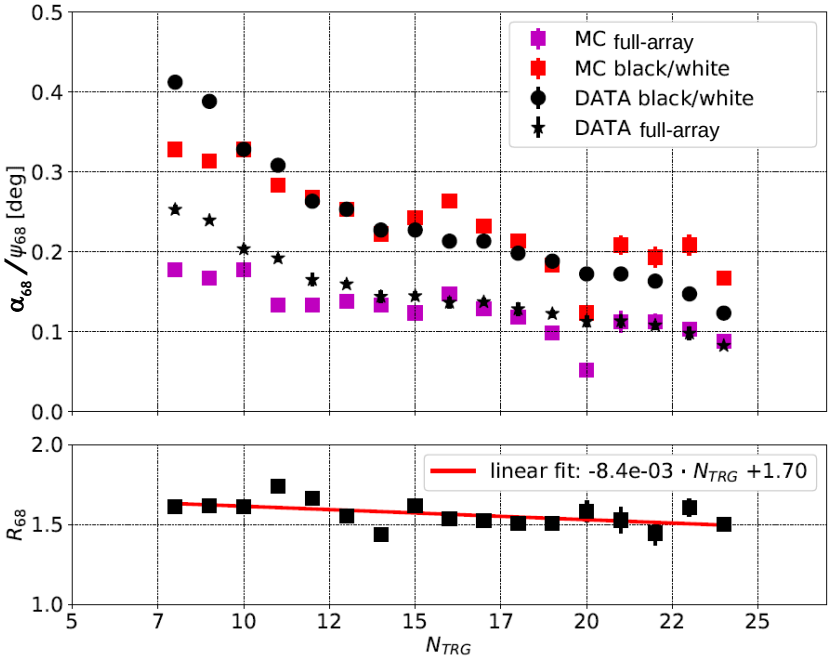

Figure 5.21: HiS28 angular resolution with chessboard method. Top: ψ^{68} as a function of total triggered stations, N_{TRG}. Black dots: ψ^{68} for data run 25/03/2015. Red squares: ψ^{68} for MC. Purple squares: α^{68} for MC (full array angular resolution). Black stars: estimated data full array angular resolution, $\alpha^{data,68}$, obtained with equation 5.5. (b) Ratio between MC ψ^{68} and α^{68}, as a function of the triggered stations, N_{trg}. Red line: linear fit.

Results. Figure 5.20(b) gives the distribution of $\psi_{Black/White}$ for one data run (black), showing a good agreement with the expected distribution for the MC (red). The MC full-array angular error distribution, $\alpha_{FullArray}$ (purple) shows a peak at lower angle w.r.t $\psi_{Black/White}$.

The upper pad of figure 5.21 shows the distribution of $\psi^{68}_{Black/White}$ (i.e. $\psi_{Black/White}$ at 68% of containment) as a function of the total number of triggered stations, N_{TRG}. Again, a good agreement is observed between data and MC. Assuming two completely independent sub arrays, the angle $\psi^{MC}_{Black/White}$ (red squares) should be twice larger than $\alpha^{MC}_{FullArray}$ (purple squares) (Alexandreas et al., 1992). The factor 2 comes from the fact that (a) two independent measurements with about the same error are used, with the two errors added quadratically, (b) each sub array has half of the stations in the full array (Merck et al., 1996; Sciascio and Rossi, 2007). The lower pad of figure 5.21, showing the ratio $R_{68} = \psi^{68}_{Black/White}/\alpha^{68}_{full-array}$ as a function of the total number of triggered stations, N_{TRG}, shows that this assumption is not

correct for this case. The reason for this is that the two sub arrays are not fully independent, due to the full-array core used in the reconstruction. A linear fit returns:

$$R_{68} = 1.7 - 8.4 \cdot 10^{-3} \cdot N_{TRG} \tag{5.4}$$

with an average value $< R_{68} >= 1.55$ for $N_{TRG} \in [10, 24]$. The HiS28 angular resolution as a function of the event multiplicity can be finally obtained with the following relation:

$$\alpha^{68}_{data}(N_{TRG}) = \psi^{68}_{data}(N_{TRG})/R_{68}(N_{TRG}) \tag{5.5}$$

The result of equation 5.5 is shown in upper panel of figure 5.21 (black stars): an average value $< \alpha^{68}_{data} >= (0.15 \pm 0.05)^\circ$ is obtained, compatible with the MC expectation for the full-array, $< \alpha^{68}_{MC} >= (0.12 \pm 0.05)^\circ$.

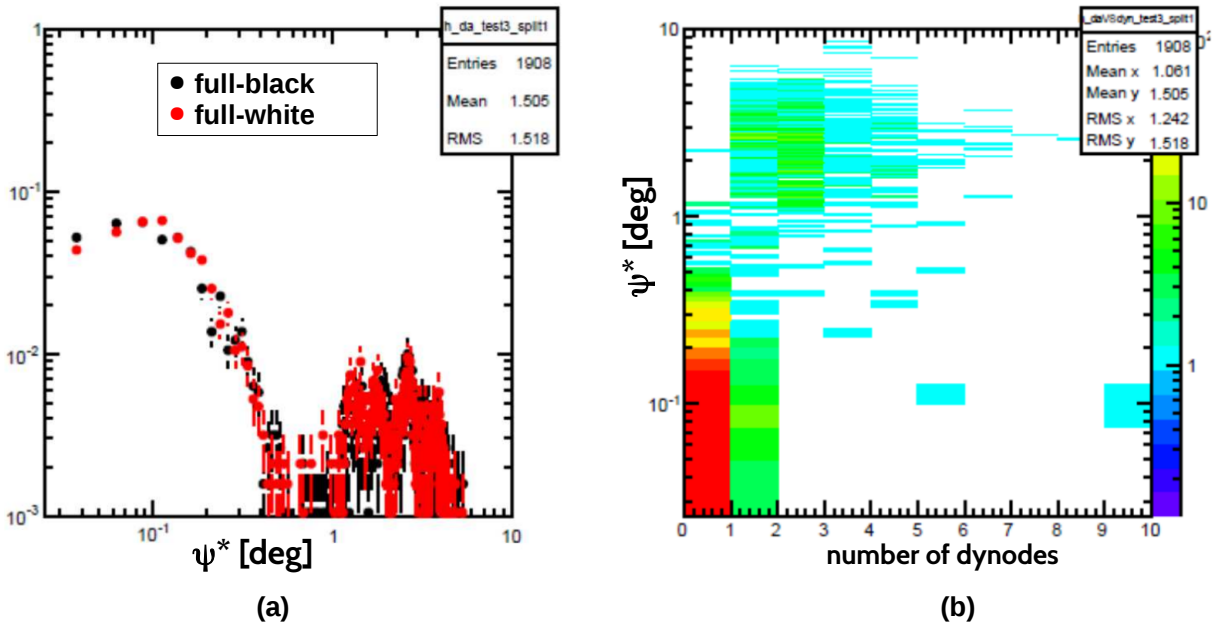

Figure 5.22: (a) Distribution of the space angle, ψ^*, between the reconstructed directions obtained with the full array and one of the two sub arrays. (b) ψ^* as a function of number of dynodes signals. The peaks at $\psi^* > 1^\circ$ depend on the presence of non calibrated dynodes signals times in the array events, that introduce a systematic mispointing angle in the arrival directions reconstruction.

Data quality check. The chessboard analysis is also a useful tool to check the data quality and the reconstruction procedure. An example is given in figure 5.22, showing a result obtained in the early stage of the HiS28 data processing and reconstruction.

Figure 5.22(a) shows the distributions of ψ^*, space angle between the two reconstructed directions obtained with the full array and one of the two sub arrays. Several peaks are observed at $\psi^* > 1^\circ$, indicating something wrong in the data and/or in the event reconstruction. After several checks, the peaks were found to be correlated with the number of stations with dynode (instead of anode) signals used in the reconstruction, as shown in figure 5.22(b). In particular, it was found that the times of the dynodes channels were not correctly calibrated, introducing a systematic mispointing between the different arrays.

5.5 Summary and conclusions

This chapter introduced the TAIGA-HiSCORE 28 detector, and presented the analysis performed on the data collected during the three observation seasons 2015/16, 2016/17 and 2017/18. The detector consists on the extension up to 28 stations of the TAIGA-HiSCORE 9 array (chapter 4), and represents the first step of the $1\,\mathrm{km}^2$ TAIGA detector. The larger instrumented area ($0.25\,\mathrm{km}^2$), the reduced station spacing ($106\,\mathrm{m}$), and optical boxes tilted 25° southward have the goal to maximize the detector sensitivity below $100\,\mathrm{TeV}$, in particular to the gamma-ray flux coming from the Crab nebula.

The main part of the data analysis focused on the array time calibration, which is needed to correct the systematic station time offsets that worsen the detector angular resolution, and introduce a systematic mispointing. A partial LED array calibration is used to check the detector performance, showing a single station time resolution, $\sigma_t \sim 0.3\,\mathrm{ns}$. The LED calibration is also used as a reference for the different full-array calibration methods, and actively used in the hybrid time calibration. A preliminary calibration method (HD), based on the a *Residual correction* iterative procedure, with pre-calibrated station offsets (PMT transit times), shows large difference up to $5\,\mathrm{ns}$ between the starting values and estimated corrections. As discussed in chapter 3, this result is a clear indication for a partial reduction (not full correction) of the average detector mispointing. As an alternative to the HV method, the hybrid calibration method (HYB, presented in chapter 3) has been tested on the HiS28 data, showing a better agreement with LED calibration, and a higher stability over the season. An average mispointing of $\sim 0.05^\circ$ is observed between the HV and HYB calibration methods. Finally, a systematic study of the HYB calibration results returns two interesting results: (a) using only 6 LED calibrated stations it is already possible to achieve a stable calibration; (b) the method can be used to check the data quality, being able to highlight strange behaviours of few isolate stations.

The shower reconstruction returned interesting results as well. A dedicated MC simulation has been used to estimate the reconstruction accuracy for the EAS core (using ADF model) and arrival direction (using PARAB model), obtaining an angular resolution $\alpha_{68} \leq 0.15^\circ$ for $N_{trg} \geq 10$. The data-MC comparison showed a good level of agreement for the core and arrival direction acceptance. Looking more in detail, the analysis of the reconstructed θ angle distribution revealed a higher energy threshold in the data (compared to detector response

simulation), estimated to be ~ 80 TeV for proton, and ~ 50 TeV for gamma-ray. The detector angular resolution is also estimated applying the chessboard method on the experimental data. The results confirmed the MC expectation, returning a full-array angular resolution $\alpha_{68}^{HiS28} \leq 0.15^{\circ}$ for multiplicity ≥ 10.

All the analysis presented here, from the LED and HYB calibration revealed to be also useful tools to check the data quality, and are proposed to be part of the the standard TAIGA-HiSCORE data analysis chain.

-.

Chapter 6

The CATS-LIDAR detection with the TAIGA-HiSCORE 28 timing array

The analysis of the HiS28 data collected during observation season 2015/16 led to a serendipitous discovery: the detection of short-time intervals with very high trigger rate, characterized by high amplitude signal events that did not fit with the normal EAS amplitude-time patterns. Eventually, this was associated with the 532 nm laser of the Cloud-Aerosol Transport System (CATS) on-board the International Space Station (ISS). The signal has been observed in several runs during the two observation seasons 2015/16 and 2016/17 thanks to the fortunate combination of the ISS orbital trajectory and the location of the TAIGA experiment that favour vertical ISS passages (close to Zenith) with a few days repetition period.

The CATS laser beam turns out to be a unique tool to verify the TAIGA-HiSCORE direction reconstruction precision. In particular, the absolute detector pointing can be verified (and corrected) based on the knowledge of the ISS position from independent sources. Such an absolute pointing calibration of the TAIGA-HiSCORE detector is particularly important, while a strong gamma source has not et been detected.

This chapter presents the analysis of the CATS signal detected with the HiS28 detector. Section 6.1 presents the CATS experiment (section 6.1.1), the analysis of the ISS-events alone to verify the station time resolution and detector angular resolution (section 6.1.2), and in combination with the CATS data to obtain a consistent description of the detection process (sections 6.1.3). Section 6.2 presents the combined analysis of the ISS-events with the independent CATS-LIDAR light detection obtained with the robotic optical telescope MASTER-Tunka. Finally, section 6.3 discusses possible utilization of the ISS-events for TAIGA-HiSCORE calibration and station/array performance checks. In particular, a time calibration of the HiS28 array is performed using the ISS-events (section 6.3.1), comparing the results with those obtained by standard time calibration methods (see section 5.3).

6.1 Observation of the CATS-LIDAR on-board the ISS

This section presents the analysis of all the CATS-LIDAR detected passages during observation seasons 2015/16 and 2016/17. A total of 11 ISS passages have been detected and analysed, as reported in tables 6.1 and 6.2.

First, a brief description of CATS is given, together with the CATS data used in the analysis. The HiS28 ISS-events are introduced, describing the main signal features, the reconstruction methods, and the selection criteria. The combined analysis between ISS-events and CATS data allows to obtain a consistent description of the CATS-LIDAR signal detection with the HiS28 detector array.

Understanding the ISS-events detection process allows to use this special events as a tool for station/array performances check, full array amplitude and time calibration, and test the EAS reconstruction accuracy.

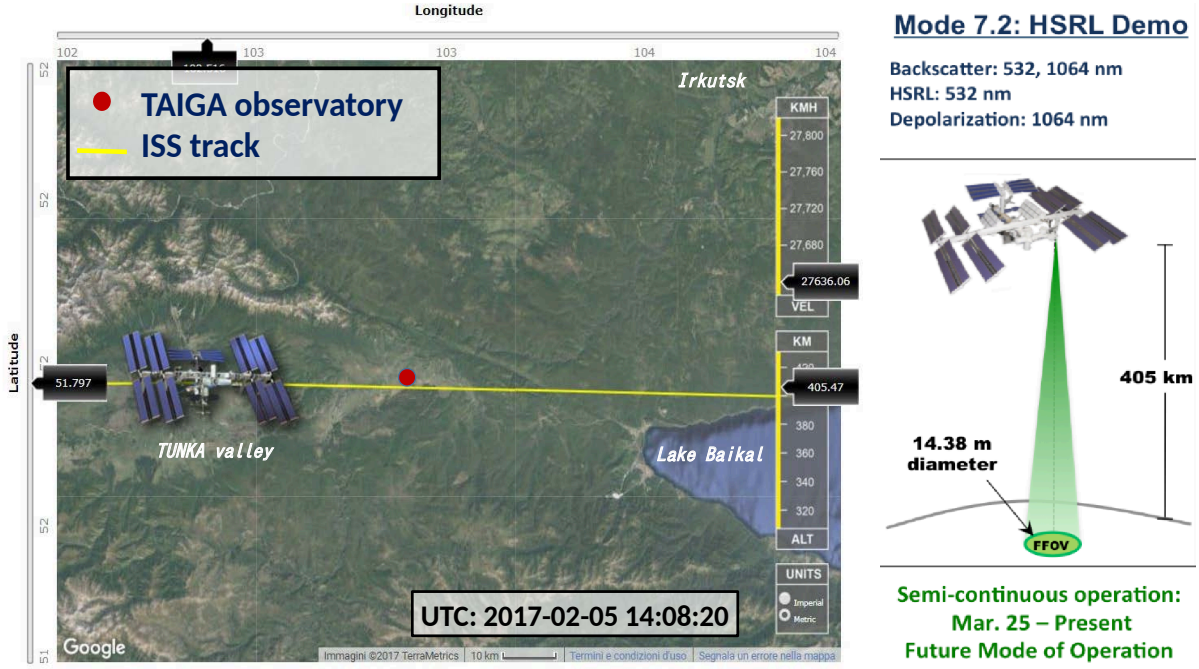

(a) (b)

Figure 6.1: CATS/LIDAR detection with the TUNKA-HiSCORE detector. (a) Illustration of the detected ISS passage on 05/02/2016. The yellow line shows the West-to-East trajectory of the ISS, passing almost vertically ($\theta_{ISS} \leq 1°$) above the Tunka site (red dot). The ISS position is shown ~ 10 s before the detection time. Image adapted from ISS-Tracker (2017). (b) Scheme of the CATS-LIDAR operation modes 2, active since March 2015.

6.1.1 The Cloud-Aerosol Transport System (CATS)

The Cloud-Aerosol Transport System (CATS, (McGill et al., 2012)) is a LIDAR remote sensing instrument that provides profile measurements of atmospheric aerosols and clouds, operating since January 2015. The instrument is located on the Japanese Experiment Module-Exposed Facility (JEM-EF (2012)) on the ISS (NASA ISS web page, 2018; NASA, 2015) orbiting at the speed of about $7.66\,\mathrm{km/s}$ on a 51° inclined orbit at an altitude of about $405\,\mathrm{km}$ a.s.l.. Figure 6.1(a) shows a sketch of the characteristic ISS West-to-East passage above the TUNKA site ($51^\circ 48' 35''$ N, $103^\circ 04' 02''$ E, $675\,\mathrm{m}$ a.s.l.), detected by HiS28 on 05.02.2016.

CATS consists of two high repetition rate ($4 - 5\,\mathrm{kHz}$) low intensity ($1 - 2\,\mathrm{mJ}$) 2Nd:YVO4 lasers operating at three wavelengths (1064, 532, and $355\,\mathrm{nm}$), a receiver with a $60\,\mathrm{cm}$ beryllium telescope with a $110\,\mu\mathrm{rad}$ field of view (FOV), and a data acquisition system to provide amplitude and timing of the backscattered photons. The FOV is defined as the angular area of the atmosphere and surface viewed by CATS in a given operation mode. It is configured with four different *i*FOV orientations (*L*eft, *R*ight, *F*ore and *A*ft), each of them of $115\,\mu\mathrm{rad}$, 0.5° off nadir of the +X direction of the ISS. Since March 2015 CATS is operated in mode 2, using only the FFOV (see fig. 6.1(b)). More details on the CATS instrument design can be found in the CATS Algorithm Theoretical Basis Document (ATBD, Yorks et al. (2016)). The CATS Data Products Catalogue (DPC, Palm et al. (2016)) describes the CATS Automated Processing System (CAPS), and the data management structure used to convert the CATS raw data into scientific data products. The final CATS data products are available in Hierarchical Data Format (HDF, theHDFGroup (2018)) to the scientific community.

CATS data The CATS Level 1B data files (CATS collaboration, 2016), used in section 6.1.3, contain information about the ISS position and the CATS-FFOV pointing direction, as a function of UTC time. ISS position information, reported at a rate of 1 Hz, are given in the Broadcast Ancillary Data section (BAD, Hornyak, David M. (2013)), and includes ISS position and velocity vectors in the geocentric Conventional Terrestrial Reference System (CTRS, ISS Program (2008)), and the three ISS attitude angles (yaw, roll and pitch).

The geodetic coordinates for the ISS (ϕ_{ISS}, λ_{ISS}, h_{ISS}) and the CATS-FFOV spot on the earth surface (ϕ_{FFOV}, λ_{FFOV}, h_{FFOV}) are calculated starting from the ISS information found in BAD, together with the known angular offset of the FOV laser line-of-site vectors from the instrument nadir vector. The algorithm used for this calculation are described in the ATBD. The time resolution of the CATS data is $0.05\,\mathrm{s}$, resulting in a spatial resolution of the ISS and the FFOV position on ground of $\sim 350\,\mathrm{m}$ at ISS speed of $7.66\,\mathrm{km/s}$.

6.1.2 HiS28 ISS-events

The standard analysis of the HiS28 data runs revealed the presence of few $\sim 1 - 2\,\mathrm{s}$ short high-rate peaks ($2 - 3\,\mathrm{kHz}$) emerging from the low $\sim 15 - 20\,\mathrm{Hz}$ EAS array trigger rate. An example is given in figure 6.2, showing the array trigger rate for events with multiplicity ≥ 4

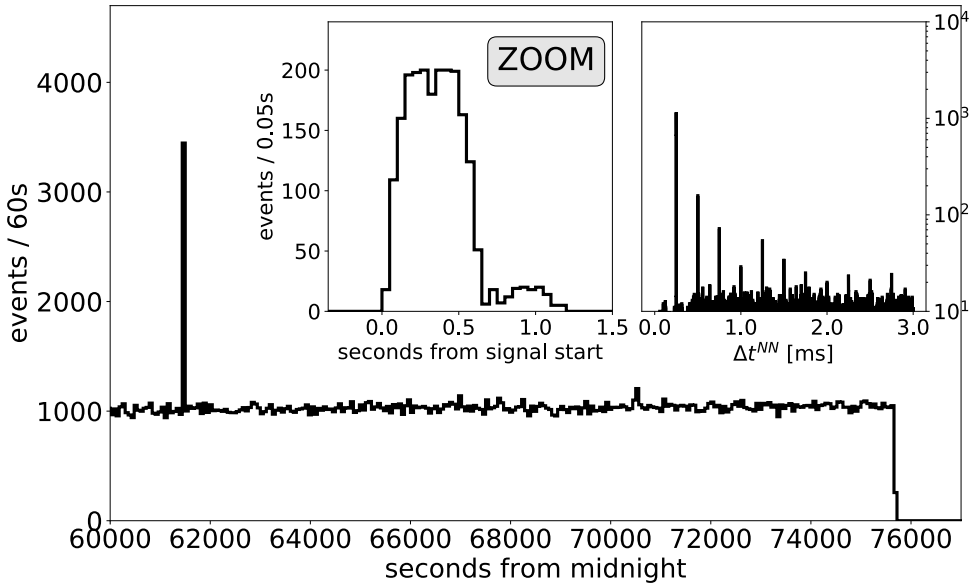

Figure 6.2: Typical HiS28 array trigger rate (run 25.03.2017, event multiplicity ≥ 4) containing the detected CATS-LIDAR signal, indicated by the clear high-rate spike at ~ 61500 sec from midnight above the low EAS trigger rate ~ 15 Hz). Left insert: zoomed trigger rate time structure of the ~ 1.2 s long CATS-LIDAR signal (ISS-events), with a DAQ dead time induced sharp drop after ~ 0.7 s from the signal start. Right insert: time difference between consecutive HiS28 events, Δt^{NN}. The peaks at multiple of $250\ \mu$s are the consequence of the 4 kHz frequency detected laser.

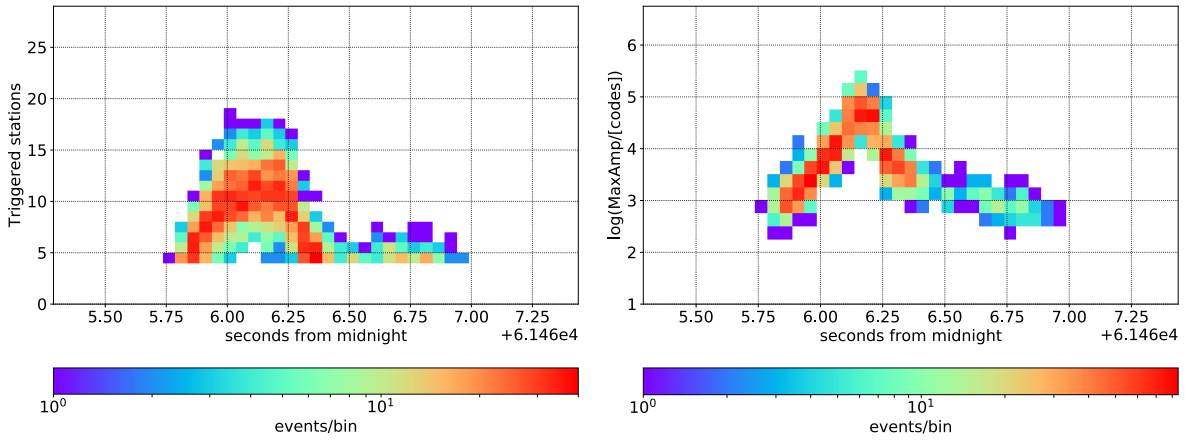

(a) (b)

Figure 6.3: Example of ISS-events time evolution (run: 25.03.2017). (a) Triggered stations $Ntrg$. (b) event max amplitude Amp_{max}.

during run 25.03.2017, with the ISS-events peak at ~ 61500 sec. Looking at the distribution of the time difference between neighbours events, Δt^{NN}, given in the insert on the right of figure 6.2, it is possible to distinguish the ISS-events from the normal EAS-events: the first appear as a delta functions at multiple of 0.25 ms ($= 1/4\,\text{kHz}^{-1}$, with 4 kHz the frequency of CATS-LIDAR laser 2), the second are randomly distributed, appearing as a flat background at this Δt^{NN} scale.

Figure 6.3 shows an example of the time evolution of two important ISS-event variables: the event multiplicity on the left, N_{trg}, and the largest amplitude recorded among the triggered stations on the right, Amp_{max}. The two variables present a similar behaviour: from a starting point of low multiplicity and low amplitude, they both increase up to a maximum point $< t_{rise} > \sim 0.32$ s after the signal start, and soon after followed by a slow fall to the initial state $< t_{fall} > \sim 0.52$ s after the signal start. The maximum number of triggered stations for the single event is limited by the station DAQ readout dead time, ~ 0.6 ms in 2015/16 and ~ 0.4 ms in 2016/17, reducing the single station trigger rate to 1/3 and 2/3 of the CATS-LIDAR pulse rate respectively.

It must be noted that HiS28 stations are operated independently. Therefore, the detected array-rate for the ISS-events depends in a complicated way on the CATS-LIDAR beam intensity and the number of triggered stations for each laser pulse. In addition, local buffering increases the station DAQ readout dead time for a certain initial interval (up to 0.5 s at ISS conditions). These DAQ-related complications make an unbiased rate-intensity precision measurement extremely difficult for the 4 kHz CATS-LIDAR pulses (the TAIGA-HiSCORE DAQ system was designed for local rates ≤ 100 Hz.)

Date	ISS-events (Selected)	CATS data	MASTER Image
16/11/15	2780 (1760)	YES	NO
19/11/15	50 (7)	YES	NO
06/12/15	3830 (1850)	YES	NO
05/02/16	1990 (1320)	YES	NO
08/02/16	3421 (1056)	NO	NO
27/09/16	2040 (1590)	YES	NO
26/11/16	1821 (0)	YES	NO
25/01/17	2300 (1730)	YES	NO
28/01/17	2140 (1300)	YES	NO
25/03/17	2140 (1710)	YES	YES
31/03/17	1780 (13)	YES	NO

Table 6.1: Detected ISS passages with the HiS28 array during the observation seasons 2015/16 and 2016/17. For each passage, the number of triggered (and selected) ISS-events is given, with the selection criteria for the ISS-events are described in section 6.1.2. The last two columns show the passages with available CATS-LIDAR data, and a MASTER telescope detection.

ISS-event arrival direction reconstruction

A distinct feature of the ISS-events is that their time pattern does not fit the EAS arrival time patterns (e.g. equation 2.14). Instead, they agree in first approximation with a plane wave (PW) model (e.g. equation 2.8). To study in detail the ISS-events time pattern, a fast toy MC simulation is used. The goal is to study the best way of reconstructing the arrival direction of the light front coming from a point source at 405 km altitude, using the HiS28 detector array. The photons arrival time at each station is obtained dividing the source-station distance by the speed of light, and adding a Gaussian jitter with $\sigma = 0.5$ ns.

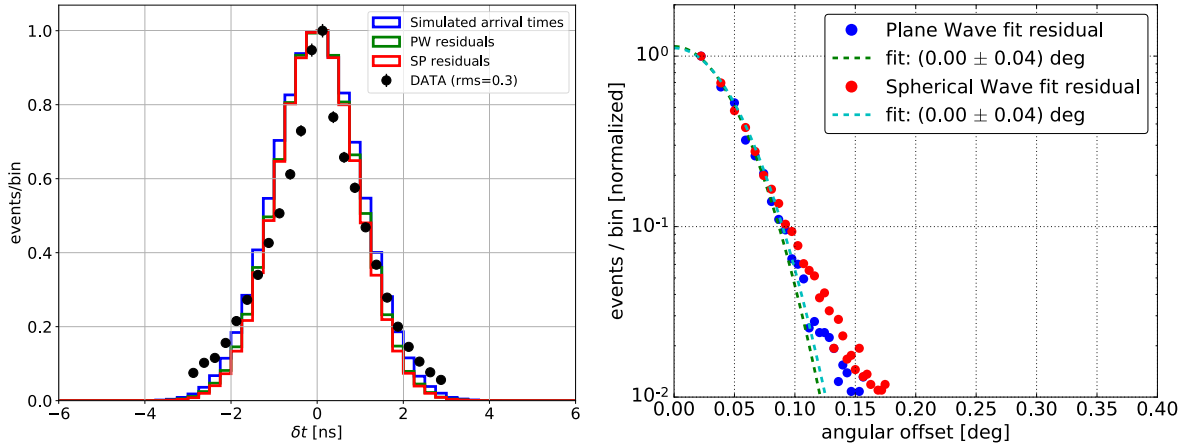

(a) (b)

Figure 6.4: MC simulation for ISS-event direction reconstruction. (a) Comparison between simulated (relative) arrival times at the stations and reconstruction fit residuals for the two front model approximations. The black dots represent residuals distribution for the real data ISS-event (PW fit). (b) Expected angular offset for spherical and planar models. The length of the bins scales with $1/r$.

Two models for the light front approximation are tested: spherical (SP, eq. 4.2) and planar (PW, eq. 2.8). The result of the event reconstruction shows no difference between the two models. A very good agreement is observed between the fit residuals and the simulated relative arrival times distribution (figure 6.4(a)), and the angular offset distributions (figure 6.4(b)). Given the absence of a considerable difference between the two light front models, the PW model is preferred for the lower number of degree of freedom, resulting in a higher stability of the event reconstruction, in particular at low multiplicity ($\sim 10\%$ more successful with respect to the SP model). An iterative procedure is used during the ISS-event arrival direction reconstruction. At each iteration the station with the largest fit residual is excluded, until all the station residuals are smaller than 3 ns. The cut is chosen looking at the distribution obtained with the toy MC (blue line in figure 6.4(a)). The ISS-events PW fit residual distribution

is also given in figure 6.4(a), showing a very good agreement with the prediction. The distribution $r.m.s = 0.3$ ns gives an upper limit for the single station time resolution, in agreement with what shown in chapter 5.

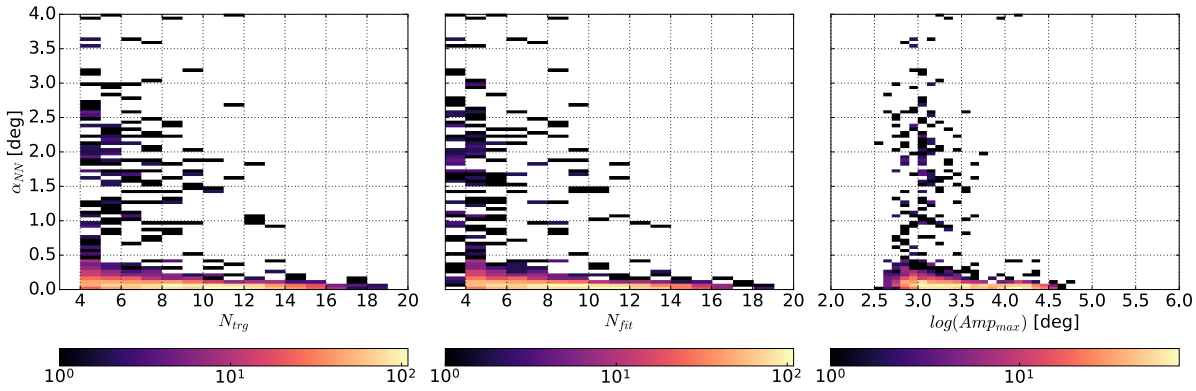

Figure 6.5: α^{NN} distribution as a function of (a) triggered stations N_{trg}, (b) fitted stations N_{fit}, and (c) largest recorded amplitude Amp_{max}.

The ISS-events can be used to determine the HiS28 angular resolution (for this type of PW-events) with high experimental statistics. Based on the fact that the pulses are separated by 0.25 ms, corresponding to $\sim 2.5 \times 10^{-4}$ degree, it is possible to compare the reconstructed directions between neighbouring (in time) ISS-events, assuming their arrival direction identical. Thus, the reconstruction quality can be checked looking at the angular distance between neighbours events reconstructed directions:

$$\alpha_i^{NN} = \arccos(\overrightarrow{dir}_i \cdot \overrightarrow{dir}_{i-1})/\sqrt{2} \tag{6.1}$$

Figure 6.5 shows the correlations between α^{NN} and N_{trg}, N_{fit} (number of stations with residual $\leq$ 3 ns) and Amp_{max}. Large values for α_i^{NN} are obtained for $N_{trg} \leq 4$, $N_{fit} \leq 4$ and $Amp_{max} \leq 10^3$. These values define the quality cuts applied for the ISS-event selection. In a similar way as done with the chessboard method and the EAS events in section 5.4.3, α^{NN} can be used as an estimator of the detector angular resolution, . Figure 6.6(a) shows the projected *r.m.s.* of α^{NN} for all reconstructed (blue dots) and selected (green dots) ISS-events. A Gaussian fit of the last ones returns a value of $\sigma_{\alpha^{NN}} = 0.05°$. The value of α^{NN} at 68% of containment is given in figure 6.6(b), as a function of N_{trg}. At low multiplicity it is very effective the application of the quality cuts, reducing the angular resolution below $0.1°$, while at multiplicity ≥ 10 a resolution of $0.05°$ is reached.

Figure 6.7 shows the ISS-events reconstructed arrival direction in the TAIGA-HiSCORE Alt-Azimuthal coordinates system. An example of the ISS-events evolution in the local sky is presented in figure 6.7(a), showing the reconstructed arrival directions as a function of time: the

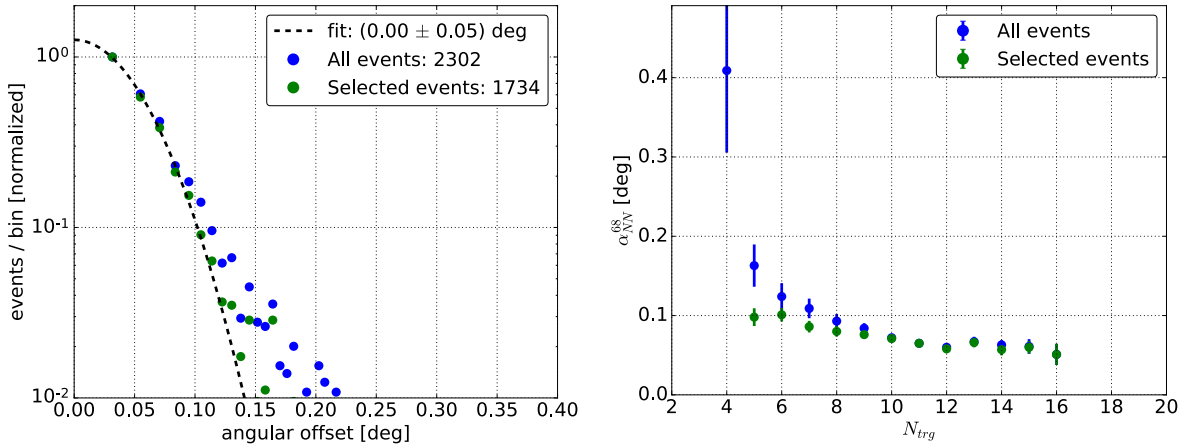

(a) (b)

Figure 6.6: HiS28 angular error for all reconstructed (blue dots) and selected (green dots) ISS-events. (a) Angular offset distribution. The length of the bins scales with 1/r. (b) α_{NN} at 68% of containment as a function of the event multiplicity.

color code gives the ISS-events trigger time, showing the light source movement from West (Azimuth $= 270°$) to East (Azimuth $= 90°$), and passing close to the Zenith. The black line shows the ISS track (also moving from West to East) predicted with SGP4 propagator (for more details see section 6.1.3) few seconds before and after the ISS-events detection. The good overlap of the ISS-events with the ISS track shows once again the high accuracy of the reconstruction. Figure 6.7(b) finally shows the distributions of the reconstructed arrival directions for all the detected ISS passages with selected ISS-events ≥ 500 (see table 6.1).

6.1.3 HiSCORE-CATS combined analysis

For each ISS detected passage (see table 6.1), a combined analysis of the HiS28 and CATS data is performed in order to understand the main characteristics of the CATS-LIDAR laser pulses seen in HiS28. The analysis is performed combining the selected ISS-events (section 6.1.2) with the information from the CATS data described in section 6.1.1.

As discussed in the next paragraph, taking the CATS data without specific checks and corrections, yields to an inconsistent picture when combining the ISS position and the CATS-FFOV on the ground with the ISS-events direction and time. For this reason, the reference position of the ISS as a function of time is obtained independently from the CATS data using the Simplified General Perturbations #4 propagator (SGP4, Hoots, Felix R. and Roehrich, Ronald L. (1980)). SGP4 uses an analytic method based on a general perturbation theory for generating ephemerides for satellites in earth-centred orbits. The propagation algorithm takes as input

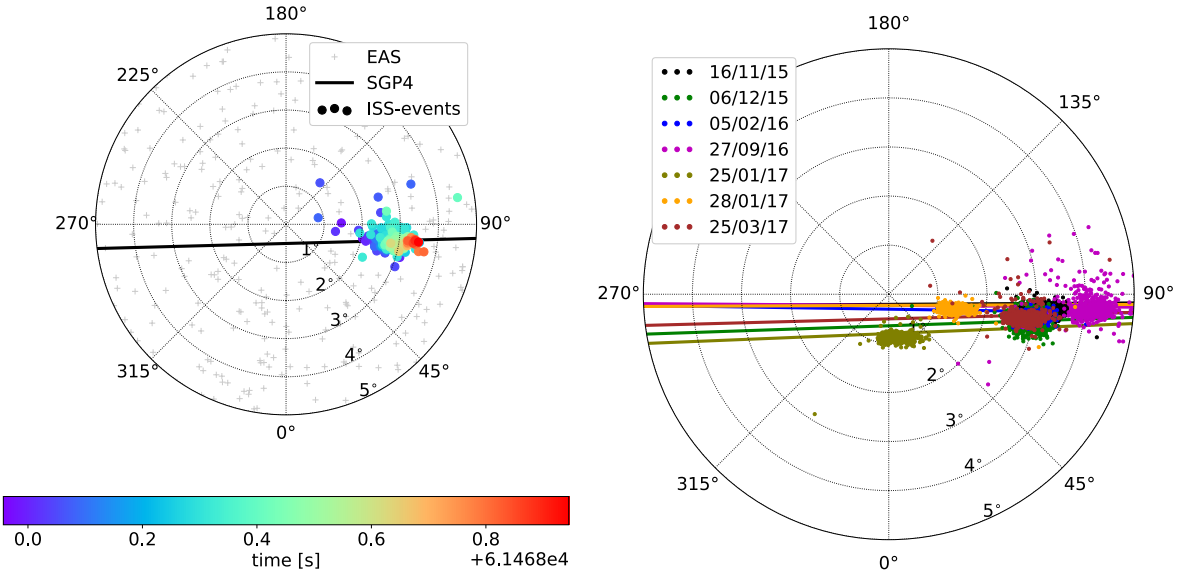

(a) (b)

Figure 6.7: ISS-events reconstructed direction in the HiSCORE Alt-Azimuthal coordinates system. The radial axis represents the Zenith angle, while the angular axis is the Azimuth. The slid lines represent the SGP4 prediction for the ISS orbital trajectory. (a) Time evolution of the reconstructed direction for a single ISS passage (25.03.2017). Grey crosses: EAS directions for $\sim$ 10 min of observation. (b) Reconstructed direction distributions for all the detected passages with selected ISS-events $\geq$ 500 (see also tables 6.1 and 6.2).

the NORAD Two Line Elements (TLE, Kelso, T. S. (2014)), that define the satellite orbit parameters at a given epoch (i.e. reference date). The SGP4 prediction of the ISS position has an error $\sim$1 km at epoch, and grows at $\sim 1 - 3$ km per day. For each detected passage, the TLE set determined at the closest epoch is used (usually few hours).

Figure 6.8(a) shows the ISS looking angles (Zenith and Azimuth) obtained from CATS data (red dashed line) and SGP4 prediction (black line), as a function of time. Comparing the time evolution of the two ISS tracks, a systematic time shift is observed, $\delta t_{CATS} \sim 1 - 2$ s. The main reason for this shift is found to be a missing transformation of the ISS Cartesian coordinates from the Conventional Terrestrial Reference System (CTRS) to the Greenwich True of Date (GTOD) system of reference before calculating the ISS geodetic coordinates, as described in (Yorks et al., 2016). This was reported in Porelli and Wischnewski (2017), and confirmed during direct discussion with CATS/NASA experts. A contribution to δt_{CATS} can also come from the systematic error observed in the CATS data timing due to problems in the ISS-CATS communication. This last effect, and the correction applied, are well described in (Yorks et al., 2016). It is not excluded that the limited precision of the SGP4 prediction could also add a small

Var name	16/11/15	06/12/15	05/02/16	27/09/16	25/01/17	28/01/17	25/03/17
Time (UTC)	22:10:34	14:12:29	14:08:26	16:29:05	16:30:22	15:30:02	17:04:26
θ_{ISS}^{min} [deg]	0.21	0.64	0.3	0.23	0.8	0.23	0.5
t_{rise} [s]	0.35	0.29	0.42	0.3	0.32	0.31	0.36
t_{fall} [s]	0.55	0.38	0.33	0.39	0.5	0.54	0.63
t_{tot} [s]	0.90	0.67	0.75	0.69	0.82	0.85	0.99
$Max(A_{max})$ [dc]	3.8e+04	1.1e+05	6.6e+04	1.7e+06	5.8e+04	1.6e+04	2.8e+05
R_{FFOV}^{mim} [km]	3.8	2.98	3.03	1.15	4.43	4.9	2.1
α_{FFOV}^{mim} [deg]	0.82	0.68	0.79	0.33	0.89	0.93	0.58
δt_{CATS} [s]	-2.1	-1.7	-0.8	-0.45	-3.15	-2.0	-2.0
δt_{TLE} [s]	0.75	0.71	0.75	0.55	0.8	0.78	0.55
passage type	SSS	SSN	SNN	SNN	SSN	SSS	SSN

Table 6.2: Summary table for HiSCORE-CATS combined analysis, reporting the ISS-events signal main parameters. The analysis is performed on runs with selected ISS-events ≥ 500.

contribution to δt_{CATS}. While the systematics here discussed are negligible for the final CATS results (the final resolution on ground is $\sim$5 km), they must be taken into account in this analysis. The decision taken here was applying an "ad-hoc" correction to the CATS data to reduce almost to 0 the difference with SGP4 prediction, as shown in figure 6.8(a). Table 6.2 gives the δt_{CATS} correction applied to each passage.

When comparing the ISS-events reconstructed directions with the SGP4 prediction, an additional small time adjustment is required in order to reach the best agreement. This small correction, $\delta t_{TLE} \sim 0.7$ s, as suggested by the name is believed to be due the limited precision of the SGP4/TLE prediction, since HiSCORE UTC-times are well understood (GPSDO/RbClock controlled) and precisely measured (Budnev et al., 2017b,c).

Figure 6.8(a) gives also the final picture of HiSCORE-CATS combined analysis, after correcting for the systematic errors described before. The ISS-events reconstructed directions not only (almost) perfectly match the ISS track (as shown already in fig. 6.7), but also its time evolution. A confirmation of the correct data alignment is presented in figure 6.9(a), where the ISS-events Amp_{max} time evolution (blue dots) is plotted against the distance of the CATS-FFOV spot on ground from the center of the HiS28 array (red solid line). As expected, the minimum of the FFOV distance coincide with the maximum of the recorded Amp_{max}. The correlation between Amp_{max} and CATS-FFOV distance is given in figure 6.9(b), showing the expected behaviour of a detected signal as a function of the distance of the detector from its source. Finally, figure 6.10 shows a 3D illustration of the 25.03.2017 ISS passage above the HiSCORE site.

The result of the combined HiSCORE-CATS analysis presented in this section is that HiSCORE detects unscattered light coming directly from the CATS laser. This component, here dubbed *direct light*, is interpreted as the tail of the CATS-LIDAR laser beam intensity distribution, that

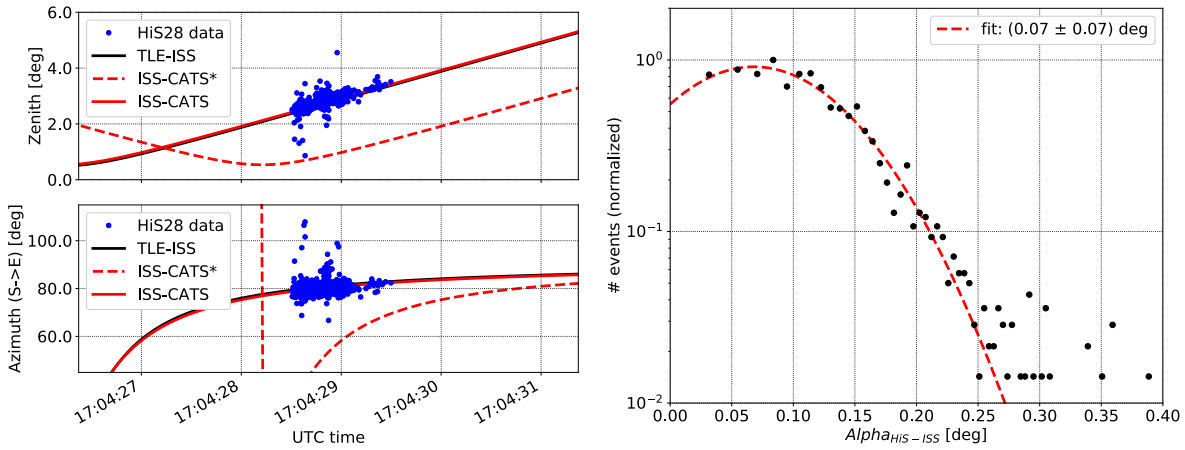

(a) (b)

Figure 6.8: HiSCORE-CATS combined analysis: ISS position reconstruction for run 25.03.2017. (a) ISS Zenith (top) and Azimuth (bottom) looking angles vs UTC time, for SGP4 prediction (black line) and CATS data (full/dashed red lines: after/before δt_{CATS} correction). On top the reconstructed direction for the ISS-events (blue dots). (b) Angular offset between ISS-events reconstructed direction and the ISS position.

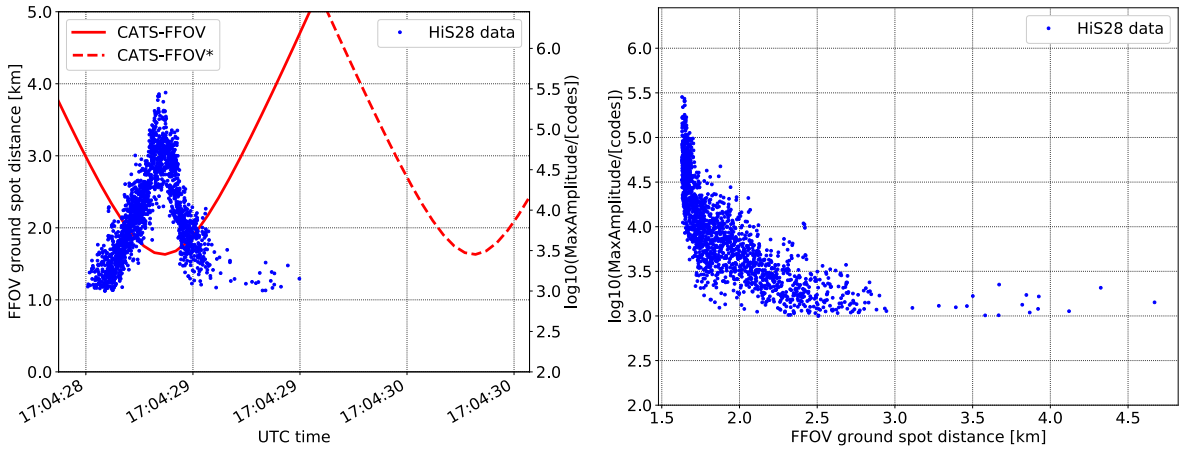

(a) (b)

Figure 6.9: HiSCORE-CATS combined analysis: CATS-FFOV position for run 25.03.2017. (a) CATS-FFOV distance from HiS28 (red solid line) and ISS-event Amp_{max} (blue dots) as a function of time. For comparison, the CATS-FFOV distance before δt_{CATS} correction is given (red dashed line). (b) ISS-events Amp_{max} vs CATS-FFOV distance.

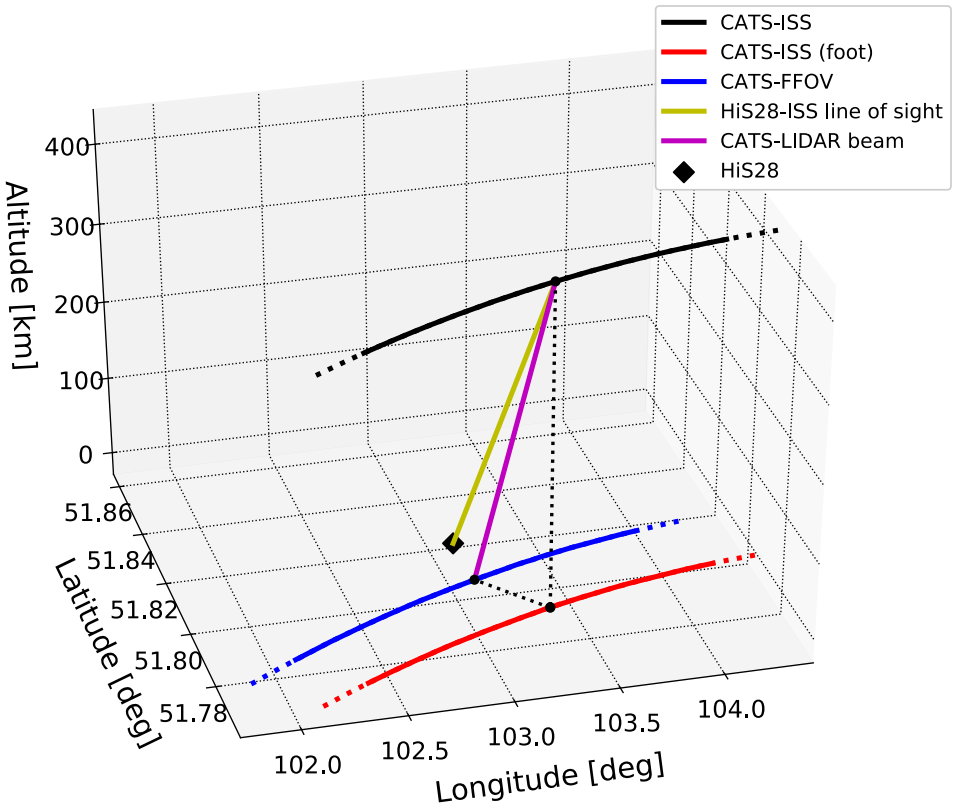

Figure 6.10: 3D visualization of a CATS-LIDAR detected passage (run 25.03.2017). The three tracks represent the ISS orbit (black), its foot point on Earth surface (red line) and the CATS-LIDAR FFOV spot on ground (blue line). The purple and yellow segments respectively show the FFOV laser trajectory and ISS line of sight from the TAIGA-HiSCORE location (black diamond) at the moment the larger Amp_{max} is detected.

is predicted by CATS to be Gaussian with 1σ ground spot diameter ~ 15 m.

6.1.4 Cloud-scattered light detection

The analysis of the CATS-LIDAR light detected by HiS28 revealed the presence of a secondary components, referred to as *cloud light*, different from the *direct light* discussed above. Figure 6.11(a) shows the ISS-events reconstructed directions for the full 06.12.2015 passage. This plot shows the sky for $\theta \leq 30°$, different from the zoomed region ($\theta \leq 5°$) shown in figure 6.7. At large zenith angles ($10 - 20°$), and for a short time interval (~ 300 ms) before the *direct light* detection, a fast moving light source is detected. This source seems not to be related to the ISS track in figure 6.11(a). Eventually, the *Cloud light* was found to be originated when the CATS-

LIDAR laser hits clouds at ~ 10 km height (e.g. ice-clouds), with consequent scattering of the light at large angles towards the TAIGA-HiSCORE detector.

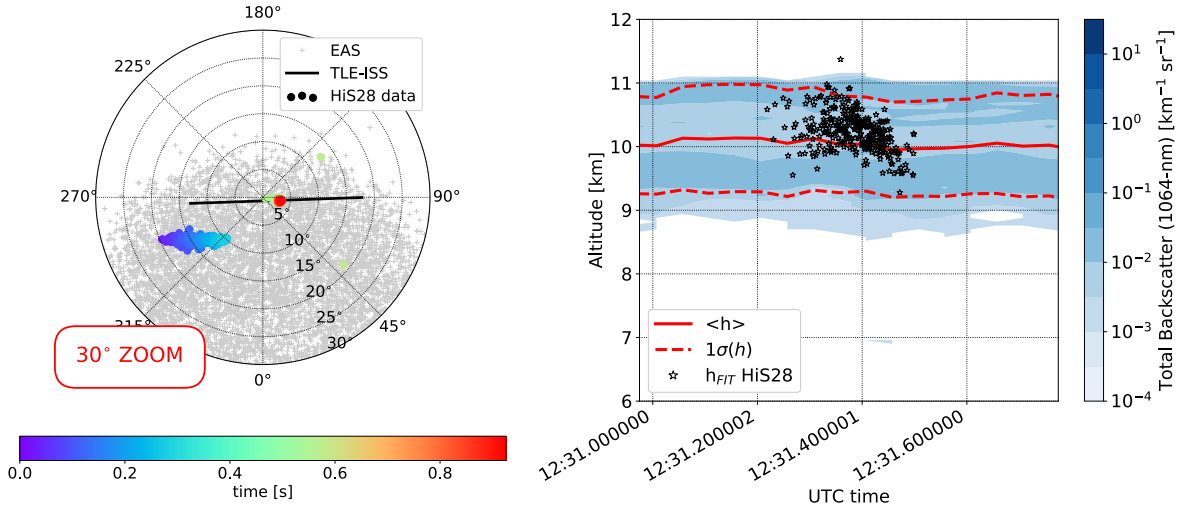

(a) (b)

Figure 6.11: ISS passage (06.12.2015) with detected *cloud light*. (a) Reconstructed direction for both *direct* and *cloud light*, as a function of time. Early events (time < 0.3 s) are *cloud light*. The *direct light* events are aligned on the ISS track (black line). The grey crosses represent the reconstructed direction of the triggered EASs. (b) Reconstructed h_{cloud} for the *cloud light* ISS-events. For comparison, the color plot dive the CATS measured backscattered light as a function of the atmosphere altitude. According to CATS classification, the scattering region is associated with ice-clouds.

This *cloud light* secondary components is used here to test the ISS-events reconstruction precision, the HiSCORE-CATS data alignment obtained in the previous section, and investigate the possibility of studying the atmosphere using LIDAR forward-scattered light with a ground based detector like TAIGA-HiSCORE. The test consists in reconstructing the clouds height using the ISS-events reconstructed directions and the information on the ISS and the CATS-FFOV from the CATS data. Figure 6.12 sketches how the CATS-LIDAR light is scattered by the cloud and redirected toward the HiSCORE detector. The cloud altitude, h_{cloud} is given by:

$$h_{cloud} = R_0 / \tan \psi \tag{6.2}$$

where R_0, the distance of the projection on the ground of the point P_0 from HiSCORE, can be

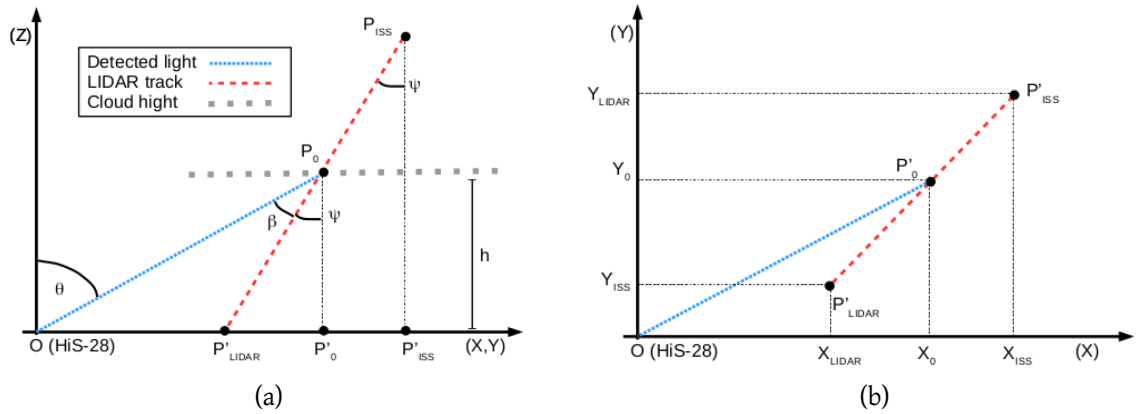

Figure 6.12: Geometrical scheme for CATS-LIDAR light scattering by clouds toward the HiSCORE detector. Red dashed line: CATS-LIDAR beam trajectory. Light-blue dotted line: detected *cloud light*. Grey dots: clouds height. (a) X-Z and (b) X-Y plane views.

expressed as:

$$R_0 = \sqrt{X_0^2 + Y_0^2} \tag{6.3a}$$

$$X_0 = X_{FFOV} + (X_0 - X_{FFOV}) = X_{FFOV} + (X_{ISS} - X_{FFOV})h_{cloud}/h_{ISS} \tag{6.3b}$$

$$Y_0 = Y_{FFOV} + (Y_0 - Y_{FFOV}) = Y_{FFOV} + (Y_{ISS} - Y_{FFOV})h_{cloud}/h_{ISS} \tag{6.3c}$$

Replacing the expression for R_0 given in 6.3 in equation 6.2, h_{cloud} can be obtained from the following second grade equation:

$$ah_{cloud}^2 + bh_{cloud} + c = 0 \tag{6.4}$$

where

$$a = \tan^2\psi - \tan^2\theta \tag{6.5a}$$

$$b = -2\left[R_{FFOV}^2 - (X_{ISS}X_{FFOV} + Y_{ISS}Y_{FFOV})\right]/Z_{ISS} \tag{6.5b}$$

$$c = R_{FFOV}^2 \tag{6.5c}$$

Equations 6.4 and 6.5 show the correlation between h_{cloud} and the ISS position $(X_{ISS}, Y_{ISS}, Z_{ISS})$, the CATS-LIDAR FFOV ground spot location (X_{FFOV}, Y_{FFOV}), the FFOV pointing angle ψ, and the reconstructed arrival direction angle θ. Figure 6.11(b) shows the reconstructed values for h_{cloud} as a function of time (black stars), obtained from the CATS data and the ISS-events re-

constructed direction. For comparison, the CATS measured backscattered light altitude profile is also given (color plot), showing a very good agreement with the h_{clouds} values obtained by HiSCORE.

Studying light propagation in the atmosphere by a ground instrument like TAIGA-HiSCORE might complement the ISS-LIDAR technology by detecting the forward scattering component, as demonstrated for scattering in dense clouds.

6.2 HiSCORE-MASTER combined analysis

In May 2017, a few attempts were made to obtain an independent detection of the ISS/CATS-LIDAR with the robotic telescope MASTER-Tunka (Lipunov et al., 2010), located ~ 500 m from the centre of the HiS28 array. Eventually, on 25.03.2017 the MASTER-Tunka very wide-field camera (VWF) successfully recorded the CATS laser passage, as shown in figure 6.13(a)). This synchronous and independent observation of the CATS-LIDAR signal yields a stable, reliable and precise measurement of the ISS position (track), that allows to check HiS28 absolute pointing precision [1]. The astrometric analysis of the MASTER picture here presented is performed using *Astropy-v2.0.1* (Robitaille et al., 2013).

Since the MASTER detection consists of a single 10 s exposure picture, it is only possible to retrieve the precise sky coordinates of the ISS track, but not its time evolution. For this reason, in order to reduce the uncertainties of the analysis, the estimation of HiS28 pointing accuracy is obtained comparing only a specific and well defined part of both MASTER and HiS28 CATS-LIDAR detections, i.e. the brightest parts, which are in the following referred to as *peaks*.
The *peak* of the MASTER image is calculated with a weighted average of the pixels coordinates, using the pixels intensity as weight. The result is shown in figure 6.13(b). The HiS28 *peak* consists of ISS-events inside a 0.1 s time window centred around the events with the highest Amp_{max} recorded. To improve the quality of reconstruction of the selected events, a cut on the number of triggered stations ($N_{trg} > 6$) and on the amplitude ($Amp_{max} > 5e4$ codes) are also applied.

Before comparing the two observation *peaks*, one of the two has to be corrected for the parallax effect. Due to the close distance of the ISS (~ 405 km) and the different locations of the two detectors (different local system of reference), the ISS positions observed in the two local (Alt-Azimuthal) systems of reference are projected into different points in equatorial coordinates. The result of the parallax effect is clearly visible in figure 6.13(b), showing the projection in equatorial coordinates of the ISS looking angles (predicted with SGP4) in the two detectors systems of reference. Due to the short duration of the signal and the close location of the two detectors (~ 500 m), the parallax correction, obtained comparing the SGP4 predictions, results in a small linear translation: $\delta R.A. = 0.069°$ and $\delta Dec = 0.046°$. After correcting for the parallax effect, the MASTER *peak* coordinates are projected into the HiS28

[1] From public available data, the ISS position determination is too imprecise, and does prevent pointing precision of $0.1°$ or less.

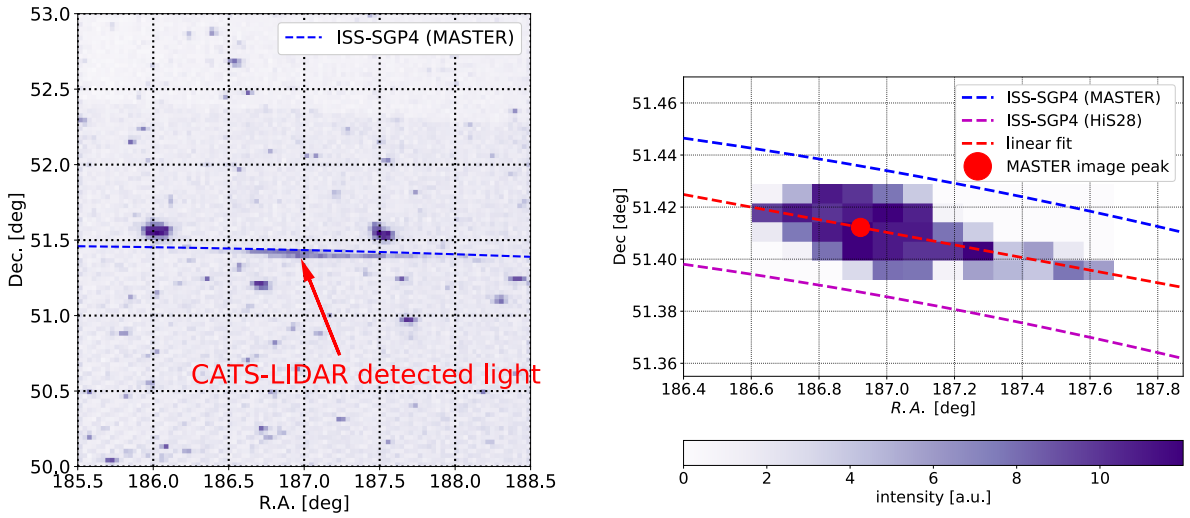

(a) (b)

Figure 6.13: MASTER detection of CATS-LIDAR light on 25.03.2017 ISS passage. (a) CATS-LIDAR optical detection obtained with the MASTER-VWF camera in equatorial coordinates. Blue dashed line: ISS track obtained with the SGP4 propagator. (b) MASTER image analysis: the position of the brightest point (red dot) is determined with a weighted average of the image pixels coordinates, using the pixel intensities as weight. Red line: linear fit of the pixels coordinates, using the pixels intensities as weight. Blue (purple) line: predicted ISS track projection in equatorial coordinates, for an observer in the MASTER (HiS28) system of reference. The prediction for the ISS tracks are obtained initializing SGP4 with the closest epoch TLE set to the passage.

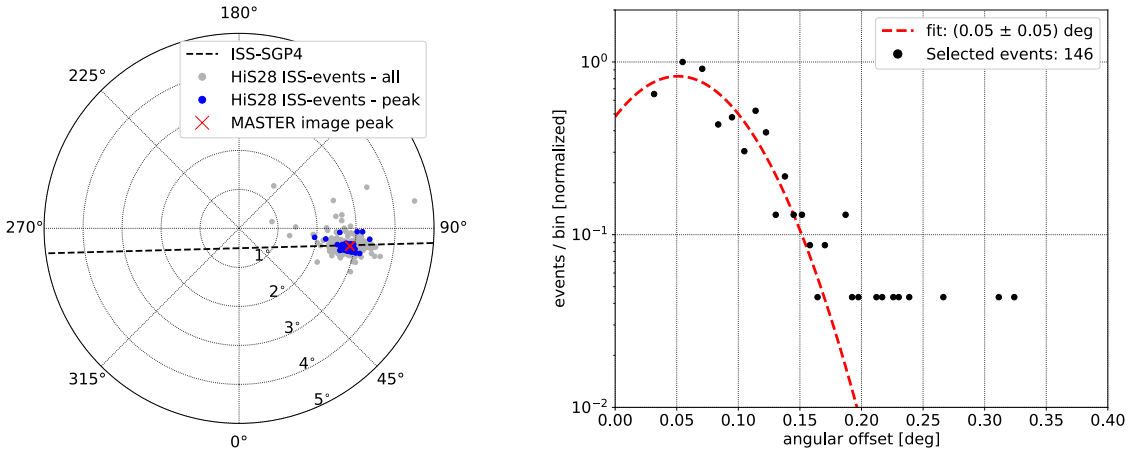

(a) (b)

Figure 6.14: HiS28-MASTER combined analysis. (a) Reconstructed arrival directions for the ISS-events as detected with HiS28. Grey dots: full passage. Blue dots: selected *peak* ISS-events. The red cross corresponds to the MASTER image peak in the HiS28 system of reference. (b) Estimated angular offset between HiS28 reconstructed *peak* events and the MASTER image *peak*. A systematic offset of $\sim 0.05 \pm 0.05^{\circ}$ is obtained.

horizontal system (red cross in fig. 6.14(a)).

Finally, the HiS28 pointing precision, α_{MIS}, is obtained by fitting the distribution of the angular offset between the MASTER peak and the HiS28 peak events. The result is shown in figure 6.14(b). Taking into account all the uncertainties of this analysis, an upper limit on the HiS28 mispointing is set, with $\alpha_{MIS} \lesssim 0.1^{\circ}$. From further coincident HiSCORE-MASTER observations (including also the high-resolution MASTER-II camera), it would be possible to improve the precision of this method, to finally allow a fine adjustment of the HiSCORE pointing.

6.3 ISS-events applications

The analysis performed in the previous sections gives a clear and coherent picture of the CATS-LIDAR light detection with the HiS28 detector array, making of the ISS-events a perfect test-beam to check the HiSCORE detector performance. The following list shows how the ISS-events (from both *direct* and *cloud light*) have been, or can be used:

1 Single station time resolution measurements (section 6.1.2)

2 Check array angular resolution (section 6.1.2) and absolute pointing precision (section 6.2)

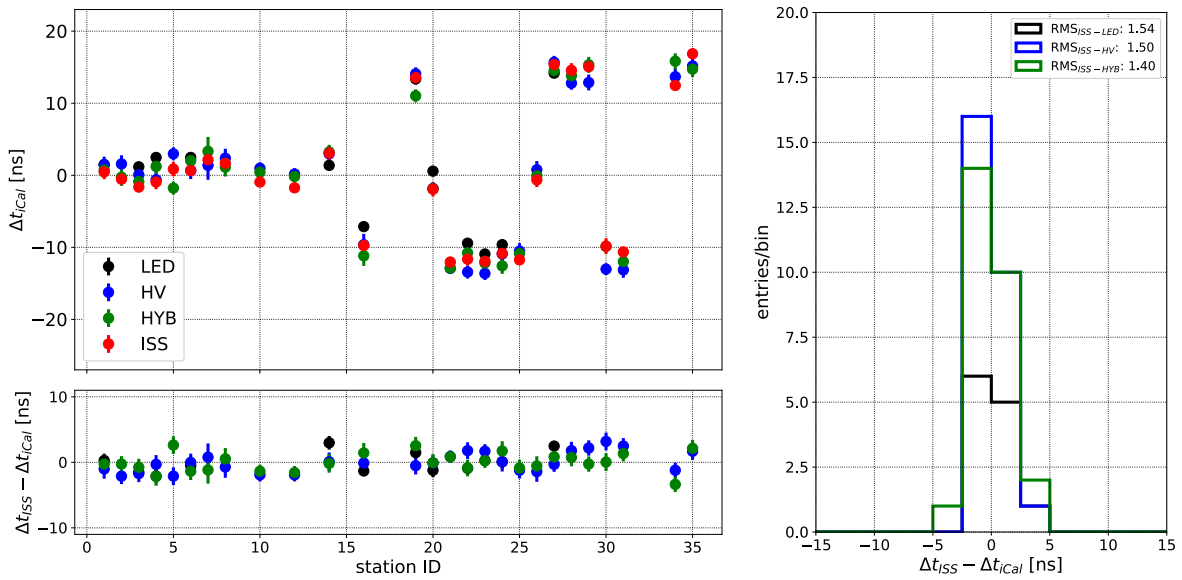

(a) (b)

Figure 6.15: Array time calibration. (a) Top: calibration constants, Δt_{iCal} obtained with different methods, as a function of station ID. Bottom: calibration constants difference, $\Delta t_{ISS} - \Delta t_{iCal}$, as a function of station ID. (b) Calibration constant difference distributions.

3 Array time calibration: station time offsets measurement (section 6.3.1)

4 Check of station/array amplitude calibration (see figure 6.9(b)).

5 Atmosphere study through forward-scattered LIDAR light detection (section 6.1.4).

6 Perform low level technical checks: optimization of raw data extraction procedures (pulse extraction, amplitude definition), identification of small systematic effects (masked by stochastic dominated EAS analysis)

7 Verification of data-analysis procedures, EAS reconstruction, etc.

The result of the array time calibration performed using the ISS-events from *direct light* (point 3) is presented in the next section.

6.3.1 Array time calibration with ISS-events

This section presents the results of a preliminary HiS28 array time calibration obtained using all the available informations for the 25.03.2017 passage. The calibration is performed in a

similar way as done for the LED time calibration (see section 4.2.1, 5.3): the CATS-LIDAR on the ISS is the light source of known position, and a plane-wave model is used for the light front propagation from the source to the stations. To simplify the calibration procedure, the MASTER *peak* in the HiS28 Alt-Azimuth coordinate system (red cross in fig. 6.14(a)) is used as fixed position for the ISS/CATS-LIDAR.

The time offset for the *i*-th station is given by the difference between the measured, t_i^{ISS}, and the expected, $t_i^{PW(\theta_{ISS},\phi_{ISS})}$, arrival times at the station:

$$\Delta t_i^{ISS} = t_i^{ISS} - t_i^{PW(\theta_{ISS},\phi_{ISS})} \tag{6.6}$$

where $(\theta_{ISS}, \phi_{ISS})$ are the ISS Alt-Azimuth coordinates. Like done for the LED time calibration, a scaling with respect to a reference station is needed, with the time offset for the *i*-th station rewritten as:

$$\Delta t_i^{ISS} = t_i^{ISS} - t_{Ref}^{ISS} - (t_i^{PW(\theta_{ISS},\phi_{ISS})} - t_{Ref}^{PW(\theta_{ISS},\phi_{ISS})}) \tag{6.7}$$

Figure 6.15 summarizes the results of the time calibration using the ISS-events. The top panel of figure 6.15(a) shows the values of the calibration constants obtained with the ISS-events (red dots), as a function of the stations ID. As a comparison, also the calibration constants for the same run, obtained with different methods (LED, HV, HYB), are shown. Despite the simplistic approach, a very good agreement is observed between the "ISS calibration" and the other methods, with the calibration constants distributed in the three characteristic offset groups (see section 5.3), with average values respectively 0, -10, +15 ns. Looking at the distributions of the differences with respect to the other calibration methods (bottom panel of figure 6.15(a) and figure 6.15(b)), they are very well centred around 0, with an $r.m.s \leq 2$ ns, reproducing the same result obtained in section 5.3, where the different calibration methods are compared to each other.

The results obtained using ISS-events to calibrate the full array time offsets are another proof of the important role that the CATS-LIDAR signal can have in the HiSCORE experiment.

6.4 Summary and conclusions

This chapter presented the first ground level observation of the CATS-LIDAR light on-board the ISS by the TAIGA-HiSCORE gamma-ray facility, and by the MASTER-Tunka Robotic telescope. A total of 11 ISS passages have been detected and analysed during observation seasons 2015/16 and 2016/17. The understanding of the detection process turns the ISS CATS-LIDAR into a unique calibration tool, establishing a new method to verify the HiSCORE angular resolution and absolute pointing, and thus preparing TAIGA-HiSCORE for gamma-ray astronomy.

The results of the combined analysis of signal detected by HiS28 (ISS-events) and CATS data are compatible with HiS28 seeing unscattered laser light events coming from the ISS (*direct light*), up to several km distance to the FFOV beam ground spot, well approximated by a plane wave front with sub-ns time jitter. The analysis of the ISS-events reconstructed directions

gives an upper limit estimation for the single station time jitter (0.3 ns) and a full array angular resolution of $\sim 0.05^{\circ}$ at medium-high event multiplicity.

The combined analysis with the MASTER telescope observation gives an estimation for the absolute pointing, $\leq 0.1^{\circ}$. Finally, a full array time calibration is performed, using the ISS-events together with the MASTER detection. The results obtained match with good precision with the results of the other calibration method, making of the CATS test-beam not only a passive tool for performance check, but also an active tool for detector calibration. In a similar way, a calibration of the array stations can be obtained.

Besides the detection of the *direct light*, a different components is observed, named *cloud light*, consisting on the CATS-LIDAR light scattered by ice-clouds suspended in the atmosphere at tens of km altitude, and redirected in the HiSCORE direction. Using the reconstructed directions of this secondary ISS-events component, together with informations on the ISS and CATS FFOV positions, it was possible to reconstruct with very good precision the clouds height (10 km a.s.l.). Studying light propagation in the atmosphere by a ground instrument like TAIGA-HiSCORE might complement the ISS-LIDAR technology by detecting the forward scattering component, as demonstrated for scattering in dense clouds. It is possible that also other instruments using the atmosphere as active target, like Imaging Air Cherenkov Telescopes, will benefit from light sources like the CATS-LIDAR.

Chapter 7

Search for a Crab signal with HiS28 three years data

The last two chapters (5 and 6) presented the analysis of the data collected with the HiS28 array during 3 years of operations. Chapter 5 focused on the array time calibration and the shower reconstruction, proving a detector angular resolution of $\leq 0.2^{\circ}$ for event multiplicity $N_{trg} \geq 10$, while chapter 6 presented the analysis of the serendipitous detection of the ISS/CATS-LIDAR signal, that allowed to estimate the absolute detector mispointing, $\alpha_{Mis} \leq 0.1^{\circ}$.

In this chapter we present the first systematic point source analysis (PSA) developed for TAIGA-HiSCORE in stand-alone mode. Section 7.1 summarizes the main information about the Crab observation at the Tunka site, together with a description of the data sample used for the analysis. Section 7.2.1 presents a qualitative study, based on MC simulation, of the detection potential of the HiS28 array in both stand-alone and hybrid (HiSCORE+IACT) operations. In section 7.3, the PSA is applied to the HiS28 three years data (stand-alone operations), with a focus on the sky region around Crab Nebula as a standard candle. The limitations of the current analysis are discussed, and improvements are proposed to increase the detection potential of the analysis. Finally, section 7.4 presents first results of the analysis of coincidence events, detected with both HiS28 and the first operational TAIGA-IACT during season 2017/18.

The results presented here are not final, as the work is still preliminary and in progress. The main goal is to document the current status of the analysis and its potential for gamma-ray signal detection.

7.1 Crab observation at Tunka site

As discussed in chapters 2 and 5, one of the goals of the new TAIGA experiment is a proof-of-principle for the hybrid Cherenkov technique (HiSCORE+IACT) by detecting the gamma-ray signal from the standard candle Crab ($R.A. = 05^h34^m31.94^s$, $\delta = +22^{\circ}00'52.2''$ in J2000 epoch). To maximize the detector exposure to the Crab, the HiS28 stations have been deployed with a tilting angle of 25° southward, i.e. with the station axis pointing at Zenith $= 25^{\circ}$ (Al-

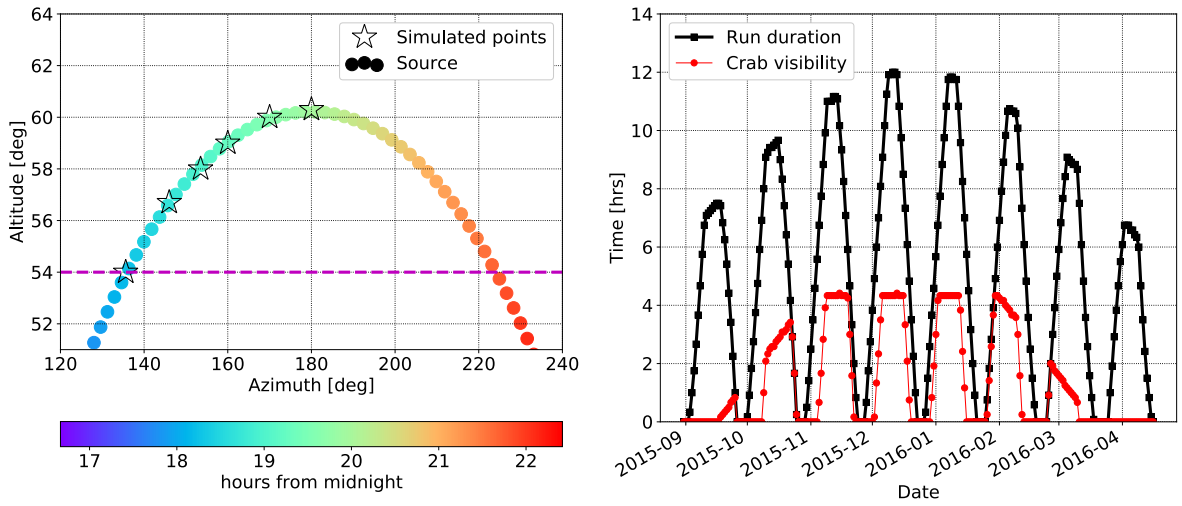

(a) (b)

Figure 7.1: Crab ($R.A. = 05^h34^m31.94^s$, $\delta = +22°00'52.2''$ in J2000 epoch) observation at Tunka site ($51°48'35''$ N, $103°4'2''$ E, 675 m a.s.l.). (a) Crab daily visibility in the local sky for an HiS28 FOV of $30°$ opening angle. Dashed line: minimum altitude for Crab visibility after acceptance cut $\psi < 25°$. Black stars: simulated points for the dedicated MC simulation (discussed in section 7.2.1). (b) Typical seasonal observation schedule at Tunka site (season 2015/16). The detector is put in operation when the Sun altitude $< -18°$ and the Moon altitude $< 0°$. The run duration (black dots) and the exposure to the Crab during the run (red dots) are given as a function of run date.

titude = $65°$) and Azimuth ($N \rightarrow E$) $= 180°$. Figure 7.1(a) shows the Crab visibility in the local sky at the Tunka site ($51°48'35''$ N, $103°4'2''$ E, 675 m a.s.l.), for a HiS28 detector FOV of $30°$ opening angle. The daily detector exposure to the Crab depends on the detector operation conditions, i.e. clear Moonless nights. A typical seasonal operation schedule is given in figure 7.1(b) (season 2015/16), assuming optimal weather conditions and stable detector operations. The black dots show the run duration as a function of date, obtained for Sun altitude $\leq -18°$ and Moon altitude $\leq 0°$, for a total amount of ~ 1100 h of data taking per season. The red dots give the exposure to the Crab during the run. The maximum daily exposure to the Crab is ~ 4.2 h, and it is reduced to ~ 3.7 h after acceptance cut $\psi \leq 25°$ (dashed line in figure 7.1(a), see section 5.4 for details on acceptance cuts). The total exposure to the Crab over one season is ~ 322 h, reduced to ~ 265 h after acceptance cut.

7.1.1 HiS28 three years data sample

The analysis presented here is performed on the complete HiS28 three years data set (2015-2018), i.e. all those runs that went through the full data processing and the event reconstruc-

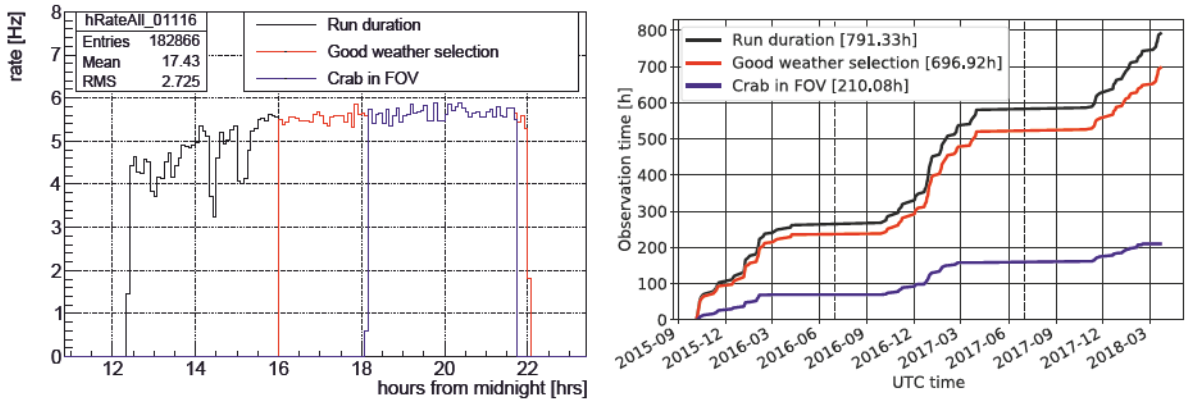

(a) (b)

Figure 7.2: Run selection for HiS28 point source analysis. (a) Run 01.11.2016 event rate for $N_{trg} \geq 4$ and after selection cuts. The full run length is indicated by the black line, while the selected "good weather" interval is given by the red line (stable rate). The blue line shows the time interval when the Crab is inside the detector FOV (25° opening angle). (b) Integrated observation time for all ($\sim$ 807 h, black line) and selected ($\sim$ 704 h, red line) runs, and detector exposure to Crab ($\sim$ 210 h, blue line) as a function of run date. The vertical dashed lines separate (for visualization) the three observation seasons.

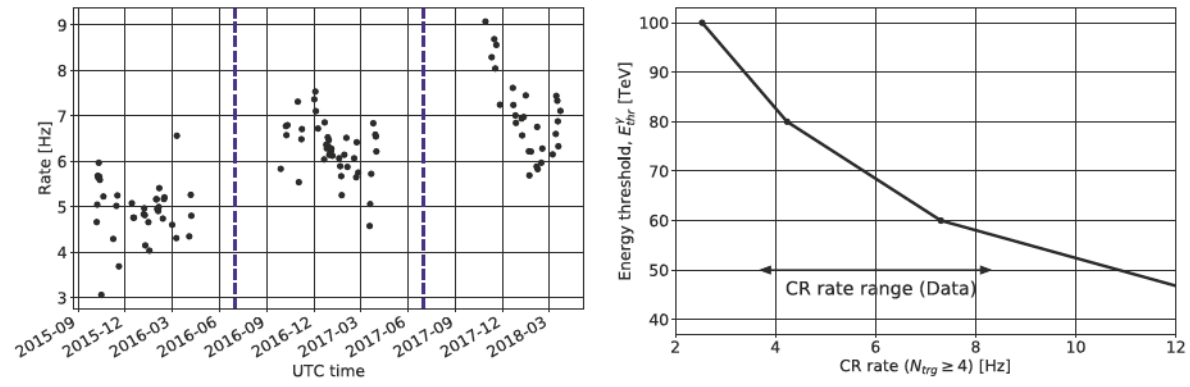

(a) (b)

Figure 7.3: HiS28 event rate after selection cuts, for $N_{trg} \geq 4$. (a) Event rate as a function of run date. The vertical dashed lines separate (for visualization) the three observation seasons. (b) Estimated HiS28 energy threshold as a function of CR rate, obtained with dedicated Crab signal MC simulation.

tion discussed in chapter 5. The data sample consists of 144 nights (runs), for a total observation time of 807 h ($\sim$ 25% of the total 3×1100 h available). A run-quality cut based on the weather conditions is applied to select only runs (or parts of them) with stable rate for $N_{trg} \geq 4$. This reduces to 108 the number of selected runs, for a total observation time of 704 h. The resulting three years detector exposure to the Crab is ~ 210 h, corresponding to ~ 25% of the available exposure time estimated in the previous section (3×256 h). An example of run selection is showed in figure 7.2(a), while figure 7.2(b) gives the cumulative observation time for the three seasons.

Concerning the event selection, besides the standard acceptance cuts shown in figures 5.17(a) and 5.17(b), a *low multiplicity* cut discussed in section 7.2.1 is also applied. The final data sample counts a total of $\sim 1.53 \cdot 10^7$ events. Figure 7.3(a) shows the final event rate for $N_{trg} \geq 4$ and after selection cuts, as a function of the run date, for the three observation seasons. The clear increase of the average event rate as a function of the observation season is due to a lowering of the station trigger thresholds and a reduction of the DAQ readout dead time.

7.2 MC study of HiS28 detection potential

This section presents a qualitative study, based on a dedicated MC simulation, of the HiS28 potential for detecting a signal from the Crab. The sensitivity is estimated for two different search strategies: (a) using an energy dependent search region, proportional to the detector angular resolution, and (b) using a fixed search region, as done with the real data PSA presented in section 7.3.

7.2.1 Crab signal simulation

EAS generation and detector response. A dedicated EAS production (see section 2.3.1) is used for this analysis in order to study in detail the detector performance at energy ≤ 100 TeV. The energy of the primary particles (gamma-ray for signal, proton for CR background) is generated between 20 and 200 TeV, with spectrum $dN/dE \propto E^{-1}$. The energy range up to 200 TeV is chosen to take into account, as much as possible, the edge effects due the "outrigger events", i.e. medium-high energy showers having their core outside the array, and that trigger few stations at the edge of the array. The arrival direction of the primary particle is defined by 6 points on the Crab path in the local sky, as shown in figure 7.1(a) (black stars). For each point, 10^4 EASs are generated, with core location uniformly scattered in a rectangular area, up to 400 m from the array edge.

The detector response (*sim_score*) and the EAS reconstruction are discussed in section 5.4.1. Again, it must be noted that the detector setup in *sim_score* is set to a lower detector energy threshold, E_{thr}, with respect the real experiment. A simple procedure is then used for a rough estimation of the detector response at higher energy threshold: the HiS28 performance figures (effective areas and angular resolution) are shifted to higher energy. The detector threshold is

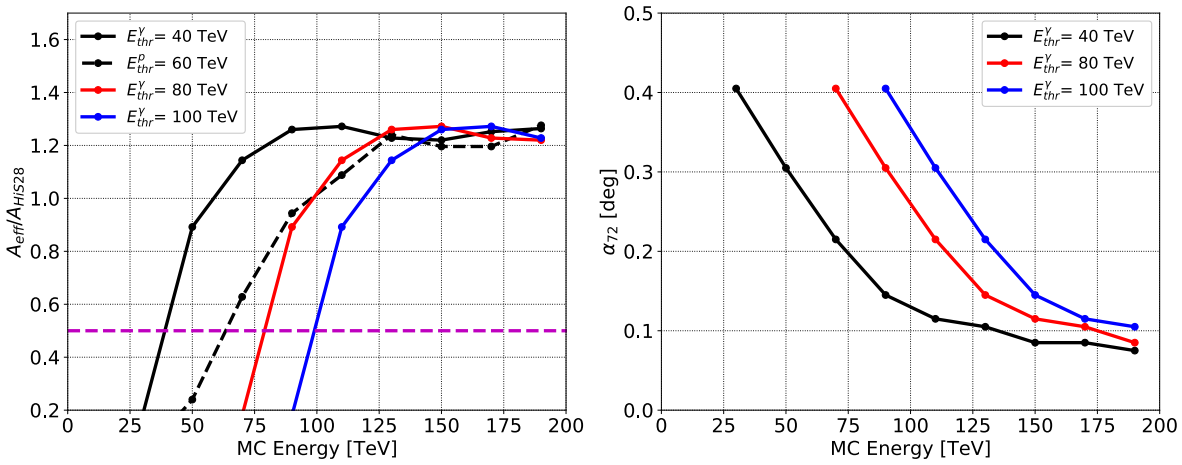

Figure 7.4: HiS28 performance figures after selection cuts, as a function of the primary particle true energy, for different detector energy thresholds. Left: Effective area for gamma-ray (solid lines) and proton (dashed line), normalized to the HiS28 instrumented area ($A_{HiS28} = 0.25\,\mathrm{km}^2$). The purple line gives the energy threshold, E_{thr}, defined as $A_{eff}(E_{thr}) = 0.5 \cdot A_{HiS28}$. Right: Angular resolution.

here defined as the energy at which the effective area is equal to half the instrumented detector area, $A_{eff}(E_{thr}) = 0.5 \cdot A_{HiS28}$. Figure 7.4 presents the effective area (left) and the angular resolution (right) for primary gamma-ray particles, obtained for different energy thresholds. The performance figures are give after acceptance cuts, including the *low multiplicity* cut discussed below.

Low multiplicity acceptance. The detector sensitivity to a point source signal strongly depends on an optimal detector angular resolution. The smaller the angular resolution, the smaller is the number of integrated background events that suppress the signal in the search region. As shown in section 5.4 (figure 5.16(b)), a large angular resolution ($> 0.2°$) is obtained for event multiplicity ≤ 7. The main contribution to the large angular resolution at low multiplicity comes from bad reconstructed outrigger events.

To reduce this effect, the correlation between the angular resolution and the number of triggered stations on the array perimeter, N_{edge}, has been studied. Figure 7.5(a) shows the HiS28 angular resolution (68% containment) as a function of the event multiplicity, for different values of N^{max}_{edge}. The main effect is observed for $N_{trg} \leq 6$, with the angular resolution improved up to $0.2°$ for $N^{max}_{edge} \leq 1$. Based on this result, two *low multiplicity* cuts are applied to events with $N_{trg} \leq 6$, in addition to the standard acceptance cuts:

- **LM-1:** $N_{trg} \leq 6$ AND $N_{edge} \leq 1$
- **LM-2:** ($N_{trg} \in$ [5,6] AND $N_{edge} \leq 2$) OR ($N_{trg} = 4$ AND $N_{edge} \leq 1$)

The angular resolution for the different cuts is shown in figure 7.5(b) as a function of energy, showing an average improvement of $\sim 0.1^\circ$ below 100 TeV. While both cuts yield the same angular resolution as a function of energy, LM-2 selects a larger number of events ($\sim$ 10%), and it s therefore preferred to LM-1. Note that the results discussed here apply to the Crab simulation, as compared to the full sky data set discussed in chapter 5.

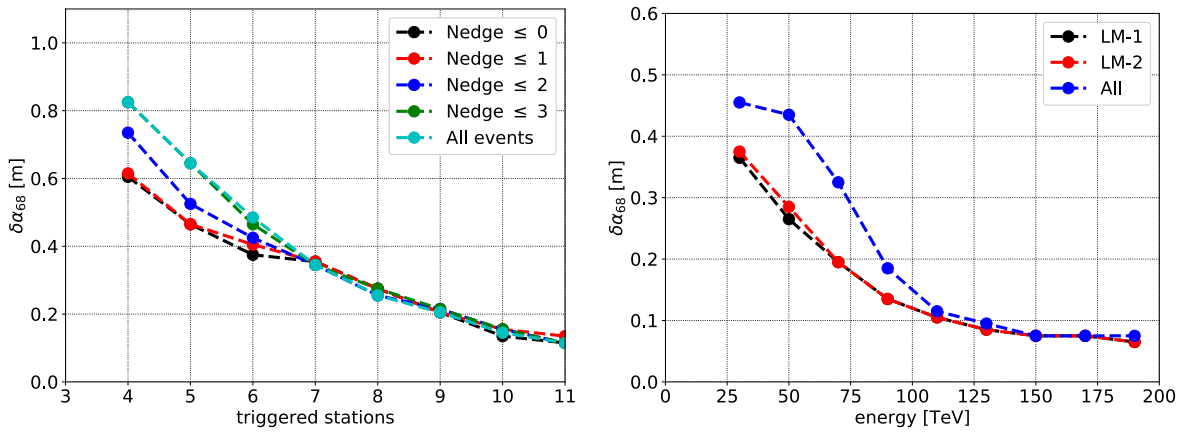

(a) (b)

Figure 7.5: Low multiplicity cut. (a) Angular resolution (68% containment) as a function of the event multiplicity, for different values of N_{edge}^{max}. (b) Angular resolution as a function of true primary energy, for standard acceptance cuts only (blue), and with low multiplicity cut LM-1 (black) and LM-2 (red). An improvement is obtained at energies $\leq$ 100 TeV. LM-2 is preferred to LM-1 for the larger number of selected events below 100 TeV ($\sim$ 10%).

Signal and background rate. After the event reconstruction and selection (acceptance and LM-2 cuts), the effective areas for gamma-ray and proton are calculated, as a function of the true primary energy. The signal and background rate coming from the source region are obtained by folding the effective areas with the differential Crab flux ϕ_{Crab} (Kevin Meagher for the VERITAS Collaboration, 2015), and CR flux ϕ_{CR}:

$$\phi_{Crab}\,[\mathrm{TeV}^{-1}\,\mathrm{m}^{-2}\,\mathrm{s}^{-1}] = 3.75 \cdot 10^{-7} \left(\frac{E}{TeV}\right)^{-2.467-0.16\log(E)} \tag{7.1a}$$

$$\phi_{CR}\,[\mathrm{TeV}^{-1}\,\mathrm{m}^{-2}\,\mathrm{s}^{-1}\,\mathrm{sr}^{-1}] = 0.096 \left(\frac{E}{TeV}\right)^{-2.7} \tag{7.1b}$$

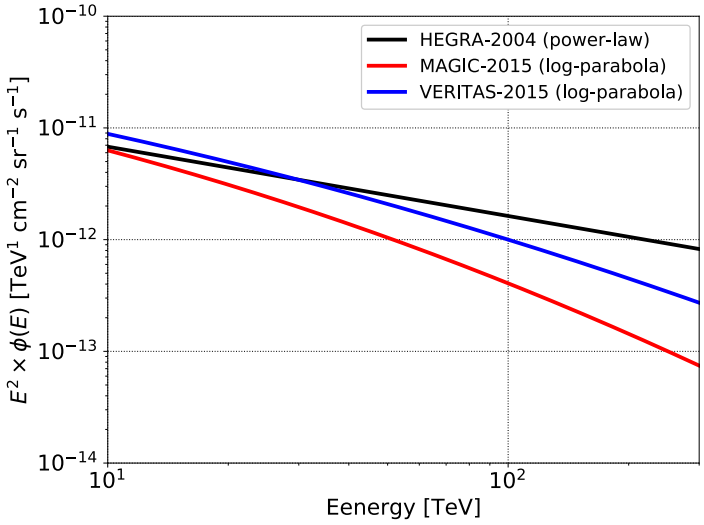

Figure 7.6: Different Crab flux models for energy above 1 TeV. The flux parametrizations are obtained by fitting the measured Crab spectrum with a power-law model (HEGRA-2004 Aharonian et al. (2004)) and a log-parabola model (MAGIC-2015 Aleksić et al. (2015), VERITAS-2015 Kevin Meagher for the VERITAS Collaboration (2015)).

7.2.2 HiS28 sensitivity

As discussed in section 2.4.8, the detector point source sensitivity, $\Phi(E \geq E_0)$, represents the minimal integral flux above a given energy E_0, needed to see a weak gamma-ray signal over a large CR background in the source region. To be classified as detected, the signal has to have a detection significance $S \geq 5$. Additionally, a minimum of 10 gamma-ray events are required. For this qualitative analysis, the detection significance is approximated by

$$S \simeq \frac{N_\gamma}{\sqrt{N_{BG}}} \tag{7.2}$$

with

$$N_\gamma = T_{obs} \cdot \int dE\, \Phi_{Crab}(E) \cdot A^\gamma_{eff}(E) \cdot n^\gamma(\theta_S(E)) \tag{7.3a}$$

$$N_{BG} = T_{obs} \cdot \int dE\, \Phi_{CR}(E) \cdot A^{proton}_{eff}(E) \cdot \Omega(\theta_S(E)) \tag{7.3b}$$

where T_{obs} is the observation time, $n^\gamma(\theta_S(E))$ is the fraction of events expected inside a circular search region of radius θ_S, and $\Omega = 2\pi(1 - \cos\theta_S)$ is the solid angle defined by the search region. The estimation of the HiS28 sensitivity to Crab signal below 200 TeV is here obtained

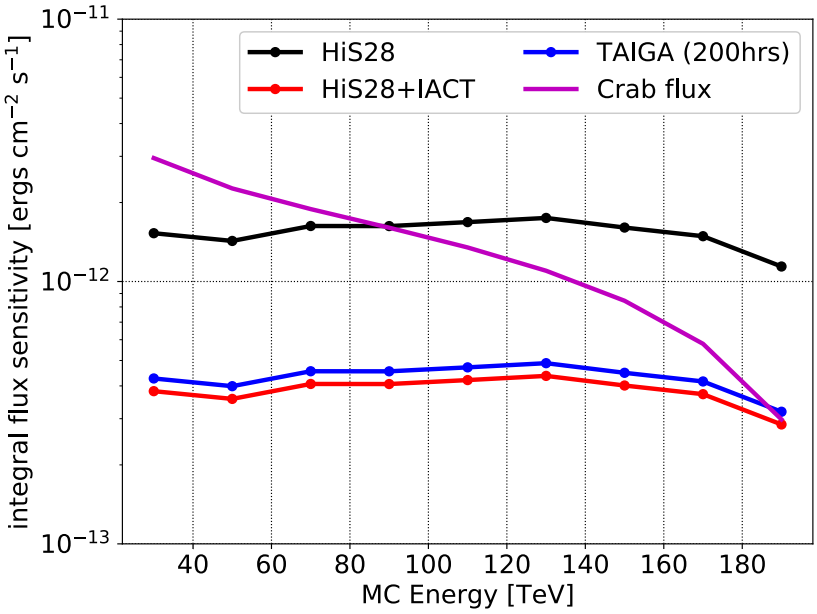

Figure 7.7: Estimated TAIGA-HiSCORE sensitivity to Crab flux below 200 TeV, using an energy dependent search region of radius $\theta_S(E) = \alpha_{72}(E)$, and for $T_{obs} = 1000$ h (5 years). The performance figures for the nominal detector energy threshold are used (black lines in figure 7.4). Black line: HiS28 in stand-alone mode. Red line: HiS28+IACT hybrid mode with $Q_{\gamma/g}^{IACT} = 4$. Blue line: 1 km^2 TAIGA hybrid mode ($Q_{\gamma/g}^{IACT} = 4$) for $T_{obs} = 200$ h (1 year). Purple line: integrated Crab flux, $E_0^2 \cdot \Phi_{Crab}(E \geq E_0)$.

following two different approaches, based on different definitions of the search region.

Energy-dependent search region. The first sensitivity estimation is obtained in a similar way as done in section 2.4.8, using a circular energy-dependent search region with radius $\theta_S(E) = \alpha_{72}(E)$ (angular resolution at 72% of containment). This choice allows to maximize the signal-to-background ratio by reducing the number of background events at higher energy while keeping the number of signal events constant (Alexandreas et al., 1993; Sciascio and Rossi, 2007). The performance figures used here are obtained for the standard detector setup in *sim_score* (black lines in figure 7.4, $E_{thr}^{\gamma} = 40$ TeV, $E_{thr}^{p} = 60$ TeV), while no energy reconstruction error or bias is taken into account. An observation time $T_{obs} = 1000$ h (5 years) is assumed.

The goal of this first exercise is to obtain a qualitative (although optimistic) estimation of the HiS28 potential to detect a signal from the Crab. Figure 7.7 shows the sensitivity obtained for different detector configuration, with the Crab integrated flux given for comparison (purple line). For HiS28 in stand-alone operation mode (black line), the sensitivity is below the Crab flux for energy $E_\gamma \leq 70$ TeV. It is interesting to note that the detector is in principle able

to see a signal without gamma-hadron separation, thanks only to the good angular resolution. The red line in gives the result for HiS28+IACT in hybrid operation mode, showing a sensitivity to the Crab flux up to $\sim$ 180 TeV. The contribution from the IACT is assumed here to give a gamma-hadron separation factor $Q_{\gamma/g}^{IACT} = 4$. Finally, the blue line gives an estimation of the sensitivity for the future 1 km^2 TAIGA hybrid detector, for $T_{obs} = 200$ h (1 year). The curve is obtained by scaling the HiS28 detector area by a factor 4 and assuming a $Q_{\gamma/g}^{IACT} = 4$ from IACT, showing the same performance as obtained in 5 years of HiS28+IACT hybrid operation.

The scenario discussed in figure 7.7 is somewhat optimistic. The sensitivity given here relies on good energy estimation, also at energies close to threshold, which is experimentally difficult to reach in the real experiment.

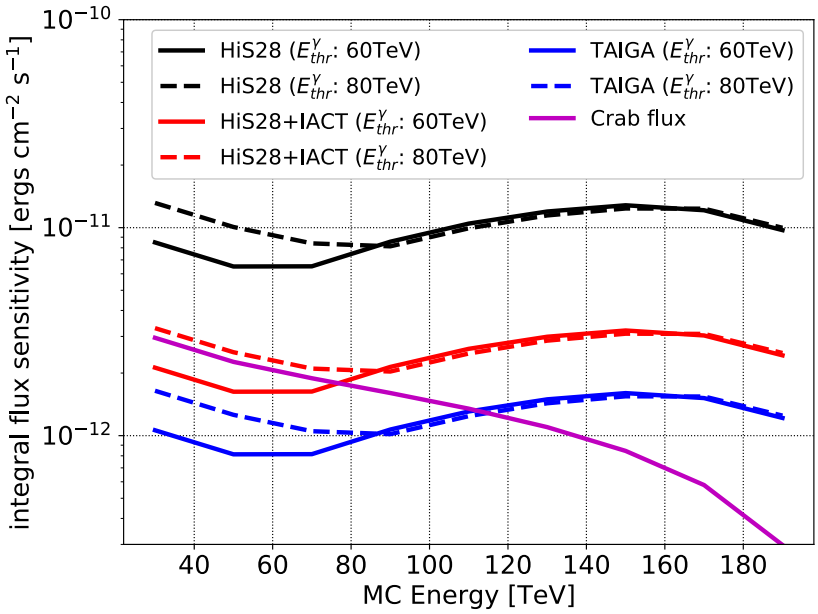

Figure 7.8: TAIGA-HiSCORE sensitivity to Crab flux below 200 TeV ($T_{obs} = 210$ h), using a fixed search region of radius $\theta_S = 0.3°$, and for an simulated detector energy threshold of 60 TeV (solid lines) and 80 TeV (dashed lines). Black line: HiS28 in stand-alone mode. Red line: HiS28+IACT hybrid mode with $Q_{\gamma/g}^{IACT} = 4$ from IACT. Blue line: 1 km^2 TAIGA hybrid mode ($Q_{\gamma/g}^{IACT} = 4$ from IACT) for $T_{obs} = 200$ h (1 year). Purple line: integrated Crab flux, $E_0^2 \cdot \Phi_{Crab}(E \geq E_0)$.

Fixed-radius search region. This second approach aims at a qualitative estimation of the HiS28 potential to detect a signal from the Crab, using the data collected in the first three years of operations. The sensitivity is calculated following the same search method applied on the experimental data (section 7.3), i.e. using a fixed search radius, $\theta_S = 0.3°$. As for the previous case, the value of the search radius is chosen in order to maximize the signal-to-background ratio, also taking into account a possible $0.1°$ mispointing like in the real exper-

iment. Figure 7.3(b) shows the estimated detector energy threshold as a function of the CR event rate (after quality selection). The range of CR rates after acceptance cuts observed in the data (figure 7.3(a)) indicates a detector threshold between 60 and 80 TeV over the 3 years. The performance figure obtained for these to values are used to estimate the range of the expected sensitivity.

Figure 7.8 shows the expected sensitivity to the Crab flux below 200 TeV for $T_{obs} = 210$ h. For HiS28 in stand-alone (black lines) the expected sensitivity is a factor 3-4 larger than the Crab flux. A better result is obtained for HiS28+IACT in hybrid mode, assuming a $Q_{\gamma/g}^{IACT} = 4$ from IACT, with the detector being sensitive to the Crab flux below $\sim$ 75 TeV if a detector threshold $E_{thr}^{\gamma} = 60$ TeV is assumed. Finally, a sensitivity up to 100 TeV is reached with the 1 km^2 TAIGA array.

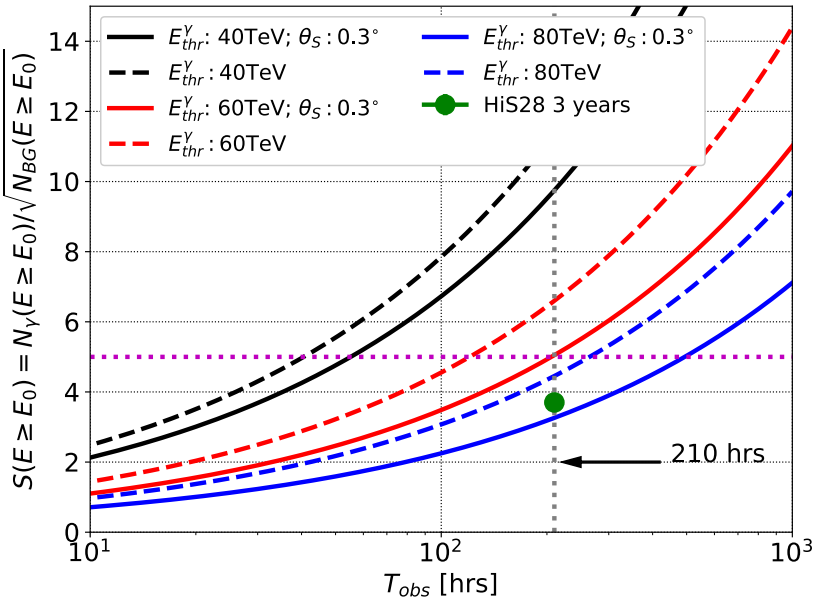

Figure 7.9: Crab signal detection significance, $S = N_\gamma/\sqrt{N_{BG}}$, as a function of the observation time, T_{obs}, for HiS28 in stand-alone mode. The solid lines give the results obtained by using an energy dependent search radius, $\theta_S = \alpha_{72}$ (angular resolution at 72% of containment). The dashed lines are obtained using a fixed search radius, $\theta_S = 0.3°$. The colors indicate different simulated detector thresholds. Green diamond: estimated significance in the source region for HiS28 three years data ($T_{obs} = 210$ h).

Detection significance Vs. observation time. Figure 7.9 the HiS28 expected signal significance in the source region, S, as a function of the observation time, T_{obs}, for the two search approaches here discussed: variable search region (dashed lines), and fixed search region (solid lines). The significance is calculated for a detector energy threshold of 40, 60 and 80 TeV, with

array operating in stand-alone mode ($Q_{\gamma/g}^{IACT} = 1$).

As expected, the first approach requires less observation time to detect a signal above $5\,\sigma$ with respect to the second approach. For a detector threshold of 40, 60 and 80 TeV, a T_{obs} of about 40, 120 and 250 h respectively is required using the energy-dependent search region, while a T_{obs} of about 50, 180 and 450 h is required using a fixed-radius search region.

The green dot in figure 7.9 gives an (optimistic) estimation of the expected significance in the Crab direction, for the HiS28 three years data. Such estimation is obtained summing up the signal and the background events collected during the 3 seasons, and it is found to be between 3 and $3.5\,\sigma$. For each season, a $T_{obs} = 70$ h is assumed, and a detector threshold of $E_{thr}^{\gamma} = 80$, 70 and 60 TeV is used for the first (2015/16), second (2016/17) and third (2017/18) season respectively.

To conclude this section, the MC simulation qualitatively shows the potential of the TAIGA detector to observe a signal from the Crab. A long observation time ($T_{obs} \sim 1000$ h) is needed for a detection with TAIGA-HiSOCRE in stand-alone mode. On the other hand, the hybrid detection mode (HiSCORE+IACT) shows the potential for a signal detection in much less time, thanks to the gamma-hadron separation supplied by the IACT. An important boost to reduce the observation time needed for a signal detection will come from the future extension of the detector area up to $1\,\text{km}^2$. An important role is also played by the detector energy threshold, that can be reduced by lowering the station trigger threshold. Another option to reduce the energy threshold is represented by the hybrid reconstruction of the detected EAS, by using the IACT as "station".

7.3 Crab search with HiS28 three years data

This section presents the point source analysis (PSA) developed for TAIGA-HiSCORE in stand-alone operation mode. Different background estimation methods are tested and compared, and the Li&Ma statistical approach is used to determine the detection significance. While the PSA developed allows a full search in the observed sky, the results presented here focus only on the region of sky around the Crab position. The analysis if performed on the three years HiS28 data sample calibrated with the HYB calibration method, and for a search radius $\theta_S = 0.3°$. Results obtained for the HV calibration method, and for a search radius $\theta_S = 0.2°, 0.4°$ are given in Appendix A.

7.3.1 Background estimation

The search for gamma-ray events is usually obscured by the overwhelming CR background contamination ($\sim 99\%$). A correct background estimation is a fundamental task in a PSA, even more if no gamma-hadron separation is available. An underestimation of the background

could cause fluctuations to appear as real signals, while an overestimation could cause real signals to be hidden in the data.

In this work, the background estimation is obtained using two different methods: the *Direct Integration* (DI, Alexandreas et al. (1993)), widely used in ground-based wide-angle gamma-ray detectors such as MILAGRO (Atkins et al., 2003) or HAWC (Smith, 2015), and the *Ring-Background* method (Ring, Funk (2005); Berge et al. (2006)), used in IACT point source analysis (Aharonian et al., 2005b). A description of the two methods, and their implementation is given in the following.

Direct Integration (DI). The number of detected background events expected to fall within a bin centred in (RA, δ), and size ΔRA in right ascension and $\Delta\delta$ in declination, is given by

$$N_{BG}(RA,\delta) = \int_{\Delta T}\int_{\Delta\Omega} \epsilon(\theta,\phi,RA,t) R_{BG}(\theta,\phi,t) d\cos\theta d\phi dt \tag{7.4}$$

where $R_{BG}(\theta,\phi,t)$ is the background event rate per solid angle in the local sky, and $\epsilon(\theta,\phi,RA,t)$ is a delta function equal to 1 if (θ, ϕ, t) are such that the event falls inside the bin ΔRA, $\Delta\delta$. The integration range are defined by the solid angle determined by the bin (ΔRA, $\Delta\delta$), $\Delta\Omega$, and by the integration time interval, ΔT. Thus, a correct estimation of the background depends on the correct estimation of $R_{BG}(\theta,\phi,t)$.

The DI method is based on the assumption that, within the integration time ΔT, the detector acceptance in the local sky, $E(\theta,\phi)$, is constant and independent from the overall background event rate, $R'_{BG}(t)$. This allows to redefine the background event rate as

$$R_{BG}(\theta,\phi,t) = E(\theta,\phi) R'_{BG}(t) \tag{7.5}$$

The two new functions, $E(\theta,\phi)$ and $R'_{BG}(t)$, are much easier to determine, simplifying the integration in equation 7.4. Following Alexandreas et al. (1993), two different implementation of the DI method are tested in this work. In both cases, 1000 fake events (N^{DI}_{fake}) are generated for each true event, and the selected "good-weather" time interval (red line in figure 7.2(a)) is used as integration time, ΔT.

In the first DI implementation (DI-Time), the time of the fake events is randomly generated with uniform distribution within the selected run time interval, while keeping the arrival direction (θ, ϕ) of the true event. The time scrambling (or time swapping) using a uniform distribution is justified by the stable rate, $R^{'}(t)$, of the selected runs (figure 7.2(a)).

In the second implementation (DI-Direction), the arrival direction of the fake events is randomly generated using as probability function the detector acceptance, $E(\theta,\phi)$, and keeping the time of the true event. $E(\theta,\phi)$ is obtained as follow: first, the arrival direction of the selected events (figure 5.17(b)) is mapped into a 2D histogram, and second, the histogram is smoothed using an uniform kernel of size 1°, in order to reduce fluctuations coming from the low statistics in the small map binning ($0.1^\circ \times 0.1^\circ$). Finally, the content of each bin is divided

by the integral of the histogram, in order to obtain the detector acceptance PDF.

A third variation of the DI method is also possible, where both time and arrival direction of the fake events are randomly generated. However the implementation and test of such variation is not pursued in this work.

Ring-Background method (Ring). For each bin centred in (RA, δ), and size ΔRA and $\Delta\delta$, the number of background events, $N_{BG}(RA, \delta)$, is obtained by integrating all the events with reconstructed direction falling inside a ring around the given direction. The two radii that define the background ring, θ^{max}_{Ring} and θ^{min}_{Ring}, are here set equal to $2.4°$ and $1.6°$ respectively.

7.3.2 Signal, Background and Excess maps

This section describes how the Signal and Background maps are built, how the Excess maps are produced, and how the Significance maps are calculated. The full procedure here described is applied to each of the 108 selected runs. The Excess and Significance maps calculation here described is also used for the full sample analysis, presented in the next section. All the maps hereafter discussed are built with a $0.1°$ binning in both RA (x axis) and δ (y axis).

Signal map. A first "raw" Signal map is obtained from the event arrival direction distribution in equatorial coordinates (RA, δ). The final Signal map is then obtained by smoothing the raw map, using a uniform kernel of size $\theta_S = 0.3°$. The number of events in each bin of the resulting Signal map is hereafter referred to as N_{on}.

Background maps. For each run, three background maps are built following the procedures discussed in section 7.3.1, one for each method: DI-Time, DI-Direction and Ring. In addition, the "raw" DI background maps are smoothed using the same uniform kernel used for the Signal map. No smoothing is applied to the Ring background map, as the method itself consists in a sort of smoothing, with the profile of the uniform kernel defined by the background ring. The number of events in each bin of the Background maps is hereafter referred to as N^i_{off}, where *i* indicates the different methods. An example of Signal and Background maps obtained for a single run (29.12.2016) is given in figure 7.10.

Before the background estimation, all the detected ISS-events are removed from the data sample by cutting a 30 s time interval around the ISS passage time, for each known detected passage (see chapter 6). The exclusion of known signals is necessary to avoid a background contamination, causing an overestimation of the background, and reducing as a consequence the detection potential of the analysis. In case of "known gamma-ray sources", a region of the sky around the source position is usually excluded from the data sample used for the background estimation. At this point of this PSA development, such a procedure is not implemented yet, and it is one the future improvements discussed in section 7.3.5.

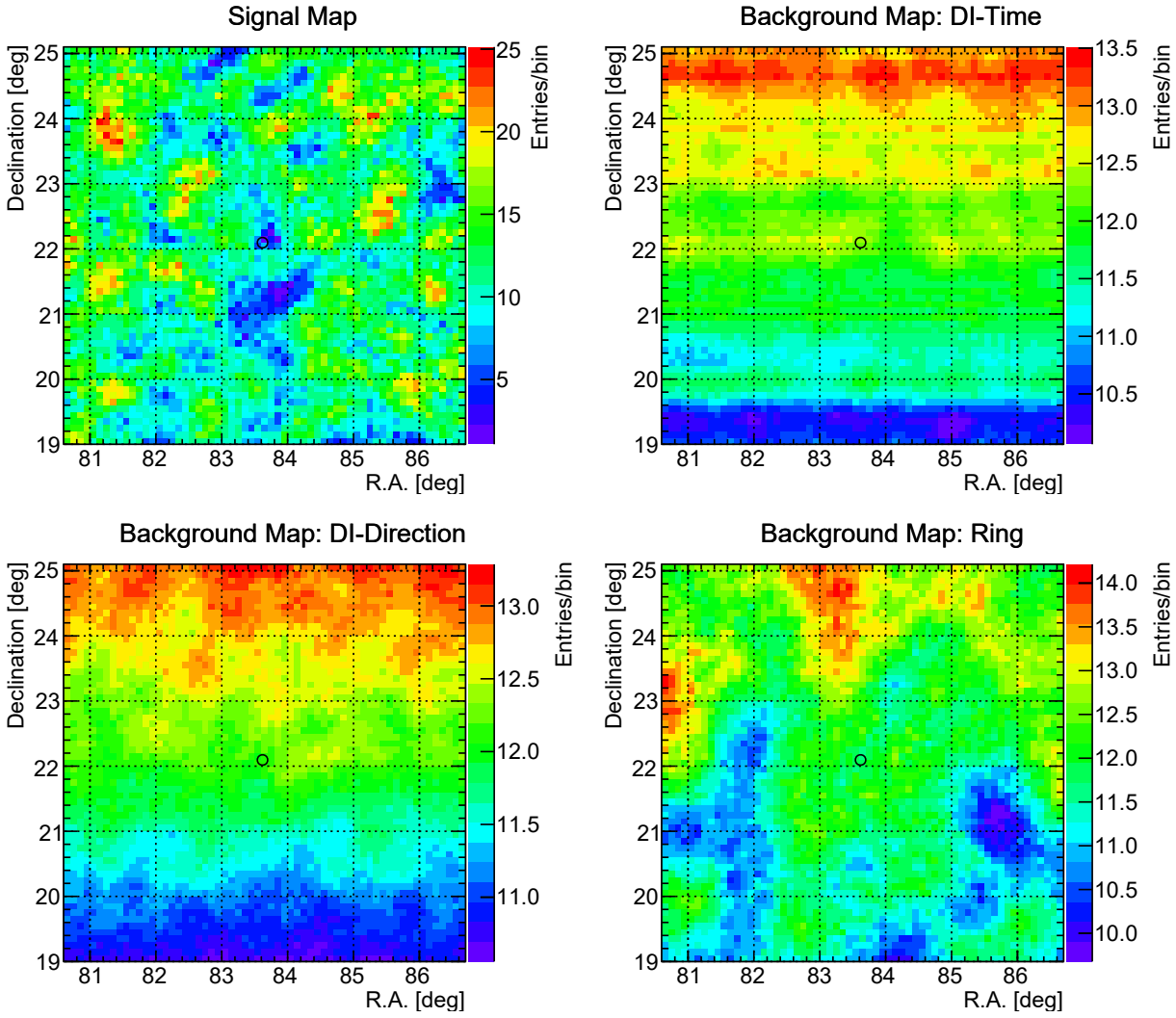

Figure 7.10: Example of Signal and Background maps, obtained for run 29.12.2016. Top-left: Signal map. Top-right: DI-Time background map. Bottom-left: DI-Direction background map. Bottom-right: ring background map. The bin content of the background maps is scaled by the corresponding background factor, α^i. The black circle is centred around the Crab position. The maps are produced using the Hybrid time calibration (HYB) and a search (smoothing) radius $\theta_S = 0.3°$.

Excess and Significance maps. The Excess map is obtained subtracting the Background map from the Signal map. For each bin (RA, δ), the number of positive (or negative) excess events is given by

$$N^i_{excess}(RA,\delta) = N_{on}(RA,\delta) - \alpha^i N^i_{off}(RA,\delta) \tag{7.6}$$

with α^i the background scale factor for the *i*-th background method. For the DI method (both implementations), the background scale factor is given by $\alpha^{DI} = 1/N^{DI}_{fake} = 10^{-3}$. For the Ring method, α^{Ring} is given by the ratio between the areas of the search region and of the background ring: $\alpha^{Ring} = \pi\theta^2_S/\pi[(\theta^{max}_{Ring})^2 - (\theta^{min}_{Ring})^2] = \theta^2_S/3.2$. However, this definition underestimates the correct value of α^{Ring} for the actual implementation of the Ring-Background method. The reason is that both the Signal map smoothing and the Ring background estimation are implemented directly on the "raw" Signal maps, i.e. the event integration is obtained summing up the content of all those bins with centre inside the given integration region (either search region or background ring). Thus, the correct estimation of α^{Ring} is given by the ratio between the number of bins with centre falling inside the search region, and those with centre inside the background ring.

The statistical significance of the bin content in the Excess maps is obtained using the Li & Ma approach (Li and Ma (1983), formula 17):

$$S = \sqrt{2}\sqrt{N_{on}\ln\left[\frac{1+\alpha}{\alpha}\left(\frac{N_{on}}{N_{on}+N_{off}}\right)\right] + N_{off}\ln\left[(1+\alpha)\left(\frac{N_{off}}{N_{on}+N_{off}}\right)\right]} \tag{7.7}$$

with S nearly normally distributed even for small count numbers (N_{on}, $N_{off} \gtrsim 10$). Figure 7.11 gives an example of Significance maps (first row) for a $6^\circ \times 6^\circ$ portion of the sky around the Crab position (black circle) obtained for run 29.12.2016, and the relative full sky Significance distributions (lower row). The Significance distributions are well approximated by a Gaussian centred a 0 and $\sigma = 1$, as shown by the Gaussian fit (red lines). In general, the three background estimation methods do agree with each other.

7.3.3 Full data sample analysis

The previous section described the procedure applied to each of the 108 selected runs. The Signal and the Background maps for the full three years period are obtained summing up all the Signal and Background maps of those runs passing a background-quality selection discussed later in the text. The Excess and Significance maps for the full three years period are finally calculated using equations 7.6 and 7.7, respectively.

Background-quality run selection. Before summing up all the data in a single sky map, and performing the final step of the PSA, the quality of the background estimations for each run is checked. For each run, a Gaussian fit between [-4, 4] is performed on the full sky Significance

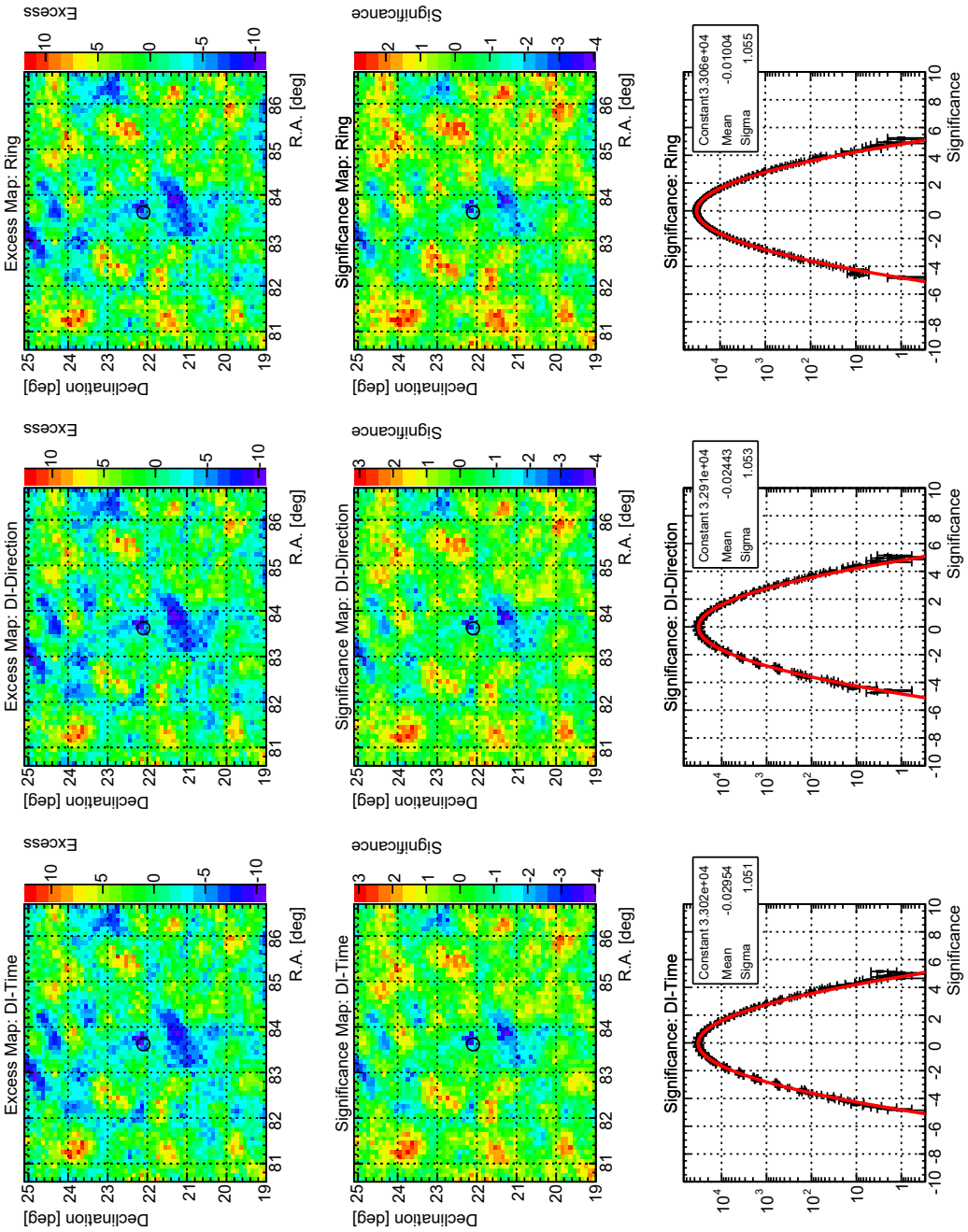

Figure 7.11: Excess maps (upper row) and relative Significance maps (middle row) obtained for one run (29.12.2016), using the three different background estimation methods. The methods show very close results, producing almost the same Excess and Significance maps in the region of interest. The Significance distributions (lower row) follow the expected Gaussian shape ($\mu = 0$ and $\sigma = 1$), as shown by the Gaussian fit (red lines).

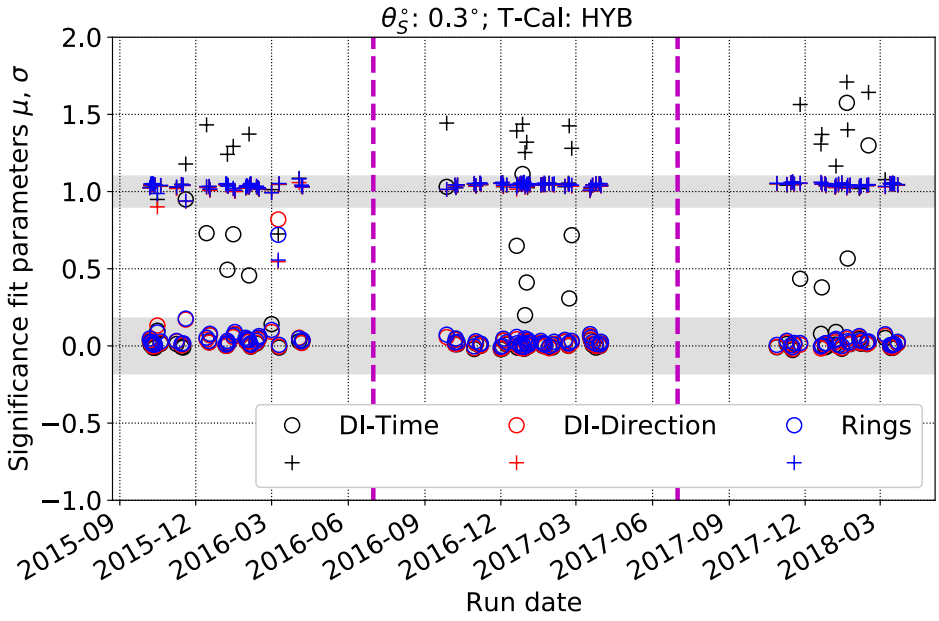

Figure 7.12: Run-wise background estimation quality check, based on a Gaussian fit of the full sky Significance distribution. The circles and crosses represent the fitted μ and σ, respectively. The grey bands give the background quality cuts: $|\mu(S)| \leq 0.2$ and $|\sigma(S)| \leq 0.1$.

distribution obtained for every background method, as shown in figure 7.11. Figure 7.12 shows the distribution of the Gaussian fit parameters as a function of the run date, for the different background methods. Only runs with $|\mu(S)| \leq 0.2$ and $|\sigma(S)| \leq 0.1$ (grey bands) are selected for the final sky maps.

Looking at figure 7.12, The DI-Time method (black) results to be less stable, with 19 runs (18%) showing parameters outside the selection regions. This effect is mainly due to the approximation with a uniform distribution of the overall background events rate, $R'_{BG}(t)$. Indeed, the excluded runs present small variation in time of the overall event rate, causing an overestimation of the background when the rate is below the average rate, and an underestimation when the rate is above. The final Significance distribution is then distorted, with the Gaussian fit returning different parameters from the expected ones. As a consequence, the excluded runs reduce the total exposure time to the Crab from 210 to 162 h. The DI-Direction and the Ring methods yield very close results, with only one run excluded (the same run, with no exposure to the Crab). Appendix A shows the Background-quality check for a search radius $\theta_S = 0.2°$ and $0.4°$ (figure A.1).

HiS28 three years Significance maps. The first step of the PSA on the HiS28 three years data sample consists of producing the total Signal and Background maps, using both DI method

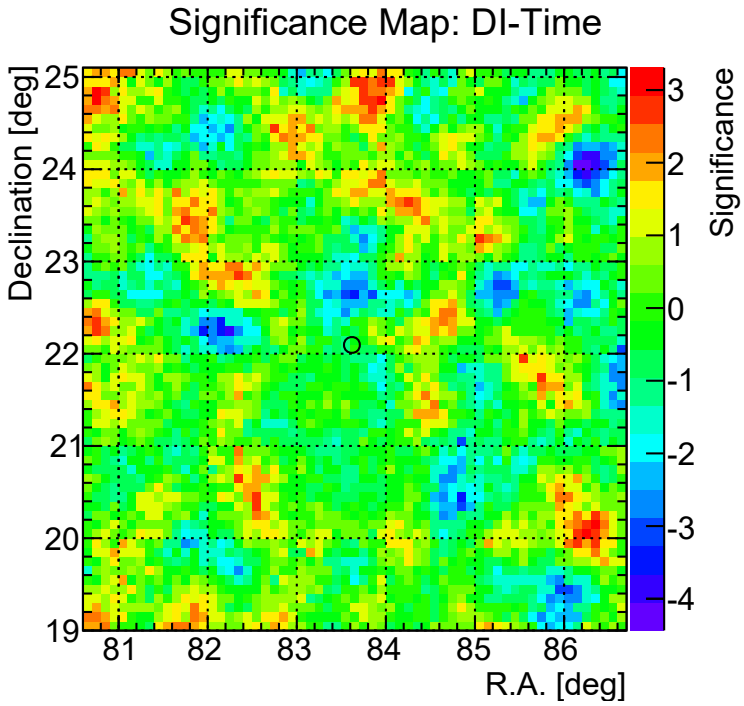

(a) Significance map for a $6° \times 6°$ sky area centred around the Crab position (black circle)

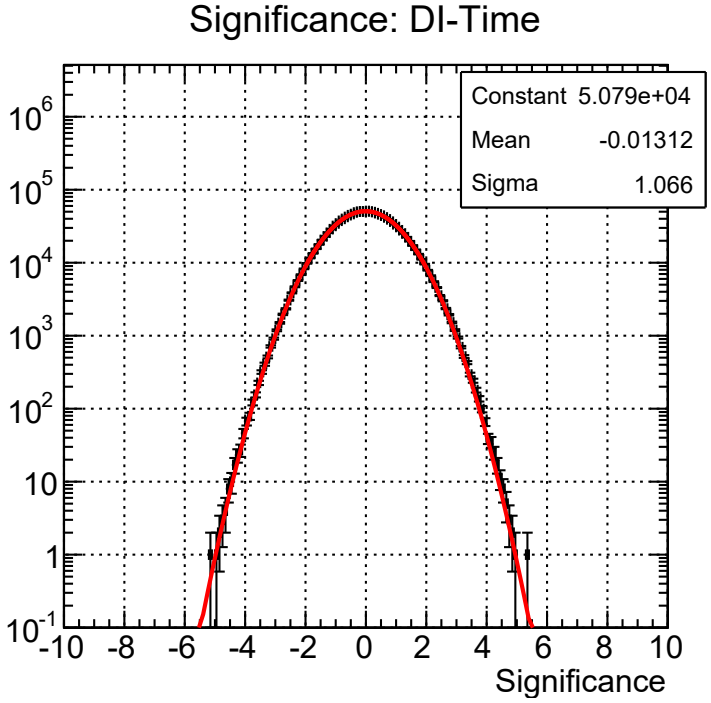

(b) Full sky Significance distribution. The stats box shows the results of a Gaussian fit (red line): $< S >= -0.01$ and $\sigma(S) = 1.07$.

Figure 7.13: HiS28 three years Significance map using DI-Direction background method.

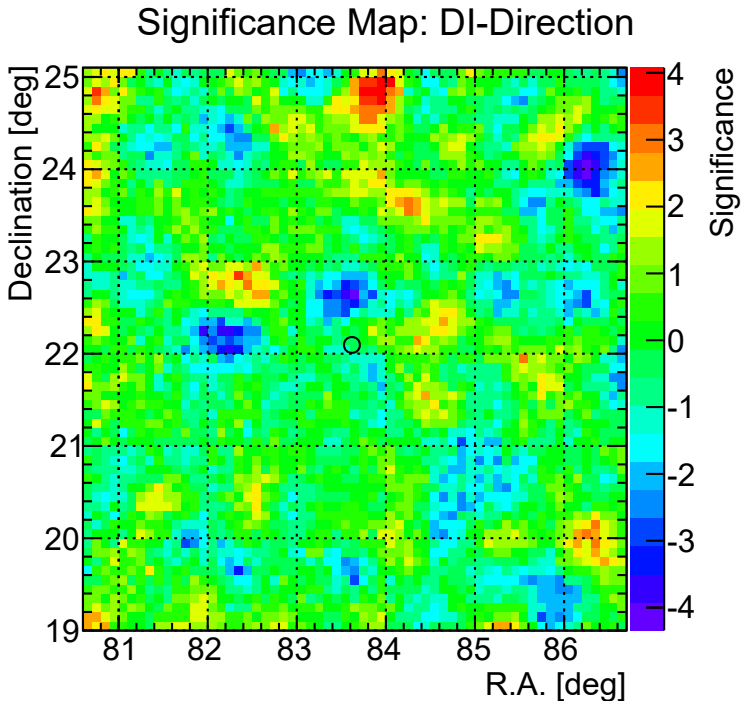

(a) Significance map for a $6° \times 6°$ sky area centred around the Crab position (black circle)

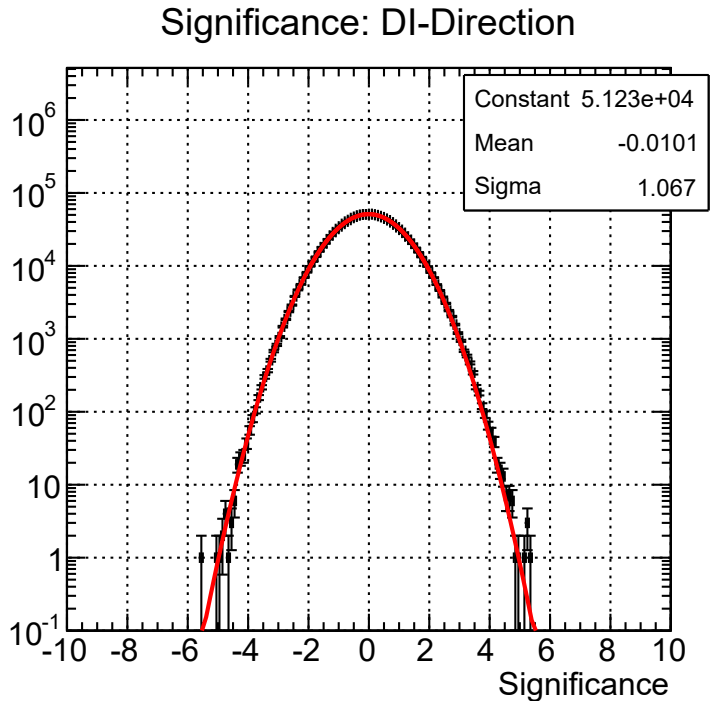

(b) Full sky Significance distribution.The stats box shows the results of a Gaussian fit (red line): $< S >= -0.01$ and $\sigma(S) = 1.07$.

Figure 7.14: HiS28 three years Significance map using DI-Direction background method.

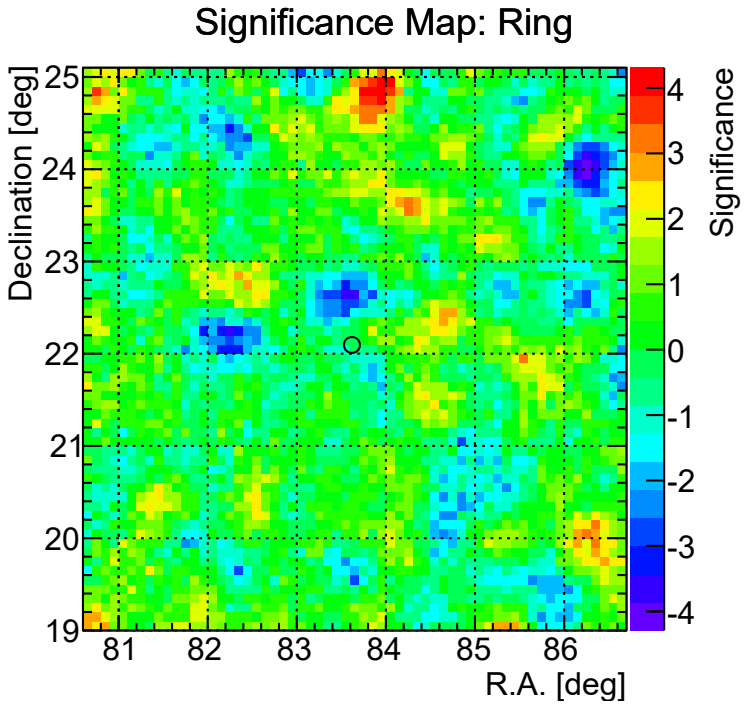

(a) Significance map for a $6° \times 6°$ sky area centred around the Crab position (black circle).

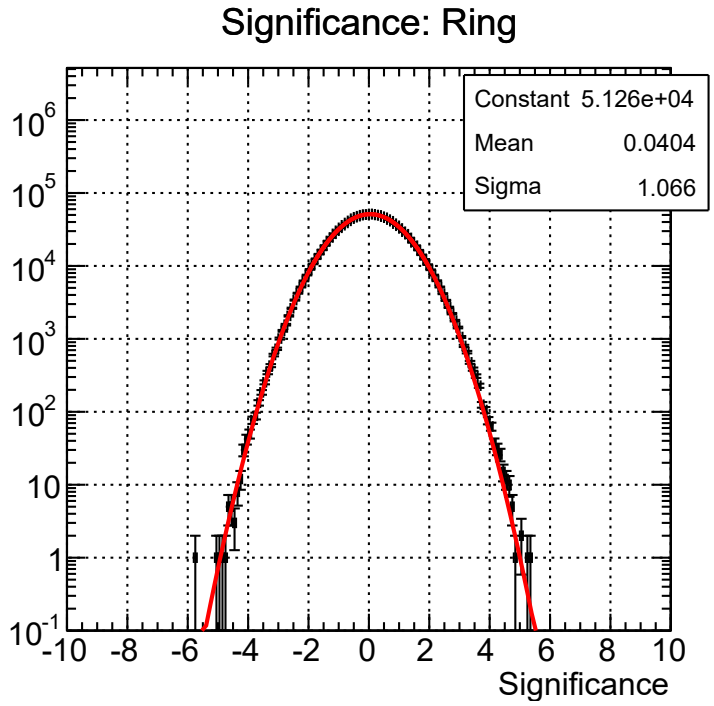

(b) Full sky Significance distribution.The stats box shows the results of a Gaussian fit (red line): $< S >= 0.04$ and $\sigma(S) = 1.07$.

Figure 7.15: HiS28 three years Significance map using Ring background method.

implementations and the Ring method. This is obtained by summing up all the Signal and Background maps of those runs passing a background quality selection. The total Signal and the Background maps are then used to produce the total Excess maps using equation 7.6, and to calculate the final Significance maps using equations 7.7. As mentioned already, the total exposure time is 210 h for DI-Direction and Ring methods, and 162 h for DI-Time method.

The final results of the PSA on the HiS28 three years data sample are presented in figures 7.13 (DI-Time), 7.14 (DI-Direction), and 7.15 (Ring). The full sky Significance distributions are given in figures 7.13(b), 7.14(b), and 7.15(b). All the three methods reproduce the expected distribution for the background fluctuation: a Gaussian distributions well centred at 0 and with $\sigma \simeq 1$.

Figures 7.13(a), 7.14(a), and 7.15(a) present the Significance maps for a $6^\circ \times 6^\circ$ portion of the sky centred at the Crab position (black circle). The maps obtained with the DI-Direction and Ring methods (figures 7.14(a), 7.15(a), same exposure) present the same structures (location of peaks/valleys) in the background fluctuations, characterized by almost the same significance values. Some of these structure are also observed in the significance map for the DI-Time method, despite a ~ 50 h shorter exposure. A further investigation is needed to understand the nature of such structures, and their correlation with the smoothing radius, θ_S.

As expected (section 7.2.2), no event excess with significance above $5\,\sigma$ is found in the source bin. The Significance in the nominal Crab position is $S \sim 0\,\sigma$, independently of the background method and the exposure. The direction reconstruction is known to be affected by an average absolute mispointing $\alpha_{Mis} \leq 0.1^\circ$ (HiS28-MASTER combined analysis, section 6.2), and the PSF varies from 0.1° up to 0.6° (sections 5.4, 5.4.3). Thus, a scan around the Crab bin is performed, with the scanned region a square of side 1°, centred at the source bin. The scan is performed on all three significance maps. The average location of largest significance fluctuation ($S \simeq 1.6\,\sigma$) in the scanned region is found at ($< RA >= 22.2^\circ$, $< \delta >= 83.9^\circ$), with an angular distance of $\sim 0.35^\circ$ from the Crab position (see figure A.4).

In Appendix A, the scan is also given for search radius $\theta_S = 0.2^\circ$ and 0.4°, and to the data sample calibrated with the HV method (figure A.4). While the location of the peak is almost the same ($< RA >= 22.1^\circ$, $< \delta >= 84.0^\circ$), a significance $S = 2.5 - 3\,\sigma$ is obtained for $\theta_S = 0.2^\circ$.

We do not find, from this preliminary full sky search, a signal at the nominal position of the Crab, and only a small excess of significance up to $2.5 - 3\,\sigma$ is found at 0.35° from the Crab, after a scan of the source neighbouring region. The preliminary status of the analysis requires further investigations, and improvements of the method are planned, as discussed in section 7.3.5.

7.3.4 Signal detection check

The analysis presented in the previous section shows no signal detection ($S \geq 5\,\sigma$) in the search region around Crab position, as expected from MC simulations. A scan of the Significance map around the Crab bin shows a peak of significance $2.5 - 3\,\sigma$ (depending on the

analysis parameters), at $\sim 0.35°$ from the Crab nominal position. In the absence of a strong gamma-ray source, the PSA method is checked by using known signals: (1) the ISS-events discussed in chapter 6, and (2) an artificial (fake) signal injected at the Crab position in the data sample. Again, the Excess and Significance maps are calculated using equations 7.6 and 7.7.

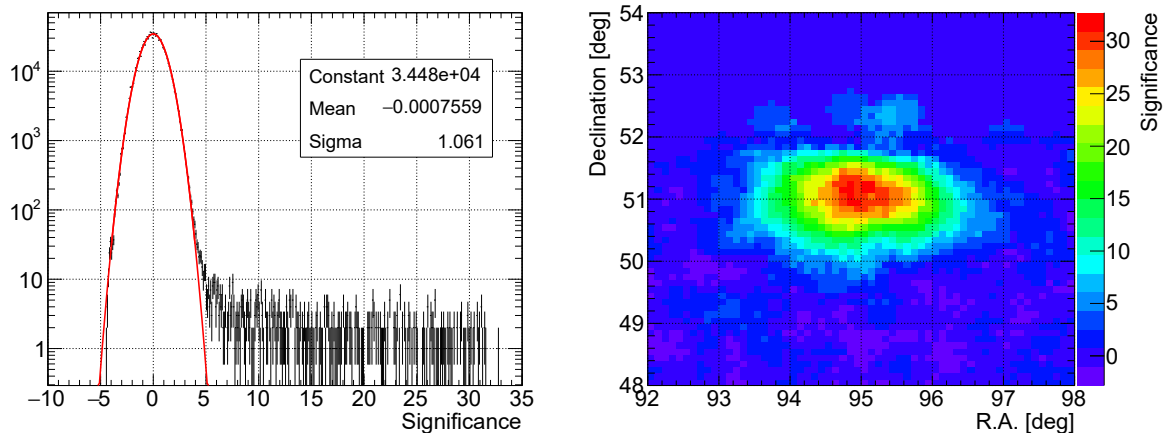

(a) (b)

Figure 7.16: Signal detection check using ISS-events signal (run 02.05.2016). (a) Full sky Significance distribution, showing the expected Gaussian distribution for the background fluctuation ($\mu = 0$, $\sigma = 1$), and the signal "tail" for $S \geq 5\,\sigma$. Box: Gaussian fit results (red line). (b) Significance map ($6° \times 6°$) for the DI-Direction method. The ISS/CATS-LIDAR signal is detected with a significance $S = 33\,\sigma$. Similar results are obtained using Ring method.

ISS-events signal detection. This test checks the developed PSA detection potential by using the ISS-events detected on 05.02.2016. The Signal and Background (DI-Direction) maps are produced following the full procedure described in sections 7.3.1 and 7.3.2 (3 years data sample). The ISS-events signal is included in the raw Signal map for run 05.02.2016, before the smoothing procedure. All the other known ISS-events are excluded (see section 7.3.2).

The result is presented in figure 7.16. The full sky Significance distribution is given in figure 7.16(a). The background fluctuations are well described by a Gaussian distribution centred at 0 and width $\simeq 1$. The "tail" for $S \geq 5\,\sigma$ shows the number of bins containing signal events candidates. The distribution in the sky for these bins is given in figure 7.16(b), showing a $6° \times 6°$ sky region around the known position of the detected ISS passage (Zenith ~ 0 in local coordinates, see 6.2). The signal is detected with a Significance of up to $\gtrsim 30\,\sigma$, in agreement with the expectations.

As the ISS-events come from a moving source, the shape of the source is expected not to be the typical one for point sources, but extended. This is confirmed by the shape of the signal

source in figure 7.16(b), spanning over few degrees in both RA and δ.

This first test shows the potential of the PSA developed for HiSCORE to detect a strong signal above the CR background, as the ISS-events. The shape of the full sky Significance follows the expected Gaussian distribution of the background fluctuations, and shows the signal for $S \geq 5\,\sigma$. This indicates that the background is correctly estimated, and the Significance correctly calculated. The extended source shape reproduced, as expected for a moving source, demonstrate the potential of the analysis to study extended gamma-ray sources, thanks to the good detector angular resolution.

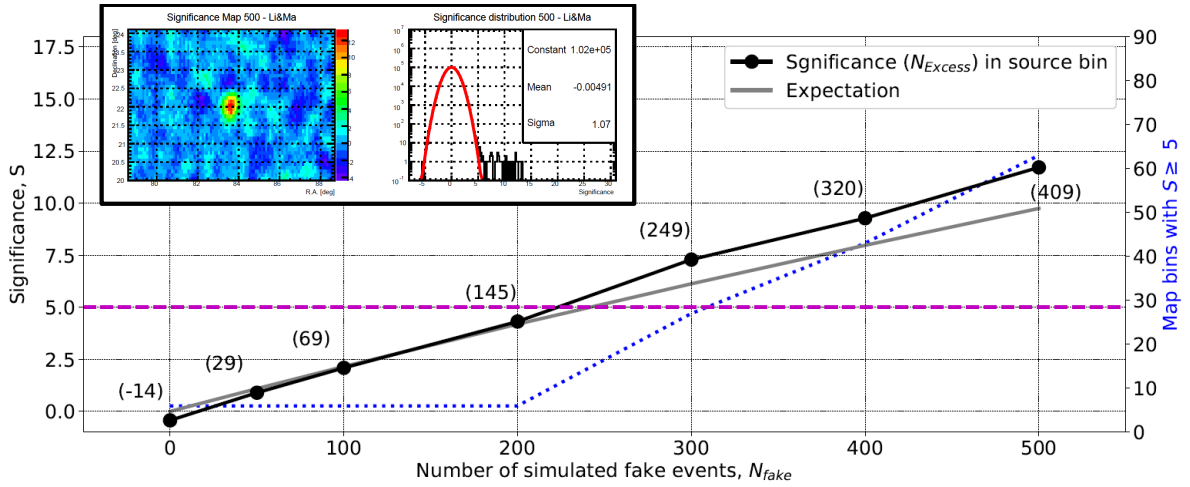

Figure 7.17: HiS28 PSA signal detection check with fake Crab signal and blind data (see text for detail). The Significance (DI-Direction) in the source bin, S, is given as a function of the number of simulated fake events, N_{fake}. For the background given here ($N_{off} \sim 6.5 \times 10^5$), a detection significance $S \geq 5\,\sigma$ is reached for $N_{Excess} \gtrsim 150$ (in parenthesis). A good agreement is observe with the expected significance (grey line). Inserts: Significance map around the around the fake source position (top-left), and corresponding full sky Significance distribution, for $N_{fake} = 500$. The Significance distribution shows the expected Gaussian distribution for the background fluctuations ($\mu = 0$, $\sigma = 1$), and the signal tail for $S \geq 5\,\sigma$. Red line: Gaussian fit.

Fake Crab signal. In this test, fake signal events are injected into the three years data sample. The fake signal is simulated by generating N_{fake} events with symmetrical 2D Gaussian distribution and $\sigma = 0.2°$, centred at the Crab position. The signal is then injected into the "raw" signal map of one single run, before the smoothing procedure. The Background map is the same used for the first test, i.e. the final three years Background map obtained for the DI-Direction method. The test is repeated for N_{fake} varying between 0 and 500.

Figure 7.17 summarizes the results. The significance, S, in the source bin (black dots) is given as a function of the number of simulated fake events, N_{fake}, together with the corre-

sponding number of Excess events (in parenthesis). The estimated significance agrees with the expectations for $N_{off} \sim 6.5 \times 10^5$ and $\alpha^{DI} = 10^{-3}$. A signal detection with significance above $5\,\sigma$ (purple line) is reached for $N_{fake} \gtrsim 250$. Finally, the blue line shows the number of bins in the full sky Significance map with $S \geq 5\,\sigma$ (right y-axis). An example of Significance map and the corresponding Significance distribution obtained for $N_{fake} = 500$ are given in the two inserts in the figure.

We conclude from this test that the PSA method works correctly if a point source signal is present in the sky map.

7.3.5 Improvements to the TAIGA-HiSCORE point source analysis

The previous section presented the first systematic PSA developed for the TAIGA-HiSCORE detector. By applying such analysis on the HiS28 three years data sample, no signal above $\geq 5\,\sigma$ has been found in the search region around the Crab ($T_{obs} = 210\,\text{h}$), confirming the MC prediction presented in section 7.2.2. We emphasize the preliminary status of the presented PSA strategy. Additional cross-checks are in preparation, and several improvements are planned.

The work presented here is a first step towards a more accurate (and sensitive) PSA for the TAIGA-HiSCORE detector, not only to detect a signal from the Crab, but to perform a search in the full observed sky for point-like and extended gamma-ray sources. In the following, some of the limits of the current analysis are discussed, together with possible improvements.

Event sample splitting. The PSA presented here is performed integrating over all the selected events, limiting the optimization of the search parameter, e.g. the smoothing radius θ_S. As shown in section 7.2.2, this approach increases the number of integrated background events in the search region, worsening the signal detection potential. A solution is represented by splitting the data sample in different event multiplicity (or energy, if available) bins, allowing a better definition of the optimal search parameters for each bin.

Maps smoothing. The Signal and Background maps are here smoothed using a uniform kernel of size $\theta_S = 0.3^\circ$, estimated by taking into account the average detector PSF obtained with the chessboard method (section 5.4.3), and an absolute angular mispointing of 0.1° (section 6.2).

As shown in figure 7.18, MC simulations show a PSF of the HiS28 detector (all events) well described by a double Gaussian distribution. Using a smoothing kernel described by such distribution will improve the Signal and Background integration in the search region. If the data sample is split as discussed in the previous point, an event multiplicity (or energy, if available) dependent smoothing can be applied, e.g. using a Gaussian kernel proportional to the differential angular resolution, like in the sensitivity calculation in section 7.2.2.

Significance estimation. The Li&Ma statistics gives a good estimation of the detection significance for large number of events in the Signal and Background map bins ($N_{on} \geq 10$ and

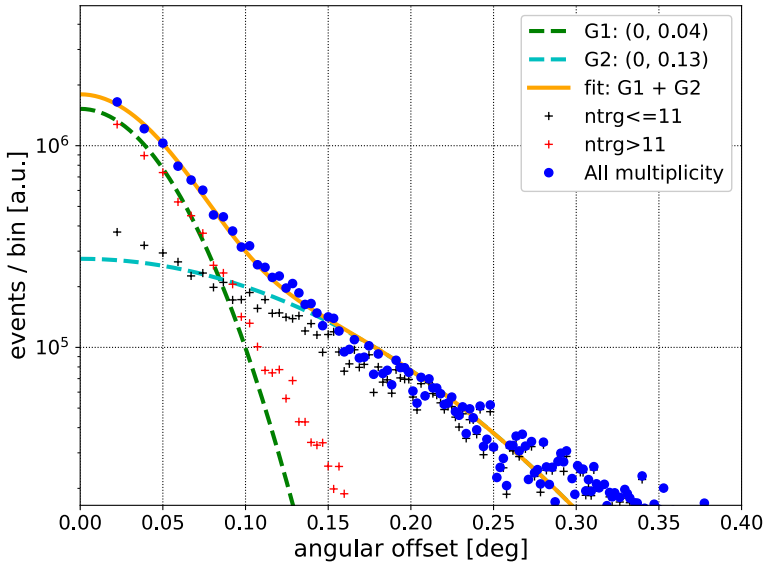

Figure 7.18: HiS28 double Gaussian point spread function (PSF), obtained with the dedicated Crab signal MC simulation, and using all the selected events (blue dots). The two Gaussian distributions, $G_1(0, 0.04)$ and $G_2(0, 0.13)$, are obtained by selecting events with $N_{trg} \leq 11$ and $N_{trg} > 11$.

$N_{off} \geq 10$). However, this could represent a limit when splitting the event sample in energy (or multiplicity) bins, with very low statistics at large energy (multiplicity). For this reason, a Likelihood ratio test approach could bring an improvement in the calculation of the detection sensitivity.

Remove known gamma-ray sources in background estimation. In the background estimation methods used here (DI and Rings), no region of interest with known gamma-ray emission has been excluded from the analysis (only the known ISS-events are excluded). In case of medium-strong signals, this can lead to a overestimation of the background in the declination band of the source region (DI) or can generate fake structures in the background fluctuation (Rings), reducing the detection potential of the analysis. For this reason, any future PSA for TAIGA-HiSOCRE should consider the exclusion of the main regions of interest, with known PS or extended gamma-ray emissions.

Background estimation with DI method. The main assumption of the DI method is that the detector acceptance and the event rate are constant and independent from each other, within the integration time window, ΔT. In this analysis ΔT is taken equal to the run duration ("good weather" selected interval), and changes from run to run. Using a fixed ΔT (e.g. 2 h) will allow for a better control of the events rate stability, and a uniform background estimation for

all the runs, reducing possible fluctuation in the calculation of the detection significance (as observed for the DI-Time method).

Further outlook. In general, an improvement of the analysis can come from a better event reconstruction as well as selection, in particular at small multiplicity. Additional informations coming from the shower energy and X_{max} reconstruction can help to better define the quality of the reconstructed events, to reduce the CR background by applying the gamma-hadron separation presented in section 2.4.7, and to split the data sample as discussed above. Moreover, the hybrid detection (HiSCORE+IACT) of known sources will definitely improve the gamma-hadron separation, and could be used to train modern machine learning algorithms to reject the hadronic background in those regions of the sky observed by TAIGA-HiSCORE in stand-alone mode.

7.4 HiS28-IACT coincidence events

At the end of 2016, the first TAIGA-IACT (IACT) was deployed at the Tunka, and put into test operations during the second half of season 2016/17 (Budnev et al., 2017b). During season 2017/18, it was possible to run a first observation campaign using both TAIGA Cherenkov detectors (Postnikov et al., 2017).

This section presents a first analysis of the HiS28-IACT coincidence events, i.e. showers detected and reconstructed with HiS28 that also triggered the IACT. The analysis is limited to the study of the IACT detector efficiency (w.r.t. HiS28 alone) by using reconstructed HiS28 events, and the IACT event trigger time informations (≥ 2 pixels from ≥ 1 clusters). At the time of this analysis, an established IACT image data set, based on a calibrated and analysis chain, was still in preparation by the collaboration.

7.4.1 Data sample

The data sample analysed here consists of 14 runs, taken between 14.11.2017 and 12.02.2018. The runs are selected in order to have good weather condition and stable operation of both IACT and HiS28 detectors. During these selected runs, the IACT is constantly pointing to the Crab direction.

HiS28-IACT coincidence events. Figure 7.19(a) shows the event rate for different types of HiS28 events. The black line gives the HiS28 event rate, after selection cuts, for the full run. The blue line shows the time interval where both HiS28 and IACT are in operation, and the Crab is inside the HiS28 FOV ($\psi_{Crab} \leq 20°$), while the red line gives the coincidence event rate in this time interval. The cut at $\psi_{Crab} \leq 20°$ is needed to have the full IACT FOV inside the HiS28 FOV, allowing for a uniform monitoring of the telescope acceptance at any time.

The HiS28-IACT coincidence events are extracted from the full HiS28 data sample by looking

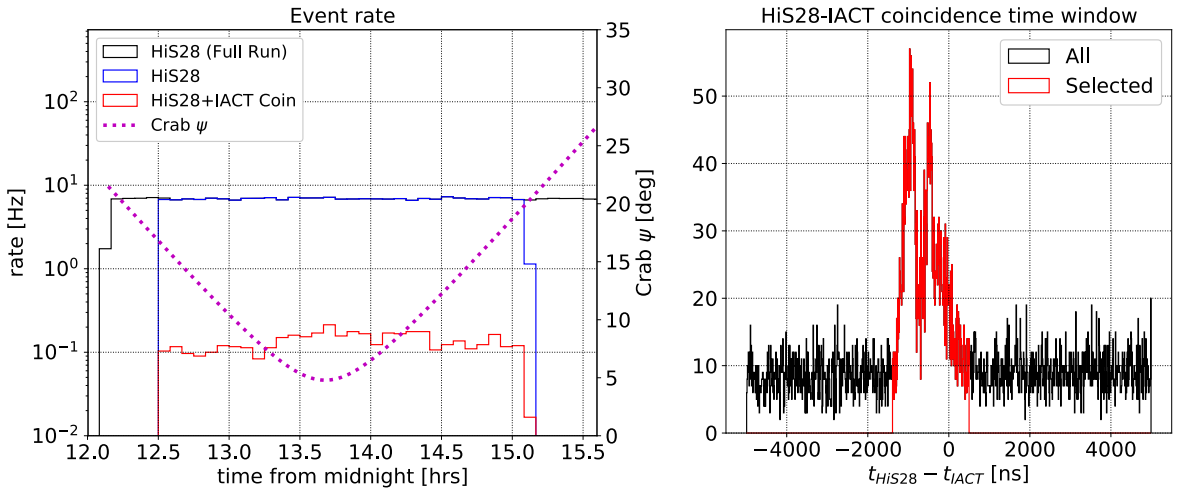

(a) (b)

Figure 7.19: HiS28-IACT coincidence events. (a) HiS28 event rate after selection cuts, for the full run (black line), HiS28 events detected while IACT is operating and $\psi_{Crab} \leq 25°$ (blue line), and HiS28-IACT coincidence events. Purple line: Crab angular distance from the HiS28 pointing as a function of time. (b) Time difference between HiS28 and IACT events, for $|t_{HiS28} - t_{IACT}| \leq 5\,\mu$s (black line), and $-1400\,\mu$s $|t_{HiS28} - t_{IACT}| \leq 500\,\mu$s (red line).

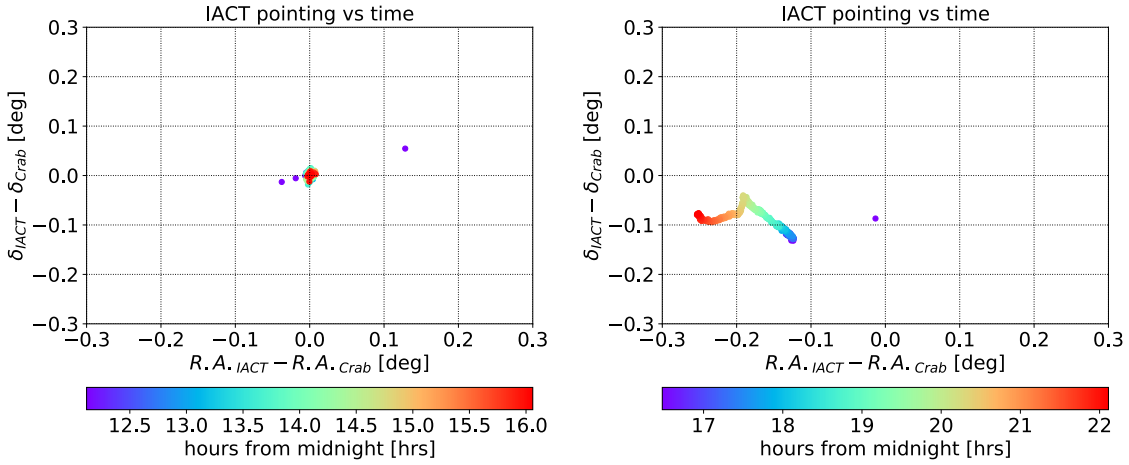

(a) (b)

Figure 7.20: TAIGA-IACT pointing direction relative to the Crab position, as a function of time. (a) on-source stable pointing - run 05.02.2018. (b) off-source varying pointing - run 28.10.2017.

at the time difference between HiS28 and IACT detected events. Here, t_{HiS28} is the time of the HiS28 events, while t_{IACT} is the time of the IACT events. Figure 7.19(b) shows the distribution of the time difference between t_{HiS28} and t_{IACT}, i.e. the trigger time of the HiS28 and IACT events. A first selection of the HiS28-IACT coincidence events is obtained selecting all those events for which $|t_{IACT} - t_{HiS28}| \leq 5\,\mu$s (black line). To reject the purely random coincidence, we require $-1400\,\mu\text{s} \leq t_{IACT} - t_{HiS28} \leq 500\,\mu$s (red line).

IACT pointing. For the selected runs, the IACT is supposed to point to the Crab position. Since the telescope tracking was in commissioning during most of the time, the IACT pointing precision varies in time. Figure 7.20 gives an example of stable on-source pointing, and slightly off-source pointing (b) of the IACT as a function of the distance from the Crab and time, as obtained from CCD camera images.

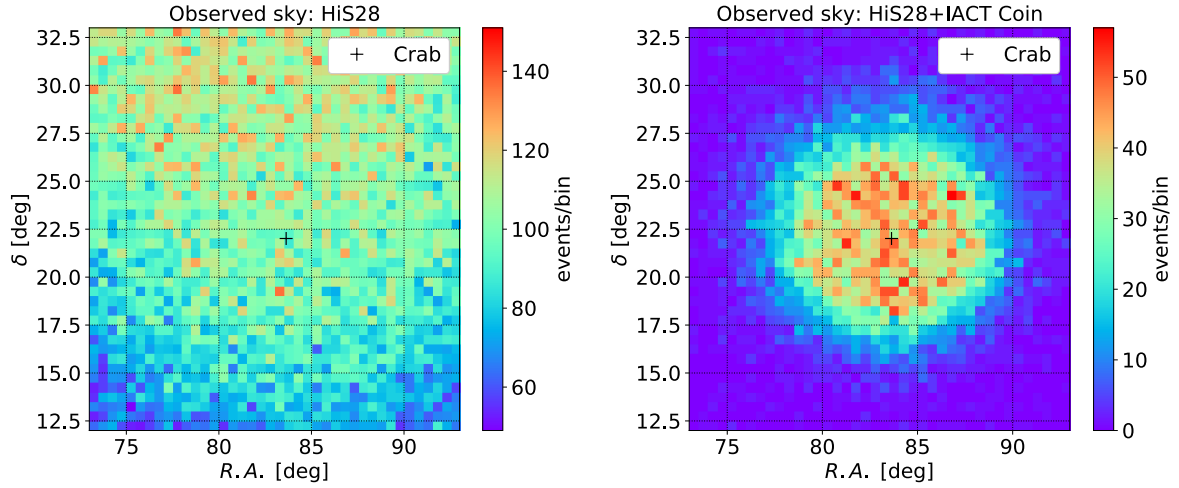

(a) (b)

Figure 7.21: HiS28-IACT coincidence events acceptance in equatorial coordinates ($R.A.$, δ), for all the 14 selected runs. Black cross: Crab position. (a) HiS28 all selected events (no IACT coincidence condition). (b) HiS28-IACT coincidence events.

7.4.2 Coincidence events detection efficiency

The HiS28-IACT coincidence events allow for an indirect study of the IACT detector acceptance, by looking at their arrival direction distribution. This method relies only on the accurate reconstruction of the HiS28 events. Figure 7.21 shows the arrival direction distribution around the Crab position (black cross), for all the selected HiS28 events (7.21(a)), and for the

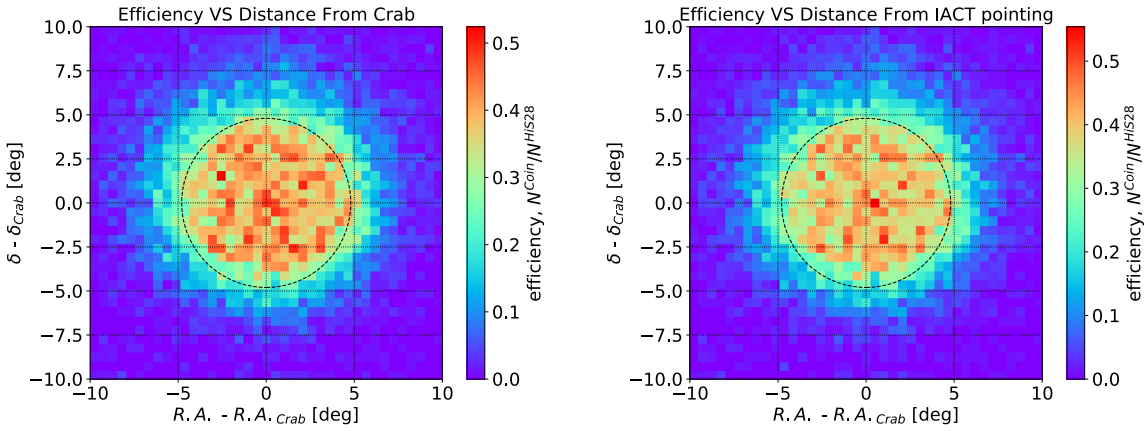

(a) (b)

Figure 7.22: IACT detection efficiency, as a function of the distance from (a) the Crab position, and (b) the IACT pointing direction. The efficiency maps are obtained dividing the two acceptance maps of figure 7.21. The circle of radius $4.8°$ indicated the radius of the telescope FOV.

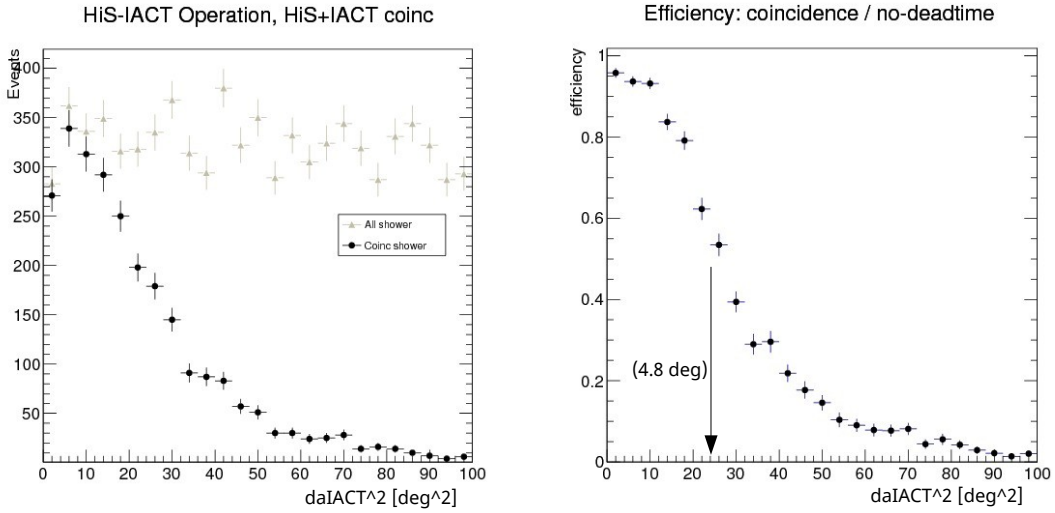

Figure 7.23: HiS28-IACT coincidence efficiency as a function of the angular distance from the IACT pointing, $\delta\alpha^2_{IACT}$, taking into account the IACT camera dead time. Data from 28.10.2017. Left: all HiS28 shower (grey dots), and HiS28-IACT coincidence (black dots). Right: HiS28-IACT detection efficiency (ratio between black/grey dots of left plot). The efficiency is $\sim$ 95% for $\delta\alpha^2_{IACT} \leq (3°)^2$, and drops beyond 50% for $\delta\alpha^2_{IACT} \geq (4.8°)^2$.

sub-sample of coincidence events (7.21(b)). The last figure shows the circular acceptance of the IACT dish.

Figure 7.22(a) shows the IACT detection efficiency, equal to the ration of figure 7.21(b) and 7.21(a). The total efficiency reaches $\sim 50\%$ for the centre of the telescope, and is dominated by the camera dead time effect in the commissioning time.

Figure 7.23 presents the results for the dead time corrected event sample, obtained by removing all the HiS28 events triggered within $250\,\mu$s after the last IACT trigger. The figure on the left shows the distribution of the coincidence events (black dots) as a function of $\delta\alpha^2_{IACT}$, where $\delta\alpha_{IACT}$ is the distance from the detector pointing. The grey dots give the distribution of all the HiS28 selected events, showing the expected uniform distribution. The figure on the right shows the IACT efficiency as a function of $\delta\alpha^2_{IACT}$, obtained dividing the two distribution in the left figure. We find a 95% IACT efficiency up to $\sim 3^\circ$, 50% at 4.8°, which is the radius of the circular telescope FOV.

7.5 Summary and conclusions

This chapter presented the first systematic point source analysis (PSA) developed for the TAIGA-HiSCORE detector in stand-alone mode, and for future application in hybrid detection mode (HiSCORE+IACT). This analysis was beyond the original scope of this thesis, and is a first and preliminary attempt to detect a signal from the Crab Nebula.

A dedicated MC simulation of the expected signal and background from the Crab region is used in section 7.2 for a qualitative study of the detection potential of the TAIGA experiment. No $5\,\sigma$ signal detection is expected with the HiS28 three years data ($T_{obs} = 210\,$h), mainly because of the small instrumented area ($0.25\,$km^2), the high detector energy threshold (estimated to be $\sim 60 - 80\,$TeV for the Crab), and no gamma-hadron separation available so far. The $1\,$km^2 TAIGA detector, with its larger instrumented area, and combining the HiSCORE event reconstruction with the gamma-hadron separation from the IACT (assumed here to provide a $Q^{\gamma/h}_{IACT} = 4$), is expected to be sensitive to the Crab gamma-ray flux below $200\,$TeV after a $T_{obs} \sim 200\,$h. The detection potential of TAIGA-HiSCORE (in stand-alone or hybrid mode) below $100\,$TeV strongly depends on the detector energy threshold. In a future analysis, an effort should be made to determine the experimental energy threshold of HiSOCRE, with a precision of $10 - 20\,$TeV, to improve the reliability of the detector sensitivity estimation. New methods need to be probably developed, as discussed in section 5.4.2.

The second part of the chapter (section 7.3) describes the PSA developed for TAIGA-HiSCORE in stand-alone mode, and the results for the HiS28 three years data sample. One of the keys for a sensitive PSA is the background estimation, obtained here using two different methods: the Direct Integration (DI) and Ring-Background (Ring). The methods result very stable, and yield similar results. The background estimation and the detection potential of the PSA are checked using "known signals": the ISS-events (chapter 6), and an artificial Crab signal injected in the data sample. This qualifies the developed PSA to detect medium-large signals, if present in

the data. A preliminary analysis of the HiS28 three years data shows no significant event excess in the observed sky, including the region around the Crab position. Scanning a small Crab neighbouring region, the largest excess fluctuation is found at an angular distance of $\sim 0.35^{\circ}$, with a detection significance of $2.5 - 3\,\sigma$. Being aware of the limits of this preliminary analysis, several improvements to enhance the detection potential of the PSA developed for the TAIGA-HiSCORE detector are discussed.

The last section of this chapter presents a first analysis of the combined HiS28 and IACT data collected during season 2017/18. Here, the IACT detector efficiency is studied using reconstructed HiS28 showers which also trigger the IACT, while it is tracking the Crab Nebula.

List of Figures

List of Tables

Appendices

Appendix A

HiS28 point source analysis

Chapter 7 shows the results of the PSA performed on the three years HiS28 data sample calibrated with the HYB method, and for a search radius $\theta_S = 0.3°$. This Appendix summarizes the results of the PSA obtained for different values of the search radius ($\theta_S = 0.2°$, $0.3°$, and $0.4°$), different background estimation methods (DI-Time, DI-Direction, and Ring), and for data calibrated using both the HYB and the HV time calibration methods.

Background-quality check. Figure A.1 shows the result of the background quality check, for a search radius $\theta_S = 0.2°$, $0.3°$, and $0.4°$, and for a data sample calibrated using the HYB time calibration methods. Similar results are obtained with the HV calibration.

Final three years Significance maps. Figure A.2 and A.3 present the Significance maps obtained for a search radius ($\theta_S = 0.2°$, $0.3°$, and $0.4°$), different background estimation methods (DI-Time, DI-Direction, and Ring), and for a data sample calibrated using the HYB and HV time calibration methods.

Scan around the Crab location. Figure A.4 shows the results of the scan of the Significance maps around the Crab position, as discussed in section 7.3.3. The results are obtained for a search radius ($\theta_S = 0.2°$, $0.3°$, and $0.4°$), different background estimation methods (DI-Time, DI-Direction, and Ring), and for a data sample calibrated using the HYB and HV time calibration methods. The scan is performed inside a squared region of side $1°$, centred at the Crab position.

Figure A.4(a) gives the Significance in the Crab bin, as a function of the search (smoothing) radius. Figure A.4(b) gives the largest Significance in the scan region, as a function of the search (smoothing) radius, while figure A.4(b) shows the corresponding bin position. The circles indicate the size of the uniform smoothing kernel, θ_S.

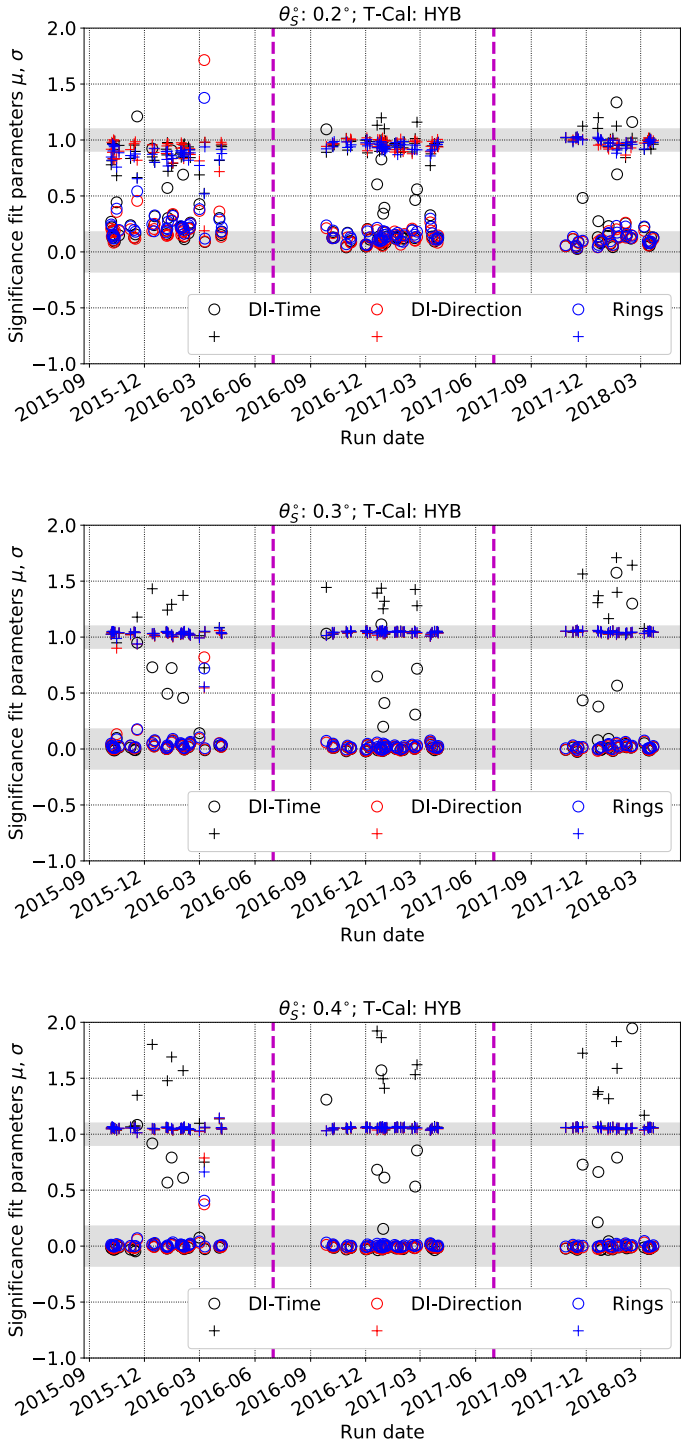

Figure A.1: Run-wise background quality check, based on the Gaussian fit of the observed sky Significance distribution (see figure 7.11, for the different background estimation methods: DI-Time (black), DI-Direction (red), and Ring (blue). The circles (crosses) represent the fitted Gaussian centre, μ, and width, σ. (a) $\theta_S = 0.2°$. (b) $\theta_S = 0.3°$. (c) $\theta_S = 0.4°$.

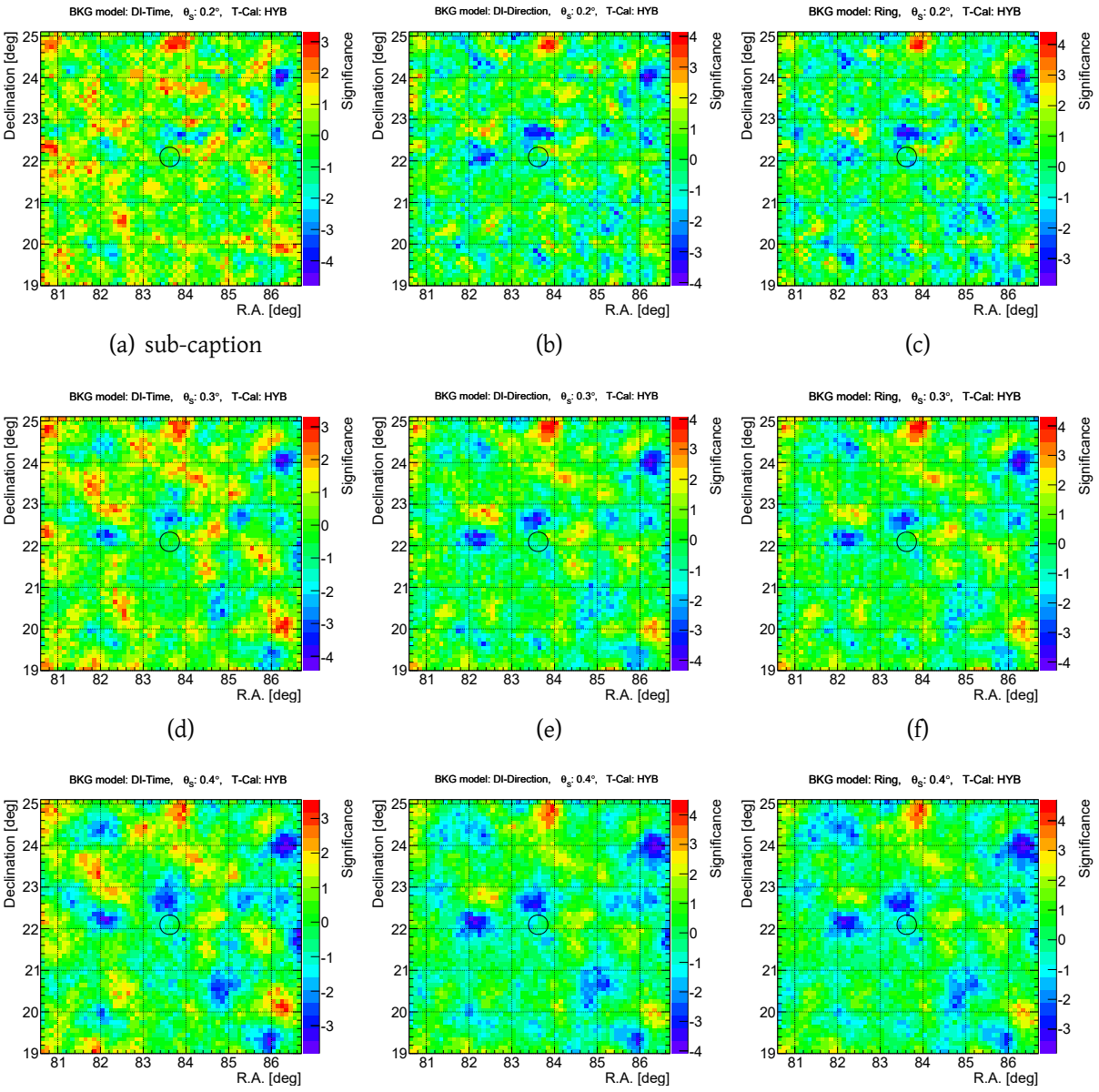

(a) sub-caption (b) (c)

(d) (e) (f)

(g) (h) (i)

Figure A.2: Significance maps for the data sample calibrated with the HV time calibration, for different background estimation and search (smoothing) radius, θ_S. Background estimation method, from left to right: DI-Time, DI-Direction, Ring. Search (smoothing) radius, from top to bottom: $\theta_S = 0.2^\circ$, 0.3°, and 0.4°.

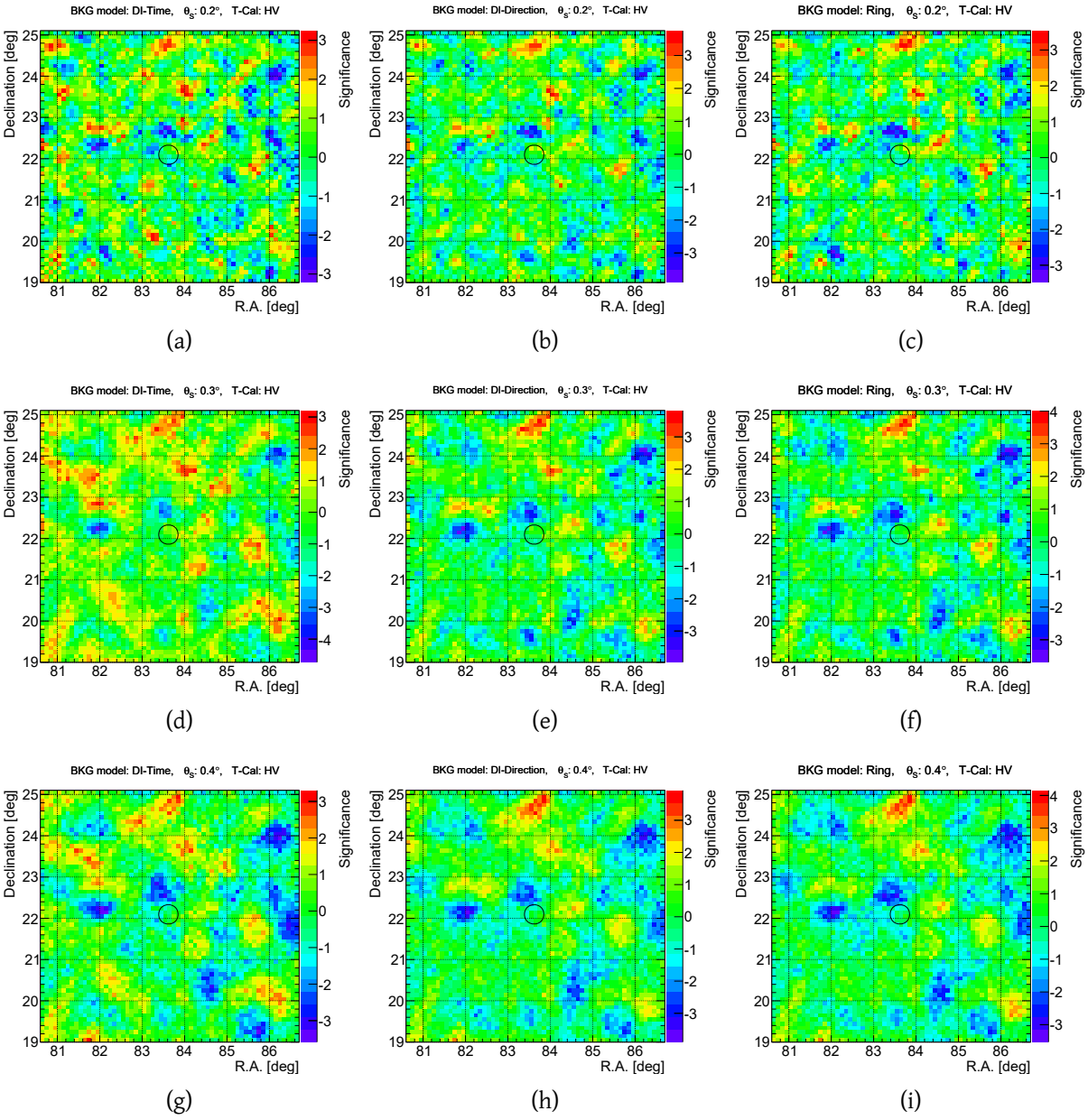

Figure A.3: Significance maps for the data sample calibrated with the HV time calibration, for different background estimation and search (smoothing) radius, θ_S. Background estimation method, from left to right: DI-Time, DI-Direction, Ring. Search (smoothing) radius, from top to bottom: $\theta_S = 0.2°$, $0.3°$, and $0.4°$.

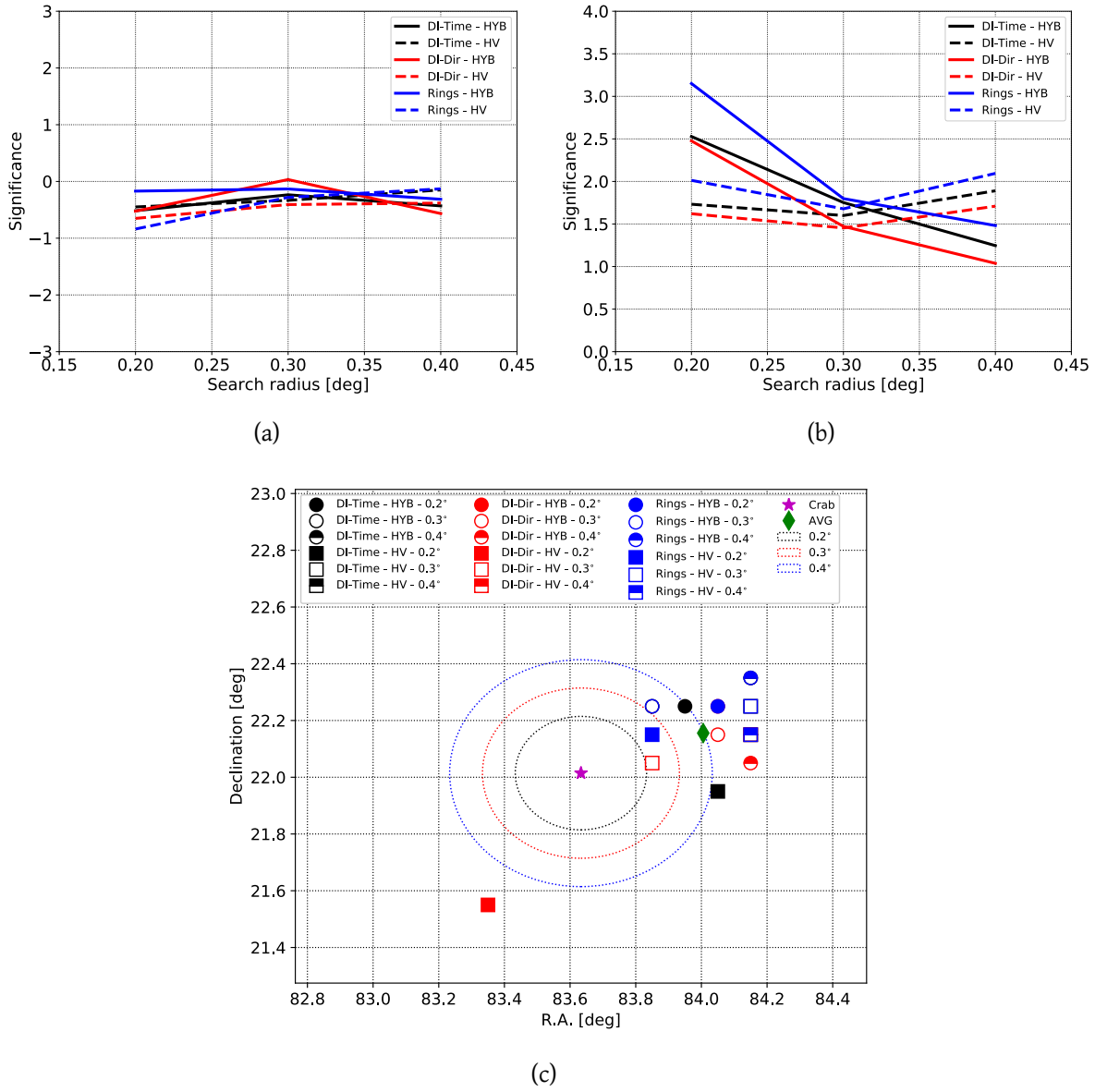

Figure A.4: Systematic scan around the Crab region. (a) Significance in the source bin, as a function of the search (smoothing) radius. (b) Largest Significance found in the scan region, as a function of the search (smoothing) radius. (c) Location of the bins found with the largest significance, S, in the scan region.

Bibliography

Aab, A., Abreu, P., Aglietta, M., et al. (2015). The Pierre Auger Cosmic Ray Observatory. *Nucl. Instruments Methods Phys. Res. Sect. A Accel. Spectrometers, Detect. Assoc. Equip.*, 798:172–213, arXiv:1502.01323.

Aartsen, M. G., Abbasi, R., Abdou, Y., et al. (2013). OBSERVATION OF COSMIC-RAY ANISOTROPY WITH THE ICETOP AIR SHOWER ARRAY. *Astrophys. J.*, 765(1):55, arXiv:1210.5278.

Abbasi, R., Abdou, Y., Abu-Zayyad, T., et al. (2010). Measurement of the anisotropy of cosmic-ray arrival directions with icecube. *Astrophys. J. Lett.*, 718(2 PART 2):L194–L198, arXiv:arXiv:1005.2960v1.

Abbasi, R. U., Abe, M., Abu-Zayyad, T., et al. (2014). Indications of intermediate-scale anisotropy of cosmic rays with energy greater than 57 EeV in the northern sky measured with the surface detector of the Telescope Array experiment. *Astrophys. J. Lett.*, 790(2):21–21, arXiv:1404.5890.

Abbasi, R. U., Abu-Zayyad, T., Allen, M., et al. (2008). First observation of the greisen-zatsepin-kuzmin suppression. *Phys. Rev. Lett.*, 100:101101.

Abdo, A. A., Allen, B., Aune, T., et al. (2008). Discovery of localized regions of excess 10-TeV cosmic rays. *Phys. Rev. Lett.*, 101(22):221101, arXiv:0801.3827.

Abdo, A. A., Allen, B., Berley, D., et al. (2007). Discovery of TeV Gamma-Ray Emission from the Cygnus Region of the Galaxy. *Astrophys. J.*, 658(1):L33–L36, arXiv:0611691.

Abdo, A. A., Allen, B. T., Aune, T., et al. (2009). Milagro Observations of Multi-TeV Emission from Galactic Sources in the Fermi Bright Source List. *Astrophys. J.*, 700(2 PART 2), arXiv:0904.1018.

Abraham, J., Abreu, P., Aglietta, M., et al. (2007). Correlation of the Highest-Energy Cosmic Rays with Nearby Extragalactic Objects. *Science*, 318(5852):938–943.

Abraham, J., Abreu, P., Aglietta, M., et al. (2008). Observation of the suppression of the flux of cosmic rays above $4 \cdot 10^{1}9$ev. *Phys. Rev. Lett.*, 101:061101.

Abraham, J., Aglietta, M., Aguirre, I., et al. (2004). Properties and performance of the prototype instrument for the Pierre Auger Observatory. *Nucl. Instruments Methods Phys. Res. Sect. A Accel. Spectrometers, Detect. Assoc. Equip.*, 523(1-2):50–95.

Abramowski, A., Aharonian, F., Benkhali, F. A., et al. (2016). Acceleration of petaelectronvolt protons in the Galactic Centre. *Nature*, 531(7595):476–478, arXiv:1603.07730.

Acero, F., Aharonian, F., Akhperjanian, A. G., et al. (2010). First detection of VHE γ -rays from SN 1006 by HESS. *Astron. Astrophys.*, 516(8):A62, arXiv:1004.2124.

Ackermann, M., Ajello, M., Allafort, A., et al. (2013). Detection of the characteristic pion-decay signature in supernova remnants. *Science (80-.).*, 339(6121):807–811, arXiv:arXiv:0905.2433v1.

Agasa Collaboration (2006). AGASA results. *Nuclear Physics B Proceedings Supplements*, 151:3–10.

Aglietta, M., Alekseenko, V. V., Alessandro, B., et al. (2009). Evolution of the cosmic-ray anisotropy above 1014eV. *Astrophys. J.*, 692(2):L130–L133, arXiv:0901.2740.

Aguilar, M., Ali Cavasonza, L., Ambrosi, G., et al. (2016). Precision Measurement of the Boron to Carbon Flux Ratio in Cosmic Rays from 1.9 GV to 2.6 TV with the Alpha Magnetic Spectrometer on the International Space Station. *Phys. Rev. Lett.*, 117(23).

Aharonian, F. (2004). *Very High Energy Cosmic Gamma Radiation. A Crucial Window on the Extreme Universe*. Elsevier.

Aharonian, F., Akhperjanian, A., Barrio, J. A., et al. (2002). Search for point sources of gamma radiation above 15 TeV with the HEGRA AIROBICC array. *Astron. Astrophys.*, 390(1):39–46, arXiv:0209402.

Aharonian, F., Akhperjanian, A., Beilicke, M., et al. (2004). The Crab Nebula and Pulsar between 500 GeV and 80 TeV: Observations with the HEGRA Stereoscopic Air Cerenkov Telescopes. *Astrophys. J.*, 614(2):897–913, arXiv:0407118.

Aharonian, F., Akhperjanian, A. G., Aye, K.-m., et al. (2005a). Discovery of extended VHE gamma-ray emission from the asymmetric pulsar wind nebula in MSH 15-5 2 with HESS. *Astron. Astrophys.*, 435(1):L17–L20, arXiv:0504120v1.

Aharonian, F., Akhperjanian, A. G., Aye, K.-M., et al. (2005b). H.E.S.S. observations of PKS 2155-304. *Astron. Astrophys.*, 430(3):865–875.

Aharonian, F., Akhperjanian, A. G., Barres de Almeida, U., et al. (2008). HESS very-high-energy gamma-ray sources without identified counterparts. *Astronomy and Astrophysics*, 477(1):353–363, arXiv:0712.1173.

Aharonian, F., Akhperjanian, A. G., Bazer-Bachi, A. R., et al. (2006). First detection of a VHE gamma-ray spectral maximum from a cosmic source: HESS discovery of the Vela X nebula. *Astron. Astrophys.*, 448(2):L43–L47, arXiv:0601575.

Aharonian, F., Akhperjanian, A. G., Bazer-Bachi, A. R., et al. (2006). A detailed spectral and morphological study of the gamma-ray supernova remnant RX J1713.7-3946 with HESS. *Astronomy and Astrophysics*, 449:223–242, arXiv:astro-ph/0511678.

Aharonian, F., Akhperjanian, A. G., Bazer-Bachi, A. R., et al. (2006). Discovery of very-high-energy gamma-rays from the Galactic Centre ridge. *Nature*, 439(7077):695–698, arXiv:0603021.

Aharonian, F., Akhperjanian, A. G., Bazer-Bachi, A. R., et al. (2007). Primary particle acceleration above 100 TeV in the shell-type supernova remnant RX J1713.7-3946 with deep HESS observations. *Astronomy and Astrophysics*, 464:235–243, arXiv:astro-ph/0611813.

Aharonian, F., Akhperjanian, A. G., Bazer-Bachi, A. R., et al. (2007). H.E.S.S. Observations of the Supernova Remnant RX J0852.0-4622: Shell Type Morphology and Spectrum of a Widely Extended Very High Energy Gamma Ray Source. *Astrophys. J.*, 661(1):236–249, arXiv:0612495.

Ahlers, M. and Mertsch, P. (2017). Origin of small-scale anisotropies in Galactic cosmic rays.

Aielli, G., Assiro, R., Bacci, C., et al. (2006). Layout and performance of rpcs used in the argo-ybj experiment. *Nuclear Instruments and Methods in Physics Research Section A: Accelerators, Spectrometers, Detectors and Associated Equipment*, 562(1):92 – 96.

Aielli, G., Bacci, C., Bartoli, B., et al. (2009). Software timing calibration of the ARGO-YBJ detector. *Astropart. Phys.*, 30(6):287–292.

Albert, J., Aliu, E., Anderhub, H., et al. (2008). VHE γ-Ray Observation of the Crab Nebula and its Pulsar with the MAGIC Telescope. *Astrophys. J.*, 674(2):1037–1055, arXiv:0705.3244.

Aleksić, J., Ansoldi, S., Antonelli, L., et al. (2015). Measurement of the Crab Nebula spectrum over three decades in energy with the MAGIC telescopes. *J. High Energy Astrophys.*, 5-6:30–38, arXiv:1406.6892.

Alexandreas, D., Allen, R., Biller, S., et al. (1992). The CYGNUS extensive air-shower experiment. *Nucl. Instruments Methods Phys. Res. Sect. A Accel. Spectrometers, Detect. Assoc. Equip.*, 311(1-2):350–367.

Alexandreas, D., Berley, D., Biller, S., et al. (1993). Point source search techniques in ultra high energy gamma ray astronomy. *Nucl. Instruments Methods Phys. Res. Sect. A Accel. Spectrometers, Detect. Assoc. Equip.*, 328(3):570–577.

Aliu, E., Anderhub, H., Antonelli, L. A., et al. (2008). Observation of Pulsed -Rays Above 25 GeV from the Crab Pulsar with MAGIC. *Science*, 322(5905):1221–1224, arXiv:0809.2998.

Amenomori, M., Ayabe, S., Cui, S. W., et al. (2005). Large-Scale Sidereal Anisotropy of Galactic Cosmic-Ray Intensity Observed by the Tibet Air Shower Array. *Astrophys. J.*, 626(1):L29–L32, arXiv:0505114.

Amenomori, M., Bi, X., Chen, D., et al. (2011). Time dependence of loss-cone amplitude measured with the tibet air-shower array. In *Proc. 32nd Int. Cosm. Ray Conf. ICRC 2011*, volume 1, pages 62–65.

Anderhub, H., Backes, M., Biland, A., et al. (2011). FACT - The first Cherenkov telescope using a G-APD camera for TeV gamma-ray astronomy. *Nuclear Instruments and Methods in Physics Research A*, 639:58–61.

Anderson, C. D. (1933). The positive electron. *Phys. Rev.*, 43:491–494.

Ansoldi, S., Antonelli, L. A., Antoranz, P., et al. (2016). Teraelectronvolt pulsed emission from the Crab Pulsar detected by MAGIC. *Astron. Astrophys.*, 585(18):A133, arXiv:1510.07048.

Apel, W., Arteaga-Velázquez, J., Bekk, K., et al. (2013a). Kascade-grande measurements of energy spectra for elemental groups of cosmic rays. *Astroparticle Physics*, 47:54–66.

Apel, W. D., Arteaga, J. C., Badea, A. F., et al. (2009). Energy spectra of elemental groups of cosmic rays: Update on the KASCADE unfolding analysis. *Astropart. Phys.*, 31(2):86–91, arXiv:0812.0322.

Apel, W. D., Arteaga-Velàzquez, J. C., Bekk, K., et al. (2013b). Ankle-like feature in the energy spectrum of light elements of cosmic rays observed with KASCADE-Grande. *Phys. Rev. D - Part. Fields, Gravit. Cosmol.*, 87(8):081101, arXiv:1304.7114.

Arteaga-Velazquez, J. C., Apel, W. D., Bekk, K., et al. (2013). Study of the muon content of very high-energy EAS measured with the KASCADE-Grande observatory. *33rd Int. Cosm. Ray Conf.*, 1308(August):3202, arXiv:1308.3202.

Astapov, I., Bezyazeekov, P., Borodin, A., et al. (2019). Scintillation detectors for the TAIGA experiment. *Nuclear Instruments and Methods in Physics Research Section A: Accelerators, Spectrometers, Detectors and Associated Equipment*, 936:254–256.

Atkins, R., Benbow, W., Berley, D., et al. (2003). Observation of TeV Gamma Rays from the Crab Nebula with Milagro Using a New Background Rejection Technique. *Astrophys. J.*, 595(2):803–811, arXiv:0305308.

Atkins, R., Benbow, W., Berley, D., et al. (2000). Milagrito, a tev air-shower array. *Nuclear Instruments and Methods in Physics Research Section A: Accelerators, Spectrometers, Detectors and Associated Equipment*, 449(3):478 – 499.

Auger, P., Ehrenfest, P., Maze, R., et al. (1939). Extensive cosmic-ray showers. *Rev. Mod. Phys.*, 11:288–291.

Axford, W. I., Leer, E., and Skadron, G. (1977). The acceleration of cosmic rays by shock waves. *International Cosmic Ray Conference*, 11:132–137.

Baillon, P., Behr, L., Danagoulian, S., et al. (1993). Gamma ray spectrum of the crab nebula in the multi tev region. *Astroparticle Physics*, 1(4):341 – 355.

Bartoli, B., Bernardini, P., Bi, X. J., et al. (2014). Evidence of a geomagnetic effect on extensive air showers detected with the ARGO-YBJ experiment. *Phys. Rev. D - Part. Fields, Gravit. Cosmol.*, 89(5):52005–1550.

Bartoli, B., Bernardini, P., Bi, X. J., et al. (2013). Medium scale anisotropy in the TeV cosmic ray flux observed by ARGO-YBJ. *Phys. Rev. D - Part. Fields, Gravit. Cosmol.*, 88(8):082001, arXiv:1309.6182.

Bell, A. R. (1978). The acceleration of cosmic rays in shock fronts. I. *Monthly Notices of the Royal Astronomical Society*, 182:147–156.

Benbow, W. (2017). Highlights from the VERITAS AGN observation program. In *AIP Conf. Proc.*, volume 1792, page 050001.

BenZvi, S. (2015). First Results from the High-altitude Water Cherenkov Observatory. In *Phys. Procedia*, volume 61, pages 399–408.

Berezhnev, S. F., Besson, D., Budnev, N. M., et al. (2012). The Tunka-133 EAS Cherenkov light array: Status of 2011. *Nucl. Instruments Methods Phys. Res. Sect. A Accel. Spectrometers, Detect. Assoc. Equip.*, 692:98–105, arXiv:arXiv:1201.2122v1.

Berezhnev, S. F., Budnev, N. M., Büker, M., et al. (2015). First results from the operation of the prototype Tunka-HiSCORE array. *Bull. Russ. Acad. Sci. Phys.*, 79(3):348–351.

Berge, D., Funk, S., and Hinton, J. (2006). Background Modelling in Very-High-Energy gamma-ray Astronomy. *Astron. Astrophys.*, 466(3):1219–1229, arXiv:0610959.

Berger, M. J. and Seltzer, S. M. (1964). Tables of energy losses and ranges of electrons and positrons.

Bernardini, P., Melcarne, A. K. C., Catalanotti, S., et al. (2005). Time Calibration of the ARGO-YBJ experiment. *29th Int. Cosm. Ray Conf.*, 5:147–150.

Bernlöhr, K. (2000). Impact of atmospheric parameters on the atmospheric Cherenkov technique. *Astropart. Phys.*, 12(4):255–268, arXiv:9908093.

Bernlöhr, K. (2008). Simulation of imaging atmospheric Cherenkov telescopes with CORSIKA and sim_telarray. *Astropart. Phys.*, 30(3):149–158, arXiv:0808.2253.

Bezyazeekov, P., Budnev, N., Gress, O., et al. (2016). Radio measurements of the energy and the depth of the shower maximum of cosmic-ray air showers by tunka-rex. *Journal of Cosmology and Astroparticle Physics*, 2016(01):052.

Blandford, R. D. and Ostriker, J. P. (1978). Particle acceleration by astrophysical shocks. *Astrophysical Journal*, 221:L29–L32.

Blasi, P. (2013). The Origin of Galactic Cosmic Rays. *Astron. Astrophys. Rev.*, 21(1):70, arXiv:1311.7346.

Blasi, P., Epstein, R. I., and Olinto, A. V. (2000). Ultra-High-Energy Cosmic Rays from Young Neutron Star Winds. *Astrophys. J. Lett.*, 533(2):L123, arXiv:9912240.

Blümer, J., Engel, R., and Hörandel, J. R. (2009). Cosmic rays from the knee to the highest energies. *Prog. Part. Nucl. Phys.*, 63(2):293–338, arXiv:0904.0725.

Brückner, M. and Wischnewski, R. (2013). A White Rabbit setup for sub-nsec synchronization, timestamping and time calibration in large scale astroparticle physics experiments. *33rd Int. Cosm. Ray Conf.*

Brückner, M., Wischnewski, R., Berezhnev, S., et al. (2013). Results from the WhiteRabbit subnsec time synchronization setup at HiSCORE-Tunka. *33rd Int. Cosm. Ray Conf.*

Budnev, N., Astapov, I., Barbashina, N., et al. (2017a). The TAIGA experiment: From cosmic-ray to gamma-ray astronomy in the Tunka valley. *Nucl. Instruments Methods Phys. Res. Sect. A Accel. Spectrometers, Detect. Assoc. Equip.*, 845(5):330–333.

Budnev, N., Astapov, I., Barbashina, N., et al. (2015). The Tunka detector complex: from cosmic-ray to gamma-ray astronomy. *J. Phys. Conf. Ser.*, 632(1):012034.

Budnev, N., Astapov, I., Bezyazeekov, P., et al. (2017b). The TAIGA experiment - a hybrid detector for very high energy gamma-ray astronomy and cosmic ray physics in the Tunka valley. In *EPJ Web Conf.*

Budnev, N., Astapov, I., Bezyazeekov, P., et al. (2017c). Taiga experiment: present status and perspectives. *Journal of Instrumentation*, 12(08):C08018.

Bühler, R. (2015). Status of space-based gamma-ray astronomy. *34th Int. Cosm. Ray Conf.*

Bykov, A. M., Ellison, D. C., Marcowith, A., et al. (2018). Cosmic ray production in supernovae. arXiv:arXiv:1801.08890v1.

Calabrese Melcarne, A. K. (2006). Time measurement with the ARGO-YBJ detector.

Caprioli, D. (2015). "Espresso" Acceleration of Ultra-high-energy Cosmic Rays. *Astrophys. J.*, 811(2):L38, arXiv:1505.06739.

CATS collaboration (2016). CATS L1B Products Quality Statements - Version Release: 2.06. https://cats.gsfc.nasa.gov/media/docs/CATS_QS_L1B_2.06.pdf.

Clark, G. W. (1957). Arrival directions of cosmic-ray air showers from the northern sky. *Phys. Rev.*, 108:450–457.

Daum, A., Hermann, G., Hess, M., et al. (1997). First results on the performance of the hegra iact array. *Astroparticle Physics*, 8(1):1–11.

Deligny, O., De Mello Neto, J., Sommers, P., et al. (2013). Review of the anisotropy working group at UHECR-2012. In *EPJ Web Conf.*, volume 53.

Deligny, O., Kawata, K., and Tinyakov, P. (2017). Measurement of Anisotropy and Search for UHECR Sources. 00000, arXiv:1702.07209.

Desiati, P. and Lazarian, A. (2013). Anisotropy of TeV cosmic rays and outer heliospheric boundaries. *Astrophys. J.*, 762(1):44, arXiv:1111.3075.

Di Sciascio, G. (2016). The LHAASO experiment: From Gamma-Ray Astronomy to Cosmic Rays. *Nucl. Part. Phys. Proc.*, 279-281:166–173, arXiv:1602.07600.

Di Sciascio, G. and Collaboration, f. t. A.-Y. (2012). ARGO-YBJ: Status and Highlights. *Acta Polytech.*, 53(SUPPL.1):646–651, arXiv:1210.2635.

DIGI (2018). Digi xbee/rf solutions. https://www.digi.com/products/xbee-rf-solutions.

DRS (2018). DRS chip web page. https://www.psi.ch/drs/.

Drury, L. O., Aharonian, F. A., and Voelk, H. J. (1994). The gamma-ray visibility of supernova remnants. A test of cosmic ray origin. *Astronomy and Astrophysics*, 287:959–971, arXiv:astro-ph/9305037.

Dyakonov, M. N. et al. (1973). . II. The lateral distribution oe EAS Cherenkov light of large sizes at sea level. *13th International Cosmic Ray Conference*, 1:2389–2390.

Elo, A.-M. and Arvela, H. (1999a). Correction of Air Shower Timing Using Shower Data. *26th Int. Cosm. Ray Conf.*, 5:324.

Elo, A.-M. and Arvela, H. (1999b). The Effect of Timing Inaccuracy on the Shower Arrival Direction. *26th Int. Cosm. Ray Conf.*, 5:328.

Elo, A.-M. and Arvela, H. (1999c). The timing measurement in the Air Shower Experiment in Turku. *26th Int. Cosm. Ray Conf.*, page 320.

Epimakhov, S. (2015). *Exploring cosmic ray origins with ground-based EAS arrays Tunka and HiSCORE*. PhD thesis, Hamburg University.

Epimakhov, S., Uckner, M. B., Budnev, N., et al. (2013). Components of the HiSCORE detector and prototype test results. *33rd Int. Cosm. Ray Conf.*, (Emi 9350):5–7.

Fermi, E. (1949). On the origin of the cosmic radiation. *Phys. Rev.*, 75:1169–1174.

Fletcher, A. (2011). Magnetic fields in nearby galaxies. arXiv:1104.2427.

Fowler, J., Fortson, L., Jui, C., et al. (2001). A measurement of the cosmic ray spectrum and composition at the knee. *Astropart. Phys.*, 15(1):49–64, arXiv:0003190.

Funk, S. (2005). *A new population of very high energy gamma-ray sources in the Milky Way*. PhD thesis, Ruprecht-Karls-Universität Heidelberg.

Gabici, S. and Aharonian, F. A. (2007). Searching for Galactic Cosmic-Ray Pevatrons with Multi-TeV Gamma Rays and Neutrinos. *Astrophys. J.*, 665(2):L131–L134, arXiv:0705.3011.

Gosse, J. C. and Phillips, F. M. (2001). Terrestrial in situ cosmogenic nuclides: theory and application. *Quat. Sci. Rev.*, 20(14):1475–1560.

Greisen, K. (1966). End to the cosmic-ray spectrum? *Phys. Rev. Lett.*, 16:748–750.

Gress, O., Astapov, I., Budnev, N., et al. (2017). The wide-aperture gamma-ray telescope TAIGA-HiSCORE in the Tunka Valley: Design, composition and commissioning. *Nucl. Instruments Methods Phys. Res. Sect. A Accel. Spectrometers, Detect. Assoc. Equip.*, 845:367–372.

Gress, O., Brüeckner, M., Berezhnev, S., et al. (2013). Tunka-HiSCORE - A new array for multi-TeV γ-ray astronomy and cosmic-ray physics. *Nucl. Instruments Methods Phys. Res. Sect. A Accel. Spectrometers, Detect. Assoc. Equip.*, 732:290–294.

Grieder, P. (2001). *Cosmic Rays at Earth - Researcher's Reference Manual and Data Book*. Elsevier.

Guillian, G., Hosaka, J., Ishihara, K., et al. (2007). Observation of the anisotropy of 10 TeV primary cosmic ray nuclei flux with the Super-Kamiokande-I detector. *Phys. Rev. D - Part. Fields, Gravit. Cosmol.*, 75(6):062003, arXiv:0508468v4.

Hamamatsu (2006). Photomultiplier tubes. basics and applications. http://psec.uchicago.edu/links/pmt_handbook_complete.pdf.

Hampf, D. (2012). *Study for the wide-angle air Cherenkov detector HiSCORE and time gradient event reconstruction for the H.E.S.S. experiment*. PhD thesis, Hamburg University.

Hampf, D., Tluczykont, M., and Horns, D. (2011). Simulation of the expected performance for the proposed gamma-ray detector HiSCORE. *25th Texas Symp. Relativ. Astrophys.*, arXiv:1104.2336.

Hampf, D., Tluczykont, M., and Horns, D. (2013). Event reconstruction techniques for the wide-angle air Cherenkov detector HiSCORE. *Nucl. Instruments Methods Phys. Res. Sect. A Accel. Spectrometers, Detect. Assoc. Equip.*, 712:137–146, arXiv:1302.3957.

Hara, T., Kifune, T., Matsubara, Y., et al. (1993). A 3.8m imaging cherenkov telescope for the tev gamma-ray astronomy collaboration between japan and australia. *Nuclear Instruments and Methods in Physics Research Section A: Accelerators, Spectrometers, Detectors and Associated Equipment*, 332(1):300–309.

Hauser, M. G. and Dwek, E. (2001). The cosmic infrared background: Measurements and implications. *Annual Review of Astronomy and Astrophysics*, 39(1):249–307, arXiv:https://doi.org/10.1146/annurev.astro.39.1.249.

He, H. H., Bernardini, P., Calabrese Melcarne, A. K., et al. (2007). Detector time offset and offline calibration in EAS experiments. *Astropart. Phys.*, 27(6):528–532, arXiv:0701291.

He, H. H., Sun, B. G., and Zhou, Y. (2005). The Effect of the Geomagnetic Field on the Trigger Efficiency of the ARGO Experiment. *29th Int. Cosm. Ray Conf.*, 6:5–8.

Heck, D., Knapp, J., Capdevielle, J., et al. (1998). CORSIKA : A Monte Carlo Code to Simulate Extensive Air Showers. FZKA 6019:98.

Heitler, W. (1954). *The Quantum Theory of Radiation*. Courier Corporation.

Henke, V. (1994). Studie zur auswertung der ankunftszeitverteilung des cerenkov-lichts ausgedehnter luftschauer. Master's thesis, Hamburg University.

Hess, V. S. (1912). Über Beobachtungen der durchdringenden Strahlung bei sieben Freiballonfahrten. *Zeitschrift für Physik*, 13:1084–1091.

H.E.S.S. Collaboration, Abdalla, H., Abramowski, A., et al. (2018). H.E.S.S. observations of RX J1713.7-3946 with improved angular and spectral resolution: Evidence for gamma-ray emission extending beyond the X-ray emitting shell. *Astronomy and Astrophysics*, 612:A6, arXiv:1609.08671.

Hillas, A. M. (1985). Cerenkov light images of EAS produced by primary gamma. *International Cosmic Ray Conference*, 3.

Hillas, A. M. (2006). Cosmic Rays: Recent Progress and some Current Questions. *Cosm. Rays*, page 12, arXiv:0607109.

Hinton, J. (2004). The status of the hess project. *New Astronomy Reviews*, 48(5):331–337. 2nd VERITAS Symposium on the Astrophysics of Extragalactic Sources.

Hinton, J. (2009). Ground-based gamma-ray astronomy with cherenkov telescopes. *New Journal of Physics*, 11(5):055005.

Hofmann, W., Jung, I., Konopelko, A., et al. (1999). Comparison of techniques to reconstruct VHE gamma-ray showers from multiple stereoscopic Cherenkov images. *Astroparticle Physics*, 12:135–143, arXiv:astro-ph/9904234.

Holder, J., Acciari, V. A., Aliu, E., et al. (2008). Status of the veritas observatory. *AIP Conference Proceedings*, 1085(1):657–660, arXiv:https://aip.scitation.org/doi/pdf/10.1063/1.3076760.

Hoots, Felix R. and Roehrich, Ronald L. (1980). SPACETRACK REPORT NO. 3: Models for Propagation of NORAD Element Sets. https://www.celestrak.com/columns/v04n03/.

Hörandel, J. R. (2003). On the knee in the energy spectrum of cosmic rays. *Astroparticle Physics*, 19:193–220, arXiv:astro-ph/0210453.

Hörandel, J. R. (2006). Cosmic-ray abundances and energy spectra at high energies: Measurements with TRACER and KASCADE. *Adv. Sp. Res.*, 38(7):1549–1557.

Horns, D. and Meyer, M. (2012). Indications for a pair-production anomaly from the propagation of VHE gamma-rays. *J. Cosmol. Astropart. Phys.*, 2012(2), arXiv:1201.4711.

Hornyak, David M. (2013). A Researcher's Guide to: International Space Station - Thechnology Demostration. https://www.nasa.gov/sites/default/files/files/2013_ISS_Tech-Demo-mini-book-web_LATEST.pdf.

Huang, C.-Y. (2003). Gamma-Ray Energy Spectra through Decays of Neutral Pions Produced in Proton-Proton Interactions. *International Cosmic Ray Conference*, 4:2297.

IceCube collaboration (2013). Measurement of the cosmic ray energy spectrum with IceTop-73. *Phys. Rev. D*, 88(4):042004, arXiv:1307.3795.

IceCube Collaboration, Aartsen, M. G., Abraham, K., et al. (2016). All-sky search for time-integrated neutrino emission from astrophysical sources with 7 years of IceCube data. *Astrophys. J.*, 835(2):151, arXiv:1609.04981.

ISS Program (2008). Space Station Reference Coordinate Systems. https://pims.grc.nasa.gov/plots/user/tibor/SSP%2030219J%20ISS%20Coord%20Systems.pdf.

ISS-Tracker (2017). ISS-Tracker web page. http://www.isstracker.com/home.

Ivanov, A. A., Egorova, V. P., Kolosov, V. A., et al. (1999). Azimuthal modulation of the event rate of cosmic-ray extensive air showers by the geomagnetic field. *J. Exp. Theor. Phys. Lett.*, 69(4):288–293.

JEM-EF (2012). Japanese Experiment Module - Exposed Facility web page. https://www.nasa.gov/mission_pages/station/research/experiments/JEMEF.html.

Just, F., Harfmann, S., Abaronian, F., et al. (1993). Measurement of the Muon Content of Extensive Air Showers With The Hegra Detector. *23rd International Cosmic Ray Conference*, 4:203.

Kampert, K.-H. (2017). The Pierre Auger Observatory: Selected Results and Future Plans. In *Proc. 7th Int. Work. Very High Energy Part. Astron. 2014*. Journal of the Physical Society of Japan.

Kampert, K.-H. and The Pierre Auger Collaboration (2012). Highlights from the Pierre Auger Observatory. *arXiv Prepr. arXiv1207.4823*.

Kampert, K. H. and Unger, M. (2012). Measurements of the cosmic ray composition with air shower experiments.

Karle, A. (1991). The angular resolution of the Hegra scintillation counter array at La Palma. In *AIP Conf. Proc.*, volume 220, pages 127–131. AIP.

Karle, A., Merck, M., Plaga, R., et al. (1995). Design and performance of the angle integrating cherenkov array airobicc. *Astroparticle Physics*, 3(4):321–347.

Katsuda, S., Petre, R., Hughes, J. P., et al. (2010). X-ray measured dynamics of tycho's supernova remnant. *The Astrophysical Journal*, 709(2):1387.

Kelso, T. S. (2014). NORAD TLE. https://www.celestrak.com/columns/v04n03/.

Kevin Meagher for the VERITAS Collaboration (2015). Six years of VERITAS observations of the Crab Nebula. *Proc. Sci.*, 30-July-20, arXiv:1508.06442.

Kneiske, T., Kulbartz, J., Horns, D., et al. (2009). Diffuse gamma-ray and neutrino emission from the local supercluster. In *31st Int. Cosm. Ray Conf. ICRC 2009*.

Kneiske, T. M. and Dole, H. (2009). A strict lower-limit EBL applications on gamma-ray absorption. In *AIP Conf. Proc.*, volume 1085, pages 620–623.

Kneizys, F. X., Abreu, L. W., and Anderson, G. P. (1996). The MODTRAN 2/3 report and LOWTRAN 7 model. *Contract*, 19628(91-C):132.

Knödlseder, J. (2016). The future of gamma-ray astronomy. *Comptes Rendus Phys.*, 17(6):663–678, arXiv:1602.02728.

Kohnle, A., Aharonian, F., Akhperjanian, A., et al. (1996). Stereoscopic imaging of air showers with the first two hegra cherenkov telescopes. *Astroparticle Physics*, 5(2):119–131.

Krymskii, G. F. (1977). A regular mechanism for the acceleration of charged particles on the front of a shock wave. *Akademiia Nauk SSSR Doklady*, 234:1306–1308.

Kuhlmann, J. D., Clay, R. W., Crouch, P. C., et al. (1977). Cerenkov Light from EAS at Sea-Level. *15th Int. Cosm. Ray Conf.*, 8:239.

Kunnas, M. (2012). Bau eines triggersystems für den hiscore-detektor. Master's thesis, Hamburg University.

LabVIEW (2018). Labview software. https://www.ni.com/en-us/shop/labview.html.

Lagage, P. O. and Cesarsky, C. J. (1983). The maximum energy of cosmic rays accelerated by supernova shocks. *Astronomy and Astrophysics*, 125:249–257.

Lattes, C. M. G., Occhialini, G. P. S., and Powell, C. F. (1947). Observations on the tracks of slow mesons in photographic emulsions. *Nature*, 160:453–456.

Li, T. P. and Ma, Y. Q. (1983). Analysis methods for results in gamma-ray astronomy. *Astrophysical Journal*, 272:317–324.

Lipunov, V., Kornilov, V., Gorbovskoy, E., et al. (2010). Master robotic net. *Adv. Astron.*, 2010, arXiv:0907.0827.

Lubsandorzhiev, N., Astapov, I., Bezyazeekov, P., et al. (2017). Camera of the first TAIGA-IACT: construction and calibration. *35th Int. Cosm. Ray Conf.*

Maestro, P. (2015). Cosmic rays: direct measurements. *34th Int. Cosm. Ray Conf.*

MAGIC Collaboration, Ahnen, M. L., Ansoldi, S., et al. (2015). Very-high-energy gamma-rays from the Universe's middle age: detection of the z=0.940 blazar PKS 1441+25 with MAGIC. *Astrophys. J.*, 815(2):L23, arXiv:1512.04435.

MAGIC Collaboration, Ahnen, M. L., Ansoldi, S., et al. (2016). Detection of very high energy gamma-ray emission from the gravitationally-lensed blazar QSO B0218+357 with the MAGIC telescopes. *J. Herrera J. Hose J. Kushida J. M. Miranda J. Palacio J. M. Paredes Paredes-Fortuny J. Poutanen Prada Moroni I. Puljak J. R. Garcia I. Reichardt J. Rico J. Sitarek J. E. Ward*, 2030313233(30), arXiv:1609.01095.

MAGIC Collaboration, Ahnen, M. L., Ansoldi, S., et al. (2017). MAGIC Contributions to the 35th International Cosmic Ray Conference (ICRC2017). *eprint arXiv:1708.05153*, arXiv:1708.05153.

Maike Helena Kunnas (2017). *Studies of the performance of an IACT system for the TAIGA array*. PhD thesis, Hamburg University.

Malkov, M. A. and Drury, L. O. (2001). Nonlinear theory of diffusive acceleration of particles by shock waves. *Reports on Progress in Physics*, 64(4):429.

Marrocchesi, P. S. (2017). Charged Cosmic Rays: a Review of Balloon and Space Borne Measurements. *arXiv Prepr.*, arXiv:1704.00304.

McGill, M., Welton, E., Yorks, J., et al. (2012). CATS: A New Earth Science Capability. *The Earth Observer*, 24.

Medina-Tanco, G. A. (1999). The energy spectrum observed by the agasa experiment and the spatial distribution of the sources of ultra-high-energy cosmic rays. *The Astrophysical Journal Letters*, 510(2):L91.

Merck, M., Karle, A., Martinez, S., et al. (1996). Methods to determine the angular resolution of the HEGRA extended air shower scintillator array. *Astropart. Phys.*, 5(3-4):379–392.

Mewaldt, R. A. (1983). The elemental and isotopic composition of galactic cosmic ray nuclei. *Rev. Geophys. Sp. Phys.*, 21(2):295–305.

Meyer, M., Horns, D., and Raue, M. (2013). Revisiting the Indication for a low opacity Uni- verse for very high energy γ-rays. arXiv:arXiv:1211.6405v2.

Mirizzi, A. and Montanino, D. (2009). Stochastic conversions of TeV photons into axion-like particles in extragalactic magnetic fields. *J. Cosmol. Astropart. Phys.*, 2009(12):004–004, arXiv:0911.0015.

Mollerach, S. and Roulet, E. (2017). Progress in high-energy cosmic ray physics. *Prog. Part. Nucl. Phys.*, 98:85–118, arXiv:1710.11155.

Monkhoev, R. D., Budnev, N. M., Voronin, D. M., et al. (2017). The tunka-grande experiment: Status and prospects. *Bulletin of the Russian Academy of Sciences: Physics*, 81(4):468–470.

Moreira, P., Serrano, J., Wlostowski, T., et al. (2009). White rabbit: Sub-nanosecond timing distribution over ethernet. In *2009 Int. Symp. Precis. Clock Synchronization Meas. Control Commun.*, pages 1–5. IEEE.

Moskalenko, I. V., Porter, T. A., and Strong, A. W. (2006). Attenuation of Very High Energy Gamma Rays by the Milky Way Interstellar Radiation Field. *Astrophys. J.*, 640(2):L155–L158, arXiv:0511149.

Mukherjee, R. (2016). Recent Highlights from VERITAS. *Nucl. Part. Phys. Proc.*, 273-275:367–372.

Murase, K., Dermer, C. D., Takami, H., et al. (2011). Blazars as Ultra-High-Energy Cosmic-Ray Sources: Implications for TeV Gamma-Ray Observations. *Astrophys. J.*, 749(1), arXiv:1107.5576.

Nachtigall, R. (2011). Charakterisierung von photomultipliern und beiträge zur entwicklung eines prototypen für luftcherenkovmessungen. Master's thesis, Hamburg University.

Nachtigall, R., Kunnas, M., Epimakhov, S. N., et al. (2013). First deployment and prototype data of HiSCORE. *J. Phys. Conf. Ser.*, 409:012119.

NASA (2015). Reference guide to the International Space Station. https://www.nasa.gov/sites/default/files/atoms/files/np-2015-05-022-jsc-iss-guide-2015-update-111015-508c.pdf.

NASA ISS web page (2018). ISS web page. https://www.nasa.gov/mission_pages/station/main/index.html.

Neddermeyer, S. H. and Anderson, C. D. (1937). Note on the nature of cosmic-ray particles. *Phys. Rev.*, 51:884–886.

Ogio, S., Fukushima, M., Kakimoto, F., et al. (2005). Telescope Array; Progress of Fluorescence Detector. 8:173–176.

P. Abreu, et al. (The Pierre Auger Collaboration) (2012). Large-scale distribution of arrival directions of cosmic rays detected above 1018 ev at the pierre auger observatory. *The Astrophysical Journal Supplement Series*, 203(2):34.

P. Abreu, et al. (The Pierre Auger Collaboration) (2013). Constraints on the origin of cosmic rays above 1018 ev from large-scale anisotropy searches in data of the pierre auger observatory. *The Astrophysical Journal Letters*, 762(1):L13.

Palm, S. P., Hlavka, D. L., Selmer, P., et al. (2016). Cloud Aerosol Transport System (CATS), Data Management System, Data Products Catalog. https://cats.gsfc.nasa.gov/.

Patrignani,C., et al. (Particle Data Group) (2016). Review of Particle Physics. *Chinese Phys. C*, 40(10):100001.

Patterson, J. R. and Hillas, A. M. (1983). The relation of cerenkov time profile widths to the distance to maximum of air showers. *Journal of Physics G: Nuclear Physics*, 9(3):323.

Peters, B. (1961). Primary cosmic radiation and extensive air showers. *Il Nuovo Cimento (1955-1965)*, 22(4):800–819.

Pierre Auger Collaboration (2014). Depth of Maximum of Air-Shower Profiles at the Pierre Auger Observatory: Measurements at Energies above 10^17.8 eV. *Phys. Rev. D*, 90(12):122005, arXiv:1409.4809.

Porelli, A. and Wischnewski, R. (2017). CATS-LIDAR detection with the HiSCORE array: combined data analysis results and open questions (20/05/2017).

Postnikov, E., Astapov, I., Bezyazeekov, P., et al. (2017). Commissioning the joint operation of the wide angle timing HiSCORE Cherenkov array with the first IACT of the TAIGA experiment. *35th Int. Cosm. Ray Conf.*

Prosin, V., Berezhnev, S., Budnev, N., et al. (2016). Results from Tunka-133 (5 years observation) and from the Tunka-HiSCORE prototype. *EPJ Web Conf.*, 121(03004):03004.

Prosin, V., Budnev, N., Chvalaiev, O., et al. (2009). The Cosmic Ray Mass Composition in the Energy Range 1015- 1018 eV measured with the Tunka Array: Results and Perspectives. *Nucl. Phys. B - Proc. Suppl.*, 190(C):247–252.

Prosin, V. V., Berezhnev, S. F., Budnev, N. M., et al. (2014). Tunka-133: Results of 3 year operation. *Nucl. Instruments Methods Phys. Res. Sect. A Accel. Spectrometers, Detect. Assoc. Equip.*, 756:94–101.

Ptuskin, V., Zirakashvili, V., and Seo, E.-S. (2010). Spectrum of galactic cosmic rays accelerated in supernova remnants. *The Astrophysical Journal*, 718(1):31.

Punch, M., Akerlof, C. W., Cawley, M. F., et al. (1992). Detection of TeV photons from the active galaxy Markarian 421. *Nature*, 358:477.

RaspberryPI (2018). RaspberryPI web page. https://www.raspberrypi.org/.

Raue, M. and Mazin, D. (2010). Potential of the next generation VHE instruments to probe the EBL (I): The low- and mid-VHE. *Astropart. Phys.*, 34(4):245–256, arXiv:1005.1196.

Robitaille, T. P., Tollerud, E. J., Greenfield, P., et al. (2013). Astropy: A community Python package for astronomy. *Astron. Astrophys.*, 558:A33, arXiv:1307.6212.

Roland Winston (1970). light collection within the framework of geometrical optics. *Journal of the optical society of America*, 60(2):1964–1966.

Rowell, G., Stamatescu, V., Clay, R., et al. (2008). Tenten: A new iact array for multi-tev gamma-ray astronomy. *Nuclear Instruments and Methods in Physics Research Section A: Accelerators, Spectrometers, Detectors and Associated Equipment*, 588(1):48 – 51. Proceedings of the First International Conference on Astroparticle Physics.

Schröder, F. G. (2017). Radio detection of Extensive Air Showers (ECRS 2016). *XXV Eur. Cosm. Ray Symp.*, arXiv:1701.05496.

Sciascio, G. D. and Rossi, E. (2007). Measurement of the angular resolution of the ARGO-YBJ detector. *arXiv*, astro-ph.

Serrano, J., Lipinski, M., Wlostowski, T., et al. (2013). The White Rabbit project. *2nd Int. Beam Instrum. Conf.*, page THBL2.

Simpson, J. A. (1983). Elemental and Isotopic Composition of the Galactic Cosmic Rays. *Annual Review of Nuclear and Particle Science*, 33:323–382.

Smith, A. J. (2015). HAWC: Design, operation, reconstruction and analysis. In *Proc. Sci.*, volume 30-July-20.

Smith, A. W., Bird, R., Buckley, J., et al. (2013). CF2 White Paper: Status and Prospects of The VERITAS Indirect Dark Matter Detection Program. *ArXiv e-prints*, 1304:6367, arXiv:1304.6367.

Stamatescu, V., Rowell, G. P., Denman, J., et al. (2011). Timing analysis techniques at large core distances for multi-TeV gamma ray astronomy. *Astropart. Phys.*, 34(12):886–896, arXiv:1105.0282.

Staszak, D., Abeysekara, A. U., Archambault, S., et al. (2015). Science Highlights from VERITAS. *34th Int. Cosm. Ray Conf.*, arXiv:1510.01269.

Takita, M. (2016). The TIBET AS+MD Project; progress report 2015. In *Proc. 34th Int. Cosm. Ray Conf. - PoS(ICRC2015)*, page 969, Trieste, Italy. Sissa Medialab.

Tepe, A. t. (2012). Hawc - the high altitude water cherenkov detector. *Journal of Physics: Conference Series*, 375(5):052026.

The Cherenkov Telescope Array Consortium (2011). Design concepts for the Cherenkov Telescope Array CTA: an advanced facility for ground-based high-energy gamma-ray astronomy. *Exp. Astron.*, 32(3):193–316, arXiv:1008.3703.

The Cherenkov Telescope Array Consortium (2017). Science with the Cherenkov Telescope Array. arXiv:1709.07997.

The VERITAS Collaboration (2013). VERITAS contributions to CF6-A: Cosmic Rays, Gamma Rays and Neutrinos. *Proc. Snowmass 2013*, arXiv:1304.6764.

theHDFGroup (2018). TheHDFGroup web page. https://www.hdfgroup.org/.

Thoudam, S., Rachen, J. P., van Vliet, A., et al. (2016). Cosmic-ray energy spectrum and composition up to the ankle: the case for a second Galactic component. *Astron. Astrophys.*, 595:A33, arXiv:1605.03111.

Tibolla, O., Chaves, R. C. G., Domainko, W., et al. (2009). New unidentified Galactic H.E.S.S. sources. *31st Int. Cosm. Ray Conf.*, arXiv:0912.3811.

Tibolla, O., Vorster, M., Kaufmann, S., et al. (2013). Are most of the VHE gamma-ray unidentified sources relic PWNe? *33rd Int. Cosm. Ray Conf.*, arXiv:arXiv:1306.6833v1.

Tluczykont, M., Hampf, D., Horns, D., et al. (2011). The ground-based large-area wide-angle γ-ray and cosmic-ray experiment HiSCORE. *Adv. Sp. Res.*, 48(12):1935–1941, arXiv:1108.5880.

Tluczykont, M., Kneiske, T., Hampf, D., et al. (2009). Gamma-ray and Cosmic Ray Astrophysics from 10TeV to 1EeV with the large area (>10km2) shower detector SCORE. *31st Int. Cosm. Ray Conf.*, arXiv:0909.0445.

Tunka-HiSCORE Collaboration (2012). Gamma astronomy in the range above 10TeV: the observatory Tunka-HiSCORE.

U.S. Standard Atmosphere (1976). U.S. Standard Atmosphere. *NASA, National Oceanic and Atmospheric Administration, United States Department of the Air Force*.

Véron-Cetty, M.-P. and Véron, P. (2006). A catalogue of quasars and active nuclei: 12th edition. *Astron. Astrophys.*, 455(2):773–777.

Vietri, M. (1995). On the acceleration of Ultra High Energy Cosmic Rays in Gamma Ray Bursts. *Astrophys. J.*, 453:883, arXiv:9506081.

Vogel, H., Laha, R., and Meyer, M. (2017). Diffuse axion-like particle searches.

Wakely, S. P. and Horan, D. (2008). TeVCat: An online catalog for Very High Energy Gamma-Ray Astronomy. *International Cosmic Ray Conference*, 3:1341–1344.

Waxman, E. (1995). Cosmological gamma-ray bursts and the highest energy cosmic rays. *Phys. Rev. Lett.*, 75(3):386–389, arXiv:9505082.

Weekes, T. C., Cawley, M. F., Fegan, D. J., et al. (1989). Observation of TeV gamma rays from the Crab nebula using the atmospheric Cerenkov imaging technique. *Astrophysics J.*, 342:379–395.

Wischnewski, R., Berezhnev, S., Uckner, M. B., et al. (2013). Status of the HiSCORE experiment. *33rd Int. Cosm. Ray Conf.*, pages 1–4.

Wischnewski, R., Brueckner, M., and Porelli, A. (2015). Time synchronization with white rabbit - Experience from tunka-HiSCORE. In *Proc. Sci.*, volume 30-July-20.

Yorks, J. E., Palm, S. P., McGill, M. J., et al. (2016). CATS Algorithm Theoretical Basis Document. https://cats.gsfc.nasa.gov/.

Zatsepin, G. T. and Kuzmin, V. A. (1966). Upper limit of the spectrum of cosmic rays. *JETP Lett.*, 4:78–80.

Zhang, Y., Gou, Q. B., Cai, H., et al. (2017). New prototype scintillator detector for the Tibet ASγ Experiment. *J. Instrum.*, 12(11):P11011–P11011, arXiv:1712.06661.